Department of Chemistry

Ice-templated Porous Carbons for Energy Storage Applications

Thesis is submitted in accordance with the requirements of the
University of Liverpool for the degree of Doctor of Philosophy

by

Aled Deakin Roberts

October 2016

Acknowledgements

I would like to thank my supervisors Dr. Haifei Zhang and Dr. Xu Li for the opportunity to work in their research groups and undertake this PhD project. I thoroughly enjoyed my time at the University of Liverpool and IMRE, and the opportunity to live and work in Singapore for 2 years was a fantastic and life-changing experience. I would also like to extend a big thanks to Dr. Adham Ahmed, Dr. Mike Barrow, Dr. Robert Woodward, Ms. Ceilidh Armer, Ms. Meggi Lübke and Mr. Richard Hayes who have been helpful and supportive throughout my project, and also Dr. Suxi Wang who was my mentor at IMRE.

I would like to thank all the lab technicians who have helped me with the various analysis techniques and measurements, in particular Mr. Rob Clowes in Liverpool and Ms. Siew Yee Wong at IMRE. I also extend a big thanks to Mr. Jet Sing-Lee for help with CO_2 and H_2 uptake measurements and for letting me borrow his book on supercapacitors.

Lastly I would like to thank all my friends and family for all their support and encouragement, especially my girlfriend Ann – whom I dedicate this thesis to as a birthday present.

Acknowledgements for Contributions to Specific Chapters

In Chapter 3, I would like to acknowledge and thank Dr. Adham Ahmed for help with MIP, Dr. Haifei Zhang for SEM images, Dr. Robert Clowes for help with PXRD and gas sorption measurements, and the Microanalytical service at the University of Liverpool for elemental analysis. I would like to especially thank Dr. Suxi Wang for performing the electrochemical measurements (CV and CCP) in this chapter as we did not have the facilities in Liverpool.

In Chapter 4, I would like to thank Mr. Jet Sing-Lee and Mr. Robert Clowes for performing the H_2 and CO_2 uptake measurements. I would also like to thank Mr Lim Poh Chong for help with PXRD measurements, and Sam Fishlock and Iain Aldous for help with Raman spectroscopy.

In Chapter 5, I would like to thank Ms. Siew-Yee Wong for help with the FTIR, Mr Lim Poh Chong for help with PXRD measurements, Dr. Adham Ahmed for help with MIP and Sam Fishlock for help with Raman spectroscopy.

I would also like to further thank Dr. Mike Barrow for his help with the TGA measurements needed for my thesis corrections.

Abstract

Porous carbons prepared *via* templating methodologies have shown excellent performance for various energy storage applications, such as electrodes in batteries, supercapacitors and as gas storage materials. Despite the impressive performances often reported, various issues such as complex and multi-step synthesis strategies have impeded their implementation in practical devices, and so there is a need to develop new, low-cost and commercially viable strategies for their fabrication. This thesis explores an unconventional method for the preparation of templated carbons – a process termed *ice-templating*. Ice-templating, as will be discussed in the forthcoming chapters, is a relatively simple technique holds several advantages over more conventional templating strategies. Having its own difficulties and shortcomings, only a few papers had been published on ice-templated porous carbons (ITPCs) prior to the commencement of this PhD. This thesis describes the ways in which we explored and overcame these difficulties to successfully prepare a number of ice-templated porous carbons, before evaluating their performance as materials for various energy storage devices.

Abbreviations

3DOM	Three-dimensional Ordered Macroporous Carbon
AC	Activated Carbon
BJH	Barrett-Joyner-Halenda
BET	Brunauer–Emmett–Teller
CCS	Carbon Capture and Storage
CCU	Carbon Capture and Utilisation
CIO	Carbon Inverse Opal
CTAB	Cetyltrimethylammonium Bromide
CVD	Chemical Vapour Deposition
CMP	Conjugated Microporous Polymer
CCP	Constant Current Potentiometry
COF	Covalent Organic Framework
CV	Cyclic Voltammetry
DEA	Diethanolamine
DMSO	Dimethyl Sulfoxide
DFT	Density Functional Theory
EDX	Energy-dispersive X-ray Spectroscopy
ECDL	Electrochemical Double Layer
FTIR	Fourier Transform Infrared Spectroscopy
FE-SEM	Field Emission Scanning Electron Microscopy
FWHM	Full Width at Half Maximum Intensity
GO	Graphene Oxide
HIPE	High Internal Phase Emulsion
IGCC	Integrated Gasification Combined Cycle
IR	Infrared Spectroscopy
IUPAC	International Union of Pure and Applied Chemistry
ISISA	Ice Segregation Induced Self Assembly
ITPC	Ice-templated Porous Carbon
IHP	Inner Helmholtz Plane
LIB	Lithium-ion Battery
LIS	Lithium-sulfur Battery
MCMB	Mesosphere Carbon Microbead
MCM	Mobil Crystalline Material
MOF	Metal Organic Framework
MEA	Monoethanolamine

MIP	Mercury Intrusion Porosimetry
NMP	N-methyl Pyrrolidinone
O/W	Oil in Water
OMC	Ordered Mesoporous Carbon
PAN	Poly(acrylonitrile)
PMMA	Poly(methyl methacrylate)
PSS	Poly(sodium 4-styrenesulfonate)
PVDF	Poly(vinylidene fluoride)
PXRD	Powder X-ray Diffraction
RGO	Reduced Graphene Oxide
SEM	Scanning Electron Microscopy
SBA	Santa Barbara Amorphous
SEI	Solid Electrolyte Interphase
TIPS	Thermally Induced Phase Separation
TGA	Thermogravimetric Analysis
W/O	Water in Oil
XPS	X-ray Photoelectron Spectroscopy
XRD	X-ray Diffraction
ZIF	Zeolitic Imidazolate Framework

Formulaic Abbreviations

2θ	Scattering angle
A	Area
a_m	Cross-sectional area of one adsorbate molecule
β	Line broadening at FWHM
C	Capacitance
C_g	Gravimetric capacitance
C-rate	Current rate
C_{BET}	BET constant
C_{irr}	Irreversible capacity
C_{rev}	Reversible capacity
C_n	Capacitance at *n*th electrode
C_T	Theoretical capacity
C_{TOT}	Total capacitance
D_P	Pore diameter
E	Electrical potential

e	Elementary charge
E_1	Heat of adsorption for the first layer
E_L	Heat of adsorption for layers beyond the first
E_{pa}	Anodic peak potential
E_{pc}	Cathodic peak potential
F	Faraday’s constant
G	Gibbs free energy
I	Current
I_D	Intensity of D-band
I_G	Intensity of G-band
I_{pa}	Anodic peak current
i_{pc}	Cathodic peak current
K	Equilibrium constant
k_a	Rate constant for adsorption
k_d	Rate constant for desorption
K_S	Dimensionless shape factor
L	Length
L_c	Crystallite size along the c-axis
L_a	Crystallite size along the a-axis
m	Mass
$M_{(g)}$	Gaseous phase adsorbent
$MS_{(g)}$	Solid adsorbate
N	Total number of adsorption sites
n	An integer number
N_A	Avagadro’s constant
n_a	Amount of gas adsorbed in moles
n_e	Number of available electrons
n_m	Amount of gas adsorbed when all adsorption sites are occupied
N_s	Number of sites occupied by an adsorbate
P	Partial pressure
P_0	Saturation pressure
P_W	Power
Q	Charge
Q_A	Anodic charge
Q_C	Cathodic charge
R	Ideal gas constant
R_e	Electrical resistance

s	Potential sweep rate
$S_{(g)}$	Solid Adsorbate
SA_{lang}	Langmuir surface area
T	Temperature
t	Time
V	Volts
V_a	Volume of gas adsorbed
V_m	Volume of gas adsorbed when all adsorption sites are occupied
γ	Surface tension
ΔG	Change in Gibbs free energy
ΔG^o	Change in Gibbs free energy under standard conditions
ΔE	Potential window
θ	Fractional Coverage of Adsorbate
θ_C	Contact angle
λ	Wavelength
ρ	Resistivity
σ	Conductivity
τ	Mean crystallite size

Publications and Patents

1. Roberts AD, Li X, Zhang H (2014) *Chem Soc Rev* 43(13):4341–4356.
   “Porous carbon spheres and monoliths: morphology control, pore size tuning and their applications as Li-ion battery anode materials”

2. Roberts AD, Wang S, Li X, Zhang H (2014) *J Mater Chem A* 2(42):17787–17796.
   “Hierarchical porous nitrogen-rich carbon monoliths via ice-templating: high capacity and high-rate performance as lithium-ion battery anode materials”

3. Roberts AD, Li X, Zhang H; *Singapore patent no. 10201404439R*. Issued July 2014
   “Ice-template derived porous carbons and doped carbons and their application for energy storage”

4. Roberts AD, Li X, Zhang H (2015) *Carbon* 95:268–278.
   “Hierarchically porous sulfur-containing activated carbon monoliths via ice-templating and one-step pyrolysis”

5. Liu X, Roberts AD, Ahmed A, Wang Z, Zhang H (2015) *J Mater Chem A* 3(30): 15513-15522
   “Carbon nanofibers by pyrolysis of self-assembled perylene diimide derivative gels as supercapacitor electrode materials”

6. Woodward RT, De-Luca F, Roberts AD, Bismark A (2016) *Materials* 9(9):776-786
   “High-surface-area, emulsion-templated carbon foams by activation of polyHIPEs derived from pickering emulsions”

7. Roberts AD, Lee JSM, Wong SY, Li X, Zhang HF (2017) *J Mater Chem A* (Advance Article)
   “Nitrogen-rich activated carbon monoliths via ice-templating with high CO_2 and H_2 adsorption capacities”

Contents

Chapter 1

Introduction and Literature Review

Some contents of this chapter have been published in the journal *Chemical Society Reviews*.
(Roberts AD, Li X, Zhang H (2014). *Chem Soc Rev* 43(13):4341–4356.)

List of Figures

List of Tables

1.1. Introduction

Carbon, in the form of coal and other fossil fuels, powered the industrial revolution and fuelled the technological transformation into modern society. Today, fossil fuels account for approximately 81 % of the world's energy needs,(1) however there is now an urgent need to reduce this dependency due to the irrefutable link between associated CO_2 emissions and climate change. To achieve this, there has been a huge global effort to develop and deploy alternative and renewable energy sources such as solar, wind and hydro-electricity.(2)

One major problem faced by renewable energy sources such as these is that their output is intermittent, irregular, and often fails to correlate with demand.(3) The efficiency and dependability these resources could be greatly increased if coupled with efficient and low cost energy storage system, which would regulate the output allowing greater utilisation.(3)(4) Advanced energy storage devices would also improve the performance of, and accelerate the transition to, electric vehicles – further reducing fossil fuel dependency and global CO_2 emissions.(5)

Just as carbon fuelled the industrial revolution, carbon-based materials may offer a solution to our present energy storage needs. Graphitic carbon is currently used as the active anode material in modern lithium-ion batteries,(6) and activated carbon has been employed in the electrodes of supercapacitors,(7) fuel cells(8) and as H_2 and CO_2 gas storage materials.(7)(9)(10) With the recent discoveries of new allotropes of carbon with remarkable physical properties, such as carbon nanotubes, fullerenes and graphene, it seems almost certain that carbon-based materials will continue to be hugely important for energy storage – among other applications – well into the future.(11)(12)(13)(14)(15)(16)

1.2. Porous Materials

A porous material, as defined by The International Union of Pure and Applied Chemistry (IUPAC), is a solid with cavities, channels or interstices which are deeper than they are wide.(17) Such materials can be categorised by their sizes of the pores, where *microporous* materials have pore diameters less than 2 nm, *mesoporous* materials have pore diameters between 2 and 50 nm, and *macroporous* materials have pore diameters greater than 50 nm. Porous materials with a significant proportion of pores spanning more than one of these size categories can be defined as having *hierarchical* porosity.(18) Porous materials, which can consist of organic, inorganic or a mixture of building blocks, have a very wide variety of practical applications, including areas such as chromatography,(19)(20)(21) energy storage,(11)(22)(23)(24) heterogeneous catalysis(25)(26) and gas separation and storage.(27)(28)(29)

1.3. Carbon

Carbon, derived from the Latin word for charcoal – "*carbo*", is unique in its versatility as an element. Stemming from its ability to form stable sp^3, sp^2 and sp bonds with itself and many other elements, its compounds not only underpin the disciplines of organic- and bio- chemistry – and therefore all like that is currently known – but it can also exist as a wide variety of allotropes with widely varying physical properties.(14)(15)(16)(30)(31) Diamond, for instance, is transparent and colourless, and possesses the highest hardness and thermal conductivity of any known bulk material.(32) Graphite, on the other hand, has a grey-metallic lustre, is highly electronically conductive and is so soft that it can be employed as a dry lubricant.(31)

These forms of carbon, as well as others such as coal, charcoal and soot (carbon black), have been known and utilised by humans for millennia.(15)(16) Others forms are however very recent discoveries – yet are arguably no less significant. The fact that Nobel Prizes were awarded for the discovery of fullerenes in 1996 and graphene in 2010 highlights the significance of these new carbon allotropes to humanity.(33)(34)

Amorphous carbon is another form of carbon, which, unlike other allotropes, lacks long range crystallinity.(35) Between truly amorphous carbon and single crystal graphite, a spectrum of *polycrystalline* carbon materials exists (Figure 1.1.), *i.e.* amorphous carbon containing ever larger graphitic domains until it can be considered graphite.(14)(15)(16) For clarity, the term *semi-graphitic* is used throughout this thesis to describe carbons in this gray area, although other authors use words such as *turbostratic*, *disordered*, and *pseudographitic* to describe this form of carbon.(14)(15)(16)(36)(37)(38)(39)

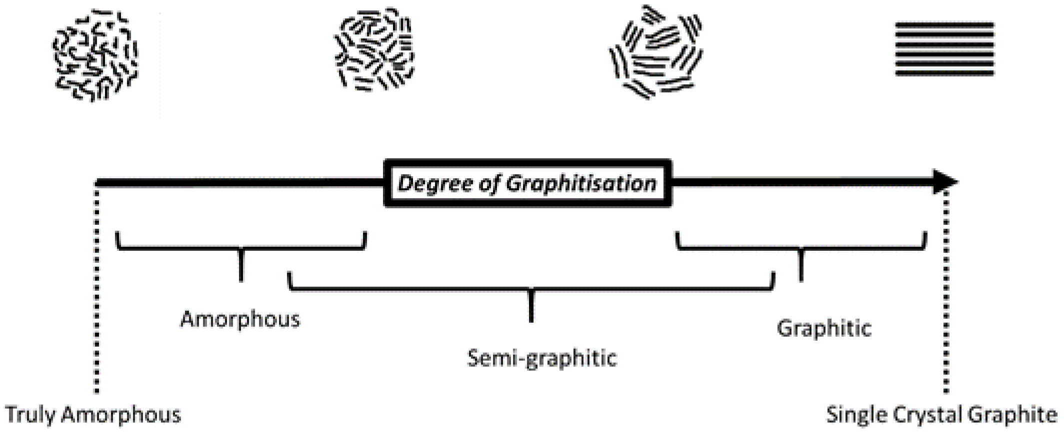

Figure 1.1. Spectrum of semi-graphitic carbons between amorphous carbon and single crystal graphite

Rosalind Franklin, prior to her pioneering work on DNA crystallography, further categorised semi-graphitic carbons as either graphitising (*soft*) or non-graphitising (*hard*) carbons.(40) By heating cokes and charcoals to temperatures up to 3000 °C, she found that whilst some would be converted into crystalline graphite as expected, some remained as porous, isotropic materials with still only very small domains of graphite-like order (*glass-like* carbon). The models she proposed are depicted in Figure 1.2. Here, graphitising *soft* carbons have almost parallel, anisotropic graphitic crystallites, whereas in non-graphitising *hard* carbons the crystallites are isotropic (randomly ordered). The size, orientation and other properties of these crystallites are often referred to as the *nanotexture* of the carbon.(41)

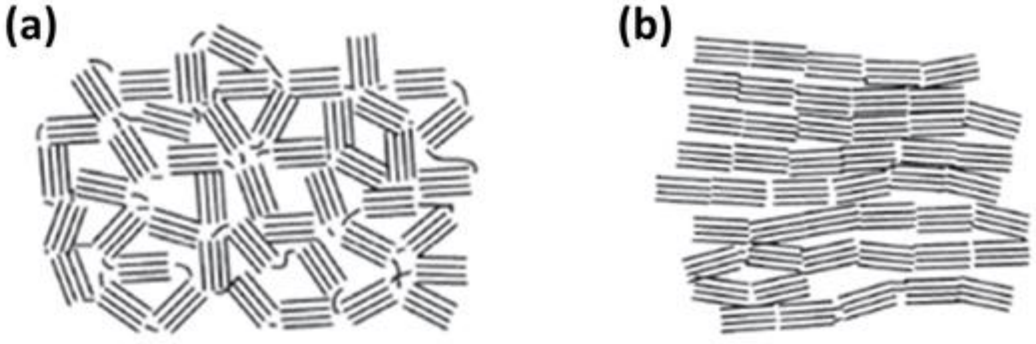

Figure 1.2. The Franklin models for the classification of a) non-graphitising and b) graphitising carbons (40)

1.4. Pyrolysis and Carbonisation

Pyrolysis, derived from the Greek words for fire "*pyro*" and separation "*lysis*", is the thermal decomposition of a material at elevated temperatures.(42) Pyrolysis of an organic feedstock is conducted in an oxygen-free atmosphere (otherwise *combustion* occurs) and can produce gaseous, liquid and/or solid by-products – where the solid residue (if any) would be a carbon-rich char.(43) The carbon content of the char, as well as the degree of graphitisation, generally increases with pyrolysis temperature and duration.(35)

Carbonisation is the conversion of a carbon containing (*carbonaceous*) substance to a residue with a higher carbon content, and can occur in the solid, liquid or gaseous phase.(44) The pyrolysis of wood into charcoal and coal into coke are examples of carbonisation, (42)(45) but other forms also exist – such as the hydrothermal treatment of biomass and the dehydration of glucose with sulphuric acid.(46)(47)

Carbonisation *via* pyrolysis is a complex process involving many simultaneous reactions, which include: heterolytic bond cleavage, dehydration, isomerisation, hydrogen transfer, C-C bond formation, dehydrogenation, cyclisation, aromatisation and polycondensation among others.(14)(15)(16)(35)(39)(48)(49) These reactions, which occur mainly within the temperature range of 600 – 1300 °C,(14) lead to the formation of various polycyclic species which, on further condensation and lateral π-π stacking, form the graphite-like crystallites associated with semi-graphitic carbons.(14)(15)(16)(39) Higher temperature treatment (~2000 to 3000 °C) can lead to further fusion of the crystallites to form graphitic carbon (*graphitisation*) or, if the carbon is non-graphitisable, a highly isotropic *glass-like* carbon.(14)(15)(16)(35) By-products of carbonisation include many gaseous species (*e.g.* CO_2, CO, $(CN)_2$, H_2O, CH_4, NO_x, N_2, H_2, SO_x), other volatile low molecular weight species (*e.g.* alcohols, keytones, aliphatic and aromatic compounds), soot and ash.(14)(16)(35)(39)

Due to the complexity of the cascade of reactions occurring during carbonisation, and their difficulty to monitor analytically, numerous theories have been proposed as to the underlying mechanisms occurring during carbonisation.(14) Further complicating matters, carbonisation processes can vary significantly depending on the nature of the precursors and carbonisation conditions;(14)(39)(50) for instance, it has been shown that vacuum carbonisation of cellulose produces a greater amount of tarry by-products than carbonisation under N_2 due to different reaction pathways occurring.(51)

In general, for the successful and high-yield carbonisation of an organic feedstock, certain rules-of-thumb should be followed, namely:

I. The feedstock should have a high carbon content, and therefore a high degree of sp^2 and/or *sp* hybridised carbon. A low carbon content will evidently lead to a low yield on carbonisation as non-carbon species are removed. sp^3 hybridised carbon (*i.e*. alkyl chains) will likely decompose and not contribute to the solid carbon char, although in some instances sp^3 hybridised carbon can undergo dehydrogenation during heat treatment (forming sp^2 hybridised carbon) and subsequently contribute to the char.(39)

II. Relatively high molecular weight precursors should be employed. Low molecular weight precursors are relatively volatile and are therefore prone to sublime during carbonisation, reducing the yield. An exception is if the species undergoes polymerisation *in-situ*, prior to high carbonisation temperatures, as is the case for glucose and other saccharides, which polymerise at elevated temperatures prior to carbonisation (*caramelisation*).(52)

III. The precursors should be covalently crosslinked, or undergo *in-situ* crosslinking, prior to carbonisation.(39)(53) This is again to prevent sublimation of various low molecular weight species', and to prevent melting of the substance prior to carbonisation. Crosslinking is especially important if the original morphology of the precursor needs to be preserved – as is the case in this thesis – and is therefore an important consideration for applications such as carbon fibre manufacture.(39) Crosslinking can be achieved in several ways, including partial pre-oxidation of the precursor (*e.g.* for PAN, cellulose and pitch),(54)(55) the incorporation of certain crosslinking agents (*e.g.* HCl, I_2, $ZnCl_2$ and ammonium sulphates and phosphates),(16)(39)(56)(57) and the use of thermosetting precursors such as phenol-formaldehyde and poly(furfuryl alcohol) which polymerise and crosslink when heated.(16)

1.5. Heteroatom Doped Carbons

The versatility of elemental carbon allows it to exist as myriad forms with widely ranging physical properties. This versatility also permits the insertion of other elements (*doping*) into the framework of amorphous, graphitic and semi-graphitic carbons, which act to modify their electronic, surface and interfacial properties.(58)(59)(60)(61) Various functional groups can also be introduced to the surface of the carbons, which may also act to alter their physiochemical properties.(61) Controlled doping and functionalisation of porous carbons can thereby be employed tune the properties for particular applications.(58)(60)(61)

Heteroatoms, namely oxygen (O), nitrogen (N), sulphur (S), phosphorous (P) and boron (B), are typically employed as carbon dopants since their atomic radii are close to that of carbon, permitting insertion into the carbon lattice without significant distortion.(58) Nitrogen doping has been the most widely studied of these since, as a neighbouring element to carbon on the periodic table, it is chemically relatively easy to bring the two elements together. Nitrogen can exist in a variety of forms within the carbon lattice (Figure 1.3.), most commonly as pyridinic, pyrrolic, quaternary and oxidised-nitrogen.(62)

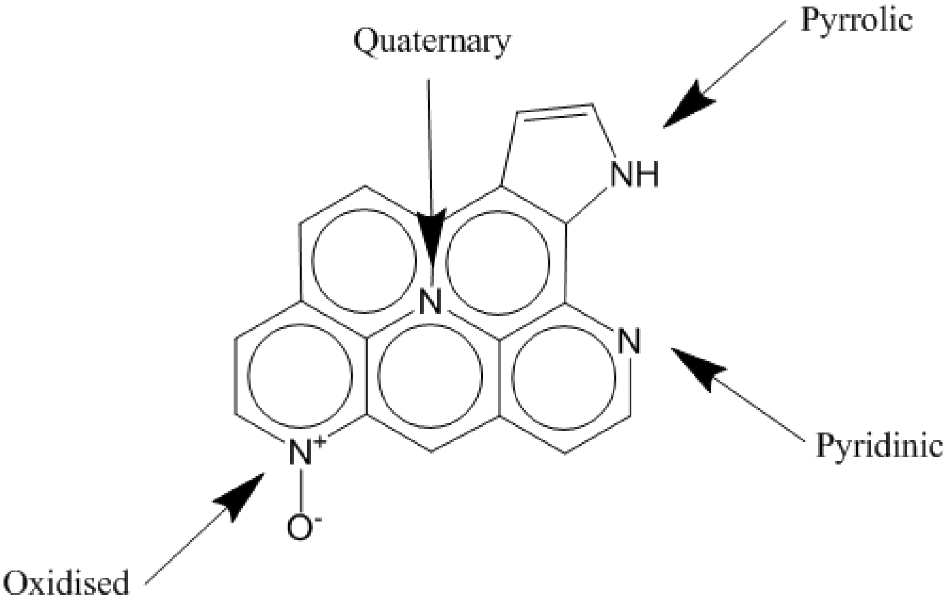

Figure 1.3. Examples of the various states nitrogen can exist as within an N-doped carbon

Possessing an extra electron at ground state, N can introduce *n*-type electronic modification to the carbon structure – which can be delocalised through the sp^2 hybridised π-bonding network of the graphitic domains.(58) This kind of modification can lead to significantly enhanced performance in the areas of energy storage, for instance in Li-ion battery anode materials,(63)(64)(65) supercapacitor electrodes,(63)(66)(67)(68) gas sorption materials,(69)(70) and electrocatalysts in the reduction of O_2 in fuel cells.(71)(72)(73)

Methods employed to introduce such dopants into the carbon structure can be classified as *pre*-treatment, *post*-treatment and *in-situ* methods.(58)(74) *Pre*- or *post*- synthetic amine modification or ammonia treatment are common methods to introduce nitrogen functionality into carbons, whereas *in-situ* doping typically relies on the incorporation of nitrogen from the precursor materials with retention upon carbonisation.(74) *In-situ* processes have advantages over the other methods in terms of simplicity and ease of processing.

1.6. Porous Carbons

Coke and charcoal were the first forms of artificial porous carbons utilised by humans and have been manufactured on a large scale for centuries.(14)(15)(16) Formed from the pyrolysis of coal and biomass respectively, they proved to be an effective fuel for heating, cooking and metalworking as they burn hotter and cleaner than their parent feedstocks.(75)

Coke had been produced in ancient China from about 300 *A.D.* where it was first used for heating and cooking, before being used as a fuel for iron working from about 1000 *A.D.*(76) The first documented use of charcoal is in 3750 *B.C.* where it was used by the Egyptians as a fuel to smelt copper, tin and zinc ores for the manufacture of bronze.(77) Today, porous carbons are manufactured *via* a myriad of techniques and are still utilised as fuels for metal smelting, for water treatment and medicinal purposes, but also many other applications such as supercapacitor electrodes, catalysis supports, and gas separation materials.(14)(16)(77)(78)

The following subsections elaborate on the specific forms of porous carbon that are relevant to this thesis.

1.6.1. Activated Carbons

Activated carbon (AC) is a form of carbon that has been processed to increase its high surface area and pore volume.(44) ACs typically have specific surface area values within the range of 500 – 3000 $m^2\ g^{-1}$.(79)

The first ACs were documented by the Romans, where the Roman researcher and writer Pliny the Elder wrote: “It is only when ignited and quenched that charcoal itself acquires its characteristic powers" – describing an early method for the steam activation of charcoal.(80) Modern forms of AC were only developed and produced industrially at the beginning of the 20th century, where they had uses which included decolourisation in the food and cosmetics industries, and in gas mask filters during the First World War.(44)

The methods employed for carbon activation can be categorised as either chemical or physical means. Physical activation, a process patented by Ostreijko in 1900, involves the exposure of the carbon precursor to a low concentration of an oxidising gas (*e.g.* H_2O, CO_2 or O_2) at temperatures typically in the region of 900 – 1200 °C.(77) This process is thought to increase porosity by burning off tarry pyrolysis by-products trapped within pores, as well as burning away more reactive areas of the carbon framework to develop porosity.(7) Chemical activation, developed by Bayer in 1915, on the other hand involves the treatment of the carbon precursor with a solid activating agent (e.g. KOH, ZnCl or H_2PO_4) at temperatures typically in the region of 400 – 800 °C.(77) Here the activation agents can act as oxidants (in the case of KOH), which develop porosity *via* oxidative etching of the carbon, or dehydration agents (in the case of H_2PO_4) which develop porosity through a crosslinking and templating mechanism.(7) It has also been proposed that during chemical activation, the intercalation of metal ions between graphene sheets causes their expansion and exfoliation, exposing high surface areas and developing microporosity.(7)

As well as extremely high surface areas, ACs possess a very large amount of micropores. Combined with relatively low cost of manufacture, these properties make ACs ideal adsorbent materials and have a variety of uses in modern society.(44) In regards to energy storage, ACs are currently employed as electrode materials in electrochemical double layer capacitors (*supercapacitors*), and are being investigated as materials for H_2 and CO_2 gas storage.(7)(44)(81)

1.6.2. Templated Carbons

Porous carbons in the form of charcoal, coke and activated carbons have a wide variety of uses and are relatively simple to fabricate. Although porosity and surface area can be controlled to some degree, *i.e.* though choice of precursor and pyrolysis/activation conditions, it is generally difficult to tailor the porosity to a high degree as can be done with other kinds of porous materials such as zeolites, MOFs, mesoporous silicas, *etc*.(82)(83)

Since some applications require, or would greatly benefit from, greater control over the pore characteristics, there has been much research over the last few decades in developing methods that control the pore size distribution of carbons.(83) The majority of this research has focused on so-called *templating* methodologies, which involve the formation of a porous architecture (the template) which directs a carbon precursor, before carbonisation and subsequent template removal to give a templated carbon.(83)(84)(85)(86) Since the porous templating entities, such as mesoporous silicas, MOFs and zeolites, can have very ordered structures with well-defined pores, highly ordered porous carbons can therefore be obtained.

The main templating methodologies can be categorised as either '*hard*' or '*soft*' methods,(85) the details of which are given in the following sub-sections. Recently, new and relatively facile templating routes have been developed for the fabrication of porous carbons – these routes, namely ice- and emulsion- templating, are also described in following sub-sections.

1.6.3. Hard Templated Carbons

Hard templating (also known as *nanocasting*) methodologies involve the pre-fabrication of a porous structure – such as a metal organic framework (MOF), zeolite, mesoporous silica, or porous assembly of silica or polymer spheres – into which carbon (or a carbon precursor, which is subsequently carbonised) is deposited.(83) Removal of the original template – typically though acid or base etching for inorganic templates – then leaves a porous carbon with a structure that is the inverse of the original template (Figure 1.5.).(83)(87)

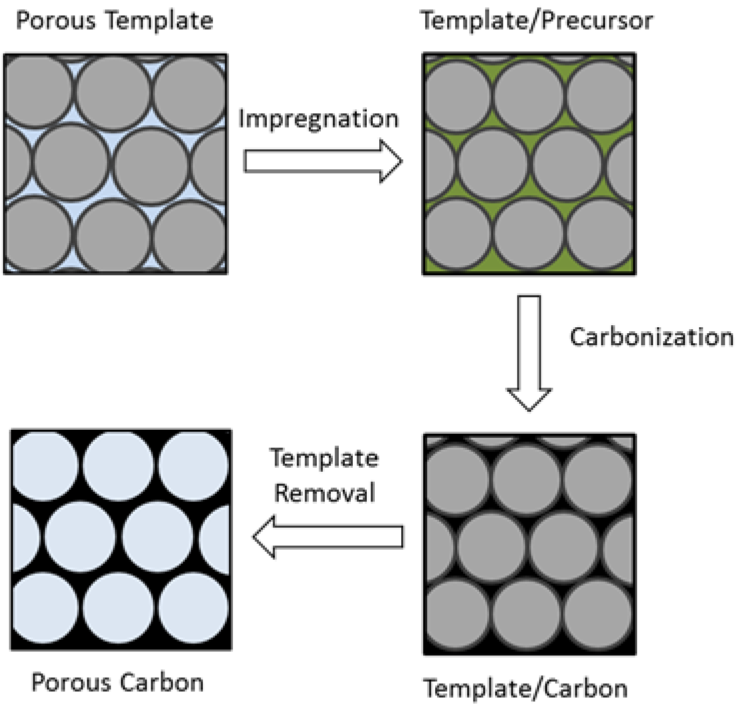

Figure 1.4. Schematic representation of the hard templating process to prepare porous carbons

The hard template carbonisation method was first reported in 1986 by Knox and co-workers, who impregnated a packed gel of silica spheres with a phenol-formaldehyde mixture, which was subsequently polymerised and carbonised at 900 °C.(88) Dissolution of the silica template with KOH revealed a porous carbon with a BET surface area up to 600 m^2 g^{-1}. Ralchenko and co-workers prepared highly ordered porous carbons in 1998 by employing a similar method;(89) here they first prepared a colloidal crystal of highly ordered silica spheres (synthetic opal) before impregnating with a furfuryl-alcohol mixture, polymerising, etching the template with HF acid and carbonising the resin. Using the same synthetic opal templates, they also introduced carbon into the pores *via* chemical vapour deposition (CVD) of propylene gas, which resulted in the carbon having a higher degree of graphitisation. They termed these templated carbons "Carbon Inverse Opals", or CIOs (Figure 1.6.).

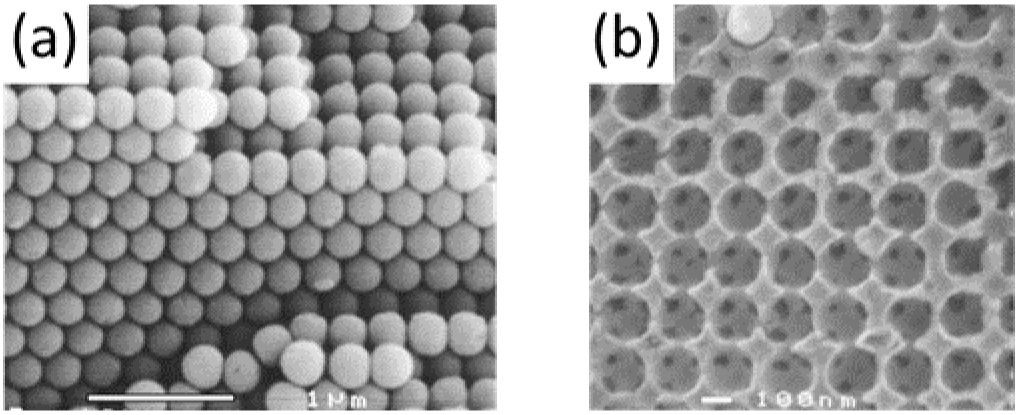

Figure 1.5. SEM images of a) porous SiO_2 opal template, b) graphitic CIO (89)

The following year, Jun and co-workers prepared a templated carbon by employing the mesoporous silica MCM-48 as a hard template and sucrose as a carbon precursor.(90) The resultant carbon, termed CMK-1, had highly ordered mesopores of about 3 nm in diameter and a high BET surface area of 1980 m^2 g^{-1}. Following this report, a number of other mesoporous silica templated porous carbons were prepared; employing SBA-1, SBA-3, SBA-15 and MCM-45 as templates, the resultant carbons were termed CMK-2, CMK-3, CMK-4 and CMK-5, respectively (Figure 1.7.).(91) Mesoporous templated carbons such as these are commonly termed "Ordered Mesoporous Carbons", or OMCs.

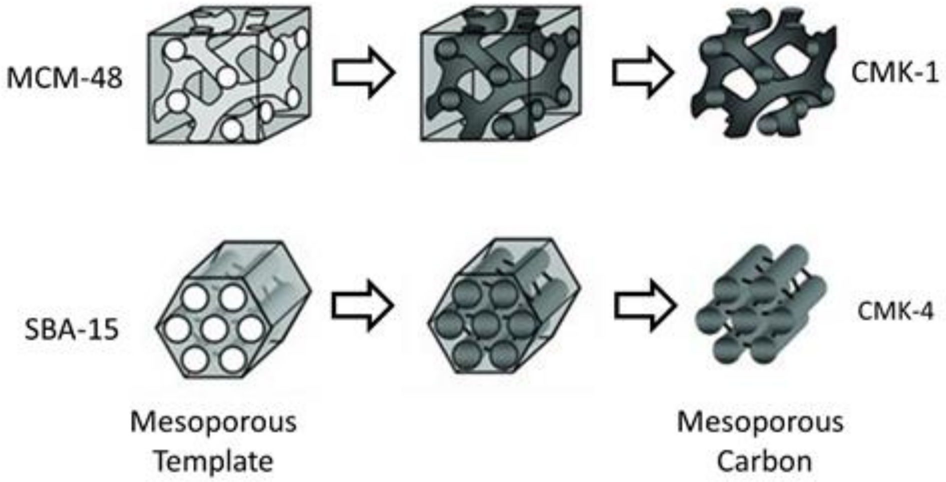

Figure 1.6. Schematic representation of the preparation of OMCs from mesoporous silica templates (82)

Similarly, zeolites have also been employed as hard templates to prepare porous carbons (Figure 1.8.).(82)(84)(92) These carbons, reflecting the nature of their parent zeolite templates, are microporous in nature and can poses extremely high BET surface areas in excess of 4000 $m^2 g^{-1}$.(82)

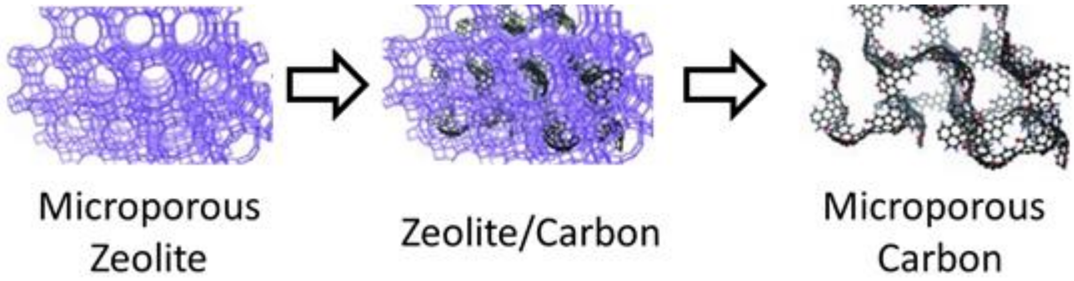

Figure 1.7. Schematic representation of the preparation of ordered microporous carbons from a zeolite template (82)

Templated carbons consisting of macropores can also be fabricated *via* hard templating routes and are often termed “3D Ordered Macroporous”, or 3DOMs. Relatively large silica or polymer spheres assembled into colloidal crystals have been employed to prepare macroporous templated carbons. For instance, Stein and co-workers utilised poly(methyl methacrylate) (PMMA) polymer spheres assembled into a colloidal crystal as a macroporous template.(93) The colloidal crystal was soaked in a resorcinol formaldehyde solution, which was then crosslinked through thermal polymerisation at 85 °C forming a resin. Carbonisation at 900 °C simultaneously converted the resin to carbon whilst removing the PMMA templates through thermal decomposition – meaning no extra steps or harsh etching agents were required to remove the templates.

It is also possible to prepare hierarchically porous carbons by employing a hierarchically porous hard template. Maier and co-workers used a bimodal porous silica as a template to prepare a hierarchical macro-/meso- porous carbon.(94) By employing mesosphere pitch as the carbon precursor, introduced into the pores by soaking, the resultant porous carbon had macropores of 1 - 4 µm, mesopores of about 7.3 nm, and a BET surface area of 330 m^2 g^{-1}. Yu and co-workers demonstrated another example of the preparation of a hierarchical porous carbon;(95) here they mixed monodisperse poly(styrene) spheres with much smaller silica spheres and allowed the mixture to self-assemble into a bimodal colloidal crystal (Figure 1.9.). Calcination burned off the poly(styrene) spheres, whilst sintering the silica to give the hierarchically porous template. The template was then impregnated with furfuryl alcohol, which was crosslinked prior to carbonisation. Subsequent etching removed the silica, giving the hierarchically porous carbon. The macropores – templated by the poly(styrene) spheres – had diameters of about 370 nm, whilst the silica-templated mesopores were about 20 nm in diameter. The BET surface area of the carbon was 1120 m^2 g^{-1}.

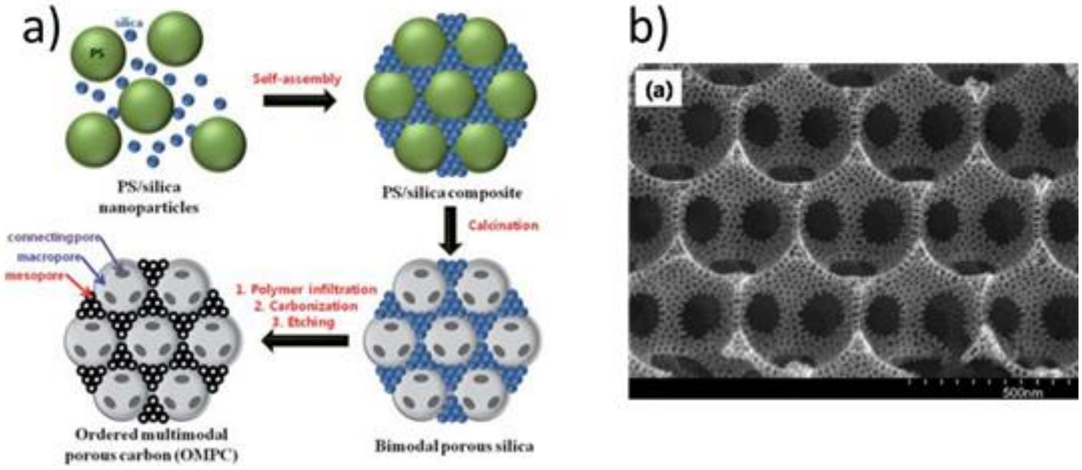

Figure 1.8. a) Schematic representation of the process to prepare a hierarchically porous carbon from a bimodal template, and b) SEM image of a bimodal porous carbon (95)

As well as the ones mentioned here, numerous other hard templates, for instance clays,(96) MOFs(97) and inorganic salts,(98) have also been employed to prepare porous carbons; with numerous books and reviews published on much as subject.(82)(84)(99) But despite the numerous merits of such hard templating methodologies – such as highly ordered structures, a wide range of precursors and templates, and a wide range of porosities and surface areas – the relatively complex synthesis strategies, involving the synthesis and subsequent removal of sacrificial templates, render the resultant porous carbons unattractive to produce commercially. However, numerous soft-templating routes, as detailed below, have been developed in order to prepare similar porous carbons *via* less complex and more economical routes.

1.6.4. Soft Templated Carbons

Rather than employing pre-formed templates as is the case for hard-templating, soft-templating methods involve the self-assembly of polymers, surfactants or colloidal materials in the presence of a carbon precursor solution, which is then crosslinked/polymerised to set the carbon precursor around the soft template (Figure 1.10.).(99)(100)(101) Removal of the solvent and subsequent carbonisation then yields the templated porous carbon, where the soft template, if not already decomposed during the carbonisation process, it then removed *via* washing, dissolution or some other means.

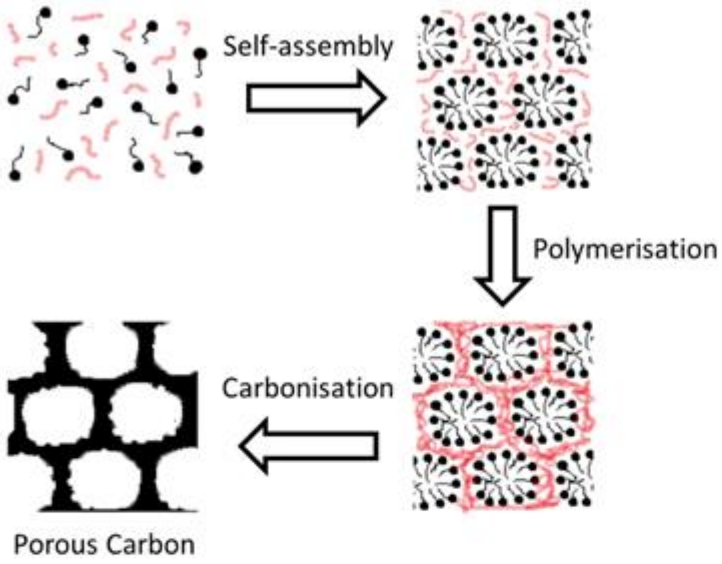

Figure 1.9. Schematic representation of a general soft-templating method to prepare a porous carbon

One of the first examples of the fabrication of a porous carbon *via* a soft templating route was by Oh and Lee in 2002.(102) Here they thermally polymerised resorcinol formaldehyde in the presence of a cetyltrimethylammonium bromide (CTAB) surfactant. The CTAB, forming micelles, encapsulated the resorcinol formaldehyde which, upon polymerisation, crosslinked to form clusters. The clusters, formed from spheres of approximately 200 nm in diameter, had sufficient mechanical stability to withstand air-drying without collapsing, and could then undergo carbonisation to give a porous carbon (Figure 1.11.). The measured BET surface area was 422 $m^2 g^{-1}$, but could be varied to a degree by changing the pH on polymerisation.

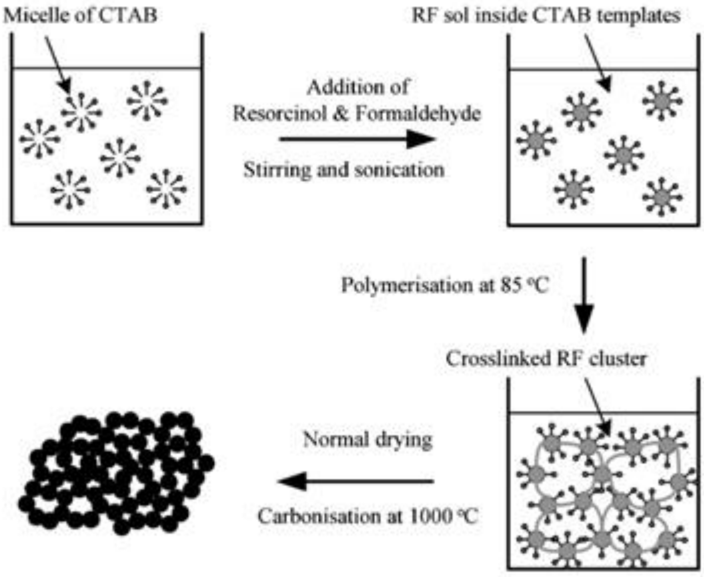

Figure 1.10. Schematic representation of the method employed by Oh and Lee to prepare a soft-templated porous carbon (102)

Another early example of a soft-templated carbon was reported by Zhao and co-workers in 2005.(103) Here they employed the amphiphilic block co-polymer Pluronic® F-127 as a soft-template and resorcinol formaldehyde again as the carbon precursor. Evaporation of an ethanol solution of these precursors induced the micellisation of the F-127, around which the resorcinol formaldehyde amassed, driven by hydrogen bonding interactions. Thermally induced polymerisation of the resorcinol formaldehyde resulted in a stable resin templated around the F-127 micelle assemblies, which – after removal of the templates and carbonization – resulted in a mesoporous carbon. This use of self-assembled F-127 as a template is analogous to the way in which some mesoporous silica frameworks are fabricated; the paper reports that by adjusting the resorcinol/F-127 ratio both 2D hexagonal and 3D cubic carbon structures and be formed – which are the carbon analogues of mesoporous silica SBA-15 and SBA-16 (Figure 1.12.).

Although the preparation of carbon materials *via* soft templating routes can be regarded as relatively facile in comparison to various hard-templating routes, by avoiding pre-fabrication and subsequent etching of the template material, the methods are not without shortcomings. For instance, the choice of carbon precursor is limited, with resorcinol-based routes almost exclusively used due to the requirement of facile polymerisation around the fragile soft templates. There are also only a limited number of suitable surfactants, meaning only a limited diversity of soft-templated carbons have been demonstrated.(104)(101)

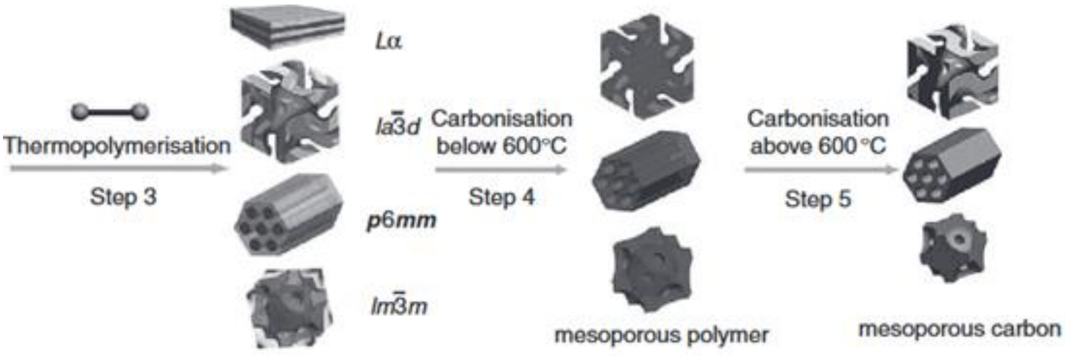

Figure 1.11. Schematic representation of the preparation of mesoporous carbons via soft templating in the presence of block co-polymers (103)

1.6.5. Emulsion Templated Carbons

Emulsions can also be used to template the structure of porous carbons. An emulsion is a mixture of two immiscible solvents (typically one hydrophobic and one water-based), where one is dispersed within another in the form of droplets.(105) If the hydrophobic solvent is in the continuous phase, and the hydrophilic solvent forms the droplets, then the emulsion is termed water-in-oil (or W/O). If the opposite, then the emulsion is termed oil-in-water (or O/W). If the volume percentage of the droplet phase exceeds 74.05 % then the emulsion is termed a high-internal phase emulsion, or HIPE.(105) Surfactants, and sometimes co-solvents, are also added to emulsions and HIPEs in order to prevent the droplets from agglomerating and the phases from separating.

If suitable monomers, initiators and crosslinking agents are dissolved within the continuous phase of the emulsion, then it can be polymerised to give a so-called emulsion templated structure, where a polymerised HIPE is termed a polyHIPE.(106) Under the right conditions, these emulsion templated structures can then be carbonised to give the corresponding emulsion templated carbons (Figure 1.13.). This process is similar to that of soft templating methods and is generally placed in that category.

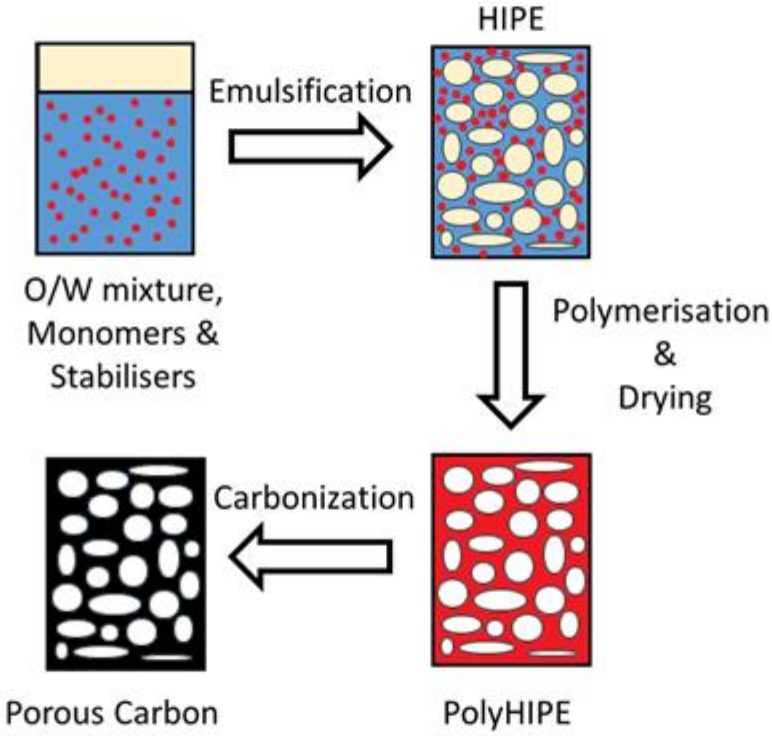

Figure 1.12. Schematic representation of the preparation of a porous carbon via emulsion templating

In 2005, Budd and co-workers demonstrated this concept by polymerising a W/O HIPE consisting of vinylbenzyl chloride, styrene and divinylbenzene (initiator, monomer and crosslinking agent, respectively) with sorbitan monooleate as a stabiliser, to prepare a polyHIPE, which was then sulfonated and carbonised to give a porous, emulsion-templated carbon monolith.(107) An analogous process was recently employed by Edstrom and co-workers, who subsequently tested the materials as Li-ion microbattery electrodes and electrode supports (Figure 1.14.).(108) Cohen and Silverstein developed another method where they prepared an emulsion-templated polyHIPE based on poly(acrylonitrile) (PAN). Here, oxidative stabilisation of the PAN followed by carbonisation resulted in the corresponding emulsion templated carbon.(109) Titirici and co-workers reported a relatively green route for the fabrication of emulsion templated carbons by employing naturally occurring furfural and phloroglucinol as carbon precursors, and employing a low-temperature hydrothermal treatment for carbonisation.(110) Their materials had high BET surface areas of up to 730 m^2 g^{-1}, and were tested for application as bio-catalyst supports for the electrooxidation of glucose.

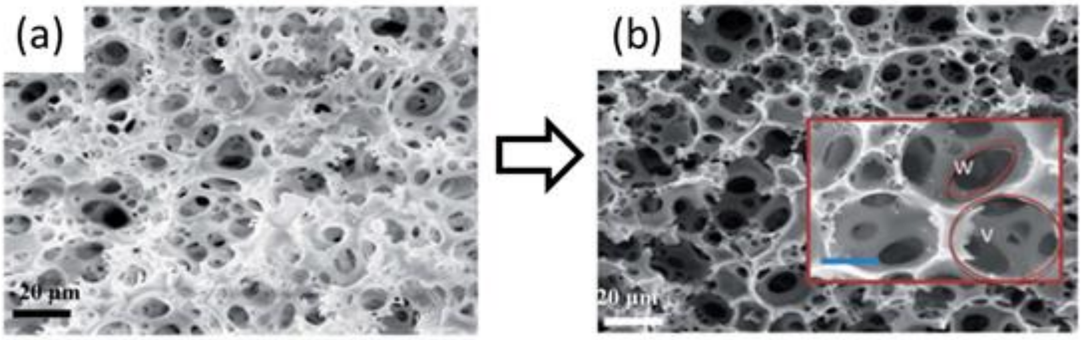

Figure 1.13. PolyHIPE prepared by Edstrom and co-workers a) before and b) after carbonisation (108)

This use of inexpensive water/oil droplets as templating entities to direct the structure of porous carbons is a relatively simple and benign way to fabricate templated porous carbons. However, disadvantages of this method include relatively large macropores (typically >1000 nm), polydisperse and disordered pores, and a limited selection of carbon precursors due to the requirement to crosslink the external phase of the emulsion prior to carbonisation.

1.6.6. Ice Templated Carbons

Frozen solvent crystals can also be employed as templates to direct the formation of porous structures.(111)(112)(113)(114) In this process a solution or colloidal suspension is frozen before removal of the solvent in its frozen state (typically by freeze drying) to give a macroporous material (Figure 1.15.).(112)(113) By orientating this freezing in a single direction (*directional*- or *unidirectional*- *freezing*) it is also possible to obtain materials with *aligned* porosity.(111)(112)(114) A more in depth description of the process is given in the following sub-section.

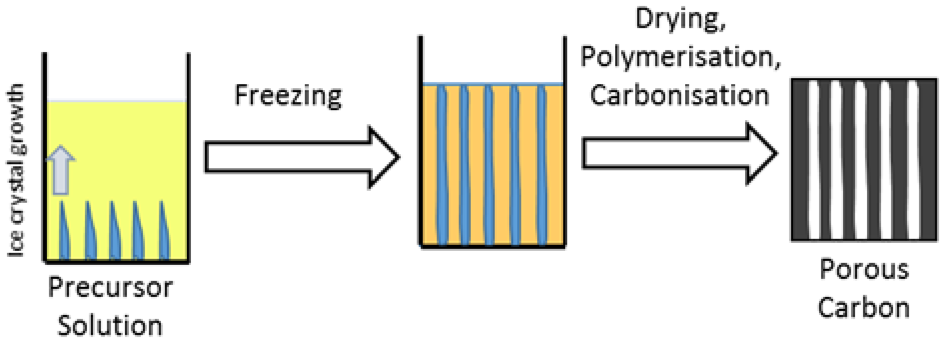

Figure 1.14. Schematic representation of the ice-templating process to prepare a porous carbon

Water is the most common solvent used for this process due to its highly solvating properties, negligible cost, environmental friendliness and ease of removal through freeze drying.(112) The use of water has led to the term *ice-templating* to describe the process, although other names such as *ice-segregation-induced self-assembly* (ISISA), *freeze-casting and freeze-gelation* have also been employed.(113)

Ice-templating is a relatively simple and facile process for the preparation of porous polymers and composites,(113)(114) however it remains a relatively unexplored method in the fabrication of porous carbon materials – with only a handful of published papers on the subject to our knowledge.(87)(116)(117)(118)(119)(120)(121)(122)(123)(124)(125) The first example of an ice-templated porous carbon (ITPC) was demonstrated by Tammon and co-workers in 2004,(123) who prepared so-called carbon cryogel microhoneycombs by directionally freezing crosslinked resorcinol formaldehyde hydrogels, before subjecting them to freeze-drying and carbonisation at 1000 °C. Goh and co-workers prepared nitrogen-doped ITPCs by directionally firstly freezing poly(styrene) in 1,4-dioxane before freeze drying at -5 °C, followed by the vapour-phase polymerisation of poly(pyrrole) onto the ice-templated poly(styrene) surface, exposure to I_2 vapour and carbonisation at 800 °C (Figure 1.16.).(124) Exposure to I_2 vapour was necessary for carbonisation, since I_2 facilitates crosslinking *via* dehydrogenation and subsequent C-C bond formation through radical recombination.(16)

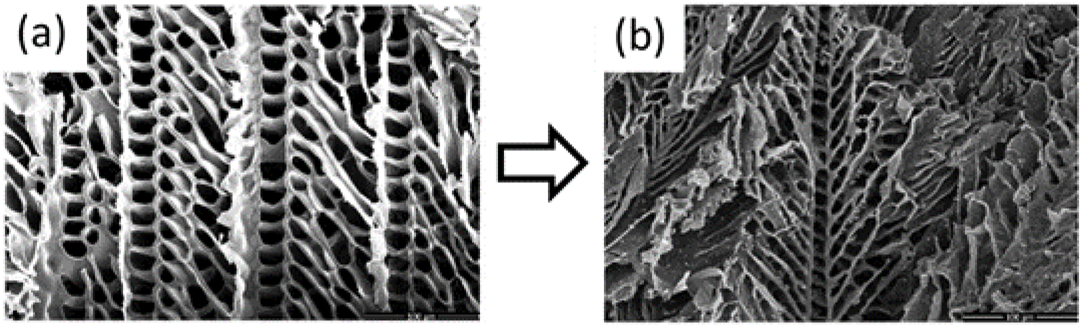

Figure 1.15. a) Ice-templated porous polymer and b) ITPC prepared by Goh and co-workers (123)

Hierarchically porous ITPCs have also been prepared by combining ice-templating along with hard templating (silica spheres) and physical activation, giving macro-, meso- and micro-pores, respectively (Figure 1.17.).(125) Here, a colloidal suspension of silica spheres in glucose (carbon precursor) was directionally frozen before removal of the ice crystals *via* freeze drying. Carbonisation and subsequent etching of the silica hard templates then gives a macro-/meso- porous carbon, which was then subject to physical activation with CO_2 gas. The carbonised and activated materials had high BET surface areas up to 2096 m^2 g^{-1}, and CO_2 adsorption capacities up to 4.1 mmol g^{-1} at 10 bar and 273 K. Graphene-based carbon monoliths have also been prepared *via* an ice-templating strategy;(126) here a partially reduced aqueous graphene oxide solution was subject to ice-templating to first prepare graphene oxide monoliths. These monoliths could be further reduced, giving ice-templated graphene monoliths, which possessed very low density, high elasticity, and high structural integrity under compression.

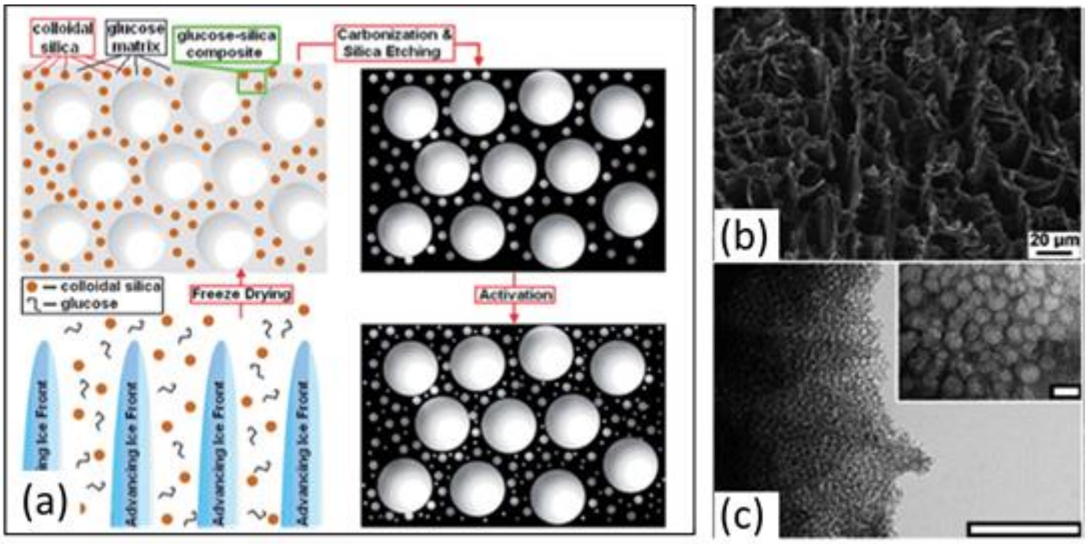

Figure 1.16. a) Schematic representation of the process employed by Giannelis and co-workers to prepare a hierarchically porous carbon via ice templating, b) SEM and c) TEM images of the material (124)

Although the ice-templating and carbonisation route holds certain advantages over other soft- and hard- templating methods, such as relative simplicity of preparation, and no need to pre-fabricate sacrificial templates, there are also several disadvantages associated with the technique. One major difficulty encountered is the need to crosslink the precursor prior to carbonisation since, in the absence of a rigid scaffold, the well-defined framework would be lost *via* melting, decomposition or foaming during pyrolysis. This need for crosslinking therefore greatly limits the pool of suitable precursors which can be utilised for this method. Another drawback of this technique is limited control of the pore size and morphology. Although variation of certain parameters such as freezing rate can affect the resultant porosity,(111) pore size and shape control is much more difficult in comparison to hard- and soft- templating routes, with pore sizes being relatively large and typically in the μm size domain (> 1000 nm).

1.6.6.1. Ice Templating Theory and Background

A solute will typically have a relatively high solubility when the solvent is in a liquid state, but a much lower solubility when the solvent is solid (frozen).(113) Due to this difference in solubility, when a solution is frozen, the forming ice crystals can displace the solute into the remaining solution – resulting in an increase in solute concentration around the growing ice crystals.(111)(113) This leads to an increase in the concentration of the liquid solution encompassing the ice crystals, which eventually becomes so great that precipitation of the solute occurs. As the ice crystals continue to expand, the precipitated solute is compressed (or templated) between adjacent ice crystals.(111)(113) Removal of the crystals *via* freeze drying then reveals a macroporous structure (assuming it is stable) of the precipitated solute, where the pores are the voids left by the removed ice crystals.(111)(113)(127)

The formation of *aligned* porous structures from the directional freezing of a solution is a more complex process.(111)(112)(128) Here, as ice crystals nucleate and grow, the local increase in solute concentration surrounding the ice crystals forms an area of constitutional supercooling, which breaks down the planer interface causing ice crystals to grow.(128) Thus, the primary ice structure depends on the destabilising solute interface concentration gradient and the surface energy which opposes cell formation – a phenomenon known as Mullins-Sekerka instability (Figure 1.18.).(112)(129)

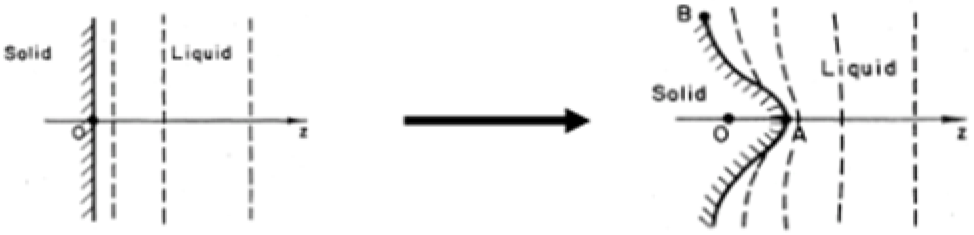

Figure 1.17. Schematic representation of Mullins-Sekerka instability leading to aligned formation of ice crystals (129)

The pore size, shape and morphology can be controlled to a degree by factors such as solute composition, solution concentration and freezing rate, where a faster freezing rate and a higher temperature gradient would lead to smaller pores due to a larger nucleation and growth rate of ice crystals.(111)(128)

The typical morphology obtained from a directionally frozen ice-templated material consists of hexagonal macropores, and is commonly referred to as a *microhoneycomb* structure.(123)(130) Other morphologies can also be obtained, such as lamellar structures and “fish-bone” type structures – which results from side-branches from the primary ice cells causing secondary instability formation. Fibrous structures can also be obtained if the solution concentration is very low (Figure 1.19.).(111)

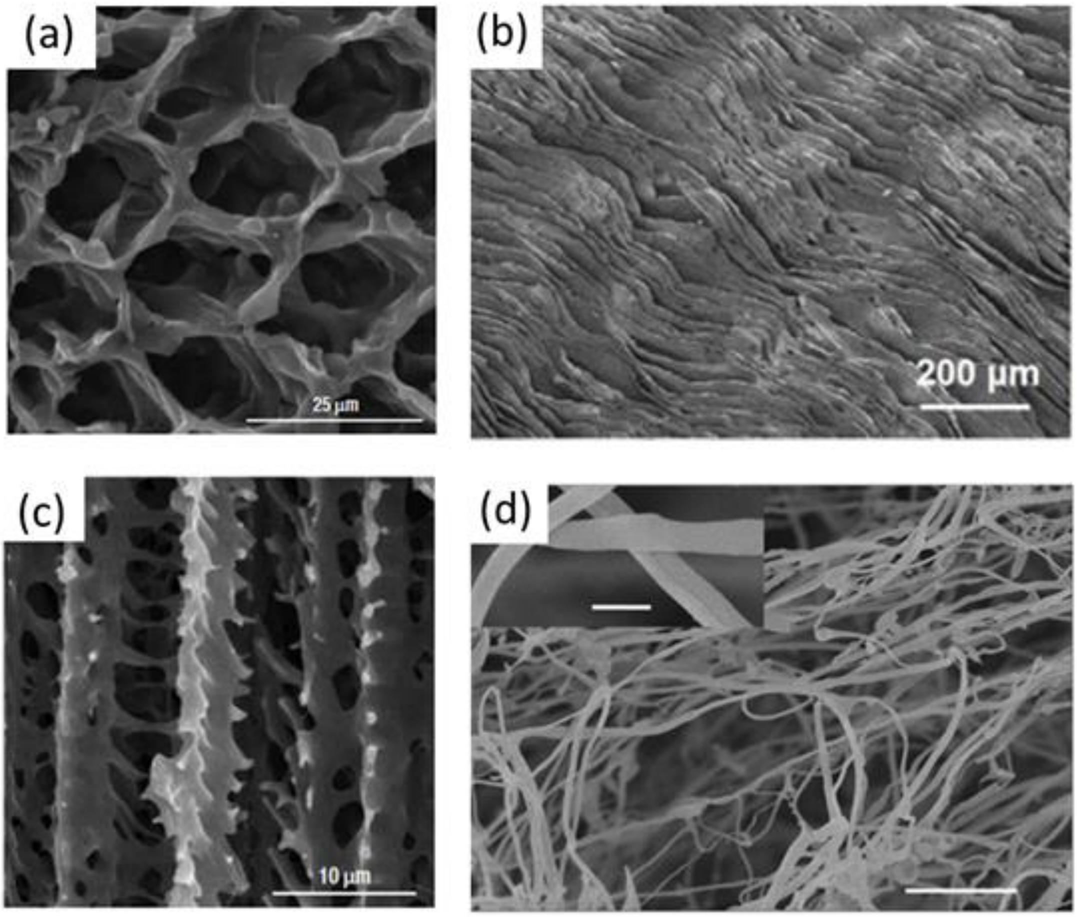

Figure 1.18. SEM images of ice-templated porous polymers with a) honeycomb, b) lamellar, c) fish-bone and d) fibrous morphologies (112)(131)(132)

Currently, ice-templated aligned porous materials have attracted the most attention in the fields of tissue engineering, aligned conductive materials and high-strength, low-density composites.(114)(133)(134)(135)(136)

1.6.7. Templated Carbons for Energy Storage

Templating methodologies offer unique strategies for the fabrication of porous carbon materials that would not be attainable *via* other synthetic routes.(82) One area where templated carbons have received a large amount of interest is that of energy storage; where their tuneable porosity, morphology, nanotexture, surface areas and heteroatom doping have resulted in materials with excellent performance in energy storage devices.(11)(22)(82) Below we outline and review the specific areas in the field of energy storage where templated porous carbons have been employed and demonstrated superior performance to materials derived from other routes.

1.6.7.1. Lithium-Ion Batteries

Readers who are unfamiliar with the concepts/terms used in the evaluation of lithium ion battery electrode materials are directed to section 2.13.3., which outlines these concepts in greater detail.

A rechargeable (or *secondary*) lithium-ion battery (LIB) is an electrochemical device capable of storing energy in chemical form, before releasing it as electrical energy on requirement.(37) LIBs achieve this feat through a process termed the *rocking-chair* mechanism; *i.e.* the reversible intercalation/extraction of Li-ions between redox active host materials (the *electrodes*) which are separated by a Li-ion conducting but electrically insulating medium (the *electrolyte*) (Figure 1.20.).(37)(137)

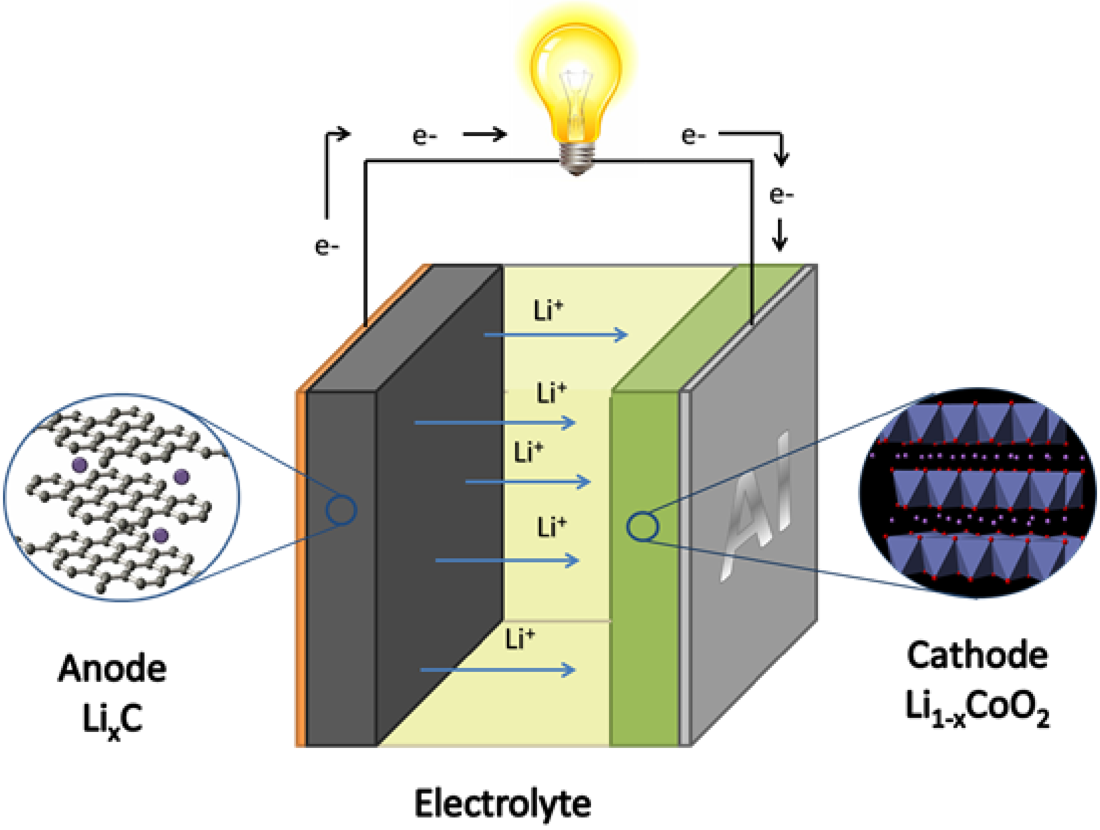

Figure 1.19. Schematic representation of a LIB undergoing discharge (87)

Since it’s commercialisation in the early 1990’s, the active material in the negative electrode (or *anode*) of LIBs has been particulate graphitic carbon.(37) Li-ions intercalate into graphite with a maximum stoichiometry of LiC_6, which corresponds to a maximum theoretical specific capacity of 372 mA h g^{-1}.(137) It has been shown, however, that some semi-graphitic carbons have exceeded this specific capacity limit, suggesting that there are means other than intercalation by which Li-ions can be inserted into the carbon electrode.(138)(139)(140)

Numerous studies have attempted to shed light on this phenomenon, with suggestions ranging from entrapment of metallic lithium clusters in ultramicropores, the formation of lithium multilayers on exposed graphene sheets, and the formation of Li_2, C-H-Li or N-Li bonds. (138)(140)

Porous carbons have also proven to hold certain advantages over the solid graphitic particles (or *mesosphere carbon microbeads*, MCMBs) currently employed as LIB anode materials.(82) The advantages can include higher power densities (*i.e.* faster rate of charging and discharging) due to enhanced Li-ion diffusion kinetics, relatively good electrical conductivity due to interconnected porous structures, tuneable porosity/surface area for optimal electrode-electrolyte contact without excessive solid electrolyte interphase (SEI) formation, reduced solid-state diffusion of Li-ions in the bulk material due to relatively thin pore walls, and reduced/eliminated need for electrochemically inert binding agents.(82) Porous carbons can also be combined with various Li-alloy forming materials, such as Sn, SnO_2 or Si, which can enhance LIB anode performance due to their relatively high specific capacity values (994, 781 and 4200 mA h g^{-1}, respectively).(141)(142)(143)(144) Alone, these Li-alloy forming materials are unsuitable as LIB anodes, due to issues such as poor electrical conductivity and destructive volumetric change on charge/discharge, but porous carbon matrixes can act as conductive supports and mechanical buffers to overcome these problems.

There are shortcomings to the use of porous carbons as LIB anodes however, which can include lower volumetric energy densities (due to more void space), higher irreversible capacities (C_{irr}) due to SEI formation from relatively high surface areas, and sloped voltage profiles if carbon is not graphitised.(87) Cost is also a significant issue; whereas graphite particles (MCMBs) are relatively low cost, templated carbons employing complex synthesis methodologies would likely struggle to compete on a commercial basis.(87)

In 2005, Lee and co-workers reported the preparation a hard templated carbon and its performance evaluation as a LIB anode material.(145) The templated carbon, prepared *via* the CVD of benzene within an inverse silica opal template, consisted of an ordered array of interconnected carbon spheres with diameters of about 200 nm, with wall thicknesses of about 20 – 30 nm and BET surface areas of between 50 – 100 m^2 g^{-1}. The specific reversible capacity (C_{rev}), measured at a current density of 40 mA g^{-1}, was slightly lower than the theoretical capacity for graphite (372 mA h g^{-1}) at 362 mA h g^{-1}. However, the material has excellent high cycle stability and high C-rate performance with very little capacity degradation after 60 charge cycles and only a small capacity drop to 303 mA h g^{-1} when the current density was increased by an order of magnitude. To increase capacity, SnO_2 nanoparticles were deposited on the carbon framework post-synthesis which increased the initial capacity to 415 mA h g^{-1} (SnO_2 loading of 18.6 wt. %), however the cycle stability was poorer than the original material.

Ichihara and co-workers prepared the mesoporous carbon CMK-3 from an SBA-15 silica template using glucose as a carbon precursor.(138) The templated carbon had a surface area of about 1030 m^2 g^{-1}, pore sizes of about 4 nm and, when tested as a LIB anode material, a very high C_{rev} of 1100 mA h g^{-1} which stabilised at about 850 mA h g^{-1} after 20 cycles – over twice the theoretical capacity for graphite (372 mA h g^{-1}). This high C_{rev} was, however, accompanied with a very large C_{irr} of about 2000 mA h g^{-1}, likely as a result of excessive SEI formation due to the high surface area for the material.

As was mentioned in section 1.6.3., Stein's group used PMMA polymer spheres to fabricate a macroporous carbon, with average pore sizes of ~100 nm, wall thicknesses of ~10 nm and a BET surface area of 326 m^2 g^{-1}.(93) When evaluated as a LIB anode material, the material displayed a C_{rev} of 299 m^2 g^{-1} at the current density of 15.2 mA g^{-1}, however there was also a fairly large C_{irr} of about 400 mA h g^{-1} and relatively poor cycle stability. C_{rev} and high rate performance was improved slightly by adding a homogenous layer of SnO_2 nanoparticles post-synthetically, however poor cycle stability persisted.

The hierarchically porous carbon also mentioned in section 1.6.3., prepared by Maier and co-workers from a bimodal porous silica template, was also tested for its LIB anode performance.(94) A high C_{rev} of 900 mA h g^{-1} was obtained at the current density of 180 mA h g^{-1}, which stabilised at 500 mA h g^{-1} after 40 cycles. The high-rate performance of the material was excellent, with a C_{rev} of 260 mA h g^{-1} at the high current density of 2.6 A g^{-1} (Figure 1.21.). This high rate performance was attributed the hierarchy of pores allowing facile Li-ion diffusion to and from the active material surface. C_{irr} was fairly high however at about 680 mA h g^{-1}, likely due to SEI formation as a consequence of the relatively high surface area (330 m^2 g^{-1}). A number of other porous carbon materials, along with their performance as LIB anode materials, are presented in Table 1.1. and Table 1.2. for comparison.

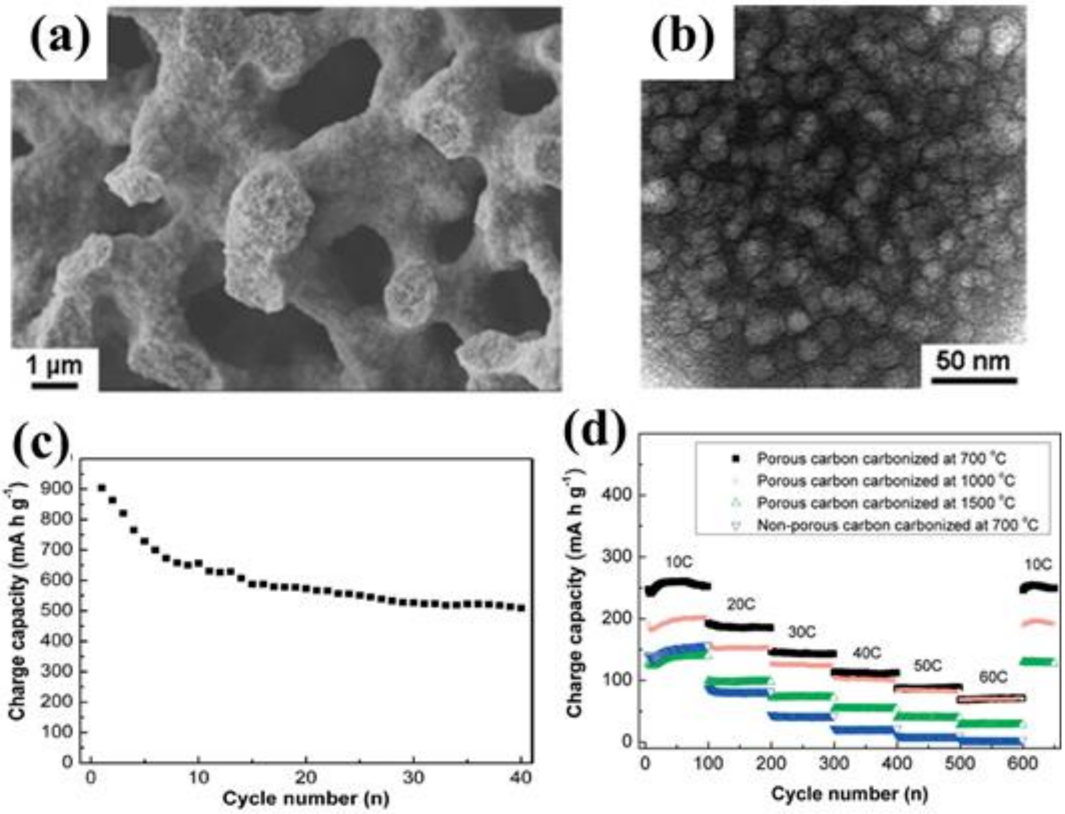

Figure 1.20. Hierarchically porous carbon prepared by Maier and co-workers: a) SEM image, b) TEM image, c) cycle stability profile and d) rate performance profile (94)

Despite the relatively good performances of such materials in comparison to the currently employed graphitic MCMB carbon as LIB anode materials, numerous shortcoming need to be overcome if such materials are to be used in practical devices. Firstly, porosity, surface areas, morphology and nanotexture need to be optimised to attain the best possible performances with regards to capacity, power density, cycle stability *etc.* The exact properties such an ideal material ought to poses is not entirely clear, although it appears, from an empirical study of the literature, that hierarchically porous, N-doped carbons have the best performances in this regard.(87) Secondly, complex fabrication procedures should be simplified and made scalable in order to compete with MCMBs on a cost-performance basis.

Table 1.1. Comparison of the reversible (C_{rev}) and irreversible (C_{irr}) capacities of a number of templated porous carbons

Template	***Carbon Precursor***	***C_{irr} (mA h g^{-1})***	***C_{rev} (mA h g^{-1})***	***Crev after N cycles (mA h g^{-1})***	***N Cycles***	***Ref.***
Silica Monolith	Mesophase pitch	680	900	500	40	(94)
Silica SBA-15	Sucrose	2000	1100	800	20	(138)
Silica particles & PS spheres	Furfuryl Alcohol	671	903	799	80	(95)
Silica SBA-15	Furfuryl Alcohol	N/A	714	583	80	(95)
Inverse silica opal	Benzene (CVD)	N/A	326	320	60	(145)
PMMA	Resorcinol Formaldehyde	400	300	150	150	(93)
DMSO Ice-templating	Polyacrylonitrile	468	745	590	50	Chapter 3

Table 1.2. Comparison of the high-rate performances of various carbon-based materials

Description	***C_{rev} at current density X (mA h g^{-1})***	***Current density X (A g^{-1})***	***Ref.***
Carbon Templated by Silica and PS Spheres	750	1	(95)
N-doped Pristine Graphene	250	10	(65)
Boron-doped Pristine Graphene	300	10	(65)
N-rich Porous Carbon Derived from Protein	210	4	(63)
N-doped Activated Carbon Nanofiber Web	320	10	(146)
N-doped Carbon Spheres (<100nm)	200	3	(147)
CPAN50	320	1	Chapter 3
15% Melamine-rGO-CPAN50	300	10	Chapter 3

1.6.7.2. Lithium-Sulfur Batteries

Readers who are unfamiliar with the concepts/terms used in the evaluation of lithium-sulfur battery electrode materials are directed to section 2.13.3., which outlines these concepts in greater detail.

Lithium-sulfur (LIS) batteries operate in a similar mechanism to conventional LIBs, *i.e.* through the reversible insertion/extraction of Li ions between two electrodes.(148)(149) The LIS battery differs from the LIB battery in that it employs metallic Li as the anode (rather than graphitic carbon) and elemental S as the active cathode material, rather than a lithium metal oxide (Figure 1.22.).(148)(149) The S, which is a low cost and highly abundant element, can accept 2 electrons per atom at ~2.1 V vs. Li/Li$^+$ to form lithium sulphide (Li_2S). This gives it a maximum theoretical specific capacity of 1675 mA h g^{-1}, which is about 5 times higher than conventional LIB cathode materials, which are in the region of ~250 mA h g^{-1}.(150) The true capacity of a working system would likely be substantially lower than this however, and numerous obstacles still remain before the LIS battery can be considered commercially viable. The use of elemental sulphur as the cathode material brings about numerous problems for instance. It's poor electrical conductivity (5x10^{-30} S cm^{-1}), large volumetric expansion on lithiation, and the solubility of the Li_2S_x intermediates in electrolytes have detrimental effects on its performance as an electrode material.(148)(149)

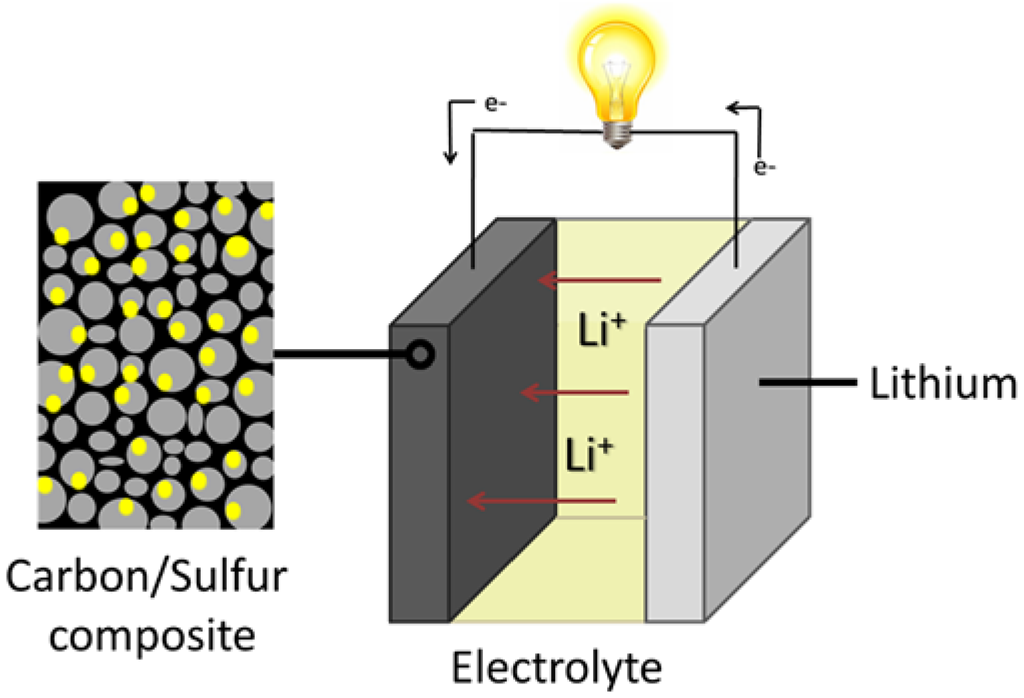

Figure 1.21. Schematic representation of the LIS battery undergoing discharge

The use of porous carbon-S composites, rather than purely elemental S, has been demonstrated to mitigate some of the abovementioned issues and has led to significant performance enhancements for the LIS battery.(148)(149)(151)(152)(153)(154)(155)(156) Here, the porous carbon matrix has several functions: firstly, it acts as an electrically conductive framework to alleviate the poorly conductive properties of elemental sulphur, secondly, it acts as a rigid mechanical support to absorb the mechanical stresses caused by the volumetric expansion of sulphur on lithiation. Lastly, convoluted pore pathways can restrict the diffusion on Li_xS intermediates into the electrolyte, which would result in capacity degradation over repeated charge/discharge cycles (poor cycle stability).(155)

Templated carbons, having highly controllable pore characteristics, have naturally been investigated for such applications. Nazar and co-workers first demonstrated this concept in 2009, by incorporating S within the pores of the mesoporous silica templated carbon (CMK-3) *via* a simple melt infusion method, attaining S loadings of up to 70 wt. % (Figure 1.23.).(154) When tested as a LIS battery cathode material, a high C_{rev} of 1320 mA h g^{-1} was attained which stabilised at ~800 mA h g^{-1} after 20 charge/discharge cycles. Inov and co-workers melt-infused S within a porous carbon prepared *via* hard templating of PMMA spheres with resorcinol formaldehyde as the carbon precursor.(152) A S loading of 82 wt. % and a C_{rev} of 1600 mA h g^{-1} were attained, however this fell to about 300-400 mA h g^{-1} after 50 charge/discharge cycles. Zhang and co-workers encapsulated S within the pores of a hierarchically porous carbon derived from the direct pyrolysis of MOF-5. Having a S loading of 54 wt. %, the material displayed a C_{rev} of 1177 mA h g^{-1}, which fell to 730 mA h g^{-1} after 50 cycles. Porous carbon microspheres with hierarchical macro-, meso- and micro- porosity have been prepared *via* a silica templating spray pyrolysis technique.(157) S was introduced into the pores (60 - 64 wt. %) *via* liquid-phase infusion before being tested as a LIS cathode material; here a high C_{rev} of 1278 mA h g^{-1} was obtained which was remarkably stable on cycling, falling to only ~904 mA h g^{-1} after 100 charge/discharge cycles. A number of other carbon-S composites, along with their electrochemical performances as LIS cathode materials, are presented in Table 1.3.

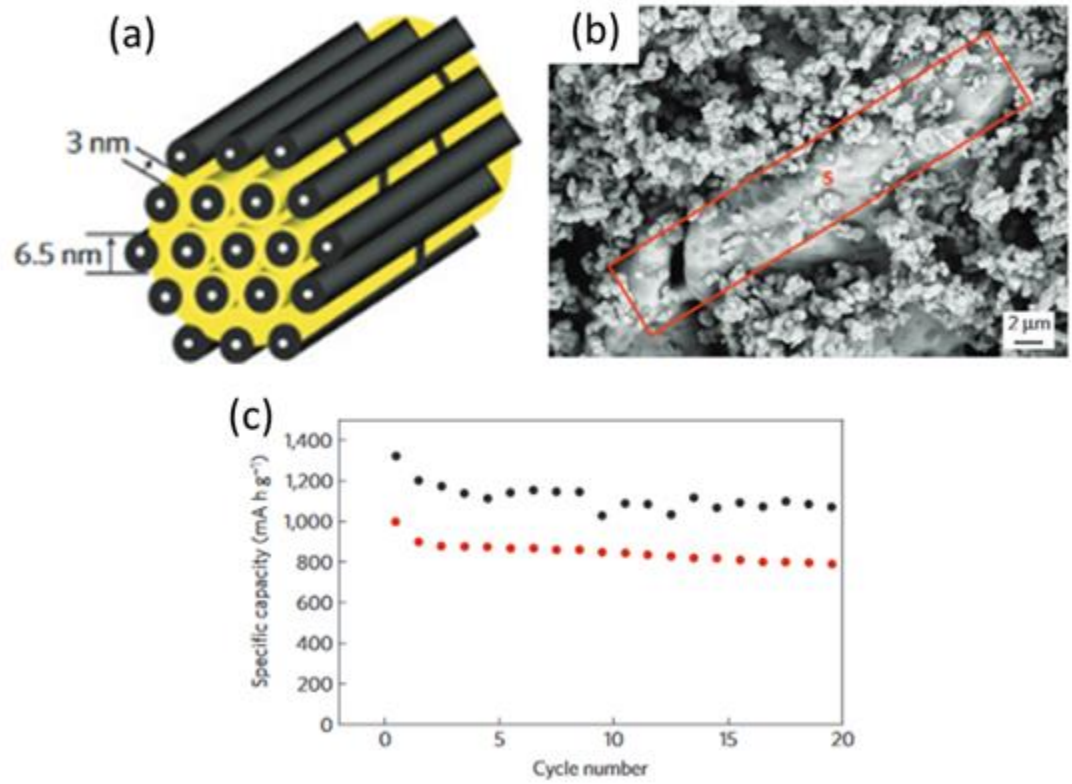

Figure 1.22. a) Diagram, b) SEM image and c) LIS battery cycling performance of the mesoporous carbon-S composite prepared by Nazar and co-workers (154)

Despite promising results such as these, the relatively complex synthesis routes associated with templating methodologies again act as a barrier to commercialisation, and negate the green and low-cost credentials held by the theoretical LIS battery over conventional LIBs. Therefore, developing facile and relatively low-cost methods for the fabrication of LIS porous carbon-S composite cathodes is an attractive area of research.

Table 1.3. Comparison of a number of carbon-sulfur composites and their performances as LIS battery cathodes

Template	***Precursor***	***Sulfur loading method***	***Sulfur loading (wt. %)***	***Current Density ($A\ g^{-1}$)***	***C_{rev} ($mA\ h\ g^{-1}$)***	***C_{rev} after N cycles ($mA\ h\ g^{-1}$)***	***N Cycles***	***Ref.***
Colloidal Silica	Poly(pyrrole)	Melt Infusion	83	0.168	1390	613	50	(158)
CMK-3	Sucrose	Melt Infusion	70	0.168	1320	800	20	(154)
Colloidal PMMA	Resorcinol Formaldehyde	Melt Infusion	82	0.168	1600	400	50	(152)
F-127 & Silica	Phenol Formaldehyde	Melt Infusion	40	1.675	995	550	100	(159)
Colloidal Silica and PS	Sucrose	Melt Infusion	50	0.168	1193	884	50	(160)
Colloidal Silica	Sucrose	Solvent Infusion	63	1.675	1278	903	100	(157)
*Sol-gel**	Starch	Melt Infusion	81	0.838	922	683	100	(161)
Ice Templating	PSS	In-situ Infusion	40	0.1	183	136	15	Chapter 5

*Not a templating method but included for comparison

1.6.7.3. Supercapacitors

Readers who are unfamiliar with the concepts/terms used in the evaluation of supercapacitor electrode materials are directed to section 2.13.3., which outlines these concepts in greater detail.

Whereas a battery stores energy in chemical form, a capacitor is a device which stores energy *via* electrostatic interactions.(79) Consisting of two parallel plates (*electrodes*) separated by a polarisable insulator (a *dielectric*), capacitors store electrical energy by having a potential difference (*voltage*) applied across the electrodes, which results in the build up of +ve and -ve charges on the electrodes of opposed polarity.

An electrochemical double layer capacitor (EDLC), or *supercapacitor*, functions in a similar way to a conventional capacitor, however – by employing an ionic solution as an electrolyte and electrodes with extremely high surface areas – supercapacitors can attain energy densities orders of magnitude higher than their counterparts.(79) Since supercapacitors store energy *via* physical, rather than chemical, interactions, they are able to charge and discharge at a much faster rate than batteries, and in a highly reversible way. This results in substantially higher power densities in comparison to batteries, albeit at a cost to overall energy density, as can be seen by a Ragone plot in Figure 1.24. This allows them to occupy niche applications where extremely rapid charging/discharging is required – such as regenerative breaking and power systems to open airplane doors in emergencies.(162)

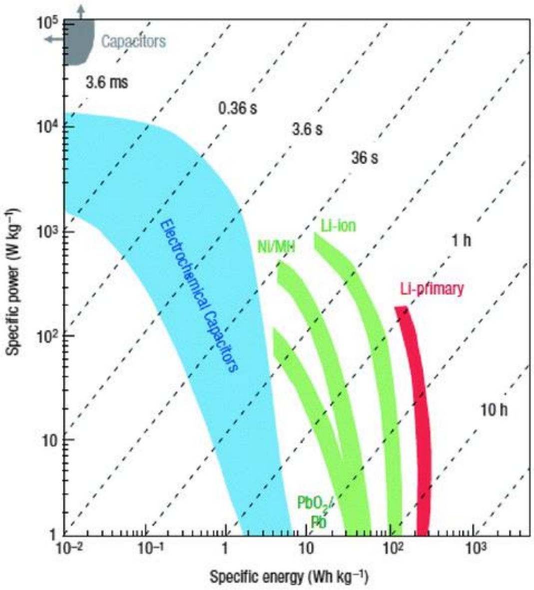

Figure 1.23. Ragone plot competing specific energy and specific power of various energy storage devices (163)

The energy storage principle behind supercapacitors was theorised by Helmoltz in the 19th century, who proposed a double-layer model for charge storage,(164) although it was subsequently refined by Guoy, Chapman and Stern to provide a more accurate description.(165)(166)(167) In this model, each electrode forms an electrostatic double layer, both behaving as an individual capacitor connected in series, where the total capacitance (C_T) is related to the individual capacitences of each electrode (C_1 and C_2) *via* the following equation:(162)

$$C_{TOT} = \frac{C_1 \cdot C_2}{C_1 + C_2}$$

Eq. 1.1.

Each electrostatic double layer consists of a build of electronic charges at the surface of the electrode, and a build up of ions in the electrolyte at (or in very close proximity to) the electrode surface (Figure 1.25.). According to the Helmholtz model, the ions in solution build up directly on the surface of the electrode – and thus the opposing charges are separated by only atomic distances. Guoy and Chapman revised the model and proposed that, instead of a build-up of ions directly on the electrode surface, there was instead a continuous distribution of electrolyte ions in the solution (driven by solvation interactions and Brownian motion), which was termed the diffuse layer. Later, Stern combined these two models – proposing both a compact layer of ions very close to the electrode surface and a diffuse layer. According to his model, the compact layer consisted of two distinct phases – a layer of de-solvated ions directly on the surface of the electrode (inner Helmholtz plane, or IHP) and a layer of solvated ions strongly adsorbed to the electrode surface.(162)

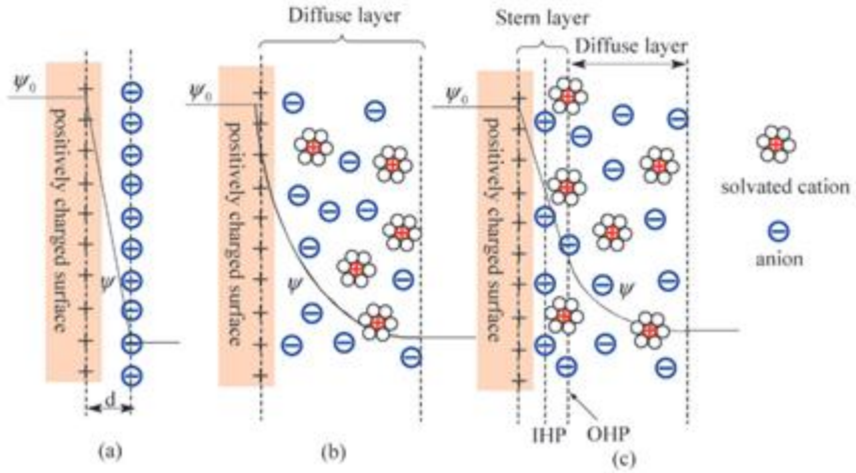

Figure 1.24. a) Helmholtz, b) Guoy-Chapman and c) Stern models for an electrical double layer surface interface (162)

Activated carbons are currently the most widely explored active materials for supercapacitor electrodes, being relatively low cost, chemically and thermally stable, electrically conductive and possessing extremely high surface areas and pore volumes.(7)(162) Although surface area is the main factor behind the performance of supercapacitors, other characteristics such as porosity, elemental doping, surface functionalisation and electrical conductivity are also important in regards to performance.(162)(168) There is therefore much potential for the development of tailored carbons with controlled features to maximise the performance of supercapacitor electrodes, with templating methods being one of the most promising strategies in this regard.

Having ordered microporous structures and high surface areas, zeolite-templated carbons have proven to be promising supercapacitor electrode materials.(82)(84)(162) For instance, Yushin and co-workers prepared nitrogen-doped zeolite-Y templated carbons *via* the CVD of acetonitrile and ethylene within the pores, before removal of the template.(169) Evaluation of the materials as supercapacitor electrodes in an electrolyte of tetraethylammonium tetrafluoroborate (NEt_4BF_4) in acetonitrile gave a capacitance of 146 F g^{-1} – which is remarkably high for an organic electrolyte. In another case, Béguin and co-workers prepared N-doped zeolite-Y templated carbons from acrylonitrile and propylene precursors (Figure 1.26.).(170) The materials had gravimetric capacitances of up to 340 F g^{-1} (current density of 0.2 A g^{-1}) in aqueous electrolytes and were stable over 10,000 cycles, despite only having a moderately high BET surface area of 1680 m^2 g^{-1}.

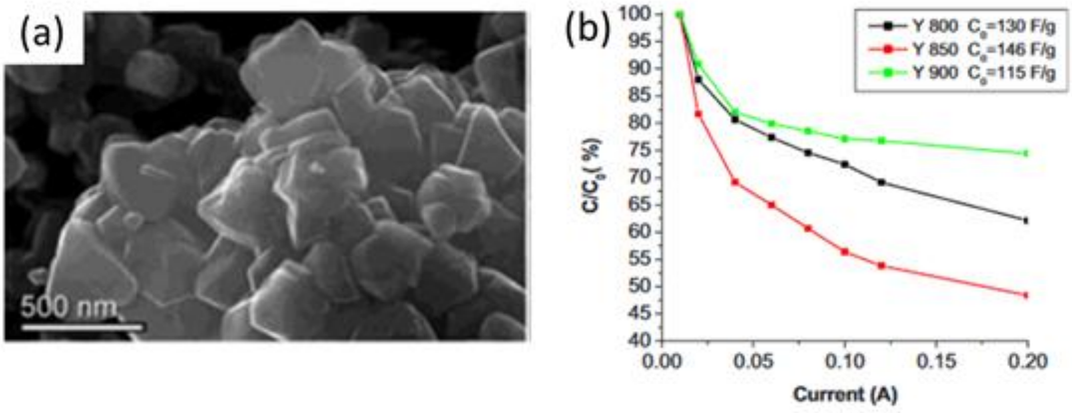

Figure 1.25. a) SEM image and b) plot of capacitance vs. current density for the zeolite-Y templated carbon prepared by Béguin and co-workers (170)

Frackowiak and co-workers employed mesoporous silica (SBA-16) templated carbons as supercapacitor electrodes:(171) derived from a furfuryl alcohol precursor, the materials has BET surface areas of about 1500 – 1900 m^2 g^{-1} and mesopores of between 2 and 8 nm. The capacitance values weren't especially high however, with the best performing material having a capacitance of 143 F g^{-1} at a current density of 1 A g^{-1}.

Cheng and co-workers prepared a hierarchically porous graphitic carbon with micro-, meso- and macroporoisty by carbonising a phenolic resin in the presence of a $Ni(OH)_2$/NiO template.(172) Having BET surface areas of up to 970 m^2 g^{-1}, the materials displayed very good performance at high current densities (~160 F g^{-1} at 50 A g^{-1}) which was attributed to facile transport of ions to the electrode surfaces *via* the hierarchy of meso- and macropores. Kudo and co-workers also showed the merits of a hierarchical pore structure with regard to supercapacitor performance, with their porous carbons prepared *via* a silica colloidal crystal templating technique (Figure 1.27.).(173) Having pore sizes between 8 and 80 nm, and BET surface areas between 1000 and 2000 m^2 g^{-1}, the materials displayed specific capacitances of up to 350 F g^{-1} with very little capacity decay after 2000 cycles. A number of other templated carbons and their performances as supercapacitor electodes are presented in Table 1.4.

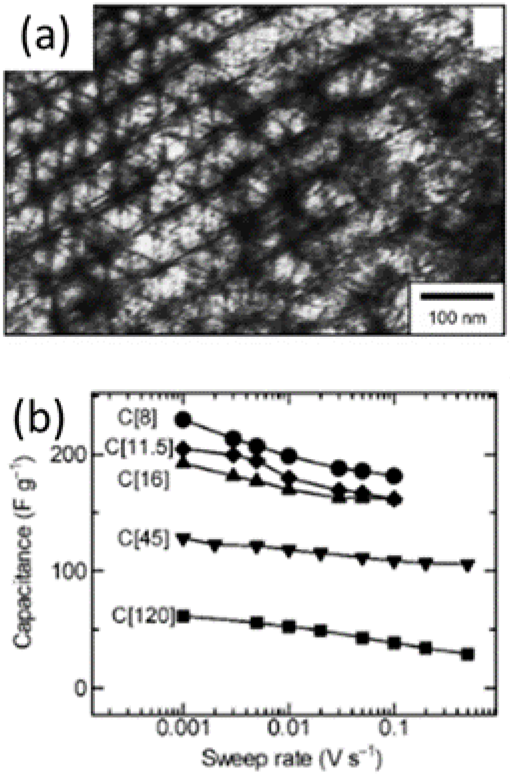

Figure 1.26. a) TEM image and b) relationship between capacitance and sweep rate for the hierarchically porous carbon prepared by Kudo and co-workers (173)

Despite these impressive performances, the very low cost of commercially available ACs would likely make such templating methods commercially unviable unless significant cost-reductions can be achieved.

Table 1.4. Supercapacitor performance of various templated carbons

Template	***Precursor***	***Surface area (m^2 g^{-1})***	***Capacitance (F g^{-1})***	***Current density***	***Ref.***
SBA-16	Furfuryl Alcohol	1900	143	1 A g^{-1}	(171)
Ni(OH)$_2$/NiO	Phenol Formaldehyde	970	160	50 A g^{-1}	(172)
Colloidal Silica	Phenol Formaldehyde	2000	350	10 mV s^{-1}	(173)
Colloidal Silica (& ZnCl$_2$ activation)	Glucose	1940	114	1 mA cm^{-2}	(174)
F127 (& KOH activation)	Phenol Formaldehyde	2060	180	20 mA cm^{-2}	(175)
F127 (& KOH activation)	Resorcinol Formaldehyde	1685	250	2 mV s^{-1}	(176)
Zeolite-Y	Acrylonitrile & Propylene	1680	340	0.1 A g^{-1}	(177)
MOF-5	Furfuryl Alcohol	3040	222	0.05 A g^{-1}	(178)

1.6.7.4. H_2 Storage

Petroleum fuels currently supply ~95 % of the energy for transport, accounting for approximately 23 % of CO_2 emissions globally.(179) Hydrogen gas has a gravimetric energy density three times higher than that for liquid hydrocarbons (142 MJ kg^{-1} vs. ~47 MJ kg^{-1}), although its volumetric density is much lower (0.126 MJ L^{-1} vs. ~34 MJ L^{-1}).(180) Producing no CO_2 on oxidation, it is being actively explored as an alternative, green transport fuel.(180) The energy released on the oxidation of H_2 can also be harvested *via* a fuel cell which, by converting chemical energy directly into electrical energy to drive a motor, can attain efficiencies over twice that of thermal combustion engines (~60 % vs. ~25 % efficiency).(180)

Despite these advantages, the use of H_2 for mobile energy storage applications faces significant hurdles. Firstly, despite being one of the most abundant elements on earth, hydrogen is not readily available in its elemental state (H_2) and needs to be produced synthetically. Whilst it can be produced readily from fossil fuels *via* steam reformation, *i.e.* the reaction of hydrocarbons with steam at high temperatures, this process also produces CO_2

which negates the benefits of using H_2 in the first place. The photocatalytic splitting of water could produce large volumes of H_2 in a clean, CO_2 emission free, process, but such a process still requires significant advances before this technology can be considered viable.(181) H_2-fuel cells also require optimisation to improve efficiency – particularly in development of efficient, low-cost and precious metal free catalysts for the splitting of H_2 and O_2 without significant energy loss.(181) Lastly, a major problem faced by H_2 as a transport fuel is the fact that exists as a gas at room temperature and pressure, making its storage for mobile applications extremely difficult. One option is to store H_2 in high pressure tanks, however even when full they would only contain about 4 % H_2 – adding a large amount of excess mass to any vehicle.(180) There are also serious safety concerns with transporting H_2 within high pressure containers – where ruptures or leakages could lead to deadly explosions. Storage of H_2 as a liquid is a more attractive option than high pressure storage in terms of storage efficiency – having a higher volumetric density (70.8 kg m^{-3}) than the pressurised gas, improving the mass ratio of H_2 to the storage container. However, at 1 bar, the condensation temperature of H_2 is extremely low at 21.3 K meaning a significant input of energy is required to attain condensation.(180) Furthermore, heat transfer through the container would lead to the loss of H_2 over time, and many of the safety concerns associated with the use of pressurised H_2 also persist.

One of the most viable options for the safe and reliable storage of H_2 for mobile applications is its physical adsorption onto high surface area materials. Here, the relatively weak van der Waals interactions between the H_2 molecules and the materials surface permits the condensation at temperatures significantly higher than the boiling point of H_2.

Numerous materials have been evaluated for such an application, including carbon nanotubes,(182) carbon nanofibers,(183) MOFs,(184) templated carbons(82)(185) and ACs.(7) Of these, ACs hold certain advantages over the other potential materials; such advantages include relatively low cost, a wide variety of precursors, and the potential to vary pore sizes, surface areas, surface functionalities and doping content.(7) Templated carbons, being able offer a very high degree of control over porosity and surface areas, are also attractive as potential H_2 storage materials – however the high costs and complexity of templating microporous templates such as MOFs and zeolites would likely most such methods unviable.

Mokaya and co-workers demonstrated a high H_2 uptake of 2.6 wt. % (at 77 K and 1 bar pressure) with an ordered microporous carbon prepared from a zeolite-β template and acetonitrile as the carbon precursor (introduced *via* CVD) (Figure 1.28.).(186) The carbons had high BET surface areas and pore volumes of up to 3200 m^2 g^{-1} and 2.41 cm^3 g^{-1}, respectively. Mokaya's group also investigated the use of different zeolite templates (zeolite 13X and zeolite Y), carbon precursors (acetonitrile and ethylene) and CVD temperatures (550 – 1000 °C) on the resultant H_2 uptake capacities.(187) H_2 storage capacities were found to be mainly dependent on the BET surface area of the porous carbons, but factors such as N-doping and graphitic content of the carbon also had an influence. Acetonitrile-derived materials templated from zeolite Y at a CVD temperature of 800 °C were found to be optimal – having a H_2 storage capacities as high as 2.0 wt. % at 1 bar and 77 K. Mokaya's group also found that the subsequent chemical (KOH) activation of zeolite templated carbons further enhances the H_2 storage capacity.(188) The activation step increased the surface area of a zeolite Y templated carbon by up to 84 % (from 1400 – 1650 to 1850 – 3100 m^2 g^{-1}) whilst more than doubling the pore volume (0.8 – 1.1 to 1.5 – 1.75 cm^3 g^{-1}). This had the effect of increasing the H_2 storage capacity (at 20 bar and 77 K) form 2.4 – 3.5 wt. % to 4.3 – 6.1 wt. %. Several other ACs and templated carbons with notable H_2 uptake performance are given in Table 1.5.

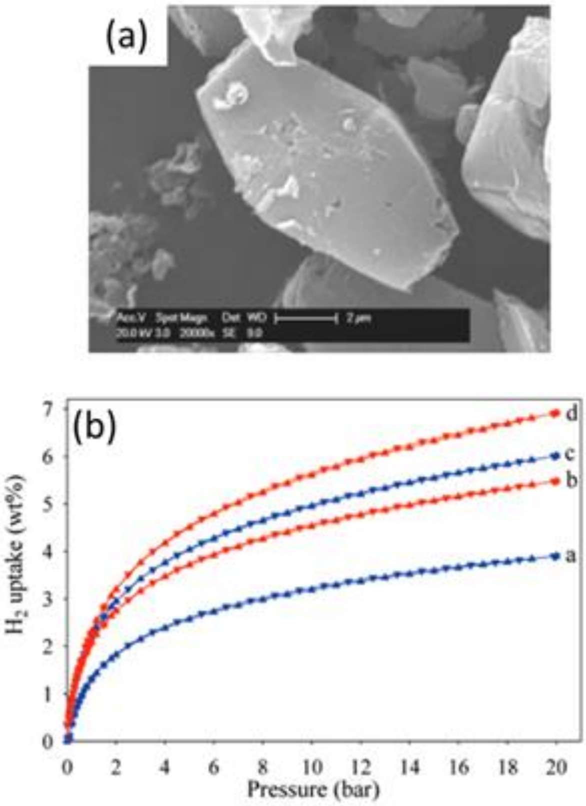

Figure 1.27. a) SEM image and b) H_2 uptake isotherms of the zeolite-β templated porous carbons prepared by Mokaya and co-workers (186)

Table 1.5. H_2 uptake capacities of various templated carbons

Template	***Precursor***	***Method***	***Surface Area (m^2 g^{-1})***	***H_2 Adsorption (wt. %)***	***Conditions***	***Ref.***
Zeolite Y	Acetonitrile	CVD, post-activation w. KOH	3064	2.6	77 K, 1 Bar	(188)
Zeolite β	Acetonitrile	CVD	3150	2.6	77 K, 1 Bar	(186)
Zeolite 13X	Acetonitrile	CVD	1589	1.6	77 K, 1 Bar	(187)
Zeolite Y	Acetonitrile	CVD	1825	2.0	77K, 1 Bar	(187)
Zeolite Y	Propylene	CVD	2117	2.0	77K, 1 Bar	(189)
Mesoporous Silica (MCM-48)	Sucrose	Aqueous impregnation & carbonization	2390	3.5	77K, 1 Bar	(190)
Mesoporous Silica (MCM-48)	Sucrose	Aqueous impregnation & carbonization	1646	2.7	77K, 60 Bar	(191)
Mesoporous Silica (KIT-6)	Polycarbosilane	Organic impregnation & carbonization	2914	3.0	77 K, 135 Bar	(192)
Mesoporous Silica (SBA-15)	Sucrose	Aqueous impregnation, carbonization & CO_2 activation	2749	2.3	77 K, 1 Bar	(193)
Colloidal Silica	Sucrose	Aerosol drying & carbonization	1995	2.0	77 K, 1.1 Bar	(194)
MOF (IRMOF-1)	MOF (IRMOF-1)	Direct carbonization (MOF acts as template and precursor)	3447	3.3	77 K, 1 Bar	(195)
ZIF-8	ZIF-8	Direct carbonization (ZIF acts as template and precursor) & KOH activation	2437	2.6	77 K, ~1 Bar	(196)
Hypercrosslinked porous polymer (COP)	Hypercrosslinked porous polymer (COP)	Direct carbonization & KOH activation	2189	2.6	77 K, 1 Bar	(197)
*Sol-gel method**	Resorcinol Formaldehyde	RF polymerization and air-drying (aerogel), carbonization	1980	4.3	77 K, 20 Bar	(81)
DMSO Ice Templating	Polyacrylonitrile (PAN)	This Work (IT-ACMAX)	2206	2.7	77 K, 1.2 Bar	Chapter 4

*Not a templating method but included for comparison

1.6.7.5. CO_2 Storage

Although not a form of energy storage *per-se*, carbon capture and storage (CCS) exists in the broader area of renewable technologies and shares the common goal of anthropogenic CO_2 emission reduction. CCS involves the separation of CO_2 from concentrated gas mixtures (typically from large point sources such as fossil fuel power plants, refineries or cement manufacturing facilities), its transport to sequestration sites (typically appropriate geological formations), and its long term storage therein.(198) This avoids its release into the atmosphere and therefore prevents its contribution to climate change. Carbon capture and utilization (CCU) is a similar process, but involves the sequestration of captured CO_2 by utilising it as a feedstock to produce higher value chemicals – rather than simple storage.(198)

The process of CO_2 capture from fossil fuel combustion can be attained *via* three main configurations, namely pre-combustion capture, post-combustion capture and the oxy-fuel combustion capture.(198) Post-combustion capture involves the separation of CO_2 from the exhaust stream mixture of gasses (flue-gas) once the fuel has been combusted in air. This process is relatively straightforward and has the advantage in that existing conventional plants can be retrofitted with the technology, however the CO_2 concentration in the flue gas is quite low (4 – 14 %) and contains numerous impurities (*e.g.* NO_x, SO_x, H_2O and soot) making capture and concentration of the gas inefficient and energy intensive.(198) Pre-combustion capture is more complex, requiring Integrated Gasification Combined Cycle (IGCC) technology to produce syngas ($CO + H_2$) from the fossil fuel precursor, which is then shifted to produce a stream of relatively pure CO_2 and H_2 (Figure 1.29.). The CO_2 can then be separated before the H_2 fuel is combusted. Since the CO_2 is at a relatively high concentration (> 20 %) its separation is easier than for post-combustion capture.

$$\mathrm{Coal} \overset{\mathrm{gasification}}{\Longrightarrow} \mathrm{CO} + H_2$$

$$\mathrm{CO} + \mathrm{H_2O} \overset{\mathrm{water-gas\ shift}}{\Longrightarrow} \mathrm{H_2} + \mathrm{CO_2}$$

$$\mathrm{CH_4} + \mathrm{H_2O} \overset{\mathrm{reform}}{\Longrightarrow} \mathrm{CO} + \mathrm{H_2}$$

Figure 1.28. Gasification and steam reformation processes to produce H_2 and CO_2 from fossil fuels (198)

In oxy-fuel combustion, rather than air, the fuel is burnt in pure O_2 to produce a stream of CO_2, H_2O and other minor impurities such as soot and SO_x. The H_2O and impurities can be removed *via* conventional methods (*i.e.* condensation of H_2O, electrostatic removal of soot, and desulfurisation to remove SO_x) to give a highly concentrated stream of CO_2 (80 – 98 %).

Further concentration to the purity required for transport and storage (> 95.5 %) can therefore be achieved far easier than the other abovementioned methods.(198) A major drawback for the oxy-fuel combustion process is that the initial air separation to produce pure O_2 (cryogenic distillation) is impractical and requires a considerable energy input.

Each of these processes requires the separation and concentration of CO_2 from impure gas mixtures. This can be attained *via* several means, the main ones being membrane separation, absorption and adsorption, and are discussed below. Membranes can be employed to selectively allow CO_2 to diffuse through, whilst excluding other gasses, and therefore produce concentrated streams of CO_2 with very little energy input. This technology is still in its infancy, with separation times and efficiencies needing to be improved before the technology can be widely adopted.(199) Absorption processes involve the use of liquid CO_2 sorbents, typically amines such as mono- or di- ethanolamine (MEA and DEA, respectively), which capture CO_2 from the gas stream before being separated and released though heating and/or depressurisation. The release of CO_2 in this way regenerates the sorbent when can then be re-used. This *amine-scrubbing* process is the conventional method currently employed for carbon capture applications, however it is inefficient and energy intensive – with the energy requirement plants employing the technology increasing 25 – 40 %, as well as the corrosive nature of the amines being problematic.(200) Adsorption processes involve the reversible adsorption and desorption of CO_2 onto the surfaces of various high surface area porous solids, such as MOFs,(201) COFs,(202) microporous polymers(203) and ACs.(8)(204)(205) Adsorption processes, unlike absorption, involve relatively weak van der Waals interactions between the CO_2 molecules and the adsorbent, allowing relatively facile regeneration of the material under relatively mild temperature or pressure swing cycles – resulting in greater energy efficiency and lower running costs. MOFs, in particular, have been championed as high capacity and high selectivity CO_2 sorption materials for carbon capture, however MOFs are often fairly expensive and suffer from relatively poor chemical and thermal stability, meaning much optimisation is required before they can feasibly be deployed for CCS on a large scale. ACs, on the other hand, can be extremely cheap and are stable with regards to temperature and the corrosive chemicals present in flue gas. ACs have demonstrated excellent performance with regards to CO_2 capture, and the versatility of carbon with regards to precursors, doping, nanotexture, surface functionalisation, porosity and surface area means there is still much potential for ACs in CO_2 capture applications. Similarly, templated carbons have room for much optimisation with regards to this application too. Templated carbons, offering greater control over various properties than ACs, could be highly promising materials for CCS, but high costs could be an issue when considering commercialisation.

Han and co-workers prepared an N-doped templated carbon using the mesoporous silica IBN-9 as a hard template, with furfuryl alcohol and diamino benzene as carbon precursors.(206) Having a very high N content of ~13 wt. % and surface area of 890 m^2 g^{-1}, the material had an excellent CO_2 uptake capacity of 10.5 mmol g^{-1} at 298 K and 8 bar of pressure. Zeolite EMC-2 was used by Zhu and co-workers to prepare a zeolite templated, N-doped porous carbon, using acetonitrile (introduced by CVD) as a carbon precursor.(207) The materials displayed very high CO_2 uptake capacities of up to 4.4 mmol g^{-1} at 298 K and 1 bar pressure, as well as good CO_2/N_2 selectivity. Porous carbons prepared from resorcinol formaldehyde precursors in the presence of a Pluronic F127 soft template were evaluated for CO_2 uptake capacity by Lu and co-workers (Figure 1.30.).(208) The materials had BET surface areas of 500 - 670 m^2 g^{-1} and a small level of N-doping (<0.5 wt. %) – due to the presence of amines during the resorcinol formaldehyde polymerisation. The material with the best performance had an excellent CO_2 uptake capacity of 3.3 mmol g^{-1} at 298 K and 1 bar. A number of other templated porous carbons which have been evaluated for CO_2 uptake capacity are presented in Table 1.6.

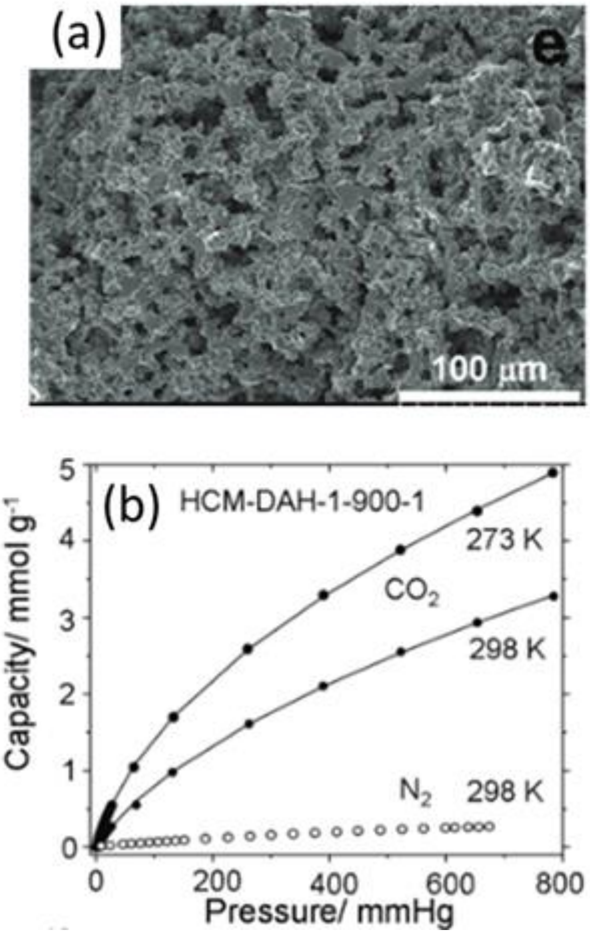

Figure 1.29. a) SEM image and b) CO_2 uptake isotherms for the porous carbon prepared by Lu and co-workers (208)

Table 1.6. CO_2 uptake capacities of various templated carbons

Template	***Precursor***	***Method***	***BET SSA (m^2 g^{-1})***	***N-content (wt. %)***	***CO_2 Adsorption (mmol g^{-1})***	***Conditions***	***Ref.***
Pluronic F127	Resorcinol Formaldehyde	RF polymerisation with amine, carbonisation	670	0.28	3.3	298 K, ~1 Bar	(208)
Pluronic F127	Resorcinol Formaldehyde	RF polymerisation with amine, carbonisation and KOH activation	1613	0.68	3.1	298 K. 0.95 Bar	(209)
Pluronic F127	Dicyandiamide, Resol	Polymerisation, carbonisation	1417	6.7	3.2	298 K, 1 Bar	(210)
Pluronic 123	Polypyrrole	Polymerisation of pyrrole, carbonisation	941	5.8	4.5	298 K, 1 Bar	(211)
Benzimidazole-Linked Polymers	Benzimidazole-Linked Polymers	Direct carbonisation (polymer acts as precursor and template) & KOH activation	1630	7.9	5.8	298 K, 1 Bar	(212)
Hypercrosslinked porous polymer (COP)	Hypercrosslinked porous polymer (COP)	Direct carbonisation & KOH activation	1950	Not given	7.6	273 K, 1 Bar	(197)
Zeolite EMC-2	Acetonitrile	CVD	2559	6 - 7	4.0	298 K, ~1Bar	(207)
Zeolite EMC-2	Acetonitrile	CVD	3360	4.7	4.4	298 K, 1 Bar	(69)
ZIF-69	ZIF-69	Direct carbonisation (ZIF acts as template and precursor) & KOH activation	2264	1.2	4.8	273 K, 1 Bar	(196)
MOF-5	MOF-5	Direct carbonisation (MOF acts as template and precursor)	2734	Not given	27.4	300 K, 30 Bar	(213)
MOF-74	MOF-74	Direct carbonisation (MOF acts as template and precursor)	2495	Not given	3.4	300 K, 1.5 Bar	(213)
Polymer microspheres (GDMA-co-MAA)	Melamine	ML polymerisation, carbonisation & KOH activation	683	14.5	2.7	298 K, 1 Bar	(214)
Mesoporous Silica (IBN-9)	Furfuryl Alcohol & p-diaminobenzene	Mixing precursors & templates, drying, carbonisation & activation	890	13	10.5	298 K, 8 Bar	(206)

Mesoporous silica (SBA-15) spheres	Ethylenediamine & carbon tetrachloride	Mixing, polymerisation & carbonisation	550	17.8	2.9	298 K, 1 ~Bar	(215)
*Sol-gel method**	Polyaniline (PANi)	PANi polymerisation (hydrogel) and freeze-drying (xerogel), carbonisation and KOH activation	4196	0.55	28.3	298 K, 30 Bar	(216)
*Sol-gel method**	Resorcinol & Formaldehyde (RF)	RF polymerisation and air-drying (aerogel), carbonisation	1521	Not given	3.0	298 K, 1 Bar	(81)
*Temperature induced phase separation (TIPS)**	Polyacrylonitrile (PAN)	Carbonisation & CO_2 activation	2501	1.8	10.6	298 K, 3 Bar	(70)
H_2O ice crystals & silica spheres	Glucose	Carbonisation and CO_2 activation	2096	0	4.1	273 K, 10 Bar	(124)
DMSO ice-crystals	Polyacrylonitrile (PAN)	Chapter 4 (IT-AC50)	1049	14.9	16.1	298 K, 10 Bar	Chapter 4
DMSO ice-crystals	Polyacrylonitrile (PAN)	Chapter 4 (IT-AC50)	1049	14.9	3.2	298 K ~1 Bar	Chapter 4

*Not a templating method but included for comparison

1.6.8. Other Applications for Templated Carbons

Templated carbons have been applied for various other applications, including other energy storage applications, such as electrodes for the Li-O_2 battery,(217)(218) and H_2 and MeOH fuel cells,(219)(220) but also other applications such as catalyst supports,(221)(222) chromatography(223) and water treatment.(224)(225) A detailed discussion of these other uses for templated carbons are beyond the scope for this thesis, however various books and reviews which cover such subjects have been published.(220)(226)

1.7. Targets and Layout of Thesis

As the introduction details, hard and soft templating methods for the fabrication of porous carbons have been widely explored, and have attained exceptional performance in the context of energy storage applications. However, significant shortcomings, namely high costs, complexity and difficulty of scale-up persist, making such methods commercially uneconomical despite the relatively good performance.

Such shortcomings cannot be overcome by incremental tweaks to existing methods – but only by exploring and developing new procedures which place simplicity and cost-effectiveness at the heart of the research and development process. Ice-templating is an example of such a process, since the templates (solvent crystals) are easily formed, removed, are low cost and benign. In this PhD, we have explored the ice-templating technique for this purpose, *i.e.* developed and optimised ice-templating and carbonisation methods, and evaluated the resultant materials for energy storage applications. This thesis compiles the most significant findings from this work.

Chapter 2 gives a broad background on the various characterisation techniques used for the work compiled in this thesis. Chapters 3, 4 and 5 are experimental chapters that summarise the most significant findings over the course of this PhD, and are written and presented in the style similar to that of scientific publications. The thesis concludes with chapter 6 which summarises the findings and gives an outlook on the possible future direction of research in this area.

1.8. References

1. Key World Energy Statistics (2009) *Internantional Energy Agency*.
2. Ellabban O, Abu-Rub H, Blaabjerg F (2014) *Renew Sustain Energy Rev* 39:748–764.
3. Carbajales-Dale M, Barnhart CJ, Benson SM (2014) *Energy Environ Sci* 7(5):1538–1544.
4. Barton JP, Infield DG (2004) *IEEE Trans Energy Convers* 19(2):441–448.
5. Pollet BG, Staffell I, Shang JL (2012) *Electrochim Acta* 84(0):235–249.
6. Ogumi Z, Wang H (2009) *Lithium-Ion Batteries: Science and Technologies* (Springer New York), pp 49–73.
7. Sevilla M, Mokaya R (2014) *Energy Environ Sci* 7(4):1250–1280.
8. Plaza MG, Garcia S, Rubiera F, Pis JJ, Pevida C (2010) *Chem Eng J* 163(1–2):41–47.
9. Jorda-Beneyto M, Suerez-Garcia F, Lozano-Castello D, Cazorla-Amoros D, Linares-Solano A (2007) *Carbon* 45(2):293–303.
10. Zhang F, Cheng S, Pant D, Bogaert G Van, Logan BE (2009) *Electrochem commun* 11(11):2177–2179.
11. Xu C, Sun F, Gao H, Wang J (2013) *Anal Chim Acta* 780(5):20–27.
12. Pumera M (2011) *Energy Environ Sci* 4(3):668.
13. Baughman RH, et al. (2002) *Science* 297(5582):787.
14. Inagaki M, Kang F (2006) *Carbon materials science and engineering: from fundamentals to applications* (清华大学出版社有限公司).
15. Inagaki M, Kang F, Toyoda M, Konno H (2013) *Advanced Materials Science and Engineering of Carbon* (Butterworth-Heinemann).
16. Inagaki M, Kang F (2016) *Materials Science and Engineering of Carbon: Characterization* (Butterworth-Heinemann).
17. Rouquerol J, et al. (1994) *Pure Appl Chem* 66(8):1739–1758.
18. Su B-L, Sanchez C, Yang X-Y (2012) *Hierarchically structured porous materials from nanoscience to catalysis, separation, optics, energy, and life science* (Wiley-VCH).
19. Xie S, Svec F, Frechet JMJ (1998) *Chem Mater* 10:4072–4078.
20. Jungbauer A (2005) *J Chromatogr A* 1065(1):3–12.
21. Nakanishi K, Tanaka N (2007) *Acc Chem Res* 40(9):863–873.
22. Guo Y-G, Hu J-S, Wan L-J (2008) *Adv Mater* 20(15):2878–2887.
23. Centi G, Perathoner S (2009) *Eur J Inorg Chem* 2009(26):3851–3878.
24. Rolison DR, et al. (2009) *Chem Soc Rev* 38(1):226–52.
25. Perego C, Millini R (2013) *Chem Soc Rev* 42(9):3956–76.
26. Parlett CM a, Wilson K, Lee AF (2013) *Chem Soc Rev* 42(9):3876–93.
27. Li J-R, Kuppler RJ, Zhou H-C, Jian-Rong Li RJK and H-CZ (2009) *Chem Soc Rev*

38(5):1477–1504.

28. Li J-R, et al. (2011) *Coord Chem Rev* 255(15):1791–1823.
29. Nugent P, et al. (2013) *Nature* 495(7439):80–84.
30. Weast RC, Astle MJ, Beyer WH (1988) *CRC Handbook of Chemistry and Physics* (CRC press).
31. Emsley J (2001) *Nature's Building Blocks: An A-Z Guide to the Elements* (Oxford University Press).
32. Grill A, Meyerson BS (1995) *Synthetic diamond: Emerging CVD science and technology*. (John Wiley & Sons).
33. Hancock Y (2011) *J Phys D Appl Phys* 44(47):473001.
34. The Nobel Prize in Chemistry 1996 *Nobelprize.org*. [Accessed July 14, 2016].
35. Fitzer E, Kochling K-H, Boehm HP, Marsh H (1995) *Pure Appl Chem* 67(3):473–506.
36. Cho SY, et al. (2015) *Nat Commun* 6:7145.
37. Park JK (2012) *Principles and Applications of Lithium Secondary Batteries* (John Wiley & Sons).
38. Li W, et al. (2015) *Energy Environ Sci* 8(10):2916–2921.
39. Frank E, Steudle LM, Ingildeev D, Spörl JM, Buchmeiser MR (2014) *Angew Chemie Int Ed* 53(21):5262–5298.
40. Harris PJF (2001) *Interdiscip Sci Rev* 3:204–210.
41. Iwashita N, Inagaki M (1993) *Carbon* 31(7):1107–1113.
42. Brownsort P (2009) *Biomass pyrolysis processes: review of scope, control and variability (*Edinburgh UK Biochar Res Cent).
43. Yaman S (2004) *Energy Convers Manag* 45(5):651–671.
44. Marsh H, Reinoso FR (2006) *Activated carbon* (Elsevier).
45. Kaegi D, et al. (2000) *Kirk-Othmer Encyclopedia of Chemical Technology* (John Wiley & Sons).
46. Xiao L-P, Shi Z-J, Xu F, Sun R-C (2012) *Bioresour Technol* 118:619–623.
47. Altundogan HS, Bahar N, Mujde B, Tumen F (2007) *J Hazard Mater* 144(1–2):255–264.
48. K. Kidena SM and MN (1996) *Energy & Fuels* 10:672–678.
49. Jiang DE, Van Duin ACT, Goddard WA, Dai S (2009) *J Phys Chem A* 113(25):6891–6894.
50. Brunner PH, Roberts P V. (1980) *Carbon* 18(3):217–224.
51. Boon J, Boer W DE, Kruyssen F (1981) *Microbiology* 1(122):119–127.
52. Sugisawa H, Edo H (1966) *J Food Sci* 31(4):561–565.
53. Tang M, Bacon R (1964) *Carbon* 2(3):211–220.
54. Karacan I, Soy T (2013) *J Mater Sci* 48(5):2009–2021.

55. Schwenker RF, Pacsu E (1958) *Ind Eng Chem* 50(1):91–96.
56. Akio S, Nakanishi Y, Soma I (1969) *Appl Polym Symp* 9:271–284.
57. Goodhew PJ, Clarke AJ, Bailey JE (1975) *Mater Sci Eng* 17(1):3–30.
58. Paraknowitsch JP, Thomas A (2013) *Energy Environ Sci* 6(10):2839.
59. Paraknowitsch JP, Zhang Y, Wienert B, Thomas A (2013) *Chem Commun* 49(12):1208–10.
60. Qing X, Cao Y, Wang J, Chen J, Lu Y (2014) *RSC Adv* 4(99):55971–55979.
61. Stein A, Wang Z, Fierke MA (2009) *Adv Mater* 21(3):265–293.
62. Wood KN, O’Hayre R, Pylypenko S (2014) *Energy Environ Sci* 7(4):1212.
63. Li Z, et al. (2013) *Energy Environ Sci* 6(3):871–878.
64. Zheng F, Yang Y, Chen Q (2014) *Nat Commun* (5):5261
65. Wu ZS, Ren W, Xu L, Li F, Cheng HM (2011) *ACS Nano* 5(7):5463–5471.
66. Alabadi A, Yang X, Dong Z, Li Z, Tan B (2014) *J Mater Chem A* 2(30):11697.
67. Chen LF, et al. (2012) *ACS Nano* 6(8):7092–7102.
68. Zhang D, et al. (2013) *J Mater Chem A* 1(26):7584–7591.
69. Xia Y, Mokaya R, Walker GS, Zhu Y (2011) *Adv Energy Mater* 1(4):678–683.
70. Nandi M, et al. (2012) *Chem Commun* 48(83):10283–10285.
71. Liu G, Li X, Ganesan P, Popov BN (2009) *Appl Catal B Environ* 93(1–2):156–165.
72. Wohlgemuth S-A, White RJ, Willinger M-G, Titirici M-M, Antonietti M (2012) *Green Chem* 14(5):1515–1523.
73. Shui J, Wang M, Du F, Dai L (2015) *Sci Adv* 1(1).
74. Deng Y, Xie Y, Zou K, Ji X (2015) *J Mater Chem A* 4(4):1144–1173.
75. Wertime TH (1961) *Coming of the Age of Steel, The* (The University of Chicago Press).
76. McNeill W (2013) *The Pursuit of Power: Technology, Armed Force and Society Since A.D. 1000* (University of Chicago Press).
77. Çeçen F, Aktas Ö (2011) *Activated carbon for water and wastewater treatment: Integration of adsorption and biological treatment* (John Wiley & Sons).
78. Candelaria SL, et al. (2012) *Nano Energy* 1(2):195–220.
79. Lu M, Beguin F, Frackowiak E (2013) *Supercapacitors: materials, systems and applications* (John Wiley & Sons).
80. Forbes R (1963) *Studies in ancient technology* (Brill Archive).
81. Robertson C, Mokaya R (2013) *Microporous Mesoporous Mater* 179:151–156.
82. Nishihara H, Kyotani T (2012) *Adv Mater* 24(33):4473–4498.
83. Lu AH, Schüth F (2006) *Adv Mater* 18(14):1793–1805.
84. Xia Y, Yang Z, Mokaya R (2010) *Nanoscale* 2(5):639–659.
85. Zhao XS, et al. (2006) *J Mater Chem* 16(7):637.
86. White RJ, Tauer K, Antonietti M, Titirici M-M (2006) *Adv Mater* 18(16):2073–2094.

87. Roberts AD, Li X, Zhang H (2014) *Chem Soc Rev* 43(13):4341–4356.
88. Knox JH, Kaur B, Millward GR (1986) *J Chromatogr* 352:3–25.
89. Zakhidov AA, et al. (1998) *Science* 282(5390):897–901.
90. Ryoo R, Joo SH, Jun S (1999) *J Phys Chem B* 103(37):7743–7746.
91. Ryoo R, Joo SH, Jun S, Tsubakiyama T, Terasaki O (2001) *Stud Surf Sci Catal* 135:150–157.
92. Kyotani T, Tomita A, Ma Z (2003) *Carbon* 41:1451–1459.
93. Lee KT, Lytle JC, Ergang NS, Oh SM, Stein A (2005) *Adv Funct Mater* 15(4):547–556.
94. Hu YS, et al. (2007) *Adv Funct Mater* 17(12):1873–1878.
95. Fang B, Kim M-S, Kim JH, Lim S, Yu J-S (2010) *J Mater Chem* 20(45):10253.
96. Barata-Rodrigues PM, Mays TJ, Moggridge GD (2003) *Carbon* 41(12):2231–2246.
97. Liu B, Shioyama H, Akita T, Xu Q (2008) *J Am Chem Soc* 130(16):5390–5391.
98. Strubel P, Althues H, Kaskel S (2016) *Carbon* 107:705–710.
99. Liang C, Li Z, Dai S (2008) *Angew Chem Int Ed Engl* 47(20):3696–3717.
100. Chuenchom L, Kraehnert R, Smarsly BM (2012) *Soft Matter* 8(42):10801.
101. Wan Y, Shi Y, Zhao D (2008) *Chem Mater* 20(3):932–945.
102. Lee KT, Oh SM (2002) *Chem Commun* (22):2722–2723.
103. Meng Y, et al. (2005) *Angew Chemie - Int Ed* 44(43):7053–7059.
104. Xia Y, Yang Z, Mokaya R (2011) *Porous Mater*:217–264.
105. Cameron NR, Sherrington DC (1996) *Advances in Polymer Science* (Springer Berlin Heidelberg), pp 163–214.
106. Zhang H, Cooper AI (2005) *Soft Matter* 1(2):107–113.
107. Wang D, Smith NL, Budd PM (2005) *Polym Int* 54(2):297–303.
108. Asfaw HD, Roberts M, Younesi R, Edström K (2013) *J Mater Chem A* 1(44):13750.
109. Cohen N, Silverstein MS (2011) *Polymer* 52(2):282–287.
110. Brun N, Edembe L, Gounel S, Mano N, Titirici MM (2013) *ChemSusChem* 6(4):701–710.
111. Zhang H, et al. (2005) *Nat Mater* 4(10):787–793.
112. Zhang H, Cooper AI (2007) *Adv Mater* 19(11):1529–1533.
113. Deville S (2013) *J Mater Res* 28(17):2202–2219.
114. Deville S, Saiz E, Nalla RK, Tomsia AP (2006) *Science* 311(5760):515–518.
115. Gutiérrez MC, Ferrer ML, Del Monte F (2008) *Chem Mater* 20(3):634–648.
116. Roberts AD, Wang S, Li X, Zhang H (2014) *J Mater Chem A* 2(42):17787–17796.
117. Roberts AD, Li X, Zhang H (2015) *Carbon* 95:268–278.
118. Ling Z, et al. (2015) *Nanotechnology* 26(37):374003.
119. Choi Y-M, et al. (2015) *Energy Technol* 4(2):278–287.

120. Szczurek A, Amaral-Labat G, Fierro V, Pizzi A, Celzard A (2011) *Sci Technol Adv Mater* 12(3).
121. Sahore R, Estevez LP, Ramanujapuram A, Disalvo FJ, Giannelis EP (2015) *J Power Sources* 297:188–194.
122. Yu JW, et al. (2016) *Synth Met* 211:35–39.
123. Nishihara H, Mukai SR, Tamon H (2004) *Carbon* 42(4):899–901.
124. Hong YB, et al. (2014) *Synth Met* 196(0):33–37.
125. Estevez L, et al. (2013) *Energy Environ Sci* 6(6):1785.
126. Wu Y, et al. (2015) *Nat Commun* 6:6141.
127. Deville S (2008) *Adv Eng Mater* (3):155–169.
128. Deville S, Saiz E, Tomsia AP (2007) *Acta Mater* 55(6):1965–1974.
129. Langer JS (1980) *Rev Mod Phys* 52(1):1–28.
130. Okaji R, Taki K, Nagamine S, Ohshima M (2012) *J Appl Polym Sci* 125(4):2874–2881.
131. Qian L, Willneff E, Zhang H (2009) *Chem Commun* (26):3946–3948.
132. Roberts AD, Zhang H (2013) *Int J Pharm* 447(1–2):241–250.
133. Wan Y, Fang Y, Wu H, Cao X (2006) *J Biomed Mater Res Part A* 80A(4):776–789.
134. Thongprachan N, Nakagawa K, Sano N, Charinpanitkul T, Tanthapanichakoon W (2008) *Mater Chem Phys* 112(1):262–269.
135. Katuri K, et al. (2011) *Energy Environ Sci* 4(10):4201.
136. Barrow M, Eltmimi A, Ahmed A, Myers P, Zhang H (2012) *J Mater Chem* 22(23):11615.
137. Winter M, Besenhard J, Spahr M, Novak P (1998) *Adv Mater* 10(10):725–763.
138. Zhou H, Zhu S, Hibino M, Honma I, Ichihara M (2003) *Adv Mater* 15(24):2107–2111.
139. Roy P, Srivastava SK (2015) *J Mater Chem A* 3(6):2454–2484.
140. Endo M, Kim C, Nishimura K, Fujino T, Miyashita K (2000) *Carbon* 38(2):183–197.
141. Yang Z, et al. (2013) *Electrochem commun* 28:40–43.
142. Pan L, et al. (2014) *Chem Commun (Camb)* 50(44):5878–80.
143. Zhang R, et al. (2014) *Adv Mater* 26(39):6749–6755.
144. Gao M, et al. (2010) *Electrochim Acta* 55(28):9067–9074.
145. Su F, et al. (2005) *J Phys Chem B* 109(43):20200–20206.
146. Qie L, et al. (2012) *Adv Mater* 24(15):2047–2050.
147. Wang Y, Su F, Wood CD, Lee JY, Zhao XS (2008) *Ind Eng Chem Res* 47(7):2294–2300.
148. Bruce PG, Freunberger S a., Hardwick LJ, Tarascon J-M (2011) *Nat Mater* 11(2):172–172.
149. Ji X, Nazar LF (2010) *J Mater Chem* 20(44):9821–9826.
150. Manthiram A, Fu Y, Su Y-S (2013) *Acc Chem Res* 46(5):1125–1134.

151. Zhang B, Qin X, Li GR, Gao XP (2010) *Energy Environ Sci* 3(10):1531.

152. Agrawal M, et al. (2014) *J Power Sources* 261(0):363–370.

153. Wang J, He Y-S, Yang J (2015) Sulfur-Based Composite Cathode Materials for High-Energy Rechargeable Lithium Batteries. *Adv Mater* 27(3):569–575.

154. Ji X, Lee KT, Nazar LF (2009) A highly ordered nanostructured carbon-sulphur cathode for lithium-sulphur batteries. *Nat Mater* 8(6):500–506.

155. Yang Y, Zheng G, Cui Y (2013) Nanostructured sulfur cathodes. *Chem Soc Rev* 42(7):3018–3032.

156. Wang D-W, et al. (2013) *J Mater Chem A* 1(33):9382–9394.

157. Zhao C, et al. (2014) *Nanoscale* 6(2):882–888.

158. Li X, et al. (2011) *J Mater Chem* 21(41):16603–16610.

159. He G, Ji X, Nazar L (2011) *Energy Environ Sci* 4(8):2878.

160. Ding B, Yuan C, Shen L, Xu G, Nie P (2013) *Chem Eur* 19:1013–1019.

161. Li J, et al. (2014) *J Mater Chem A* 2(34):13916.

162. Zhang LL, Zhao XS (2009) *Chem Soc Rev* 38(9):2520–2531.

163. Simon P (2008) *Nat Mater* 7(11):845–854.

164. Helmholtz H (1853) *Ann Phys Chem* 89(2):211–233, 353–377.

165. Gouy G (1910) *Ann Phys (Paris)* 4(9):457–468.

166. Chapman DL (1913) *Philos Mag Ser 6* 25(148):475–481.

167. Stern O (1924) Zur Theorie Der Elektrolytischen Doppelschicht. *Zeitschrift für Elektrochemie und Angew Phys Chemie* 30(21–22):508–516.

168. Pandolfo AG, Hollenkamp AF (2006) *J Power Sources* 157(1):11–27.

169. Portet C, et al. (2009) *J Electrochem Soc* 156(1):A1.

170. Ania CO, Khomenko V, Encarnaciin R-P, Parra JB, Beguin F (2007) *Adv Funct Mater* 17(11):1828–1836.

171. Fuertes AB, Lota G, Centeno TA, Frackowiak E (2005) *Electrochim Acta* 50(14):2799–2805.

172. Wang D-W, Li F, Liu M, Lu GQ, Cheng H-M (2008) *Angew Chemie Int Ed* 47(2):373–376.

173. Yamada H, Nakamura H, Nakahara F, Moriguchi I, Kudo T (2007) *J Phys Chem C* 111:227–233.

174. Zhao J-C, Lai C-Y, Dai Y, Xie J-Y (2005) *J Cent South Univ Technol* 12(6):647–652.

175. Xing W, et al. (2009) *Carbon* 47(7):1715–1722.

176. Jin J, Tanaka S, Egashira Y, Nishiyama N (2010) *Carbon* 48(7):1985–1989.

177. Ania CO, Khomenko V, Raymundo-Pinero E, Parra JB, Beguin F (2007) *Adv Funct Mater* 17(11):1828–1836.

178. Liu B, Shioyama H, Jiang H, Zhang X, Xu Q (2010) *Carbon* 48(2):456–463.

179. Metz B (2001) *Climate Change 2001: Mitigation: Contribution of Working Group III to the Third Assessment Report of the Intergovernmental Panel on Climate Change* (Cambridge University Press).
180. Schlapbach L, Züttel a (2001) *Nature* 414(6861):353–358.
181. Zittel W, Wurster R, Bolkow L (1996). Advantages and Disadvantages of Hydrogen. Hydrogen in the Energy Sector. Systemtechnik Gmbitt.
181. Chen X, Li C, Graetzel M, Kostecki R, Mao SS (2012) *Chem Soc Rev* 41(23):7909–7937.
182. Lee SM, et al. (2001) *Synth Met* 121(1–3):1189–1190.
183. Hwang JY, Lee SH, Sim KS, Kim JW (2002) *Synth Met* 126(1):81–85.
184. Langmi HW, Ren J, North B, Mathe M, Bessarabov D (2013) *Electrochim Acta* 128(2014):368–392.
185. Xia Y, Mokaya R (2007) *J Phys Chem C* 111(27):10035–10039.
186. Yang Z, Xia Y, Mokaya R (2007) *J Am Chem Soc* 129(6):1673–1679.
187. Yang Z, Xia Y, Sun X, Mokaya R (2006) *J Phys Chem B* 110(37):18424–18431.
188. Sevilla M, Alam N, Mokaya R (2010) *J Phys Chem C* 114(25):11314–11319.
189. Chen L, Singh RK, Webley P (2007) *Microporous Mesoporous Mater* 102(1–3):159–170.
190. Gadiou R, et al. (2005) *Microporous Mesoporous Mater* 79(1–3):121–128.
191. Terrés E, et al. (2005) *Chem Phys Lett* 403(4–6):363–366.
192. Oschatz M, et al. (2010) *Carbon* 48(14):3987–3992.
193. Xia K, Gao Q, Wu C, Song S, Ruan M (2007) *Carbon* 45(10):1989–1996.
194. Hu Q, Lu Y, Meisner GP (2008) *J Phys Chem C* 112(5):1516–1523.
195. Yang SJ, et al. (2012) *Chem Mater* 24(3):464–470.
196. Wang Q, et al. (2013) *Chem - An Asian J* 8(8):1879–1885.
197. Modak A, Bhaumik A (2015) *J Solid State Chem* 232:157–162.
198. Leung DYC, Caramanna G, Maroto-Valer MM (2014) *Renew Sustain Energy Rev* 39:426–443.
199. Brunetti A, Scura F, Barbieri G, Drioli E (2010) *J Memb Sci* 359(1–2):115–125.
200. D’Alessandro DM, Smit B, Long JR (2010) *Angew Chem Int Ed Engl* 49(35):6058–82.
201. Millward AR, Yaghi OM (2005) *J Am Chem Soc* 127(51):17998–17999.
202. Furukawa H, Yaghi O (2009) *J Am Chem Soc* 131(25):8875-8883
203. Woodward RT, et al. (2014) *J Am Chem Soc* 136(25):9028–9035.
204. Dantas TLP, et al. (2009) *Sep Sci Technol* 45(1):73–84.
205. Sevilla M, Fuertes AB (2012) *J Colloid Interface Sci* 366(1):147–54.
206. Zhao Y, et al. (2012) *J Mater Chem* 22(37):19726.

207. Wang L, Yang RT (2012) *J Phys Chem C* 116(1):1099–1106.
208. Hao GP, et al. (2011) *J Am Chem Soc* 133(29):11378–11388.
209. Yu J, et al. (2014) *Carbon N Y* 69:502–514.
210. Wei J, et al. (2013) *Adv Funct Mater* 23(18):2322–2328.
211. To JWF, et al. (2016) *J Am Chem Soc* 138(3):1001–1009.
212. Ashourirad B, Sekizkardes AK, Altarawneh S, El-Kaderi HM (2015) *Chem Mater* 27(4):1349–1358.
213. Srinivas G, Krungleviciute V, Guo Z-X, Yildirim T (2014) *Energy Environ Sci* 7(1):335–342.
214. Li D, et al. (2015) *ACS Sustain Chem Eng* 4(1)
215. Li Q, et al. (2010) *Nano Res* 3(9):632–642.
216. He J, et al. (2016) *Adv Energy Mater* 6(14)
217. Park J-B, Lee J, Yoon CS, Sun Y-K (2013) *ACS Appl Mater Interfaces* 5(24):13426–13431.
218. Guo Z, et al. (2013) *Adv Mater* 25(39):5668–5672.
219. Su F, et al. (2005) *Carbon* 43(11):2366–2373.
220. Antolini E (2009) *Appl Catal B Environ* 88(1):1–24.
221. Shanahan P V., et al. (2008) *J Power Sources* 185(1):423–427.
222. Yu JS, Kang S, Yoon SB, Chai G (2002) *J Am Chem Soc* 124(32):9382–9383.
223. Gilbert MT, Knox JH, Kaur B (1982) *Chromatographia* 16(1):138–146.
224. Tsouris C, et al. (2011) *Environ Sci Technol* 45(23):10243–10249.
225. Zou L, Li L, Song H, Morris G (2008) *Water Res* 42(8–9):2340–2348.
226. Béguin F, Frackowiak E (2009) *Carbons for electrochemical energy storage and conversion systems* (CRC press).

Chapter 2

Characterisation Methods and Theory

Some contents of this chapter have been published in the journal *Chemical Society Reviews*.
(Roberts AD, Li X, Zhang H (2014). *Chem Soc Rev* 43(13):4341–4356.)

List of Figures

2.1. Background and Context

This chapter describes the theory and background of the various characterisation techniques used for the work presented in this thesis. Since the experimental chapters may have used different equipment or conditions to perform the same analysis techniques (mainly a consequence of working in two different institutions), each experimental chapter contains detailed information on the specific processes and experimental conditions employed, whereas this chapter provides a broader background and concepts behind the techniques employed.

2.2. Gas Sorption

Adsorption is the term given to the adhesion of an atomic, ionic or molecular substance (the adsorbate), in either gaseous, liquid or dissolved form, to a surface (the adsorbant). *Desorption* is the reverse of adsorption, whilst *sorption* is the term given to encompass both processes.(1)

Adsorption processes can be classified as either physical or chemical, known as physisorption and chemisorption, respectively. Physisorption arises from the interaction of the adsorbate with the adsorbant surface *via* relatively weak van der Waals interactions. The weakness of these bonds tends to result in the process being reversible – with the adsorbate layer being in kinetic equilibrium with the bulk phase. Chemisorption, on the other hand, involves electron transfer between the adsorbate and adsorbant surface, resulting in the formation of stronger, less reversible, chemical bonds.(1)

Adsorption processes can be described trough isotherms, which display the amount of adsorbate on the surface of the adsorbant (at a constant temperature) as a function of pressure (for gasses) or concentration (for liquids or dissolved solids). The quantity adsorbed is generally normalised by mass or volume of the adsorbant to allow comparison of different materials, and can reveal information such as surface area, pore size distributions, pore shape and pore volume of the analysed material.(1)

The two major models which describe the adsorption of gasses on to solid surfaces are known at the Langmuir model and the Brunauer-Emmett-Teller (BET) model.(2)(3)

2.2.1. Langmuir Model

The Langmuir model is an early and relatively simple model used to describe the adsorption of gasses onto the surfaces of solids.(2) It is based on the following assumptions:

I. Adsorption sites are equivalent and may only be occupied by one adsorbate particle at a time

II. A dynamic equilibrium exists between the gas phase particles and those adsorbed on the surface of the adsorbate

III. If an adsorbate collides with a vacant adsorption site, it will form a bond to the surface. If it collides with a filled site, it will be reflected back into the gas phase. Multilayer formation is not allowed

IV. Once adsorbed, the adsorbate particles are localised and have no interaction with adjacent particles

The Langmuir model can be used to calculate the surface area of a material. This can be derived by firstly expressing assumption II as the following equilibrium mechanism:

$$M_{(g)} + S_{(s)} \rightleftarrows MS_{(s)}$$

Eq. 2.1.

Where $M_{(g)}$ is the gaseous phase adsorbant, $S_{(s)}$ is the solid adsorbate and $MS_{(s)}$ is the physisorbed adsorbant-adsorbate complex. An equilibrium constant, K, can be given as a function of rate constants for adsorption (k_a) and desorption (k_d):

$$K = \frac{k_a}{k_d}$$

Eq. 2.2.

The fractional coverage of the adsorbate, θ, can be written as a fraction of the number of sites occupied by an adsorbate, N_s, and the total number of adsorption sites N. It can also be written in terms of relative amounts or relative volumes:

$$\theta = \frac{N_s}{N} = \frac{n_a}{n_m} = \frac{V_a}{V_m}$$

Eq. 2.3.

Where n_a is the amount (in moles) of gas adsorbed and n_m is the amount adsorbed when all adsorption sites are occupied, and V_a is the volume of gas adsorbed and V_m is the volume adsorbed when all adsorption sites are occupied in the monolayer. The rate of adsorption is dependent on the number of sites not occupied by adsorbate molecules (1 – θ) as well as the partial pressure P. However, the rate of desorption only depends on the fractional coverage θ:

$$Rate\ of\ adsorption = k_a P(1 - \theta)$$

Eq. 2.4.

$$Rate\ of\ desorption = k_d \theta$$

Eq. 2.5.

At equilibrium, the rate of adsorption and desorption are equal, hence:

$$k_a P(1-\theta) = k_d \theta$$

Eq. 2.6.

Which can be rearranged to predict the fractional coverage as a function of pressure:

$$\theta = \frac{KP}{(1+KP)}$$

Eq. 2.7.

Substituting Eq. 2.3. and re-arranging, the Langmuir equation can then be written as:

$$\frac{P}{n_a} = \frac{1}{n_m K} + \frac{P}{n_m}$$

Eq. 2.8.

Where a plot of P/n_a vs. P will give a straight line of gradient $1/n_m$. Calculating the value for n_m (number of moles adsorbed when all adsorption sites are occupied) and knowing the cross-sectional area of one adsorbate molecule (a_m) then allows the Langmuir surface area (SA_{lang}) to be calculated:

$$SA_{lang} = n_m N_A a_m$$

Eq. 2.9.

Where N_A is Avagadro's constant (6.022×10^{23} mol^{-1}). SA_{lang} is typically normalised per gram of material to allow easy comparison.

2.2.2. Brunauer-Emmett-Teller (BET) Model

The Brunauer-Emmett-Teller (BET) gas sorption model is an extension of the Langmuir model which takes into account the formation of multilayers.(4) Like the Langmuir model, formation of an initial monolayer occurs with a fixed heat of adsorption, but now each adsorbed molecule (and each one adsorbed thereafter) acts as its own surface site for the adsorption of further particles – although the strength of adsorbate-adsorbate bonds are significantly weaker than the surface-adsorbate bonds. The BET model makes the following assumptions:

I. Rather than a monolayer, an infinite number of layers can adsorb on the surface of the adsorbate
II. An adsorbed particle can act as an adsorption site for another particle, but there is no other interaction between adsorption layers

III. The Langmuir model can be applied to each layer individually

The resulting BET equation, which can be derived in a similar way to the Langmuir equation, can be expressed as:

$$\frac{P}{V(P_0 - P)} = \frac{1}{V_m C} + \frac{(C_{BET} - 1)}{V_m C_{BET}} \cdot \frac{P}{P_0}$$

Eq. 2.10.

Where P_0 is the saturation pressure of adsorbates and C_{BET} is the BET constant, which can itself be expressed as:

$$C = \exp\left(\frac{E_1 - E_L}{RT}\right)$$

Eq. 2.11.

Where E_1 is the heat of adsorption for the first layer and E_L is the heat of adsorption for layers beyond the first, R is the ideal gas constant (8.314 J mol^{-1} K^{-1}) and T is the temperature in Kelvin. A linear plot can be obtained from Eq. 2.10. by plotting $P/v(P_0 – P)$ against P/P_0, giving $(C – 1)/v_mC$ as the gradient and $1/V_mC$ as the intercept. These values can then be used to determine V_m – which can then be used to calculate the BET surface area (SA_{BET}) of the material:

$$SA_{BET} = \frac{a_m v_m N_A}{V_0}$$

Eq. 2.12.

Where V_0 is the molar volume of the gas at standard temperature and pressure.

2.2.3. Gas Adsorption Isotherm Classification

In 1984 the International Union of Pure and Applied Chemistry (IUPAC) recommended that gas sorption isotherms be categorised as one of six different types and four possible hysteresis loops.(5) These categories have recently been refined and are shown in Figure 2.1.(4)

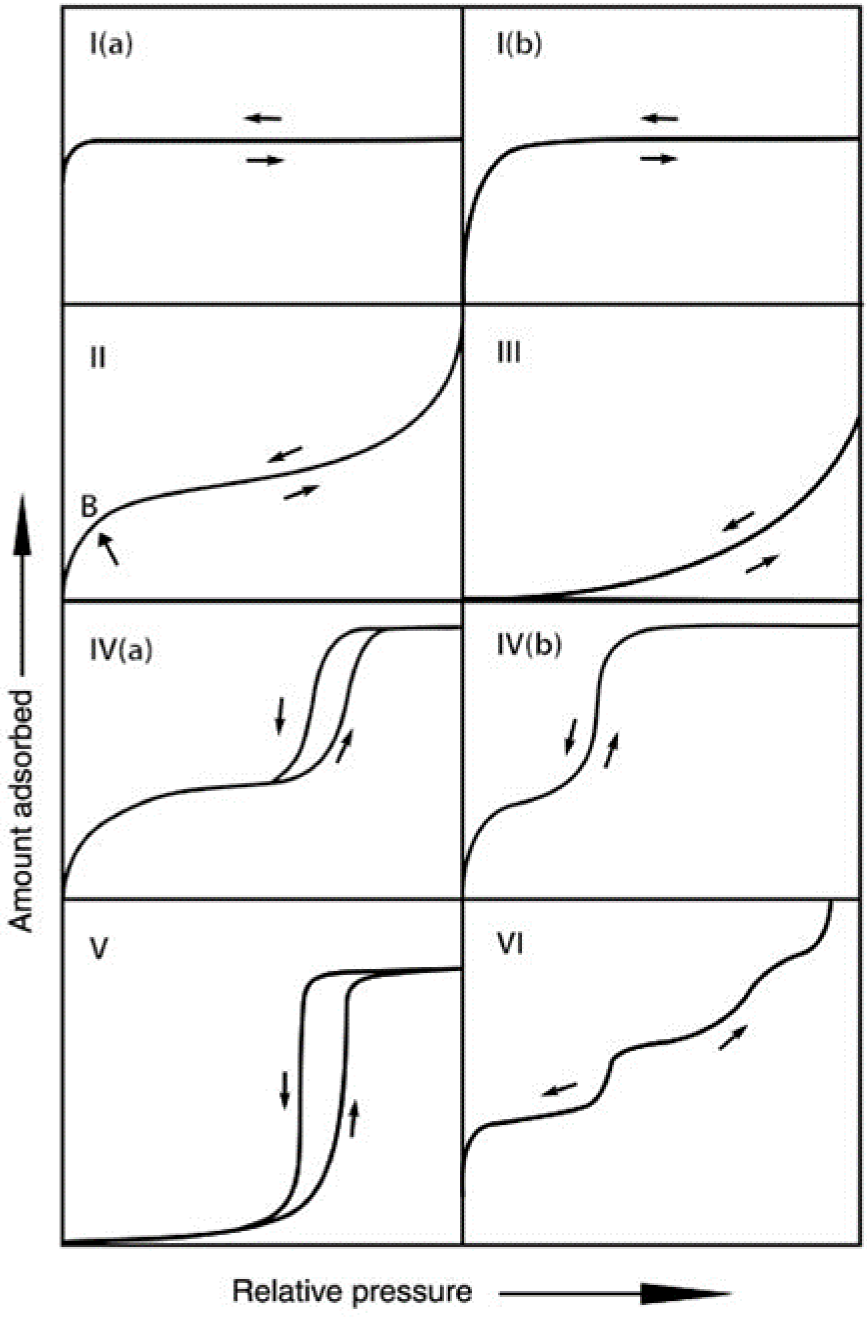

Figure 2.1. Updated classification of physisorption isotherms (4)

Type I isotherms are associated with microporous solids and have very steep uptake at low P/P_0 which is due to enhanced adsorbate-adsorbant interactions in narrow micropores. Type I(a) isotherms are associated with materials with a very narrow distribution of micropores, whereas type I(b) isotherms are associated with materials with broader distributions and possibly some narrow mesoporous.(4) Type II isotherms are typically given by macroporous adsorbents – the shape being a result of unrestricted monolayer-multilayer adsorption at high P/P_0 values. Point B on the isotherm corresponds to the completion of monolayer coverage. Type III isotherms differ as they have no point B and therefore no identifiable point of monolayer formation. Type IV isotherms are associated with mesoporous adsorbents. Here, initial monolayer-multilayer adsorption occurs on the walls of the mesopores, as it does for type II isotherms, but is followed by pore condensation – a phenomenon whereby a gas condenses into a liquid at a pressure less than the saturation pressure P_0. In type IV(a) isotherms, condensation is followed by hysteresis, which occurs when pores widths exceed a certain critical width (~4 nm for N_2) which allows capillary condensation to take place. Pores with smaller widths give type IV(b) isotherms.(4) Type V isotherms are similar to type III isotherms in the low pressure range, which can be attributed to relatively weak adsorbate-adsorbant interactions. At higher P/P_0 values condensation and pore filling can result in the observed hysteresis loop.(4) The stepwise type VI isotherm represents a layer-by-layer adsorption, with the step height representing the capacity for each adsorbed layer.(4)

2.3. Mercury Intrusion Porosimetry (MIP)

Mercury intrusion porosimetry (MIP) is an analytical technique used to determine various aspects of a material's porous nature (*i.e.* pore sizes, volumes and distributions), and is capable of evaluating pores within the size range of 0.003 – 200 µm in diameter.(6)(7) Due to the extremely high surface tension of mercury (485.5 mN m^{-1}), it will not penetrate a material's pores through capillary action alone and must be forced into the pores through application of external pressure. Since the required intrusion pressure is inversely proportional the sizes of the pores (*i.e.* relatively little pressure to intrude large pores, higher pressure to intrude smaller pores), information on the pore characteristics can be obtained by examining the pressure vs. intrusion data and interpreted through application of Washburn's equation: (7)

$$D_P = \frac{-4\gamma cos\theta_C}{P}$$

Eq. 2.13.

Where D_P is the pore diameter, γ is the surface tension (of mercury), θ_C is the contact angle and P is the applied pressure.

2.4. X-ray Diffraction (XRD)

X-ray diffraction (XRD) is a method used to determine the structure of crystalline and semi-crystalline materials. When a material is exposed to X-rays, the electrons encompassing its atoms can elastically scatter the X-rays – so long as the wavelength is roughly equal to the interatomic spacing (~1 Å). If the material has a degree of crystalline order, the scattered X-rays can interfere with one another and form nodes of constructive interference – which occurs when the angle between the plane and the X-rays results in a path length equal an integer multiple of the X-ray wavelength. This is known as the Bragg model of diffraction (Figure 2.2.) and can be represented by the Bragg equation:

$$n\lambda = 2dsin\theta_I$$

Eq. 2.14.

Where n is an integer number, λ is the wavelength (of the X-rays), d is the spacing between the atomic planes and θ_I is the incident angle between incoming and outgoing X-ray beams.

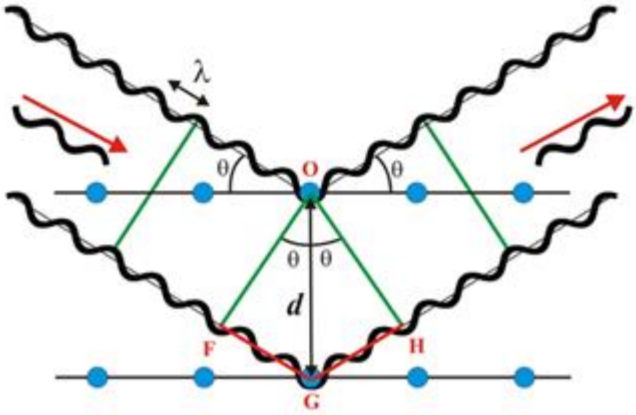

Figure 2.2. Illustration of the Bragg model of diffraction.

In single-crystal XRD, this results in a 2D diffraction pattern of regularly spaced spots. By taking such measurements at different orientations, the 2D patterns can be converted to a 3D model of the crystal using the Fourier transform algorithm.

Powder X-ray diffraction (PXRD) operates under the assumption that the crystallites within a sample are randomly arranged (as either a powder, or isotropic polycrystalline solid); this averaging of the crystallite orientation causes the regularly spaced spots observed in single crystal XRD to be replaced with smooth diffraction rings (Debye-Scherrer rings) formed around the beam axis (Figure 2.3 b)). The angle between the beam and the rings is known as the scattering angle, and is denoted as 2θ. The data are typically represented as a diffractogram – where the intensity is given as a function of the scattering angle (Figure 2.3 b)).

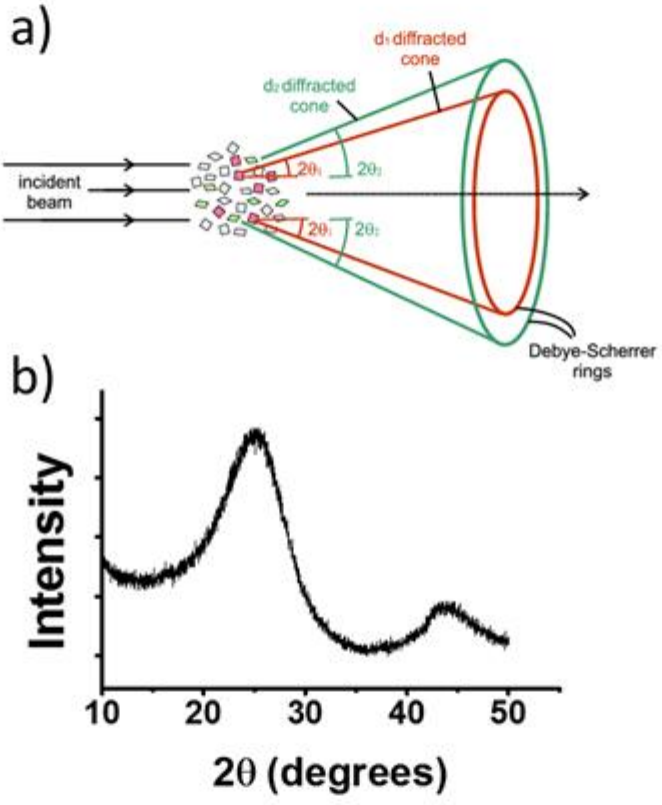

Figure 2.3. a) Illustration of the formation of Debye-Scherrer rings in a PXRD measurement b) Resultant diffractogram

The line broadening of peaks in a diffractogram can also be related to the size of the crystallites in a powder or polycrystalline solid, though application of the Scherrer equation:

$$\tau = \frac{K_S \lambda}{\beta cos\theta}$$

Eq. 2.15.

Where τ is the mean size of the crystallites, K_S is a dimensionless shape factor, λ is the wavelength (of X-rays), β is the line broadening at half the maximum intensity (FWHM) and θ_C is the contact angle (Bragg angle).

2.4.1. X-Ray Diffraction of Carbon

XRD is a useful tool in the characterisation of graphitic and semi-graphitic carbons.(8)(9) The most stable form of graphite exists as graphene sheets layered in a regular ABAB arrangement with a hexagonal unit cell and a distance of 0.3354 nm between adjacent sheets (Figure 2.4.). In non-ideal graphite however, random stacking occurs with displacive and rotational defects in the stacked structure – known as turbostratic disorder (Figure 2.5.).

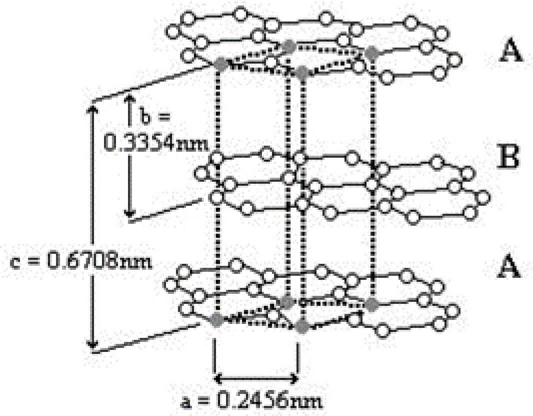

Figure 2.4. Hexagonal unit cell structure of graphite with ABAB structure (8)

The degree of turbotratic disorder, which is widely used as a measure of the degree of graphitisation, increases the average interlayer spacing between graphene sheets (d_{002}) and therefore can be measured by XRD and application of the Bragg equation.(9)

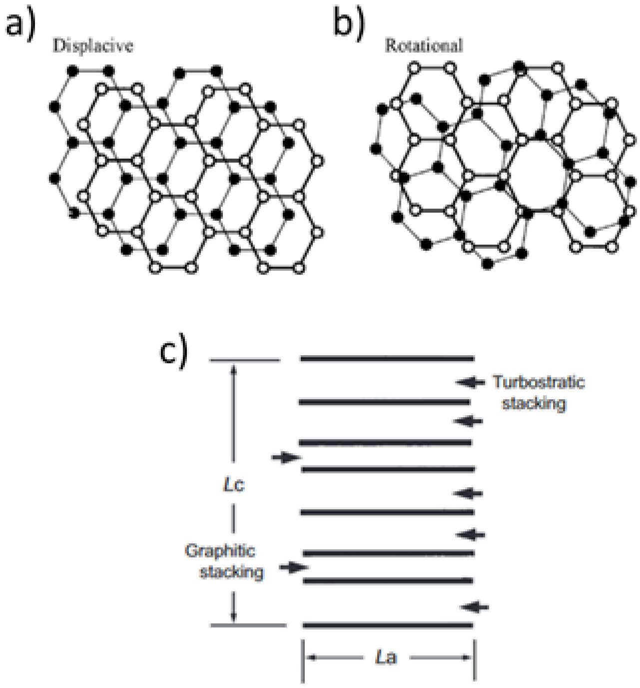

Figure 2.5. Turbostratic carbon with a) displacive and b) rotational disorder. c) Increase in average interlayer spacing (d_{002}) due to turbostratic disorder (8)

Furthermore, PXRD can be used to measure the mean crystallite size of a semi-graphitic carbon through application of the Scherrer equation. Here, the crystallite sizes along the c- and a-axes (L_c and L_a, respectively) can be calculated from the d_{002} and d_{101} diffraction peaks, respectively.

2.5. Infrared Spectroscopy (IR)

Infrared spectroscopy (IR) is an analytical technique used to determine the nature of chemical bonds and functional groups within a sample.(10) Based on the principle that that chemical bonds (or collection of bonds) absorb specific IR frequencies, the technique works by passing a beam of IR radiation through a sample and examining the transmitted light. When the frequency of the IR light matches a specific vibrational frequency of a bond (or collection of bonds), absorption occurs, allowing elucidation of the molecular structure.

An IR spectrum can be obtained by passing a monochromatic IR source through a sample, recording the absorption, and repeating for each different frequency. However, a faster and more accurate method is so-called Fourier Transform Infrared Spectroscopy (FTIR), which involves passing an IR beam containing many frequencies through the sample at once – before processing the data to infer the absorption at each wavelength. The data processing step involves the Fourier transform algorithm, hence the name given to the technique.

2.6. Raman Spectroscopy

Raman spectroscopy is an analytical technique used to characterise materials by observing low-frequency vibrational and rotational modes within a system.(11) The technique works by shining a monochromatic light (usually a visible or near-infrared laser) on a sample, which interacts with molecular excitations and shifts the energy of the light up or down. This inelastically scattered light is then detected, and reveals information on the excitations of the system.

2.6.1. Raman Spectroscopy of Carbon

Raman spectroscopy is a useful tool for investigating the structure and properties of carbon materials at the nanoscale level.(12)(13) Single crystal graphite has two Raman-active E_{2g} vibrational modes which can be identified by the Raman band at 1582 cm^{-1}. This is commonly referred to as the graphitic band or G-band. As carbon becomes increasingly disordered however, going from graphitic to semi-graphitic, another band appears at approximately 1360 cm^{-1} – the intensity of which increases with decreasing crystallite size.(12) This band has been attributed to the symmetry-breaking A_{1g} vibration of structurally disordered carbon, and is commonly referred to as the D-band.(13) The ratio of the intensity of the D- and G-bands, I_D/I_G, is commonly used as a measure of the degree of graphitisation of a carbon sample.

2.7. CHNS Elemental Analysis

CHNS elemental analysis is an analytical method that allows the determination of the mass fraction of carbon, hydrogen, nitrogen and sulfur within a sample.(14) The method works by combusting the sample at high temperatures (~1000 °C) and analysing the combustion products (*i.e.* CO_2, H_2O, N_2 and SO_2) after removal of excess O_2 gas and other impurities. Detection of the gasses can be carried out in a variety of ways, such as separation by gas chromatography followed by thermal conductivity detection, or a series of infra-red/thermal conductivity cells for the detection of individual compounds. Quantification of each element requires calibration of the instrument with a high purity reference standard.

2.8. Thermogravimetric Analysis (TGA)

Thermogravimetric analysis (TGA) is an analytical method which measures the change in mass of a sample as a function of increasing temperature with a constant heating rate.(15) TGA can provide information about various physical (*e.g.* vaporisation, sublimation, desorption) and chemical (*e.g.* dehydration, decomposition, oxidation) phenomena occurring as a sample increases in temperature. TGA can be useful to monitor the process of pyrolysis/carbonisation, and help identify any distinct temperature regions where certain reactions/decompositions occur.

2.9. Scanning Electron Microscopy (SEM)

A scanning electron microscope (SEM) is an instrument used to obtain high-magnification (between 10x and 500,000x magnification) images of samples.(16) The instrument works by scanning a focussed beam of electrons across the surface of the sample and collecting the secondary electrons emitted; this reveals information on the sample’s surface tomography which can be represented as an image.

The components of a SEM are outlined in Figure 2.6. In a typical SEM, the electrons are produced thermionically by a tungsten wire or lanthanum hexaboride filament; used for their high mechanical strength and melting points. A field emission SEM (FE-SEM) differs from a conventional SEM in that the emission of electrons is induced by a high-voltage electrostatic field. FE-SEMs can produce narrower, higher energy, electron beams and can thus obtain superior special resolution and a higher signal-to-noise ratio over conventional SEMs.

The produced electron beam, which typically has energies ranging between 0.2 to 40 keV, is focused by a number of condenser lenses, and the size of the beam is controlled by an aperture. Any distortions of the beam caused by the condenser lenses are corrected by a stigmator, *i.e.*

a small collection of electromagnetic coils. For SEM and FE-SEM imaging, samples must either be electrically conductive, or coated with a conductive layer (typically low-vacuum sputtered Au), and grounded to prevent accumulation of electrostatic charge.

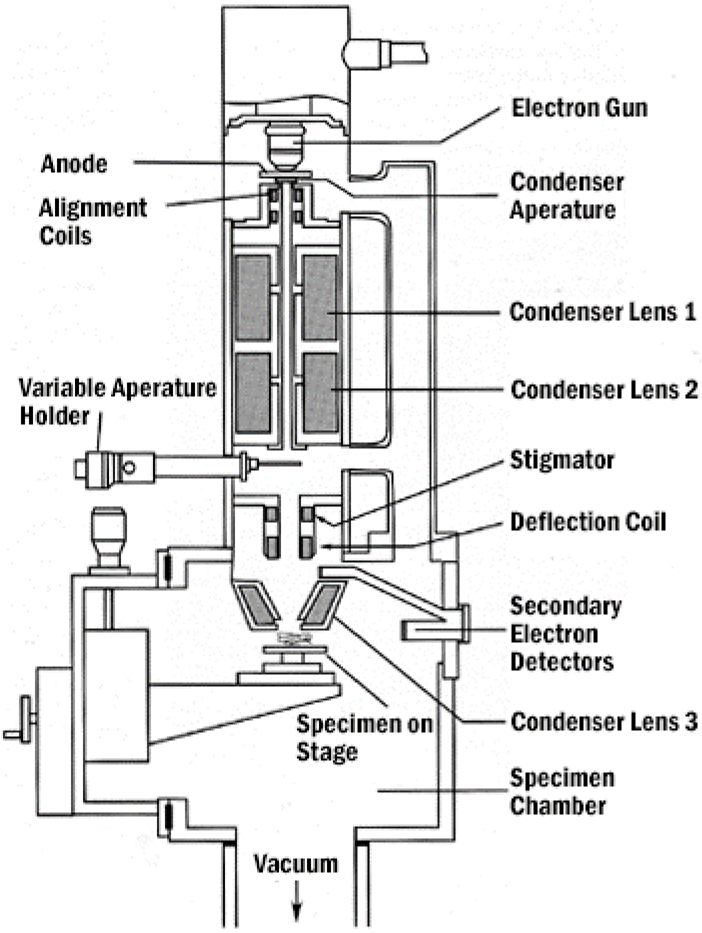

Figure 2.6. Schematic representation of a scanning electron microscope (16)

2.10. Transmission Electron Microscopy (TEM)

A transmission electron microscope (TEM) is an instrument used to obtain ultra-high magnification images of thin samples.(17) A TEM works by passing a focussed beam of electrons though a sample which, after interacting with the atoms in the specimen, are then magnified and captured by an imaging device. Information about the morphology, composition, crystal structure and defects can be obtained by a TEM. Due to the relatively small De Broglie wavelength of elections, TEMs are able to attain much higher resolutions than would be possible with visible light – and are even capable of atomic-level resolution.(18)

TEM can be a useful tool in the characterisation of carbon materials, as it can give an insight into the nanotextural properties – such as nano-crystallite size, shape and orientation – aiding the correct identification of materials.(19)

2.11. Energy-dispersive X-ray Spectroscopy (EDX)

Energy-dispersive X-ray (EDX) spectroscopy is an analytical technique used to analyse the elemental composition of the surface of a sample.(20) The method works *via* the stimulated emission of X-rays induced by the bombardment with a high-energy electron beam, which are then recorded and interpreted by a detector. Since each element has a unique electronic structure, a unique set of electronic peaks are produced allowing identification of the elements present. Since electron beams are employed as the excitation source for EDX analysis, they are often part of the same equipment as a SEM which also employs an electron beam – although a higher energy electron beam and a different detector is used for EDX analysis.

2.12. X-ray Photoelectron Spectroscopy (XPS)

X-ray photoelectron spectroscopy (XPS) is analytical technique that measures the elemental composition, and chemical and electronic state of elements at the surface of a material.(21) The method works by irradiating a material with a beam of X-rays and measuring the kinetic energy and number of electrons released through ionisation. Since the emitted electrons escape only the surface of the material before having their kinetic energy disturbed, the technique is surface specific – measuring up to ~10 nm in depth. The technique requires an ultra-high vacuum (P ~10^{-8} mbar) as gaseous molecules may disturb the kinetic energy of the electrons on route to the detector.

2.13. Electrochemical Measurements

2.13.1. Cyclic voltammetry (CV)

Cyclic voltammetry (CV) is an electrochemical technique which measures the current that develops in an electrochemical cell as an applied electrical potential (voltage) is swept back and forth at a set rate.(22)(23) A standard experimental set-up is known as a three electrode cell configuration, and consists of a working electrode, counter electrode and reference electrode submerged in a solution containing an ionic electrolyte (Figure 2.7.).

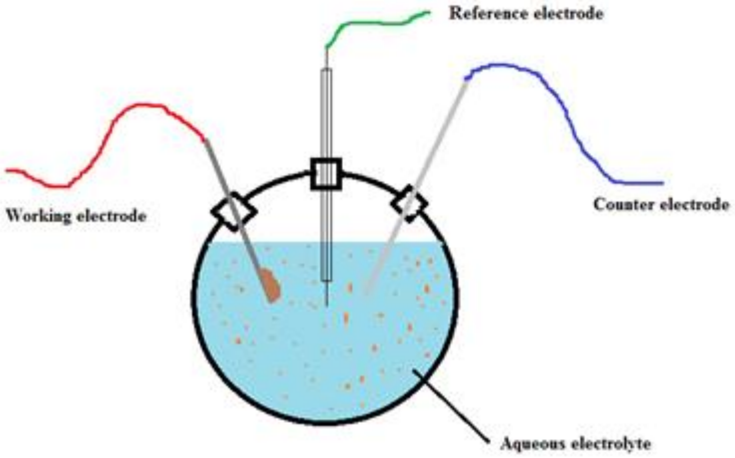

Figure 2.7. Schematic representation of a three electrode cell set-up

The reference electrode maintains a constant potential whilst the working electrode's potential is varied linearly with time (Figure 2.8. a)). The electrolyte supplies ions to the electrodes and the counter electrode oxidises or reduces these ions to balance the reactions occurring at the working electrode. As the potential of the working electrode is varied, redox reactions can occur and are monitored by the change in current. The data are plotted as a function of current (I) vs. applied voltage (E), with the result being a voltammogram which can shed light on nature of the redox reactions occurring at the working electrode. Figure 2.8. b) shows an example of a cyclic voltammogram resulting from a single electron redox reaction, where i_{pc} is the cathodic peak current, E_{pc} is the cathodic peak potential, I_{pa} is the anodic peak current and E_{pa} is the anodic peak potential.

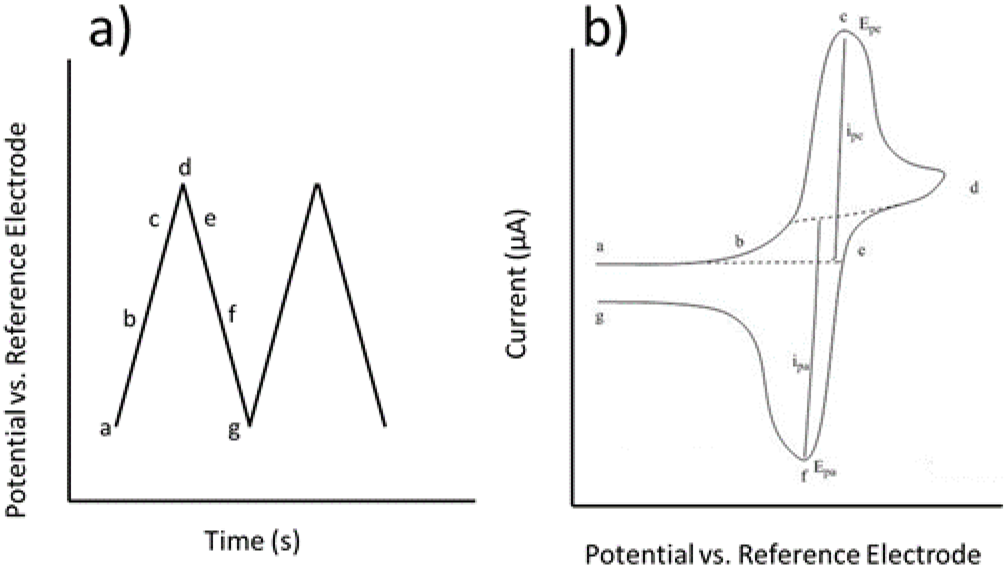

Figure 2.8. a) Variation of potential over time for a CV measurement, b) CV of a single electron redox reaction

2.13.2. Constant Current Potentiometry (CCP)

Constant current potentiometry (CCP), or chronopotentiometry, is an electrochemical analysis technique in which a constant current is made to flow between two electrodes. Like CV, CCP typically employs a three electrode configuration, where the constant current is maintained by varying the potential difference of one electrode (the working electrode) with respect to a reference electrode, with a counter electrode to balance the redox reactions occurring. The technique results in a voltage profile (Figure 2.10.) which displays the voltage as a function of time (t), or charge (Q), since the two are related by the following equation:

$$Q = It$$

Eq. 2.16

And the current (I) is kept constant.

2.13.3. Battery Performance Evaluation

Section 1.6.7.1. and 1.6.7.2. discuss the principles behind the energy storage mechanisms in rechargeable LIB and LIS batteries, respectively. This sub-section outlines the factors to be considered when evaluating the performance of electrode materials in such batteries.

2.13.3.1. Energy

The total energy stored is an important factor to consider when evaluating an electrode material, and is typically presented as either specific energy (energy per unit mass), in Wh kg^{-1}, or energy density (energy per unit volume), in Wh L^{-1}. The electrical energy available from an electrochemical cell can be expressed by the following equation:

$$\Delta G = -QE$$

Eq. 2.17.

Where ΔG is the Gibbs free energy (in Wh, where 1 Wh = 3600 J), Q is the charge (in Ah, where 1 Ah = 3600 C) and E is the electrical potential (in volts, V). The charge, *Q*, can be represented as the product of the number of available electrons (n_e) and the elementary charge (e) through the expression:

$$Q = n_e e$$

Eq. 2.18.

It may also be expressed as:

$$Q = nN_Ae$$

Eq. 2.19.

Where n is the number of moles of available electrons and N_A is Avogadro's constant (6.023 x 10^{23} mol^{-1}). This expression can then be simplified to:

$$Q = nF$$

Eq. 2.20.

Where F is Faraday's constant, which is equal to N_Ae, or the charge per mole of electrons (96,485 C mol^{-1}). Substituting Eq. 2.17. into Eq. 2.20. gives the expression:

$$\Delta G = -nFE$$

Eq. 2.21.

Or, under standard conditions:

$$\Delta G^o = -nFE^o$$

Eq. 2.22.

Therefore, the available electrical energy stored by an electrode material can be increased by increasing the number of available charge carriers (Li-ions, in this case), or by increasing the potential difference (*e.g.* by having a more electronegative anode or electropositive cathode).

2.13.3.2. Capacity

The total electric charge Q a given electrode material can deliver is known as its capacity, and is proportional to the number of available electrons n_e as given by Eq. 2.18. This value is typically quoted per unit mass as the specific capacity (in Ah kg^{-1} or mA h g^{-1}), but may also be quoted per unit volume as the charge density (in Ah L^{-1}). Since one mole of electrons has a charge of 96,485 C (Faraday's constant), the theoretical capacity (C_T) of a material can be determined with the equation:

$$C_T = n_eF$$

Eq. 2.23

Where n_e is the number of moles of electrons produced from the discharging process. Determining n_e per unit mass of active material thus gives the specific capacity – which is 372 mA h g^{-1} for graphite given that the stoichiometry when fully intercalated is LiC_6.

Since the electrical potential E of an electrode material varies depending on the conditions and extent of discharge, (see 2.13.3.8. Voltage Profile), it follows that energy ΔG also varies due to their relationship through Eq. 2.22.. Thus, the value for capacity, not energy, is generally quoted in the evaluation of electrode materials since the former in invariant with regard to electrical potential whereas the latter is not.

2.13.3.3. Power

The rate at which an electrode material can deliver energy is known as the power (P_W), and is generally as specific power (W kg^{-1}), or power density (W L^{-1}). Power is the product of the current I (in Amps) electric potential E (in Volts):

$$P_W = IE$$

Eq. 2.24.

Again, as with energy, since power is proportional to the electrical potential E, which is variable, it is typically not quoted as a specific value. Instead the performance at a specific current is quoted, along with a discussion on the shape of the voltage profile.

2.13.3.4. Current

The current output of an electrode, given in Amps (where 1 A = 1 C s^{-1}), is the rate of flow of charge and dictates how quickly an electrode material can be charged and discharged. When a high current is draw from a cell, theoretically the power should increase proportionally in accordance with Eq. 2.24. This is not the case however since, at high current densities, internal resistances, slow charge transfer rates and rate-determining kinetics of Li-ion diffusion within the bulk electrode and electrolyte can cause a drop in voltage and thus a fall in power. This drop in electrical potential, known as electrode polarisation, is a significant issue associated with the current generation of LIB electrode materials it limits the use of LIBs in high-power applications. Polarisation as a result of high current densities also induces a drop in capacity (Figure 2.9.) – this results in a drop in energy of a cell (Eq. 2.17.).

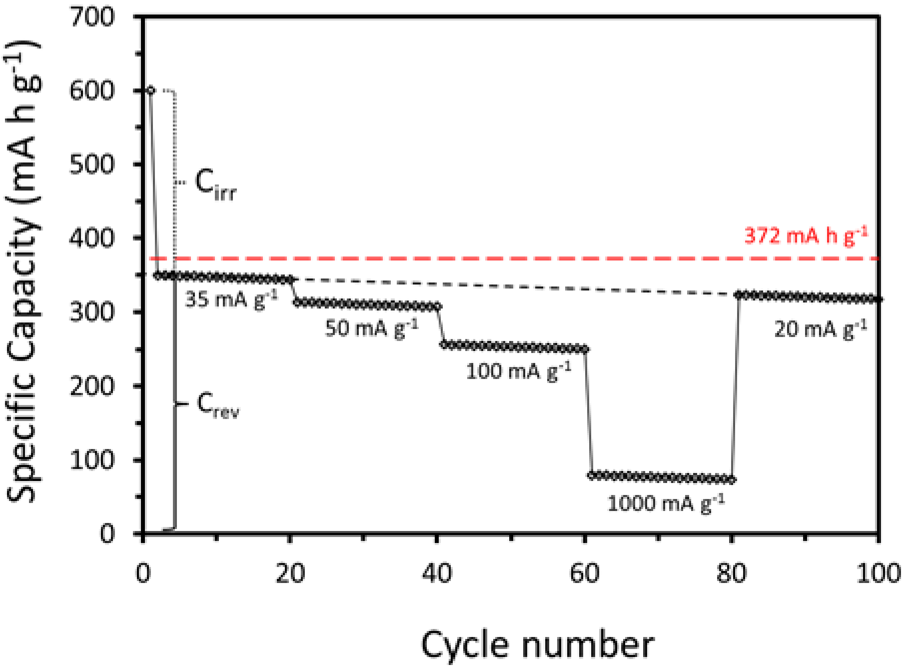

Figure 2.9. Idealised plot of specific capacity vs. cycle number for a hypothetical electrode material. Red dashed line indicates theoretical specific capacity for graphite

2.13.3.5. C-Rate and Current Density

A C-rate of 1 C is defined as the current required to fully discharge a cell in one hour (*i.e.* 100 mA g^{-1} for a 100 mA h g^{-1} cell, 200 mA g^{-1} for a 200 mA h g^{-1} cell), whereas a C-rate of 2 C is the current at which a battery would be fully discharged in ½ an hour (200 mA g^{-1} for a 100 mA h g^{-1} cell), and so forth. For making comparisons between many different electrode materials, it is more convenient to quote the current density rather than the C-value, since the former is independent of total capacity whereas the latter is not.

2.13.3.6. Reversible and Irreversible Capacity

Upon the first charging cycle of a LIB there is an irreversible capacity loss (C_{irr}) associated with electrolyte reduction at the anode-electrolyte interface, which permanently consumes Li-ions (Figure 2.9.). Further reduction on subsequent cycles, and hence further capacity loss, is suppressed however, as the initial process acts to forms stable passivation layer known as the solid electrolyte interphase (SEI) which, being permeable to Li-ions but not to the electrolyte, acts as a barrier to further degradation. Thus the initial reversible (C_{rev}) and irreversible capacities and (C_{irr}) are other important factors to bear in mind in the assessment of an electrode material. The value for C_{irr} is proportional to the anode-electrolyte interface, is therefore strongly correlated to the surface area of the materials.

2.13.3.7. Cycle stability

After the first charge/discharge cycle, and the inherent loss of capacity associated with the formation of the SEI layer, the capacity retention on subsequent cycles is another factor to consider. This is usually termed cycle life; and is the number of times a battery can be charged/discharged whilst still maintaining a reasonable capacity. The average capacity retention over a number of cycles is usually termed the cycle stability, or coulombic efficiency. For a battery with a coulombic efficiency of 99 % (99 % capacity retention on each cycle) would have less than 1 % of its original capacity after 500 cycles. Figure 2.9. gives an example of a material with a coulombic efficiency of 99.9 %. Designing electrode materials with good cycle stability is therefore an important factor to consider.

2.13.3.8. Voltage Profile

The potential at which electrode materials undergo charge/discharge is not constant, but variable depending on the extent of the process. Graphite has a fairly flat discharge profile, whereas the profile for semi-graphitic carbons is typically sloped (Figure 2.10.). Sloped voltage profiles are not desirable, particularly for applications within electronics where a flat working potential similar to given by graphite would be preferred. A higher average voltage for a given capacity also infers a higher energy, in accordance with Eq. 2.17.

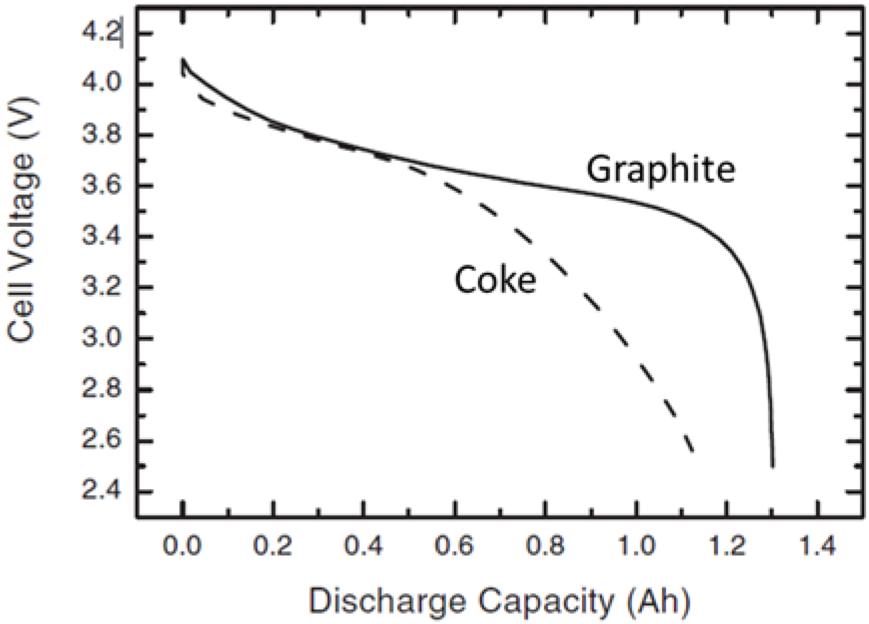

Figure 2.10. Comparison between voltage profiles for graphite and coke (semi-graphitic carbon) (24)

2.13.4. Supercapacitor Performance Evaluation

Section 1.6.7.3 discusses the principles behind the energy storage mechanisms in supercapacitors. This sub-section goes into further detail on the background and theory of supercapacitors.

2.13.4.1 Capacitance

The capacitance (C) of a body is its ability to store electrical change (Q) and is measured in Farads (F). The capacitance of a capacitor can be expressed by the following equation:(25)

$$C = \frac{Q}{E}$$

Eq. 2.25

Where E is the potential difference between the plates. Therefore, a 1 F capacitor will store one Coulomb of charge when 1 V potential difference is placed between the plates. The capacitance of an electrode material is usually normalised by mass or area to give the capacitance per gram or per square centimetre, to allow easy comparison between materials.

The gravimetric capacitance is the most significant factor considered when evaluating the performance of supercapacitor electrode materials. It is generally calculated form CV curves through application of the following equation:

$$C_g = \frac{(Q_A + Q_C)}{(2ms\Delta E)}$$

Eq. 2.26.

Where C_g is the gravimetric capacitance, Q_A and Q_C are the total anodic and cathodic charge (calculated by integrating their respective CV sweeps), m is the mass of the active material, s is the potential sweep rate and ΔE is the potential window. The specific capacitance can also be determined by CCP with the following equation:

$$C_g = \frac{It}{Em}$$

Eq. 2.27.

Where I is the discharge current, t is the discharge time and E is the average discharge potential.

2.13.4.2. Energy

Eq. 2.17. relates energy (ΔG) to the charge (Q) and potential difference (V). Substituting with Eq. 2.25. allows the determination of the of the energy stored within a capacitor through the equation:

$$\Delta G = \frac{1}{2} C E^2$$

Eq. 2.26.

Where the energy is usually normalised by mass or volume (specific energy or energy density). The maximum energy is therefore obtained when the potential difference is at a maximum.

2.13.4.3. Power

Power is the rate of energy delivery per unit time.(25) Capacitors and supercapacitors generally have lower energy densities than batteries but much higher power densities. The maximum power of a capacitor is given by the formula:

$$P_W = \frac{1}{4} \cdot \frac{E^2}{R_e}$$

Eq. 2.27.

Where R_e is the resistance of the capacitor.

2.13.4.4. Cycle Stability

Like batteries, supercapacitors also suffer from degradation of performance over time. (25) However, since supercapacitors operate through physical rather than chemical interactions, their stability over repeated charge-discharge cycles (cycle stability) is much greater than that of batteries and can often retain significant capacitance even after 10,000+ cycles.

2.14. Conductivity measurements

Two-probe resistance measurements are a fast and simple way to determine the conductivity of a bulk sample. Here a current is passed through a sample of known dimensions *via* two probes, and the resistance is measured. The resistivity (ρ) can then be calculated with the following formula:

$$\rho = \frac{R_e A}{L}$$

Eq. 2.28.

Where A is the cross-sectional area and L is the length. The conductivity (σ) is then taken as the reciprocal of the resistivity:

$$\sigma = \frac{1}{\rho}$$

Eq. 2.29.

2.15. References

1. Attard G, Barnes C (1998) *Surfaces* (Oxford chemistry primers). 59th Ed.
2. Langmuir I (1916) *J Am Chem Soc* 38(11):2221–95.
3. Brunauer S, Emmett PH, Teller E (1938) *J Am Chem Soc* 60(1):309–319.
4. Thommes M, et al. (2015) *Pure Appl Chem* 87(9–10):1051–1069.
5. Sing K (1985) *Pure Appl Chem*. 57(4)603-619
6. Rootare HM (1970) *Advanced Experimental Techniques in Powder Metallurgy* (Springer US, Boston, MA), pp 225–252.
7. Simms PH, Yanful EK (2004) *Géotechnique* 54(6):421–426.
8. Inagaki M, Kang F, Toyoda M, Konno H (2013) *Advanced Materials Science and Engineering of Carbon* (Butterworth-Heinemann).
9. Iwashita N, Inagaki M (1993) *Carbon* 31(7):1107–1113.
10. Griffiths PR, De Haseth JA (2007) *Fourier Transform Infrared Spectrometry* (John Wiley & Sons).
11. Hazle M a., Mehicic M, Gardiner DJ, Graves PR (1990) *Practical Raman Spectroscopy* (Springer Berlin Heidelberg, Berlin, Heidelberg).
12. Wang Y, Alsmeyer DC, Mccreery RL (1990) *Chem Mater* 2(5):557–563.
13. Ferrari AC (2007) *Solid State Commun* 143(1):47–57.
14. Kirsten W (1983) *Organic Elemental Analysis: Ultramicro, Micro, and Trace Methods* (Elsevier).
15. Coats AW, Redfern JP (1963) *Analyst* 88(1053):906.
16. Goldstein JI, et al. (1992) *Scanning Electron Microscopy and X-Ray Microanalysis: A Text for Biologists* (Springer Science & Business Media).
17. Carter DBW and CB (1996) *The transmission electron microscope* (Springer US).
18. Hasegawa T, et al. (1986) *Jpn J Appl Phys* 25(5):366–368.
19. Somani P, Umeno M (2007) *Mod Res Educ Top Microsc* 3:634–642.
20. Shindo D, Oikawa T (2002) *Energy Dispersive X-ray Spectroscopy* (Springer Japan).
21. Heide P Von Der (2012) *X-ray photoelectron spectroscopy: An introduction to principles and practices*. (John Wiley & Sons).
22. Skoog D, West D (1980) *Principles of instrumental analysis* (Philadelphia: Saunders College).
23. Kissinger P (1983) *J Chem Educ* 60(9):702.
24. Yoshio M, Brodd RJ, Kozawa A (2009) *Lithium-ion batteries : science and technologies* (New York: Springer).
25. Lu M, Beguin F, Frackowiak E (2013) *Supercapacitors: materials, systems and applications* (John Wiley & Sons).

Chapter 3

Nitrogen-rich ITPCs as Li-ion Battery Anode Materials

The contents of this chapter has been published in *The Journal of Materials Chemistry A* (Roberts AD, Wang S, Li X, Zhang H (2014). *J Mater Chem A* 2(42):17787–17796.)

List of Figures

List of Tables

3.1. Background and Context

As was discussed in the introduction, one of drawbacks for the ice-templating method for the preparation of porous carbons is the need to crosslink the precursor prior to pyrolysis. Since few precursors are able to undergo successful ice-templating upon freezing as well as crosslinking and carbonisation, the number of suitable precursors that can be employed by this method is limited. In this chapter, poly(acrylonitrile) (PAN) was successfully subjected to the ice-templating and carbonisation method to prepare ice-templated porous carbons (ITPCs). Here, an oxidative annealing step prior to carbonisation provided the chemical crosslinking which stabilised the structures upon carbonisation.

3.2. Introduction

Advanced energy storage systems with high power- and energy- densities are a key requirement for the transition from petroleum-based automotive transport to electrified systems.(1) Moreover, the utility of intermittent renewable energy sources such as solar and wind would be greatly increased if coupled with a low-cost and efficient large-scale energy system to level out demand.(2)(3)(4) Rechargeable Li-ion batteries (LIBs), as an established and widely commercialised technology, are regarded as the most feasible technology at present to satisfy such challenges.(5) Significant advances in terms of performance are still required however, particularly in terms of cost, cycle life, and rate performance before the full potential of such applications can be realised.(6) In order to attain such improvements, advanced materials with novel and low-cost fabrication procedures are required.(6)

There has been much interest in the development of carbon nanomaterials as alternatives to graphitic carbon as anode materials in LIBs; these include carbon nanotubes (CNTs),(7) graphene,(8) carbon spheres,(9) and carbon nanofiberes (CNFs) among others.(10)(11)(12)(13) Porous carbons – typically prepared *via* templating strategies – are another class of carbon which have been investigated as alternative materials for the LIB anode.(9)(14)(15) It has been shown that porous carbons with interconnected pores spanning the macro-, meso- and micro- size domains (*i.e. hierarchical* porosity) have displayed relatively good high-rate performance, largely due to efficient transport pathways for the Li-ions which enhances diffusion kinetics to and from the electrode surface.(16)(17)(18)(19)(20) Heteroatom modification of the carbon structure – in particular N-doping – has also been shown to enhance capacity and high-rate performance;(20)(21)(22)(23)(24) this enhancement has been attributed to donation of the lone pair of elections on nitrogen to the carbon π-states, creating an n-type effect which enhances the carbon's Li-ion affinity.(25)

A variety of templates can be employed in the preparation of porous carbons, and are typically categorised as either *hard* or *soft* templating methods as outlined in the introductory chapter.

Drawbacks of these templating strategies can include relatively complex template synthesis and subsequent removal, limited suitable precursors and difficulty in scaling up synthesises, which hinders their practical utilisation outside of the lab.(9)(15) To overcome these issues, there has recently been a drive to develop benign and relatively facile templating methods for the fabrication of porous carbons, including the use of ice-crystals or emulsion droplets as templates (*ice-templating* and *emulsion-templating*, respectively).(9) Ice-templating, in particular, is a simple and facile method for the preparation of porous polymers – which may then be converted to carbon *via* pyrolysis.

This method also faces a number of limitations however, such as the need for the precursor to dissolve sufficiently in a solvent suitable for ice-templating and freeze-drying (*e.g.* water, dimethyl sulfoxide, camphene, dioxane or t-butyl alcohol),(26) as well as being suitable for carbonisation *via* pyrolysis. In particular, the precursor ought to undergo chemical crosslinking prior to carbonisation to ensure a high carbon yield with retention of the ice-templated structure.(27)(28)

In this work, these issues were overcome by employing poly(acrylonitrile) (PAN) as the carbon precursor (Figure 3.1.). Being insoluble in water, the solvent dimethyl sulfoxide (DMSO) was used as the solvent for the ice-templating process. DMSO is a non-toxic solvent which, having a relatively high melting point of 19 °C, can be removed *via* freeze-drying at room temperature. Carbonisation of the ice-templated porous PAN was achieved after an initial oxidative annealing step – a process also employed in PAN-based carbon fibre manufacture which stabilises the structure by inducing dehydrogenation, cyclisation, aromatization, oxidation and crosslinking of the polymers.(29) After carbonisation, the monoliths were found to possess a degree of meso- and micro- porosity – in addition to the macropores derived from the ice-crystal templates – as well as unusually high N contents (between 15 – 17 wt. %.) derived from the nitrile functional groups of the original precursor.

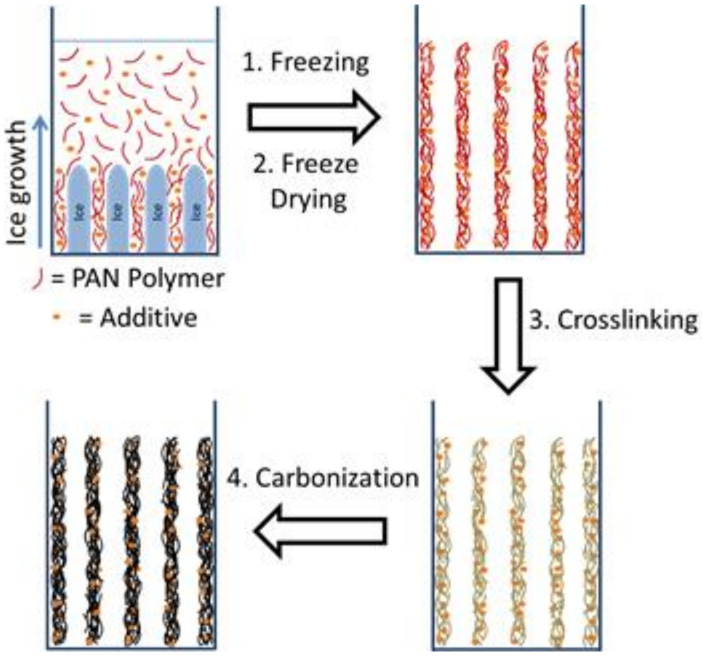

Figure 3.1. Schematic representation of the process to prepare an ITPC from a PAN precursor

When tested as anode materials for the LIB, impressive initial reversible capacities as high as 745 mA h g^{-1} were obtained at a moderate current density of 50 mA g^{-1}: twice as high as the theoretical maximum specific capacity for graphite (372 mA h g^{-1}) and comparable to many other templated carbons prepared by more complex means (Table 1.1.). The simplicity of the ice-templating approach also allowed various composites to be formed, including SnO_2, silicon nanoparticles, reduced graphene oxide (RGO) and the organic compound melamine (for further N-doping). It was found that the incorporation of both melamine and RGO would further improve the high-rate performance of the materials; with reversible capacities of about 200 and 250 mA h g^{-1}, respectively, at the ultra-high charging current density of 10 A g^{-1}. The co-incorporation of both melamine and RGO would improve rate performance still further; with a reversible capacity of about 300 mA h g^{-1} obtained at a charging current density of 10 A g^{-1} – which is among the best high-rate performance among carbon-based materials published in the literature (Table 1.2.).

3.3. Experimental

3.3.1. Chemical Reagents

Poly(acrylonitrile) (PAN, MW 150,000), poly(sodium 4-styrenesulfonate) (PSS, MW 70,000), tin (IV) chloride pentahydrate, silicon nanoparticles (<100 nm by TEM), melamine (99 %), hydrazine hydrate (40% aqueous solution), poly(vinylidene fluoride) (PVDF), ethylene carbonate (anhydrous, 99 %), dimethyl carbonate (anhydrous, >99 %), lithium hexafluorophosphate (battery grade, ≥99.99) and n-methyl pyrrolidinone (NMP) were purchased from Sigma Aldrich and used without further purification. An aqueous graphene oxide suspension (5 mg ml^{-1}) was purchased from Graphene Supermarket® and used as supplied. Super-P® carbon back was purchased from Timcal. Standard analytical grade solvents and deionised water were used routinely.

3.3.2. Preparation of Materials

Preparation of the PAN-derived Ice Templated Porous Carbon (ITPC)

PAN was dissolved into dimethyl sulfoxide (DMSO), at concentrations of 1, 2.5, 10, 25, 50, 100, 150 and 200 mg ml^{-1}, under stirring at 60 °C. After cooling naturally to room temperature, 1.5 ml aliquots of the solutions were transferred to 10 mm x 75 mm borosilicate glass test tubes (Fischer Scientific), before being immersed into a bath of liquid N_2 at a rate of approximately 5 – 10 mm min^{-1}. After complete submersion and freezing, the frozen samples were transferred to a Vitris Advantage Benchtop Freeze Drier and subject to lyophilisation for ~48 h. After lyophilisation, ice-templated porous PAN monoliths were obtained, which were denoted PANn, where n was the initial PAN concentration in mg ml^{-1}.

The ice-templated porous PAN monoliths were then subjected to oxidative annealing by heating in a Carbolite CWF 1200 chamber furnace in air to a temperature of 280 °C (heating rate of rate of 1 °C min^{-1}), before being held at that temperature for 1 h. After cooling naturally to room temperature, the annealed PAN monoliths were then pyrolysed by heating under an Ar atmosphere to a temperature of 800 °C (heating rate of 5 °C min^{-1}), before being held at that temperature for 2.5 h. This was done in the same furnace fitted with a gas line and a home-made steel pyrolysis chamber. The ice-templated porous carbon monoliths were denoted CPANn, where n was the initial PAN concentration in mg ml^{-1}.

Preparation of Si Nanoparticle Composite ITPCs

PAN was dissolved in DMSO at a concentration of 50 mg ml^{-1}, under stirring at 60 °C, before commercially obtained Si nanoparticles (< 100 nm) were added to give ratios of 1:1, 1:4 and 1:9 Si to PAN by mass. After continued stirring, the dispersions were sonicated for 20 minutes, before the abovementioned ice-templating, annealing and carbonisation procedure was followed. The composites were denoted X-Si-CPAN50, where X is the ratio of PAN to Si by mass.

Preparation of SnO_2 Composite ITPC

The method employed to prepare SnO_2 composite ITPCs was an adaption to a process described by J. Kong *et al.*, who fabricated SnO_2 composite carbon nanofibers *via* an electrospinning method.(30) PAN was dissolved in DMSO at a concentration of 50 mg ml^{-1} under stirring at 60 °C, before $Sn(OAc)_2$ was added to give a 1:1 ratio of PAN to $Sn(OAc)_2$.

After dissolution, the solution was allowed to cool naturally to room temperature before the abovementioned ice-templating and annealing procedure was followed. The material was then carbonised under an Ar atmosphere at a temperature of 550 °C (heating rate of 5 °C min^{-1}), which simultaneously converted the $Sn(OAc)_2$ to SnO_2. The ice-templated carbon-SnO_2 composite was denoted SnO_2-CPAN50.

Preparation of Melamine Composite ITPCs

PAN was dissolved in DMSO at a concentration of 50 mg ml^{-1}, under stirring at 60 °C, before melamine was added to give PAN-melamine ratios of 5, 15, 25 and 35 wt. % melamine vs. PAN (*i.e.* 2.5, 7.5, 12.5 and 17.5 mg melamine added per 50 mg PAN, respectively). After allowing to cool naturally to room temperature, the abovementioned ice-templating, annealing and carbonisation procedure was then followed to give the melamine-doped CPAN50 monoliths (denoted X%-melamine-CPAN50, where X is the wt. % of melamine vs. PAN).

Preparation of Reduced Graphene Oxide (RGO) Composite ITPC

Preparation of aqueous RGO suspension:

A poly(sodium 4-styrene sulfonate) (PSS) stabilised aqueous graphene dispersion was prepared following a modified procedure described in the literature.(31) Initially, 3 g of PSS was dissolved in 20 ml of deionised water under stirring at room temperature for 2 hours. 10 ml of a commercially obtained aqueous graphene oxide (GO) solution (5 mg ml^{-1}) was then added, and the mixture was sonicated for *ca.* 30 minutes. 2 ml of 40 % hydrazine hydrate was then added before the mixture was refluxed at 130 °C for 24 h. After cooling naturally to room temperature, the suspension was washed by subjecting to 3 cycles of centrifuging and re-dispersion in deionised water. After the final wash, the RGO was re-dispersed with deionised water to make up to a concentration of 3.3 mg ml^{-1}. This suspension was then sonicated for a further 10 minutes. Determination of the sulphur content *via* CHNS elemental analysis revealed a PSS:RGO ratio of approximately 1:1.

Preparation of RGO-CPAN50 composite:

PAN was dissolved into DMSO at a concentration of 50 mg ml^{-1} under stirring at 60 °C. 5 ml of the above-prepared 3.3 mg ml^{-1} aqueous graphene solution was then added, and the stirring was continued for *ca.* 1 h in order to obtain a homogenous dispersion. After cooling naturally to room temperature, the abovementioned ice-templating, annealing and carbonisation procedure was then followed to give the RGO-doped carbon monolith (denoted RGO-CPAN50).

Preparation of Melamine- and RGO- Composite ITPC

PAN was dissolved in DMSO at a concentration of 50 mg ml^{-1}, under stirring at 60 °C, before melamine was added at a ratio of 15 wt. % melamine vs. PAN. 5 ml of the above-prepared 3.3 mg ml^{-1} aqueous RGO solution was then added, and the stirring was continued for *ca.* 1 h in order to obtain a homogenous dispersion. The abovementioned ice-templating, annealing and carbonisation procedure was then followed to give the melamine- and RGO- doped carbon monolith (denoted 15% melamine-RGO-CPAN50).

3.3.3. Characterisation

Materials Characterisation

Surface areas and micro- and meso- pore size distributions were measured by N_2 gas sorption at 77 K using a Micromiretics ASAP 2420 volumetric absorption analyser. A pressure range of 0.05 – 0.2 P/P_0 was taken for the BET surface area calculations and BJH pore volumes were given by the total single point adsorption of pores between 1.7 and 300 nm width at $P/P_0 = 1$. Density Functional Theory (DFT) was used to calculate pore size distributions between 0.5 and 3.5 nm using the same measurements. Samples were degassed under vacuum at 200 °C for 16 h prior to analysis. Macropore size-distributions (up to 200 µm) were measured by Hg-intrusion porosimetry using a Micromiretics Autopore IV 9500 porosimeter. Powder X-ray diffraction (PXRD) analysis was performed using a PANanalytical X’Pert PRO HTS X-ray diffractometer with a Cu-α radiation source. Raman spectra were recorded using a Renishaw In via fitted with a 633 nm laser, calibrated against a silicon wafer reference. Sample micromorphology was studied *via* scanning electron microscopy (SEM) using a Hitachi S-4800 SEM, with non-conductive samples initially coated with Au using an Emitech K550X Automated Sputter Coater. Oxygen-free thermogravimetric analysis (TGA) measurements was carried out using a Q5000IR TGA; the samples were heated to 800 °C at a rate of 5 °C min^{-1} under an N_2 atmosphere. Oxidative TGA measurements were conducted on a TA Instruments SDT Q600 TGA instrument with a constant air flow of 50 mL min^{-1}. Samples were heated to 1000 °C at a heating rate of 20 °C min^{-1}. Conductivity measurements were taken *via* a two-probe method using a Keithley 2600A sourcemeter. Elemental analysis data was obtained from a Thermo FlashEA 1112 series CHNS elemental analyser using the Microanalytical service at the University of Liverpool.

Electrochemical evaluation

The electrochemical performances of the carbon monoliths were evaluated as anodes in LIBs after being ground to powders. The working electrode was fabricated by coating the slurry of the carbon sample (80 wt %), Super-P carbon black (10 wt %), and polyvinylidene fluoride

(PVDF) (10 wt %) in N-methyl pyrrolidinone (NMP) onto a copper foil. The coated copper foil was dried under vacuum at 120 °C overnight and then assembled into 2032 button cells in an argon-filled glove box with lithium foil, Celgard 2325 membrane and 1 M $LiPF_6$ in ethylene carbonate / dimethyl carbonate (1:1 v/v ratio) as the counter electrode, separator and electrolyte, respectively. The charge-discharge testing was conducted on NEWARE battery tester at different current densities with a cut-off voltage window of 0.005−3.0 V. The cyclic voltammetry (CV) tests were performed on an electrochemical workstation (PGSTAT302, Autolab) within a voltage window of 0–3.0 V and at a scan rate of 0.01 mV s^{-1}.

3.4. Results and Discussion

3.4.1. Preparation of PAN-derived ITPCs

Preparation of the PAN-derived ice-templated porous carbons (ITPCs) is outlined schematically in Figure 3.1. PAN was first dissolved in DMSO at a range of concentrations (1, 2.5, 10, 25, 50, 100, 150 and 200 mg ml^{-1}) before each solution was subject to ice-templating at 77 K *via* slow submersion into liquid N_2. The frozen samples were then freeze dried at room temperature for approximately 48 h, which removed the DMSO ice-crystal templates *via* sublimation, resulting in the porous ice-templated PAN monoliths. It was observed that the ice-templated polymer monoliths formed from relatively low PAN concentrations (1, 2.5 and 10 mg ml^{-1}) had relatively poor mechanical stability; and could easily be crushed between fingers. On the other hand, monoliths formed from higher concentrations were much more robust and could be handled easily without damaging. SEM imaging was performed to visualise the structure of the monoliths, which revealed that the monoliths form the relatively low concentrations had fibrous morphologies (Figure 3.2.), whereas the ones formed form higher concentrations had the characteristic ice-templated, aligned macroporous structures (Figure 3.3.). The sizes of the ice-templated macropores, as judged by SEM, varied between approximately 2 and 50 μm, which is consistent with ice-templating theory and other ice-templated porous polymers found in the literature.(32)

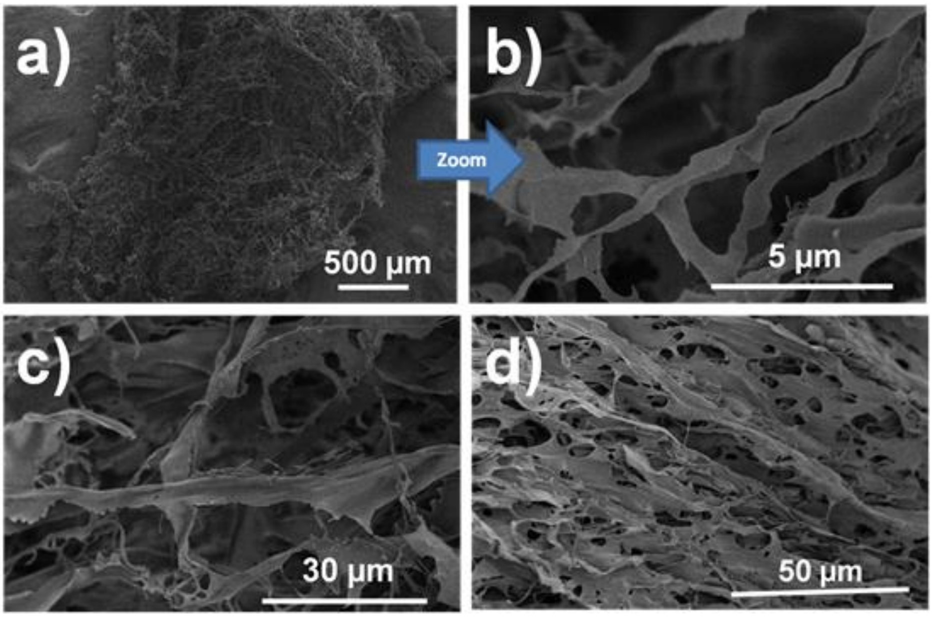

Figure 3.2. SEM images of PAN monoliths prepared from the relatively low concentrations: a) & b) 1 mg ml^{-1}, c) 2.5 mg ml^{-1} and d) 10 mg ml^{-1}

Over 90 % of carbon fibres employ PAN as a carbon precursor due to its attractive properties upon carbonisation.(29) One important property is the ability for PAN to undergo chemical crosslinking on heating to 200 – 300 °C in air (*oxidative annealing*). This process stabilises the fibres, allowing carbonisation to occur with relatively high yield (~50 %) with retention of the fibre morphology. Furthermore, the resultant semi-graphitic carbon is a soft (*graphitisable*) carbon, meaning further high-temperature treatment (~2000 – 3000 °C) will continue to increase the size of the graphitic crystallites to a point where the carbon can be considered graphite.(29)

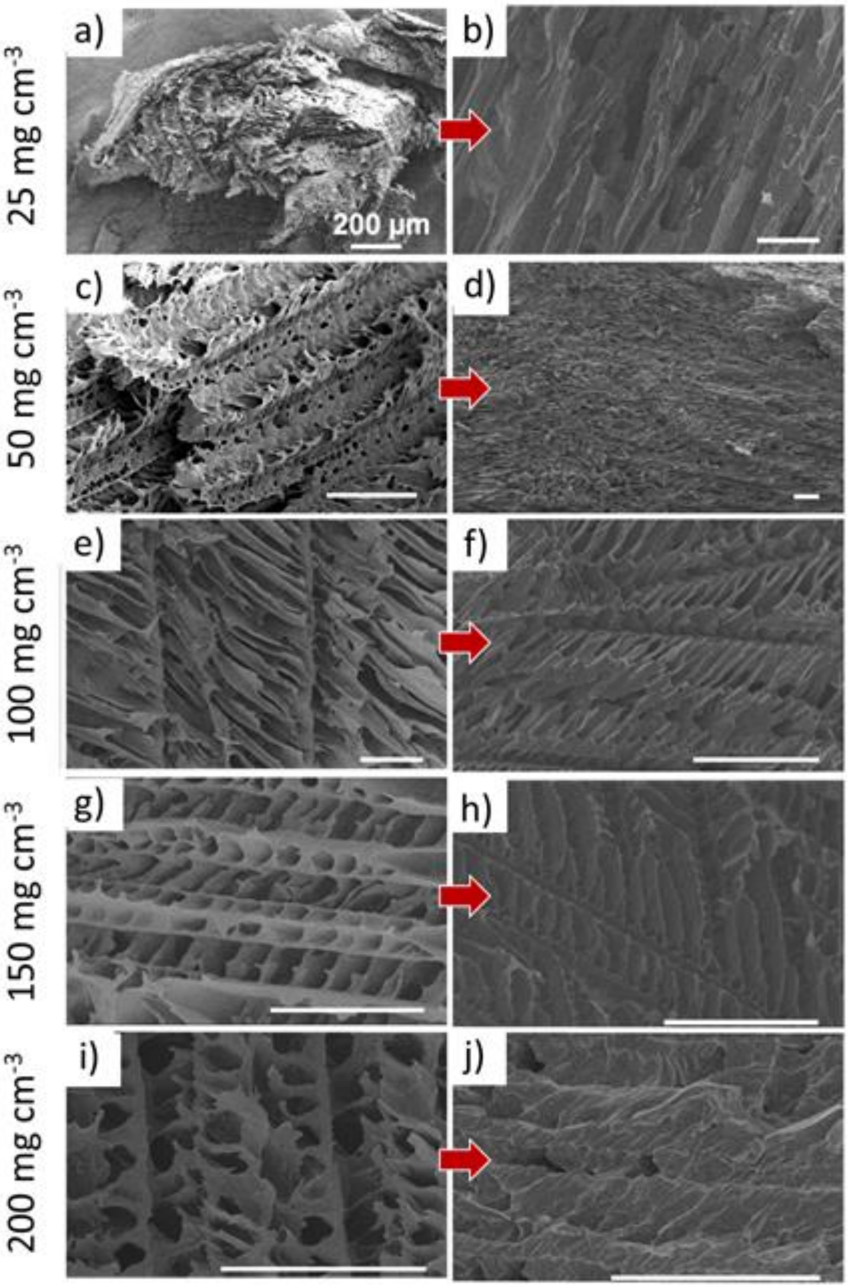

Figure 3.3. SEM images of the PAN monoliths from different initial PAN in DMSO concentrations before (a, c, e, g and i) and after (b, d, f, h, and j) crosslinking & pyrolysis. Unless otherwise stated, the scale bar represents 50 µm

The oxidative annealing process involves reactions such as cyclisation, dehydration, aromatisation and crosslinking of the polymer backbone, resulting in a stable ladder-type structure (Figure 3.4.).(29) This mechanism was exploited by us to stabilise the ice-templated PAN monoliths in order to form the ice-templated porous carbons (ITPCs). After the oxidative annealing step, the ice-templated PAN monoliths were carbonised by heating to 800 °C under an Ar atmosphere. After carbonisation, SEM images were taken which confirmed the retention of the ice-templated morphology (Figure 3.3.), although volumetric shrinkage of about 60 % had occurred in comparison to the original ice-templated PAN (Figure 3.5 a)).

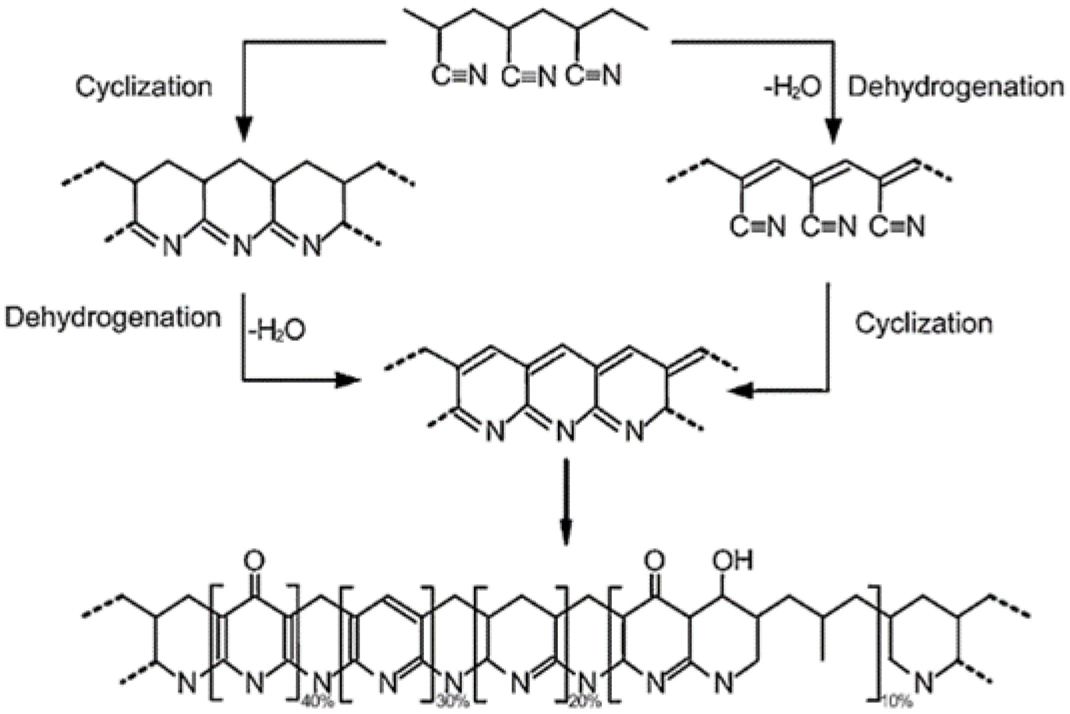

Figure 3.4. Proposed mechanism for the oxidative annealing process undergone by PAN (29)

The ice-templated porous PAN prepared from an initial PAN in DMSO concentration of 50 mg ml^{-1} (PAN50), was selected to further investigate the material's behaviour on carbonisation. Thermo-gravimetric analysis (TGA) was employed to investigate the material's behaviour on heat treatment (Figure 3.5. b)); this revealed a mass loss of about 25 % upon heating to the annealing temperature of 280 °C, before a further loss of approximately 40 % on heating to the carbonisation temperature of 800 °C. Table 3.2. summarises the mass losses of the materials after annealing and carbonisation. Mercury intrusion porosimetry (MIP) was also employed on the PAN50 sample to observe if any significant change in the pore characteristics had occurred upon carbonisation (Figure 3.5. c)). It was observed that, upon crosslinking and carbonisation, the total pore area and pore diameter shrank by ~77 % and ~38 %, respectively (Table 3.1.).

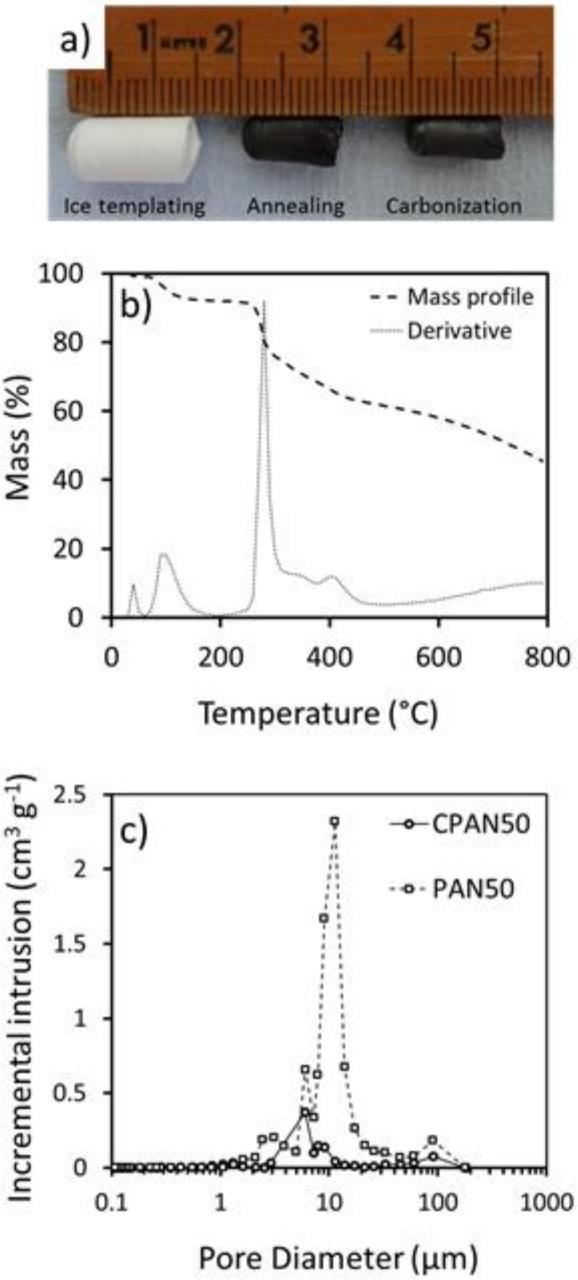

Figure 3.5.a) Visual image of the ice-templated, annealed and carbonised CPAN50 monolith. b) TGA of the PAN50 sample on heating to 800 °C, c) MIP pore size distribution profile of the PAN50 and CPAN50 monoliths

Table 3.1. Summary of the MIP pore size data for the PAN50 and CPAN50 samples

	Total Intrusion Volume	*Total Pore Area*	*Average Pore Diameter*
	(cm^3 g^{-1})	*(m^2 g^{-1})*	*(nm)*
PAN50	8.0	3.6	8990
CPAN50	1.1	0.8	5560
Difference	-85.8 %	-77.1 %	-38.2 %

Powder X-Ray Diffraction (PXRD) and Ramen spectroscopy were also performed to investigate the microstructure of the carbonised materials. PXRD revealed two broad Bragg peaks at 2θ values of 25 and 43°, characteristic of the (002) and (101) reflections of a semi-graphitic carbon, with negligible variance between samples prepared from different PAN concentrations (Figure 3.6. a)). The approximate interlayer spacing between adjacent graphene sheets, d_{002}, was calculated by employing the Bragg equation and found to be 3.55 Å. The mean crystallite sizes L_c and L_a calculated with the Scherrer equation, were found to be 2.2 and 3.1 nm, respectively. The CPAN50 material was also analysed by Raman spectroscopy as a representative sample, which revealed two overlapping peaks at 1344 and 1580 cm^{-1} (Figure 3.6. b)), respectively corresponding to the defect (D-band) A_1g mode and graphitic (G-band) E_{2g} mode of semi-graphitic carbon. The ratio of intensity of the D- and G-bands, I_D/I_G, was calculated as 1.12, indicating a relatively disordered nanotexture.

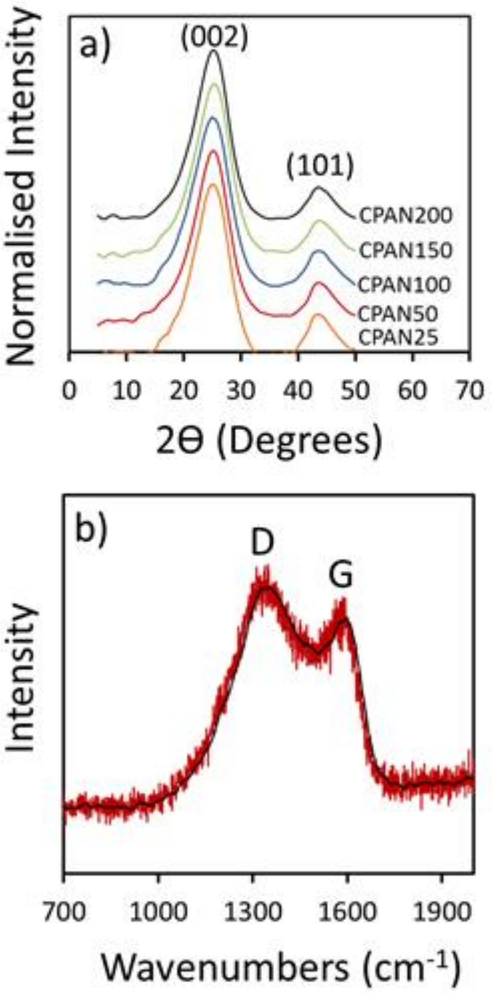

Figure 3.6. a) PXRD of carbonised materials and b) Raman spectrogram of the CPAN50 sample

Table 3.2. Comparison of the mass loss on carbonisation, elemental analysis, 7-point BET surface areas and specific capacities after 10 cycles for the ITPCs prepared from different initial PAN concentrations

PAN Concentration (mg ml^{-1})	Mass Loss on Carbonisation (%)	C (%)	H (%)	N (%)	7-point BET Surface area (m^2 g^{-1})	Specific capacity after 10 cycles (mAh g^{-1})
25	42.2	72.0	1.04	16.4	12.3	611
50	33.7	74.9	1.31	15.7	7.7	553
100	34.4	70.9	1.05	16.7	5.0	476
150	36.2	73.2	0.84	17.3	1.6	499
200	36.5	75.9	0.77	16.0	3.0	345

The conductivity of the monolithic samples was measured *via* a simple two-probe method, which revealed a linear relationship of higher conductivity with a higher initial PAN concentration (Figure 3.7.). This behaviour was simply attributed to the increased carbon density of the materials from higher initial PAN concentrations, resulting in enhanced electron percolation and hence a higher conductivity.

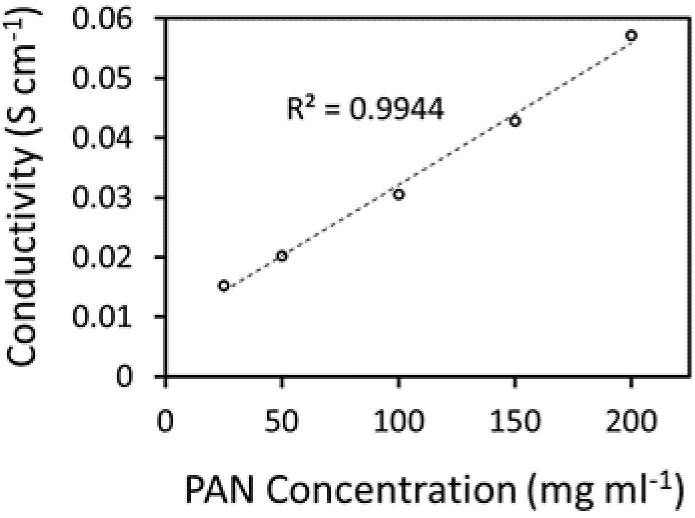

Figure 3.7. Graph showing the relationship between initial PAN concentration and electrical conductivity

N_2 gas sorption was performed on the materials to determine the surface areas and pore size characteristics of the materials. 7-point BET measurements gave relatively low surface area values of ~10 m^2 g^{-1} (Table 3.2.), however when full N_2 gas sorption isotherm measurements were conducted extremely long pressure equilibration times (sample running time ~1 week) were observed, which limited measurement to the representative CPAN50 sample. Here, a BET specific surface area of 172.9 m^2 g^{-1} was calculated from the obtained isotherm, density functional theory (DFT) analysis revealed a bimodal micropore size distribution of 1.0 and 1.4 nm and Barrett, Joyner and Halenda (BJH) analysis revealed a total adsorption pore volume of 0.019 cm^3 g^{-1} (Figure 3.8.). The Shape of the isotherm can be roughly classified as type I with a H4 hysteresis loop, according to IUPAC definition,(33) and also displayed the phenomenon of low-pressure hysteresis (LPH). LPH has been observed for other porous solids, such as micro- and mesoporous silicas, microporous polymers and activated carbons.(34)(35)(36) LPH has been suggested to be an artefact of incomplete degassing,(35) however even with a high degassing temperature of 300 °C for 24 h the phenomenon was still observed for our material, suggesting incomplete degassing was not the cause of LPH in this case. Swelling of non-rigid monoliths, and the presence of narrow pore openings and convoluted pore pathways can also account for LPH,(36)(37) the latter of which was deemed the most likely cause in our case due to the rigidity of the carbon framework preventing swelling.

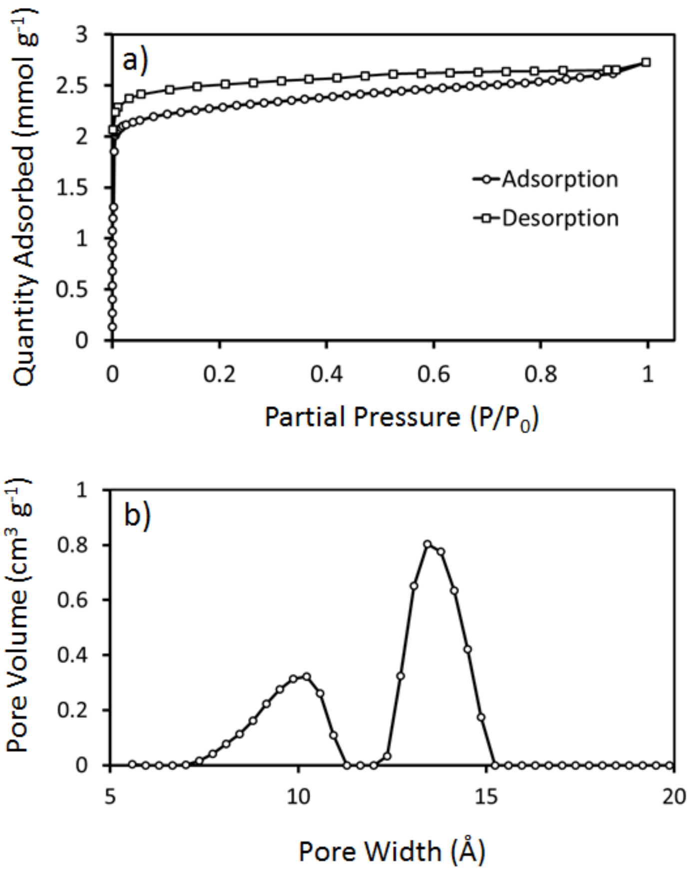

Figure 3.8. a) BET isotherm and b) DFT pore size distribution plot for the CPAN50 material

TGA was performed on the CPAN50 under air to determine the total ash content of the sample, which was found to be 3.9 % (Figure Apx.1.). CHN elemental analysis was performed to determine the weight percentage of carbon, hydrogen and nitrogen within the samples, with the majority of the remainder likely to be oxygen introduced during the crosslinking step (Table 3.2.). Interestingly, an exceptionally high N content of between 15 – 17 % was observed within the PAN materials, which is significantly higher than most other PAN-derived carbons in the literature – whose N content is typically less than 10 %.(38)(39) X-ray photoelectron spectroscopy (XPS) was performed on a representative sample, CPAN25, which confirmed a high N-content of 15.5 % (Figure 3.9.). A detailed scan of the N domain revealed four component peaks at energy levels of 398.2, 399.4, 401.1 and 402.9 eV, which were attributed to pyridinic- (37.0 %) pyrrolic- (10.5 %), quaternary- (50.0 %) and oxidised- (2.5 %) nitrogen, respectively.(40)(41) It has been reported that only pentagonal pyrrolic nitrogen is formed at low temperature around 300 °C, but can be converted to pyridinic and quaternary nitrogen at higher temperatures.(41)(42) The presence of quaternary nitrogen has been linked to enhanced LIB anode performance through the hybridisation of its lone pair of electrons with the conjugated carbon π-orbitals.(41)(43)(44) It has also been proposed that N-rich carbon can enhance LIB battery performance by creating defects which may act as additional active sites for Li-ion binding, and also *via* the direct formation of Li-N bonds.(45) Indeed, there are numerous reports which show that N-doping of a carbon framework can significantly enhance the electrochemical profile with regards to LIB anode performance, particularly in regard to enhanced capacity and superior high-rate performance.(21)(22)(46)(47)

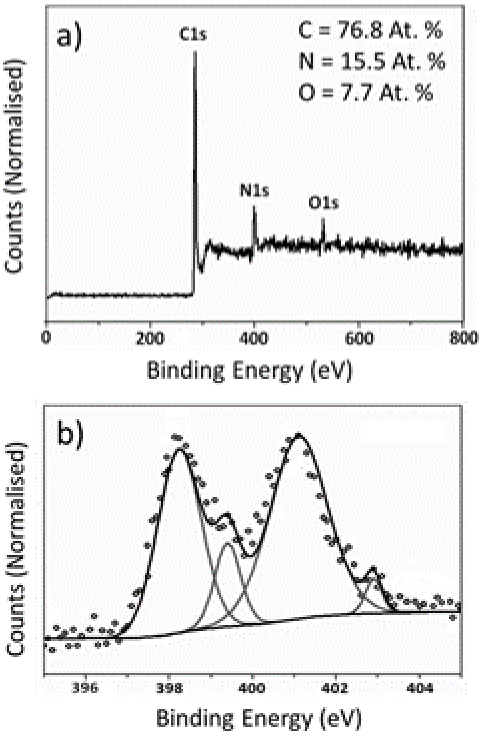

Figure 3.9. XDS data for the CPAN25 sample. a) Broad scan and b) detailed scan of the N domain

N-doping of carbons is typically achieved through the deliberate incorporation of an N-rich substance, such as NH_3 or melamine, during carbonisation,(24)(48) although in some instances carbon precursors with high intrinsic N content are employed.(24)(46)(49)(50) In our case, the only feasible source of N is from the nitrile groups of the PAN polymer, most likely aided into the carbon framework through the cyclisation and aromatisation reactions occurring during the oxidative annealing step. Okada *et al.* also reported a relatively high (~12 – 19 %) N-content for a carbonised PAN material.(51) Here they employed a procedure termed *thermally induced phase separation* (TIPS) to prepare macroporous PAN monoliths, which were subsequently annealed, carbonised and activated.

3.4.2. Anode Performance Evaluation

N-rich and hierarchically porous carbons have displayed excellent performances as Li-ion battery anode materials – especially in terms of capacity and high C-rate performance.(9) The ice-templated and carbonised PAN materials, prepared from different initial PAN concentrations, were assembled into coin cells and cycled at 50 mA g^{-1} over 10 cycles (Table 3.2.). Having the highest reversible capacity of the tested materials, CPAN25 was selected for a more in-depth evaluation of performance. Cyclic voltammetry (CV) was performed on a CPAN25 coin cell and displayed typical behaviour expected for a porous semi-graphitic carbon – with reductive intercalation occurring of Li occurring on the negative sweep at potentials approaching 0 V (vs. Li/Li^+), and oxidative de-intercalation occurring on the positive sweep at a similar potential (Figure 3.10 a)).

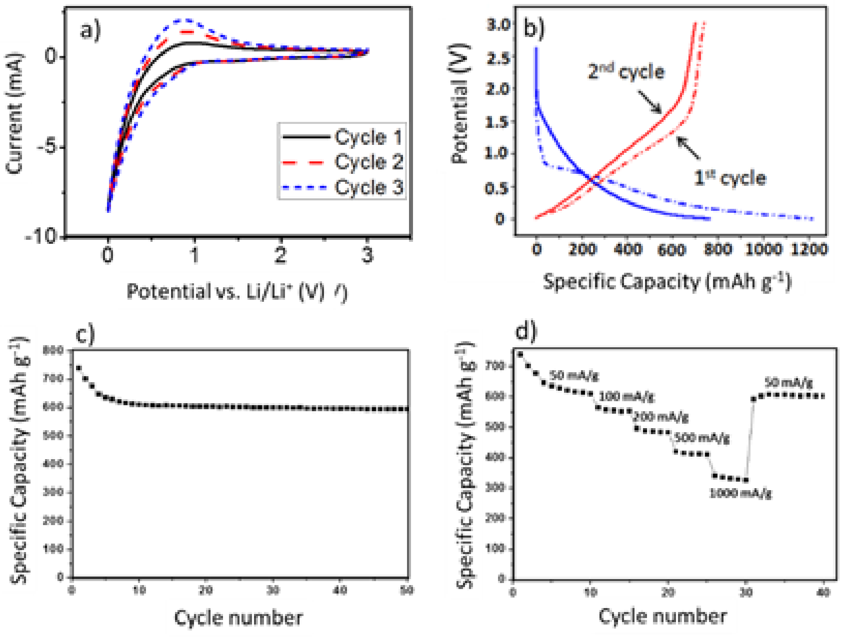

Figure 3.10. Electrochemical (Li-ion anode) evaluation of the CPAN25 material: a) CV curves, b) CCP curves at 50 mA g^{-1}, c) cycle stability over 50 cycles at 50 mA g^{-1}, d) specific capacities at increasing current densities

Constant current potentiometry (CCP), at a current density of 50 mA g^{-1}, revealed an initial irreversible capacity (C_{irr}) of 468 mA h g^{-1} and reversible capacity (C_{rev}) of 745 mA h g^{-1} (Figure 3.10 b)). The reversible capacity decayed over the first 10 cycles, before stabilising at about 611 mA h g^{-1}; considerably higher than the maximum theoretical capacity for graphite at 372 mA h g^{-1}. After the initial decay, the cycle stability at this current density was fairly good, remaining above 590 mA h g^{-1} after 50 cycles. Cycling at higher current densities demonstrated good high-rate performance too, with a reversible capacity of about 320 mA h g^{-1} obtained at a high current density of 1 A g^{-1} (Figure 3.10. d)). This performance compares favourably with other carbon anode materials reported in the literature (Table 1.1. and Table 1.2.). In particular, it should be noted that most templated carbons that display high C_{rev} values (between ~650 - 2000 mA h g^{-1}) also display high C_{irr} values, which would reduce the overall capacity of the battery in a practical context. In contrast, our materials display relatively low C_{irr} in relation to C_{rev}, which we attribute to the moderate surface area values – since high surface areas result in high C_{irr} values due to excessive formation of the solid electrolyte interphase (SEI).

This comparatively good anode performance is attributed to a number of factors. Firstly, the hierarchical pore structure of macro-, meso-, and micropores likely serves as an efficient Li^+ ion diffusion network, allowing rapid diffusion of Li^+ ions to and from the active electrode surface, as well as an interconnected conductive structure for facile electron percolation. Moreover, the moderate surface area may provide a good contact area for electrode-electrolyte interaction, without being so large as to cause excessive SEI formation with an associated high C_{irr}. There have been several other reports detailing enhanced anode performance by employing similarly hierarchical porous structures, in particular those with interconnected meso- and macro- pores.(18)(19)(46)(52) The most significant factor however is likely the high N content and large proportion in quaternary environment (50.0 %), in concordance with previous reports.(21)(22)(46)(53)(54) For example, Que *et al.* fabricated carbon nanofiber webs with high N content (~16 %) which displayed a very impressive reversible capacity of 300 mA h g^{-1} at the high current density of 10 A g^{-1}.(22) Protein-derived N-rich porous carbons have also displayed excellent high rate performances of up to 210 mA h g^{-1} at the high current density of 4 A g^{-1}.(46) A comparison of the high-rate performance of other doped materials is presented in Table 1.2.

3.4.3. Composites for Enhanced LIB Performance

A major advantage the ITPC technique holds over other templating methods is the facile way in which various composite materials can be obtained. This is achieved by simply forming a solution or suspension of the desired composite-forming material (or materials) – which can include nanoparticles, metal salts, organic compounds or carbon nanomaterials, prior to the ice-templating step. The composite material is excluded from the advancing ice front along with the polymer, becoming embedded within the ice-templated polymer wall. Upon carbonisation, the composite material (assuming it survives the carbonisation process) is then embedded within the ITPC. In this section, we detail how this method was utilised to produce a variety of composite materials, with the goal of enhancing the LIB battery performance.

3.4.3.1. Si Nanoparticle Composites

Si has the highest known theoretical specific storage capacity of any Li-alloying material with a value of 4200 mA h g^{-1} – an order of magnitude higher than graphitic carbon.(55) However Si makes a poor LIB anode material on its own since it undergoes significant volumetric expansion (~400 %) on lithiation, which results in pulverisation of the electrode and loss of capacity after a small number of charge-discharge cycles.(55) This problem can be overcome somewhat by fabricating the materials as various nanostructures, such as nanoparticles,(56) nanowires(57) and thin films,(58) which can more easily accommodate the stresses associated with the large volumetric expansion. Another route to overcome these problems is to incorporate Si within a porous carbon framework, which not only alleviates the stresses of volumetric expansion by acting as a mechanical buffer, but also serves as a conducive framework – overcoming the poor electrical conductivity of Si.(59)

It was therefore hypothesised that the incorporation of Si nanoparticles within the PAN-derived ITPCs could enhance LIB anode performance – and so was attempted using commercially obtained 100 nm Si nanoparticles. The Si nanoparticles were added to solutions of PAN in DMSO (50 mg ml^{-1} concentration) at weight ratios of 1:1, 1:4 and 1:9 Si/PAN, before being mixed and sonicated to ensure adequate dispersion. The mixtures were then ice-templated and freeze-dried, before being oxidateively annealed and carbonised following the standard procedure. PXRD of the carbonised samples revealed the (111) and (220) reflections of elemental Si (Figure 3.11a)) – confirming its presence within the material – and SEM revealed the presence of Si nanoparticles on the surface of the carbon (Figure 3.11b)). CCP was employed to evaluate the performance of the Si-CPAN50 composites, however performance was poor with C_{rev} falling to < 100 mA h g^{-1} after 20 cycles – suggesting the CPAN50 framework failed to overcome the volumetric expansion issues associated with Si as an anode material.

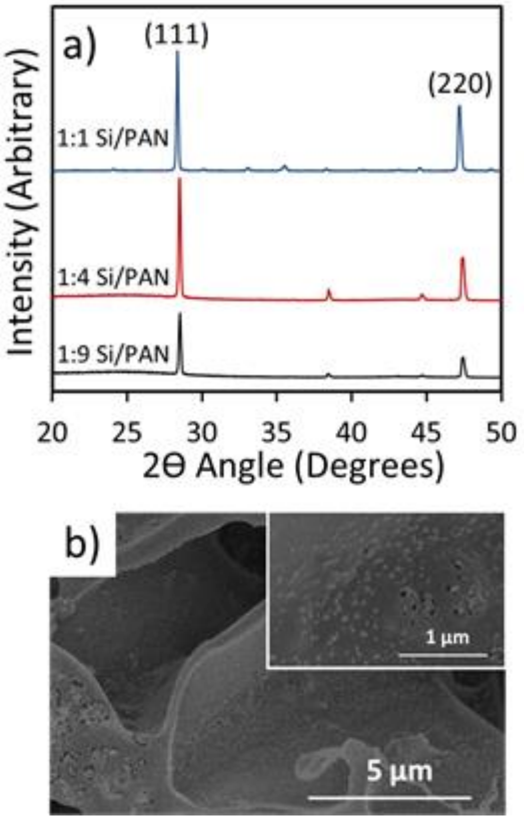

Figure 3.11 a) PXRD patterns of the Si-CPAN50 composites showing (111) and (220) reflections of Si, and b) SEM image of the 1:1 Si-CPAN50 composite (1:1 ratio Si/PAN) showing embedded Si nanoparticles

3.4.3.2. SnO_2 Composites

Like Si, SnO_2 can alloy with Li to give a relatively high theoretical specific capacity (782 mA h g^{-1}) as a LIB anode material, but also suffers from poor cyclability due to destructive volumetric change on lithiation/delithiation.(60) Porous carbon-SnO_2 composites also have been prepared in an attempt to overcome these issues; for instance Stein and co-workers coated a colloidal polymer (PMMA) templated porous carbon with SnO_2 nanoparticles by soaking the carbon in a solution of $SnSO_4$ before thermally decomposing the salt.(61) The composite displayed an initial improvement in terms of C_{rev} compared to the carbon monolith itself (278 versus 223 $mAhg^{-1}$), however this capacity fell after a short number of cycles – which was attributed to the detachment of the SnO_2 nanoparticles carbon surface.

In an attempt to improve capacity, porous carbon-SnO_2 composites were prepared *via* the PAN-derived ITPC method described in this chapter. Initially, a solution of PAN (50 mg ml^{-1}) and $Sn(OAc)_2$ (50 mg ml^{-1}) in DSMO was prepared, giving a 1:1 ratio of the polymer the Sn salt. The ice-templating method was then employed to give a porous PAN-$Sn(OAc)_2$ composite, before being annealed and carbonised at a temperature of 550 °C. A lower carbonisation temperature than the standard 800 °C was employed since SnO_2 is known to reduce to Sn above 650 °C. PXRD measurements of the materials before and after annealing, and after carbonisation confirm the presence of SnO_2 through the appearance of the associated (110), (101) and (200) diffraction peaks (Figure 3.12 a)). The mean crystallite size of the SnO_2 was calculated by employing the Scherrer equation on the (110) peak, giving a value of 17.1 nm. SEM images revealed a relatively disordered porous morphology, which may be due to the Sn salt interfering with ice-crystal formation and growth (Figure 3.12 b)). CCP of the composite gave values of 630 and 520 mA h g^{-1} for C_{rev} and C_{irr} respectively, which are poorer values than the non-doped ITPC, although capacity decay was moderate falling to only 460 mA h g^{-1} after 35 cycles.

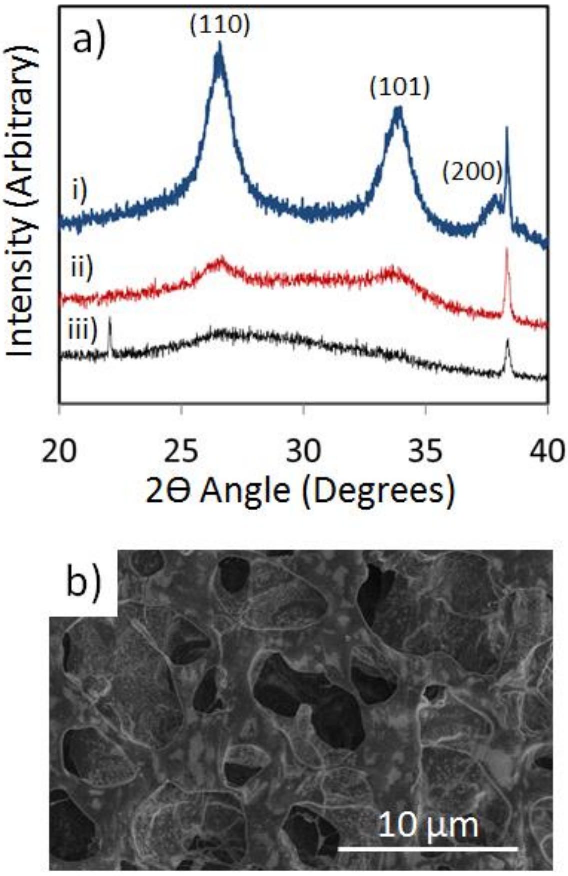

Figure 3.12. a) PXRD patterns of the SnO_2-CPAN50 composite (1:1 ratio) i) before heat treatment, ii) after annealing and iii) after carbonisation. b) SEM image of SnO_2-CPAN50 composite (1:1 ratio)

3.4.3.3. Reduced Graphene Oxide Composites

Graphene has attracted much attention in the field of energy storage since the discovery of its remarkable physical, chemical and electronic properties.(8) Graphene has been produced *via* a number of synthetic routes, one common and simple method being the reduction of graphene oxide (GO) in an aqueous suspension, stabilised by a suitable surfactant.(31) Reduced graphene oxide (RGO) was prepared by such a method and incorporated within the PAN-derived ITPCs, *via* mixing RGO with the initial PAN in DMSO solution prior to ice templating, with the aim of further enhancing the LIB anode performance. Remarkably, incorporation of RGO did seem to enhance the high rate performance in comparison to the non-doped material; giving a C$_{rev}$ of 250 mA h g^{-1} at the high current density of 10 A g^{-1} (Figure 3.13). The basis of this improved performance is not clear, however it is hypothesised that the relatively high diffusivity of Li on a graphene plane (~10^{-7} to 10- cm^{2} s^{-1}) may serve to minimise internal resistances and rate-limiting kinetics within the electrode material. A more in-depth electrochemical study would be required to shed light on this behaviour however.

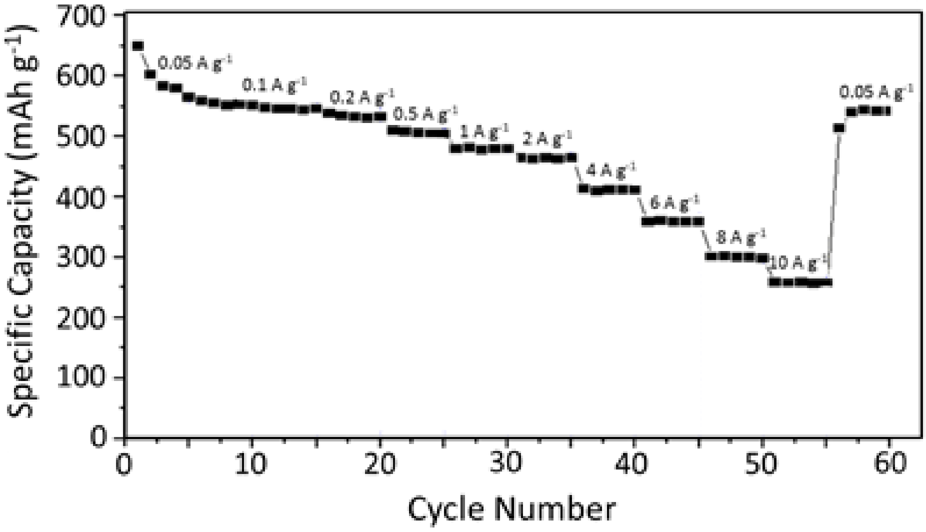

Figure 3.13. Specific capacities at increasing current densities for the RGO-CPAN50 composite

3.4.3.4. Melamine Composites

As was previously mentioned, N-doping of carbons has been shown to enhance their performance as LIB anode materials, particularly with regard to the high-rate capability.(21)(22)(46) Although the PAN-derived ITPCs already had high N contents – derived from the nitrile groups in the PAN polymer – it was investigated as to whether the incorporation of another N-rich species could further increase the level of N-doping and thereby enhance LIB anode performance further. The N-rich compound used was melamine, which was dissolved in the PAN in DMSO (50 mg ml^{-1}) solution weight percentages relative to the PAN (5, 15, 25 and 35 wt. % vs. PAN) prior to ice-templating, annealing and carbonisation. CHN elemental analysis revealed a linear relationship between amount of melamine incorporated and resultant N content (Figure 3.14 a)). Evaluation of the materials as LIB anodes found that the sample incorporated with melamine at 15 wt. % (vs. PAN) had significantly improved high rate performance in comparison to the non-doped material (Figure 3.14 b)), showing that further N doping can indeed enhance high-rate performance.

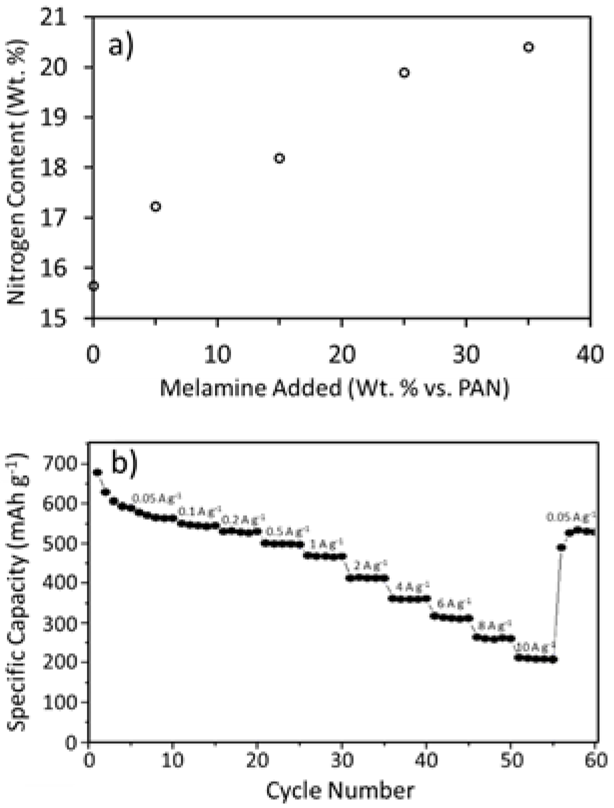

Figure 3.14. a) Relationship between amount of melamine added and N content, b) specific capacities at increasing current densities for the 15% melamine-CPAN50 composite

3.4.3.5. Melamine and RGO Co-Composites

Since the incorporation of melamine and RGO both let to enhancements of the PAN-derived ITPCs in terms of high rate performance, the effect of the incorporation of both was investigated. It was found that the high-rate performance for this system was improved still further, with a reversible capacity of about 300 mA h g^{-1} obtained at high current density of 10 A g^{-1} (Figure 3.15). This performance is on par with some of the best performing carbon-based materials in the literature (Table 1.2.), despite the relative simplicity of the ice-templating and carbonisation technique.

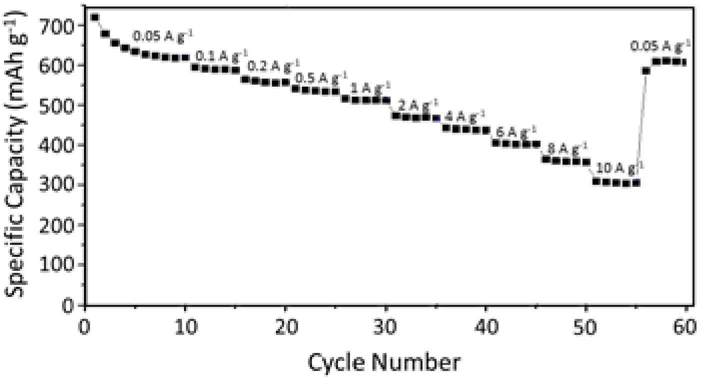

Figure 3.15. Specific capacities at increasing current densities for the 15% melamine-RGO-CPAN50 composite

3.5. Conclusions and Remarks

Hierarchically porous, PAN-derived ITPCs were prepared *via* a relatively simple ice-templating, oxidative annealing and carbonisation technique. Unlike many other templating methods for the preparation of porous carbons, which often require relatively complex and costly template fabrication and subsequent removal steps, the ice-crystal temples are easily generated and removed by simply freezing and freeze-drying, respectively. The obtained carbons, having an inherently high N-content, a high proportion of quaternary N and moderate surface areas, displayed relatively good performance as LIB anode materials despite the simple fabrication process. Moreover, it was relatively easy to produce composite materials with a variety of other entities (*i.e.* nanoparticles, metal salts, organic compounds and RGO), which led to further performance enhancement in the case of melamine (further N-doping) and RGO incorporation; with the co-doped material attaining one of the highest capacities reported at the high current density of 10 A g^{-1}.

3.6. References

1. Pollet BG, Staffell I, Shang JL (2012) *Electrochim Acta* 84(0):235–249.
2. Barton JP, Infield DG (2004) *IEEE Trans Energy Convers* 19(2):441–448.
3. Carbajales-Dale M, Barnhart CJ, Benson SM (2014) *Energy Environ Sci* 7(5):1538–1544.
4. Crabtree G (2015) *Nat Outlook Energy Storage* 526(7572):S92.
5. Nishi Y (2001) *J Power Sources* 100(1–2):101–106.
6. Armand M, Tarascon JM (2008) *Nature* 451(7179):652–657.
7. Landi BJ, Ganter MJ, Cress CD, DiLeo RA, Raffaelle RP (2009) *Energy Environ Sci* 2(6):638–654.
8. Pumera M (2011) *Energy Environ Sci* 4(3):668.
9. Roberts AD, Li X, Zhang H (2014) *Chem Soc Rev* 43(13):4341–4356.
10. Ji L, Zhang X (2009) *Carbon* 47(14):3219–3226.
11. Zhang L, Aboagye A, Kelkar A, Lai C, Fong H (2014) *J Mater Sci* 49(2):463–480.
12. Yoshio M, Brodd RJ, Kozawa A (2009) *Lithium-ion batteries : science and technologies* (New York, NY : Springer.).
13. Ogumi Z, Wang H (2009) Carbon anode materials. *Lithium-Ion Batteries: Science and Technologies*, eds Yoshio M, Brodd R, Kozawa A (Springer New York), pp 49–73.
14. Xu C, Sun F, Gao H, Wang J (2013) *Anal Chim Acta* 780(5):20–27.
15. Nishihara H, Kyotani T (2012) *Adv Mater* 24(33):4473–4498.
16. Liu B, Soares P, Checkles C, Zhao Y, Yu G (2013) *Nano Lett* 13(7):3414–3419.
17. Yi J, et al. (2011) *J Power Sources* 196(16):6670–6675.
18. Fang B, Kim M-S, Kim JH, Lim S, Yu J-S (2010) *J Mater Chem* 20(45):10253.
19. Hu YS, et al. (2007) *Adv Funct Mater* 17(12):1873–1878.
20. Hou J, Cao C, Idrees F, Ma X (2015) *ACS Nano* 9(3):2556–2564.
21. Wu YP, et al. (2000) *J Appl Polym Sci* 77(8):1735–1741.
22. Qie L, et al. (2012) *Adv Mater* 24(15):2047–2050.
23. Nan D, et al. (2014) *J Mater Chem A* 2(46):19678–19684.
24. Paraknowitsch JP, Thomas A (2013) *Energy Environ Sci* 6(10):2839.
25. Wood KN, O’Hayre R, Pylypenko S (2014) *Energy Environ Sci* 7(4):1212.
26. Deville S, Meille S, Seuba J (2016) *Sci Technol*.
27. Frank E, Steudle LM, Ingildeev D, Spörl JM, Buchmeiser MR (2014) *Angew Chemie Int Ed* 53(21):5262–5298.
28. Nishihara H, Mukai SR, Tamon H (2004) *Carbon* 42(4):899–901.
29. Rahaman MSA, Ismail AF, Mustafa A (2007) *Polym Degrad Stab* 92(8):1421–1432.
30. Kong JH, et al. (2011) *J Mater Chem* 21(40):15928–15934.
31. Stankovich S, et al. (2006) *J Mater Chem* 16(2):155–158.

32. Deville S (2013) *J Mater Res* 28(17):2202–2219.
33. Sing KSW, et al. (1985) *Pure Appl Chem* 57(4):603–619.
34. Braida WJ, et al. (2003) *Environ Sci Technol* 37(2):409–417.
35. Silvestre-albero AM, Manuel J, Silvestre-albero J (2012) *J Phys Chem C* 116(31):16652–16655.
36. Jeromenok J, Weber J (2013) *Langmuir* 29(42):12982–12989.
37. Olivares-Marin M, Palomino P, Amarilla JM, Enciso E, Tonti D (2013) *J Mater Chem A* 1(45):14270–14279.
38. Ning X, Zhong W, Li S, Wang Y, Yang W (2014) *J Mater Chem A* 2(23):8859.
39. Deng Y, Xie Y, Zou K, Ji X (2015) *J Mater Chem A* 4(4):1144–1173.
40. Chen XY, Xie DH, Chen C, Liu JW (2013) *J Colloid Interface Sci* 393:241–248.
41. Su F, et al. (2011) *Energy Environ Sci* 4(3):717–724.
42. Mou Z, et al. (2011) *Appl Surf Sci* 258(5):1704–1710.
43. Jeong HM, et al. (2011) *Nano Lett* 11(6):2472–2477.
44. Seredycha, Hulicova-Jurcakovab, Lub, Bandosza (2008) *Carbon* 46(11):1475–1488.
45. Endo M, Kim C, Nishimura K, Fujino T, Miyashita K (2000) *Carbon* 38(2):183–197.
46. Li Z, et al. (2013) *Energy Environ Sci* 6(3):871–878.
47. Kaskhedikar NA, Maier J (2009) *Adv Mater* 21(25–26):2664–2680.
48. Horikawa T, et al. (2012) *Carbon* 50(5):1833–1842.
49. Wang Z, Xiong X, Qie L, Huang Y (2013) *Electrochim Acta* 106(0):320–326.
50. Xia Y, Yang Z, Mokaya R (2005) *Stud Surf Sci Catal* Volume 156:565–572.
51. Nandi M, et al. (2012) *Chem Commun* 48(83):10283–10285.
52. Su F, et al. (2005) *J Phys Chem B* 109(43):20200–20206.
53. Wu ZS, Ren W, Xu L, Li F, Cheng HM (2011) *ACS Nano* 5(7):5463–5471.
54. Wang Y, Su F, Wood CD, Lee JY, Zhao XS (2008) *Ind Eng Chem Res* 47(7):2294–2300.
55. Kasavajjula U, Wang C, Appleby AJ (2007) *J Power Sources* 163(2):1003–1039.
56. Green M, Fielder E, Scrosati B, Wachtler M, Moreno JS (2003) *Electrochem Solid-State Lett* 6(5):A75.
57. Chan CK, et al. (2008) *Nat Nano* 3(1):31–35.
58. Ohara S, Suzuki J, Sekine K, Takamura T (2004) *J Power Sources* 136(2):303–306.
59. Wen ZS, Yang J, Wang BF, Wang K, Liu Y (2003) *Electrochem commun* 5(2):165–168.
60. Liang C, Gao M, Pan H, Liu Y, Yan M (2013) *J Alloys Compd* 575(0):246–256.
61. Lee KT, Lytle JC, Ergang NS, Oh SM, Stein A (2005) *Adv Funct Mater* 15(4):547–556.

Chapter 4

Nitrogen-rich Activated ITPCs for Gas Storage

The contents of this chapter have been published in *The Journal of Materials Chemistry A*

(Roberts AD, et al. (2017) *J Mater Chem A* (Advance Article)

List of Figures

List of Tables

4.1. Background and Context

In Chapter 3, we demonstrated a process to prepare ITPCs from a PAN percursor. The resultant materials, having relatively high N contents and moderate surface areas, displayed relatively good performance as LIB anode materials – which could be further improved with the incorporation of melamine and rGO. In this chapter, PAN-derived ITPCs were subject to chemical activation in order to artificially increase the surface area and develop microporosity. This opened up new potential applications where high surface areas are desirable, namely gas sorption (for H_2 and CO_2 storage) and as supercapacitor electrode materials. The degree of activation could also be varied which gave a degree of control over the resultant surface areas and N-content.

4.2. Introduction

With a clear link between CO_2 emissions and global warming, there is an urgent need for countries to cut their greenhouse gas emissions to mitigate the worst effects of climate change. One viable solution is the capture and storage of CO_2 from large point sources such as power plants, refineries and cement manufacturing facilities, followed by its long-term storage within geological formations or use as a feedstock for higher-value chemicals.(1)(2)(3) The large-scale deployment of such carbon capture and storage (CCS) technologies is currently hampered by problems such as high costs and systematic inefficiencies, with the energy requirements alone increasing 25 – 40 % for plants employing conventional techniques.(2) There is therefore a need for technological advances – particularly in the form of new, low cost and effective CO_2 adsorption martials – to improve efficiency and drive down costs which would allow CCS to be more widely adopted. Another priority for CO_2 emission reduction is the transition from petroleum-based automotive transport – which currently accounts for approximately 23 % of global CO_2 emissions – to low-carbon alternatives.(4) Replacing internal combustion engines with H_2-fuel cells is one option which may achieve this goal, however the development of materials capable of storing sufficient quantities of H_2 under moderate conditions remains a challenge.(5)

Various high surface area porous materials, such as MOFs,(6)(7) COFs,(8) zeolites,(9) microporous polymers(10) and ACs(11)(12)(13)(14) are able to adsorb and desorb gasses such as CO_2 and H_2 through pressure or temperature swing cycles – and are therefore being actively investigated for their utilisation in CCS and H_2 storage technology. Of these materials, ACs hold significant advantages over others, including high chemical and thermal stability, relatively low cost of manufacture and wide availability and diversity of precursors.(11) Such carbons can also possess extremely versatile properties, such as variable morphology, nanostructure, porosity, heteroatom doping and surface functionalisation, which can be tuned to a degree to optimise performance.(11)(15) Since the adsorption of gasses occurs *via* their physical interaction with a material's surface, a high surface area is one of the most important factors for a gas sorption material.

For CO_2 sorption, it's been suggested that a combination of micro (< 2 nm) and meso (2 – 50 nm) pores can lead to superior CO_2 adsorption than purely microporous materials due to multilayer adsorption within he larger pores.(16) Such a hierarchically porous structure may also enable relatively fast sorption kinetics,(17) since small and convoluted pore structures would impede the diffusion of gasses to and from the material's surface. N-doping of can also significantly increase the CO_2 sorption capacities of porous carbons due to the affinity between the acidic CO_2 molecules and the lone pair of electrons on N.(17)(18)(19)(20) In the context of H_2 storage, ultra-high surface areas and micropore volumes are regarded as the most important features for the maximisation of H_2 uptake, although a degree of heteroatom doping has also been suggested to enhance the adsorption capacity.(21)(22)

Templating methodologies are common routes for the fabrication of porous carbon materials, where either pre-formed porous structures (*hard-templating*) or self-assembled polymer/surfactant matrixes (*soft-templating*) direct the structure of precursors which are subsequently converted to carbon *via* pyrolysis.(15)(23) Once the templated carbon has been prepared, the materials may be subsequently activated in order to further increase surface areas, and hence gas adsorption capacity.(24) Although templating methods can result in well-defined porous carbons with excellent gas sorption characteristics, certain disadvantages such as the complexity of the synthesis, assembly and subsequent removal of the templates (*e.g.* HF etching for silica templates), and a limited range of available precursors (typically low molecular weight, carbon-rich and cross-linkable precursors) limit their scope and economic viability.(15) Pre-formed and self-assembled porous structures, such as MOFs and CMPs may also be directly converted to high-surface area microporous carbons in some instances,(25)(26)(27) but high costs and complexity serve as a barrier to commercialisation in these instances also. Various kinds of templated carbons have been prepared and evaluated for CO_2 and H_2 gas sorption with many displaying excellent performance. A number of the most significant examples have been summarised in Table 1.5. and 1.6 for comparison.

Recently, ice crystals have been employed as simple, low-cost templating entities (*ice-templating*) to prepare templated porous carbons in a facile and cost-efficient manner.(28)(29)(30) Here, frozen solvent crystals act as the templates to direct the formation of a porous structure.(31)(32) If suitable precursors are employed, the ice-templated structure can then be crosslinked and carbonised to form an ITPC.(28)(29)(30) Hierarchically porous carbons prepared through a combination of ice-templating, hard templating and physical activation have recently been demonstrated as effective CO_2 sorption materials.(33) Here, a colloidal suspension of silica spheres in an aqueous glucose solution was subject to ice-templating and carbonisation. Removal of the silica spheres was then achieved through HF etching, before the carbon was subject to physical activation with CO_2 gas. The prepared materials had BET surface areas of up to 2096 m^2 g^{-1}, and CO_2 uptake capacities of up to 4.1 mmol g^{-1} at 273 K and 10 bar of pressure. The commercially available polymer PAN has previously been shown to be an attractive precursor for activated carbon for gas sorption applications. Nandi *et al.* recently reported a high CO_2 adsorption of 5.14 mmol g^{-1}, at ambient pressure and temperature, for a PAN-derived activated porous carbon.(34) Here, they prepared a porous PAN monolith through their previously reported, template-free, thermally induced phase separation (TIPS) method, before crosslinking, carbonising and physical activation with CO_2. The high N content of the PAN polymer resulted in a high N-content activated carbon with excellent CO_2 sorption properties.

In this work, the ice-templating strategy was employed to prepare porous PAN monoliths, which – after impregnating with KOH – were oxidatively crosslinked before carbonisation and activation *via* pyrolysis (Figure 4.1.). The oxidative crosslinking is necessary to maintain the ice-templated structure upon pyrolysis, as it is for the manufacture of PAN-derived carbon fibres. It was found that through varying the degree of KOH impregnation, the surface areas, porosity and level of N-doping of the materials could be varied allowing tuning of the material properties for specific applications, *i.e.*, CO_2 or H_2 adsorption. The prepared materials were also evaluated for performance as supercapacitor electrodes, however the performance was fairly poor in comparison to other high surface area, N-doped ACs reported in the literature (Table 1.4.).

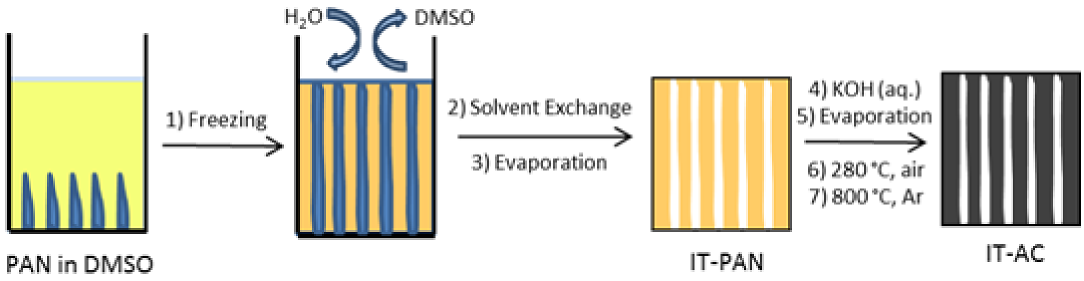

Figure 4.1. Schematic representation of the process employed to prepare the IT-ACs

4.3. Experimental

4.3.1. Chemical Reagents

Polyacrylonitrile (PAN, Mw ~150,000), potassium hydroxide (KOH, >85 %, pellets), sodium sulfate (Na_2SO_4, >99.0 %), lithium sulfate (Li_2SO_4, >98.5 %), dipotassium phosphate (K_2HPO_4, >98 %), dimethylsulfoxide (DMSO, >99.9 %, anhydrous), poly(vinylidene fluoride) (PVDF), n-methyl pyrrolidinone (NMP) and aqueous hydrochloric acid (37 %) were purchased from Sigma Aldrich and used without further purification. Super-P® carbon back was purchased from Timcal. Standard laboratory grade solvents and deionised water were used routinely.

4.3.2. Preparation of Materials

Preparation of ice-templated PAN monoliths

PAN (10 g) was dissolved in DMSO (90 ml) under stirring at 60 °C to form a 10 w/v % stock solution. After cooling to room temperature, 6 x 4 ml portions of this stock solution were transferred to 12 ml disposable glass vials before being placed on the cooling element of a freezer (-18 °C) and left overnight. The frozen samples were then transferred into approximately 2 L of deionised water cooled to 0 °C with ice, and stirred to facilitate the solvent exchange between the frozen DMSO and liquid water. The samples were left in the 0 °C water for 2 hours before the water and ice were refreshed. This process was repeated 4 times throughout the day, before the water-soaked samples were left to return to room temperature overnight. The water-soaked sampled were then soaked in acetone to displace the water and any residual DMSO. The samples were finally dried in a vacuum oven at 60 °C for 24 h. These samples are denoted IT-PAN10 (ice-templated PAN at 10 w/v % concentration).

Incorporation of activating agent

KOH (or another other salt-based activating agent) was dissolved in water to prepare 10 ml solutions at 5, 10, 20 and 50 w/v %. The prepared IT-PAN10 monoliths were separately soaked in these solutions for 2.5 h, under stirring and heating at 60 °C, before being removed and then dried in a vacuum oven at 60 °C for approximately 16 h. A ‘blank’ sample soaked in deionised water (0 % KOH) was also prepared for comparison. These samples are denoted IT-PAN10-KOHX, where ‘X’ is the concentration of the KOH solution (in w/v %) that the monolith had been soaked in. To maximise the KOH uptake, one sample was soaked in 10 ml of 50 % KOH, which was left stirring at 60 °C for 36 h. Evaporation of water over this period concentrated the KOH to the point where it had begun precipitating out of solution. This sample is denoted IT-PAN10-KOHMAX, where ‘MAX’ represents the maximum attainable KOH soaking concentration.

Annealing and carbonisation

The IT-PAN10-KOHX monoliths were subject to oxidative crosslinking by heating in a Carbolite® Horizontal Compact Tube Furnace to 280 °C in air (heating rate: 1 °C min^{-1}) for 1 h, and then allowed to cool naturally to room temperature. These annealed monoliths were then carbonised and activated by heating under a constant flow or argon (flow rate: 100 ml min^{-1}) in the same furnace to 800 °C at a rate of 5 °C min^{-1}, holding for 2.5 h at 800 °C, before cooling naturally to room temperature. The carbonised monoliths were then subject to a single acid wash (soaking in 2M HCl for about 30 mins), before being washed thoroughly with water and ethanol to remove salts and other unwanted species formed upon carbonisation. The carbonised and activated materials were then dried in a vacuum oven at 60 °C for approximately 16 h. These ice-templated, activated carbons materials are denoted IT-ACX, where 'X' is the concentration of the KOH solution (in w/v %) that the monolith had been soaked in.

4.3.3. Characterisation

The samples were imaged and morphology determined using a JSM-6700F FE-SEM instrument with an accelerating voltage of 5 keV. Prior to imaging, samples were adhered to an aluminium stud using conductive copper tape, before being sputter-coated with a thin layer (~2 nm) of gold. BET specific surface areas were obtained *via* N_2 gas sorption at 77 K using a Micromiretics ASAP 2420 volumetric adsorption analyser and BJH pore size distributions were calculated from the same measurements. A pressure range of 0.06 – 0.3 P/P_0 was used for the BET surface area calculations and the pore volumes were given by the total single point adsorption of pores less than 170 nm radius at $P/P_0 = 1$. Samples were degassed at 200 °C under vacuum (10^{-5} bar) for 16 h before analysis. PXRD patterns were obtained with a Bunker GADDS XRD system with a Cu-α radiation source. Raman spectra were recorded using a Renishaw InVia Raman Microscope fitted with a 633 nm laser, calibrated against a silicon wafer reference. XPS measurements were taken with a VG ESCA LAB-220i XL XPS instrument with an exciting source of Al. CHN elemental analysis measurements were taken using a Flash EA 1112 Series CHNS-O Analyser using cysteine sulfanilamide methionine as a standard and 8 x 5 mm pressed Sn capsules to contain sample specimens. Oxidative TGA measurements were conducted on a TA Instruments SDT Q600 TGA instrument with a constant air flow of 50 mL min^{-1}. Samples were heated to 1000 °C at a heating rate of 20 °C min^{-1}. CO_2 and H_2 uptake measurements were collected using a Micromeritics ASAP2050 at 298 K and 77.3 K respectively. All samples were degassed at 120 °C for 15 h under vacuum (10^{-5} bar) prior to analysis.

4.3.4. Electrochemical Measurements

The electrochemical performance of the materials was analysed by CV in a three-electrode cell set-up, using an Ag^+/AgCl reference electrode, a Pt wire counter electrode and an aqueous 6 M KOH electrolyte. The working electrodes were prepared as follows: an 8:1:1 ratio mixture of the pulverised active material, carbon black and PVDF was dissolved in NMP to form a viscous slurry. The slurry was then applied to a 1 cm^2 piece of porous Ni foam and the was NMP left to evaporate at 60 °C, before being pressed between another equal-sized piece of Ni foam. The total mass loading of active material was approximately 3 mg in each case. The CV tests were performed on an electrochemical workstation (PGSTAT302, Autolab) at various current densities as discussed in the manuscript.

4.4. Results and Discussion

4.4.1. Preparation of IT-ACs

Figure 4.1. depicts the process employed to prepare ice-templated and activated carbon monoliths (IT-ACs). Ice-templated PAN monoliths (denoted IT-PAN10) were first prepared by freezing 10 w/v % solutions of PAN in DMSO at -18 °C by placing them in a cooling element of a freezer. Typically, cryogenic temperatures are used for ice-templating (*i.e.* by submerging samples into a bath of liquid nitrogen at 77 K), however the method demonstrated here requires only a freezer and can therefore be regarded as a relatively simpler and greener route to prepare ice-templated materials. The fully frozen samples were then subject to solvent exchange by placing them in ice-cold (0 °C) water. To maintain the delicate structures after ice-templating, the frozen solvent crystal templates need to be removed without passing into the liquid phase (melting). If the ice crystal templates do melt, the liquid solvent can re-dissolve the templated substance resulting in loss of the ice-templated morphology. Typically, freeze-drying is employed to achieve this; *i.e.* bypassing the liquid phase by directly subliming the solvent at low pressures. However, freeze drying is a relatively energy intensive process and is not suitable for most solvents other than water. Although in Chapter 3 we had previously demonstrated the removal of DMSO from ice-templated PAN *via* freeze-drying, the solvent exchange method described here represents a simpler, faster and less energy intensive process for its removal. Since the melting point of DMSO is 19 °C and is highly miscible with water, by performing the solvent exchange at 0 °C it ensures the DMSO remains frozen as it exchanges with the water, and therefore does not disturb the ice-templated structure. By refreshing the water and ice several times, it ensures removal of the DMSO through dilution. Removal of the water and any residual DMSO is then achieved by a final solvent exchange with acetone at room temperature, which can then be removed easily by vacuum drying. SEM images confirmed the presence of an ice-templated morphology, indicating that freezing in a freezer and solvent exchanging had worked successfully (Figure 4.2.).

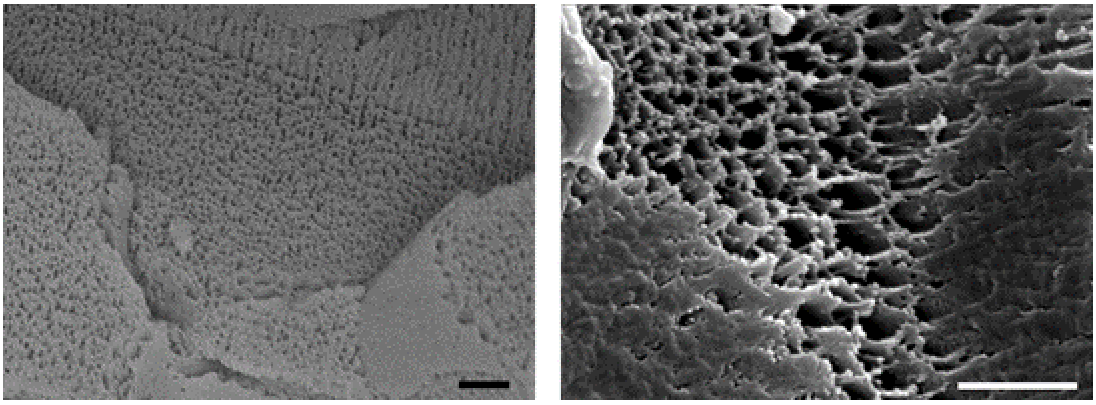

Figure 4.2. SEM images of the ice-templated PAN polymer (IT-PAN10) after solvent exchange with water at 0 °C. Scale bar = 1 µm

The dried IT-PAN10 monoliths were then soaked in aqueous KOH solutions at various concentrations (5, 10, 20 and 50 w/v %) at 60 °C for 2.5 h, before being removed from the solution and dried in a vacuum oven for approximately 16 h. To maximise KOH uptake, one sample was soaked in 50 % KOH at 60 °C for 36 h; the evaporation of water over this period increased the KOH concentration, which had begun to precipitate out of solution and crystallise on the surface and within the pores of the ice-templated PAN monolith. These KOH incorporated samples are denoted IT-PAN10-KOHX, where ‘X’ is the concentration of the KOH solution (in w/v %) that the monolith had been soaked in (or ‘MAX’ in the case of the latter sample). The masses of the samples before and after soaking are presented in Figure 4.3. and Table 4.1., where it can be seen that a higher KOH soaking concentration results in a greater uptake of KOH, as would be expected.

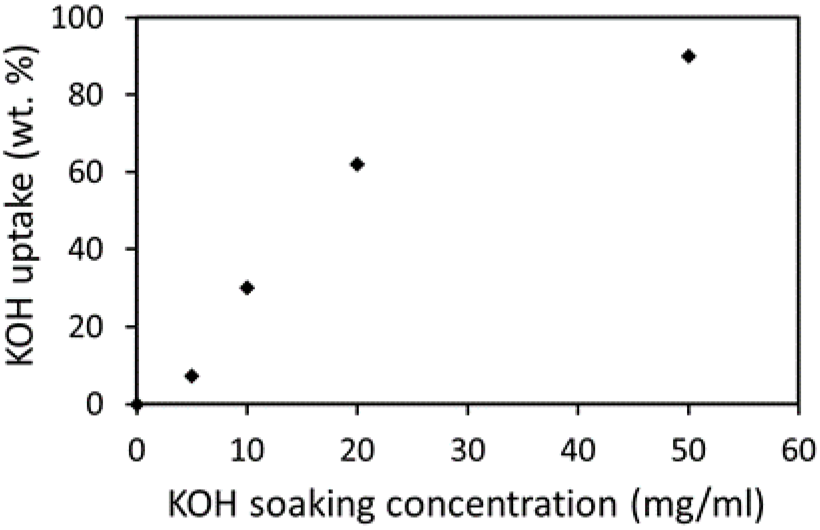

Figure 4.3. Relationship between KOH soaking concentration and KOH uptake within IT-PAN10

Table 4.1. Relationship between KOH soaking concentration and KOH uptake, BET surface area and CHN elemental content

Sample	*Mass KOH to PAN (wt. %)*	*BET surface area (m^2 g^{-1})*	*Pore volume (cm^3 g^{-1})*	*C (wt. %)*	*H (wt. %)*	*N (wt. %)*
IT-AC0	0	-	-	65.1	1.93	16.1
IT-AC5	7.2	10	0.01	71.4	0.70	17.5
IT-AC10	30.2	325	0.19	72.4	1.46	17.2
IT-AC20	62.1	792	0.43	73.4	2.03	14.8
IT-AC50	90.1	1049	0.56	71.9	1.77	14.9
IT-ACMAX	365.9	2205	1.20	84.9	2.01	1.29

It was observed that, upon soaking the samples in KOH, the monoliths changed from their original white colouration to an orange/red colour (Figure 4.4.). This was attributed to a base-catalysed intra-molecular cyclisation of the nitrile backbone of the PAN polymer leading to a conjugated ladder-type polymer backbone (Figure 4.5.).(35) This mechanism was likely catalysed by trace DSMO within the polymer; as it was recently shown that DMSO with alkali metal hydroxides will form superbasic dimethyl sulfoxy anions that can nucleophilically attack nitrile groups at room temperature.(36) The darkening of the polymer over time was attributed to an increasing extent of conjugation lowering the band gap between HOMO and LUMO molecular orbitals.(37)

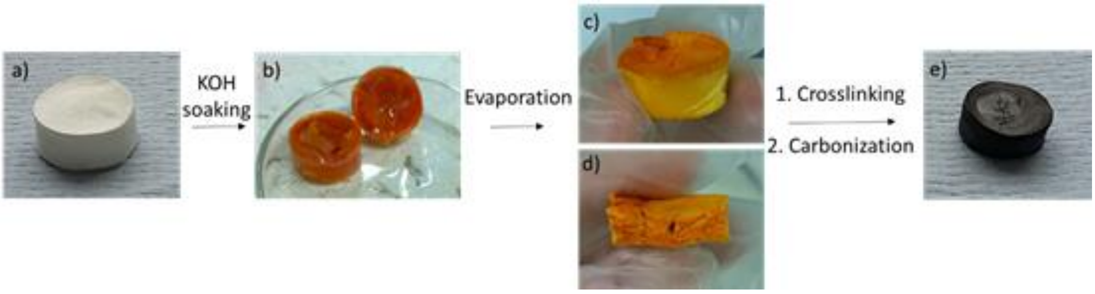

Figure 4.4. a) IT-PAN10 monolith, b) after soaking in 10 mg ml^{-1} aqueous KOH, c) after KOH soaking and drying, d) cross-sectional view after KOH soaking and drying e) after crosslinking and carbonisation (IT-AC10).

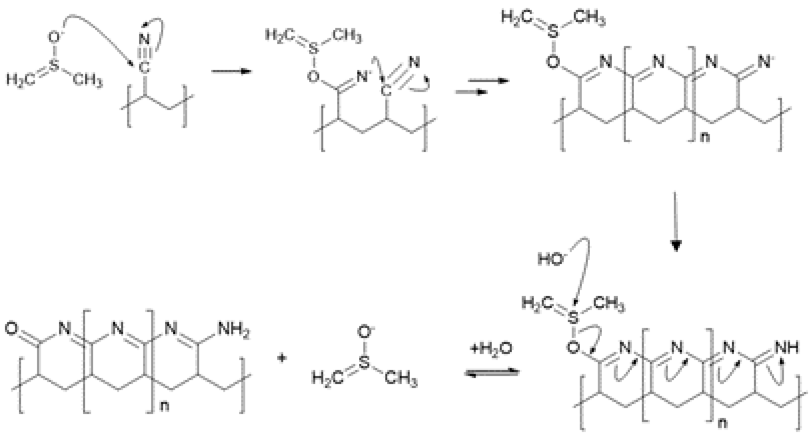

Figure 4.5. Proposed base-catalysed intra-molecular cyclisation of the nitrile backbone of the PAN polymer into a conjugated ladder-type polymer

After KOH infusion and drying, the monoliths were subject to oxidative annealing by heating in a tube furnace to 280 °C in air. This process induces cyclisation and crosslinking of the PAN polymers, increasing their stability and allowing them to retain their morphology and a high yield on carbonisation.(38) The crosslinked precursors were then carbonised by heating to 800 °C under an Ar atmosphere, before being washed with 2M HCl and then thoroughly with water, to remove any residual salts, before being dried in a vacuum oven. The materials IT-AC0, IT-AC50 and IT-ACMAX were subject to TGA in air to determine the residual ash content, which was found to be 1.0 %, 3.5 % and 2.6 %, respectively (Figure Apx.2.).

After carbonisation, the monoliths were imaged *via* FE-SEM, which confirmed the retention of the ice-templated morphology (Figure 4.6.). As a representative example, IT-AC20 was imaged in detail, and displayed aligned, ice-templated macropores pores with a broad size distribution, spanning 100 nm to over 100 µm (Figure 4.7.). Cryogenic freezing would have produced smaller and more monodisperse pores,(39) however freezing at -18 °C in a freezer was employed for these experiments to demonstrate the green credentials of this process.

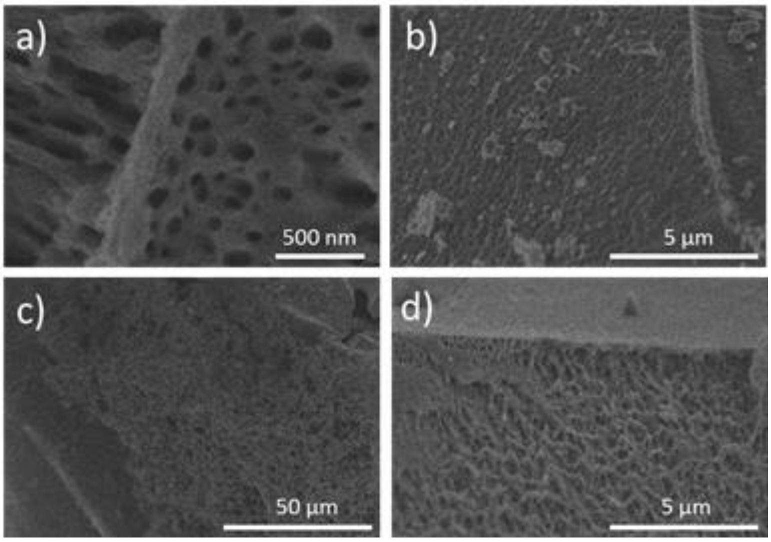

Figure 4.6. FESEM images of a) IT-AC5, b) IT-AC10, c) IT-AC50 and d) IT-ACMAX

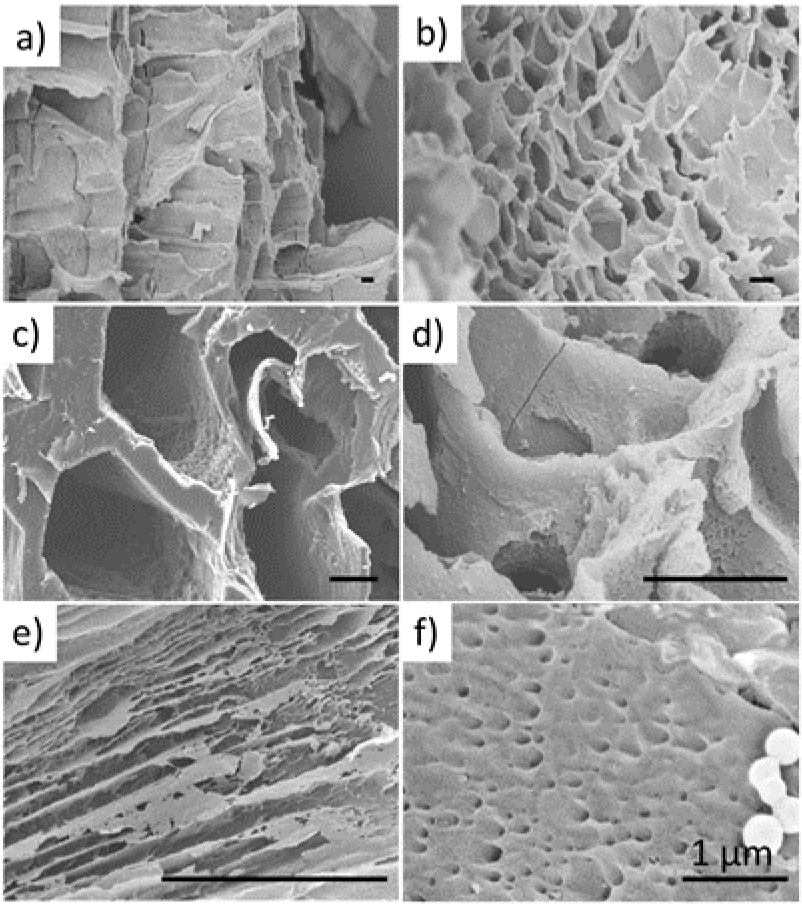

Figure 4.7. SEM images of IT-AC20 at various magnifications: a) x300, b) x700, c) x1400, d) x3700 e) x6500 f) x30000 magnification. Scale bar = 10 µm unless otherwise indicated

N_2 gas sorption measurements were performed on the samples to examine how the porosity and surface area varied with KOH uptake (Figure 4.8.). The measurement failed for the non-activated, control sample (IT-AC0) – likely due to the surface area being too low for an accurate measurement. The measurement was successful for the other samples however, which had isotherms that can be categorised as type I(b) according to IUPAC nomenclature,(40)(41) indicating a microporous structure with fairly broad pore size distributions and some small mesopores. Samples IT-AC50 and IT-ACMAX also displayed small hysteresis loops at high partial pressures, indicating the presence of mesopores with sizes above 4 nm where capillary condensation of the N_2 has been occurring.(41) Analysis of the isotherms showed that the BET surface area increased with increasing KOH uptake, suggesting a greater degree of activation with higher KOH content. With the highest KOH content, IT-ACMAX had the highest BET surface area at 2205 m^2 g^{-1}. BJH pore size analysis showed the majority of pores for the highly activated samples being in the micropore (sub 2 nm) domain, with a clear trend of an increasing micropore volume with increasing KOH content. This analysis also revealed the presence of mesoporous, mainly between the size range of 10 – 30 nm, indicating a hierarchical micro-, meso- and macro- pore structure.

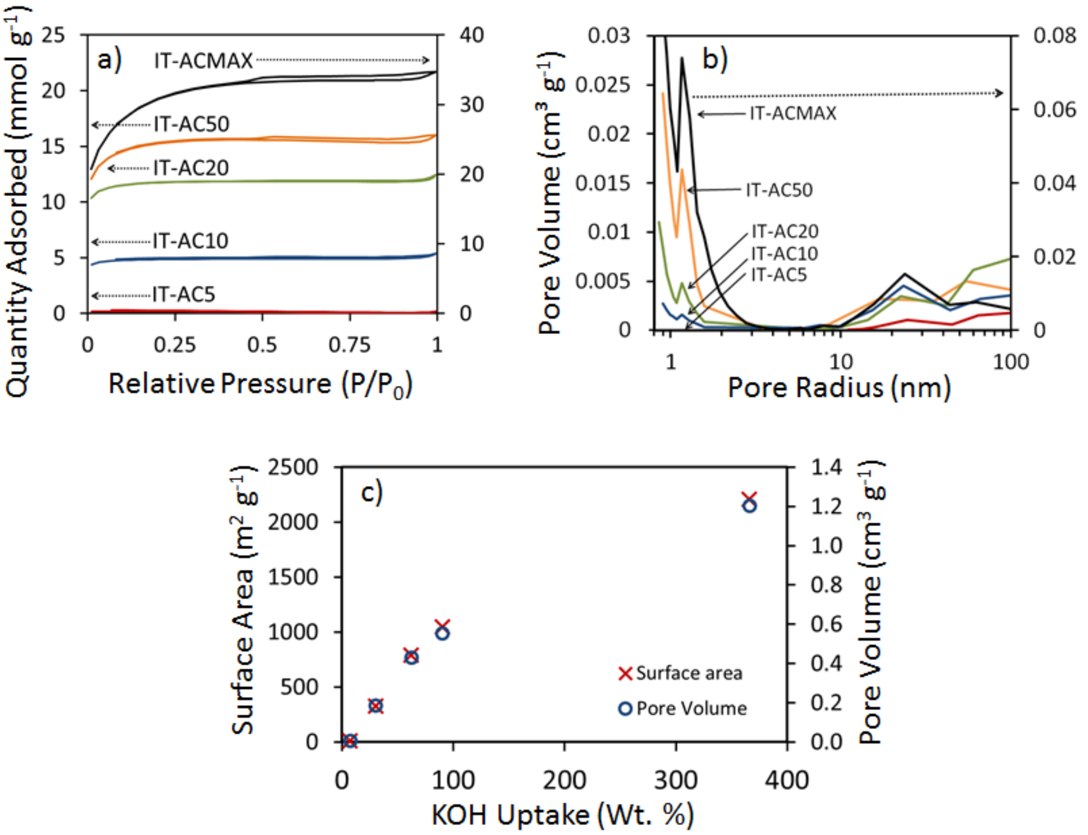

Figure 4.8. Gas sorption data for the IT-ACs: a) isotherms, b) pore size distribution charts and c) relationship between KOH uptake in porous polymer with surface area and pore volume

PXRD and Raman measurements were taken to study the nanostructure and crystallinity of the carbons (Figure 4.9.). PXRD revealed two broad Bragg reflections at approximately 25 and 44°, which were attributed to the (002) and (101) reflections typically observed for microcrystalline, semi-graphitic carbons. The average size parameters of the microcrystallites

(L_c and L_a) were calculated by employing the Scherrer equation, and the average interlayer spacing of adjacent graphite sheets was calculated by employing the Bragg equation (Table 4.2.). The data does not show a large difference between samples, indicating that the degree of KOH activation does not significantly affect the nanostructure of the carbons. First order Raman spectroscopy revealed two peaks at approximately 1340 and 1590 cm^{-1}, the former corresponding to the A_{1g} mode associated with defects in the carbon structure (D-band) and the latter corresponding to the E_{2g} mode of graphitic carbon (G-band).(42) The ratio of the intensity of the D- and G- bands (I_D/I_G) for the carbons was calculated and is presented in Table 4.2. As with PXRD, no clear trend between KOH uptake and these parameters were observed.

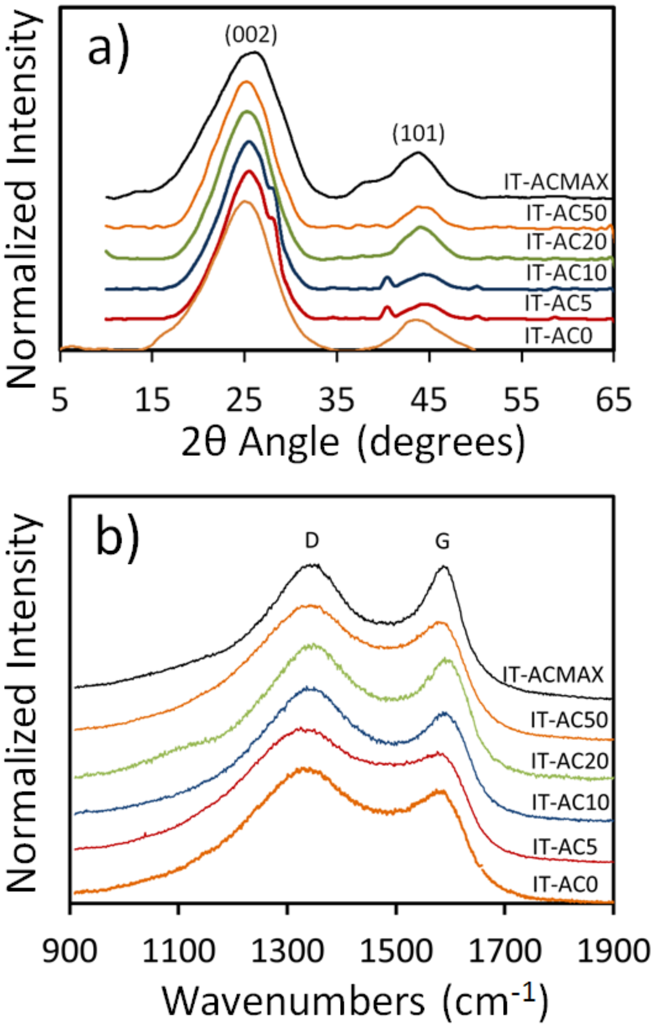

Figure 4.9. a) XRD and b) Raman data for the IT-AC samples

Table 4.2. Summary of XRD and Raman data for the IT-ACs

Sample	L_c (Å)	L_a (Å)	d_{002} (Å)	*Sheets per crystallite*	I_D/I_G
IT-AC0	21.15	29.90	3.562	5.96	1.128
IT-AC5	24.46	35.22	3.494	7.00	1.220
IT-AC10	23.94	33.94	3.527	6.79	1.234
IT-AC20	22.64	35.44	3.530	6.41	1.095
IT-AC50	23.30	46.30	3.465	6.72	1.142
IT-ACMAX	19.71	26.99	3.410	5.78	1.012

CHN elemental analysis and XPS were employed to investigate the elemental content of the samples. The results of the elemental analysis are given in Table 4.1. and show high N contents (15 – 17 wt. %) for all samples other than IT-ACMAX, which had a much lower N content at 1.29 wt. %. This decrease in N content could be attributed to the oxidative nature of the KOH activation agent, which at high concentrations preferentially reacts with the relatively less stable C-N bonds over C-C bonds, resulting in a lower N content. The same trend was also observed with XPS, which detected 10 – 15 At. % N for all samples other than IT-ACMAX – for which it detected zero (Figure 4.5). Due to the quantitative nature of the CHN elemental analysis, it was taken as the more reliable measurement for bulk N content within the samples (XPS is a surface specific technique). The N1s spectrum of the XPS was analysed in order to determine the chemical environment of the N within the IT-ACs (Figure 4.5, inset). Each sample, other than IT-ACMAX, could be fitted into two component peaks at approximately 398 and 401 eV, corresponding to pyridinic and quaternary nitrogen, respectively. The relative ratios of the peaks are reported in Table 4.3, which show little change as KOH uptake increases from minimal loading (IT-AC5) to high loading (IT-AC50).

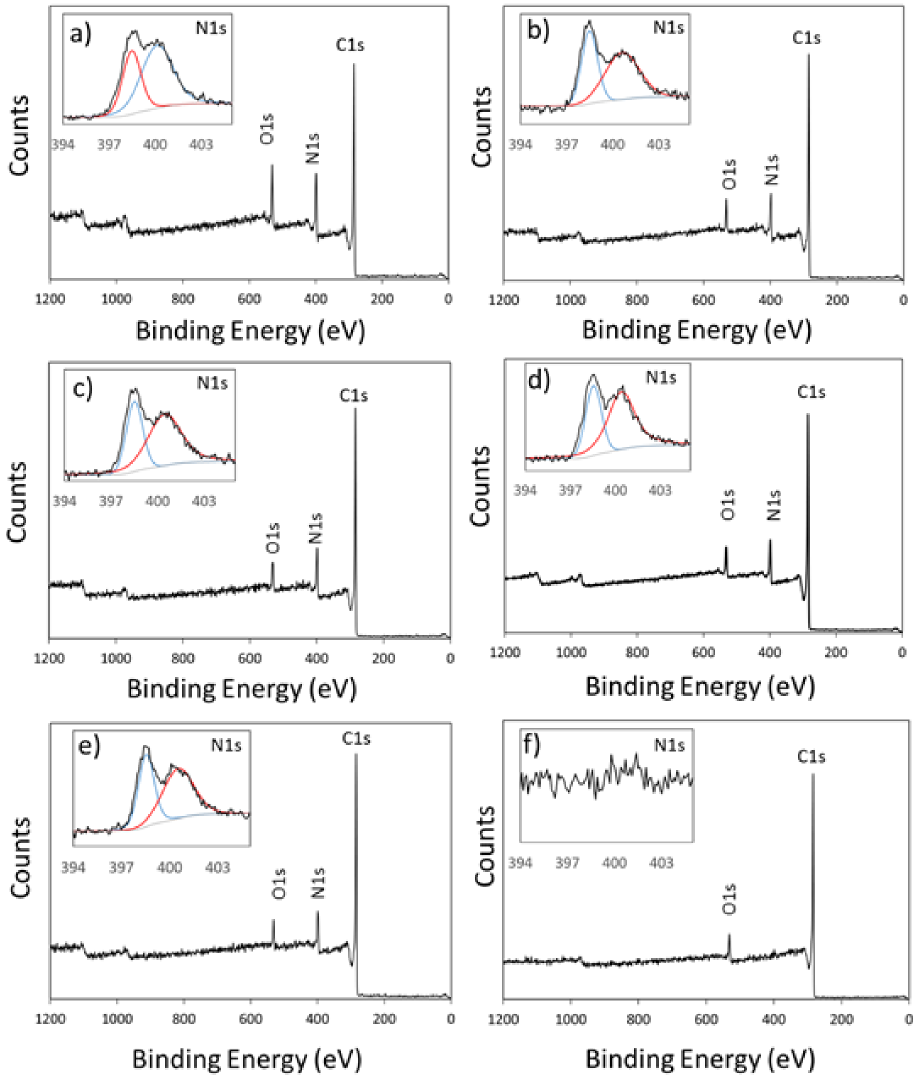

Figure 4.10. XPS data for a) IT-AC0, b) IT-AC5, c) IT-AC10, d) IT-AC20, e) IT-AC50 and f) IT-ACMAX, with N1s scans inset

4.4.2. CO_2 Uptake Performance

A CO_2 uptake study of the IT-ACs was performed at conditions of 298 °C and 10 bar pressure, the results of which are presented in Figure 4.11. and Table 4.3. It can be seen that as the soaking concentration of KOH increases, the CO_2 uptake also increases in a roughly linear fashion, up to a maximum of 16.12 mmol g^{-1} for sample IT-AC50. However, for the sample with the highest KOH loading (IT-ACMAX), the CO_2 uptake drops to 11.19 mmol g^{-1}. This trend can be explained by the change in surface areas and N content as the KOH loading increases: for samples IT-AC5, IT-AC10, IT-AC20 and IT-AC50, the increased KOH loading increases the surface area whist only having a minor effect on the N content. The increasing surface area provides a greater area for the physisorption of CO_2 molecules and thus the CO_2 adsorption is increased. However, for the IT-ACMAX sample, although the surface area is over twice as high as the IT-AC50 sample, the N content is significantly lower (1.29 wt. %, vs. 14.9 wt. %). Since a high N content improves CO_2 adsorption, *via* the Lewis acid-base interaction of the lone pair of electrons on N with acidic CO_2,(17) it results in a lower CO_2 adsorption overall. The shapes of the CO_2 sorption isotherms also suggest different mechanisms occurring between the samples: whilst the IT-AC50 sample has a very reversible adsorption-desorption cycle, IT-ACMAX has significant hysteresis suggesting retention of CO_2 after the pressure drops. The adsorption of 16.12 mmol g^{-1} for the IT-AC50 sample is very high in comparison to previous literature reports under similar conditions, as can be seen in Table 4.4. Table 1.6. in the introduction also compares the performance of the material with other templated carbons reported in the literature. Moreover, the highly reversible sorption characteristics as indicated by the shape of the isotherm would allow facile regeneration of the materials. There is scope for even higher adsorption at further increased pressures as the isotherm for IT-AC50 has yet to plateau even at 10 bar.

Table 4.3. Summary of the XPS, and CO_2 and H_2 adsorption data for the IT-ACs

KOH conc. (wt. %)	*C (wt. %)*	*N (wt. %)*	*O (wt. %)*	*Pyridinic (%)*	*Quaternary (%)*	*CO_2 uptake (mmol g^{-1})*	*H_2 uptake (wt. %)*
0	76.91	12.13	10.96	63.2	36.8	2.81	0.45
5	81.79	12.36	5.85	41.8	58.2	3.43	0.844
10	80.68	14.59	4.73	37.6	62.4	4.13	0.834
20	82.91	11.34	5.76	37.9	62.1	7.71	No data
50	87.29	10.34	2.38	43.1	56.9	16.12	1.30
MAX	95.06	0	4.94	0	0	11.19	2.66

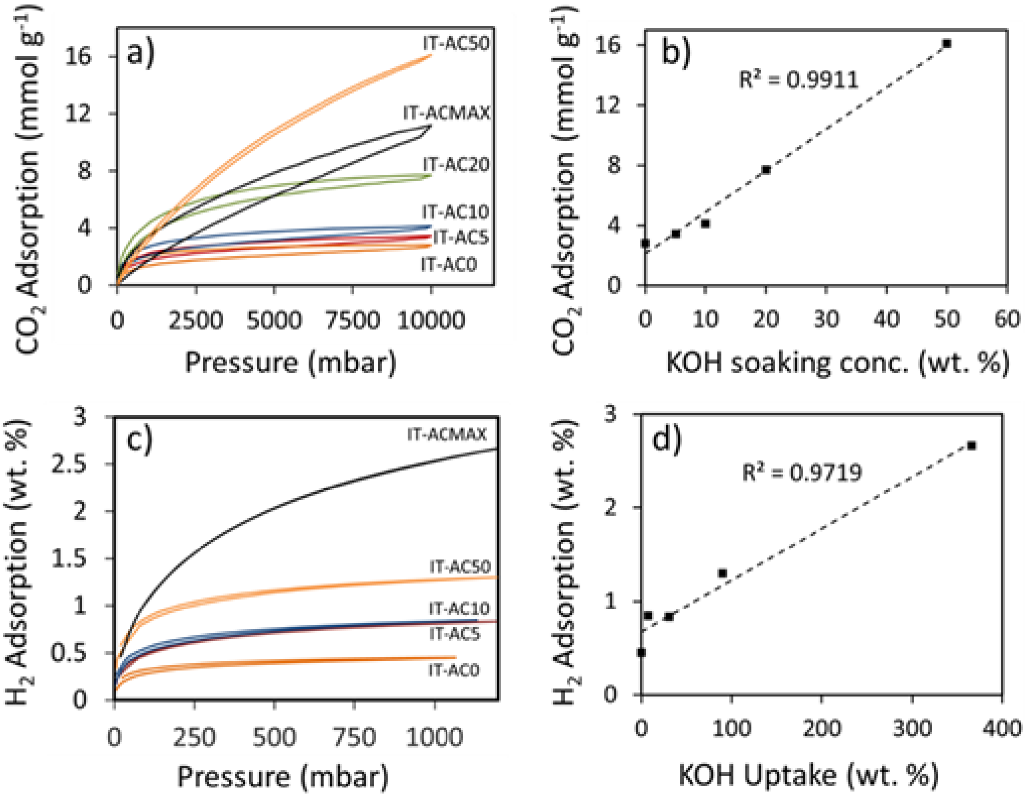

Figure 4.11. a) CO_2 adsorption isotherm, b) relationship between CO_2 adsorption and KOH soaking concentration, c) H_2 adsorption isotherms and d) relationship between H_2 adsorption and KOH uptake in the ice-templated porous polymers

Table 4.4. Comparison of CO_2 uptake performances of various materials under similar test conditions

Material	*BET Surface area (m^2 g^{-1})*	*N content (wt. %)*	*CO_2 Adsorption (mmol g^{-1})*	*Test Conditions*	*Ref.*
Direct carbonization of MOF-5	2734	N/A	12.5	300 K, 10 bar	(16)
Mesoporous silica (IBN-9) templated & activated carbon	1181	13	10.5	298 K, 10 bar	(47)
Carbonized polyaniline cryogel	4196	0.55	14.5	298 K, 10 bar	(48)
MOF-205	4460	0	10.9	298 K, 10 bar	(49)
COF-102	3620	0	15.5	298 K, 10 bar	(8)
Porous polymer network (PPN)-4	6461	0	11.6	295 K, 10 bar	(50)
Carbonized hyper-crosslinked porous polymer Py800	4334	1.42	22.0	298 K, 10 bar	(51)
Porous carbon via ice-templating and KOH activation	1049	14.9	16.1	298 K, 10 bar	This Work

4.4.3. H_2 Uptake Performance

A H_2 uptake study of the IT-ACs was also performed at 77 K and 1.2 bar pressure (Figure 4.11. and Table 4.3). This showed a roughly linear increase between KOH uptake and H_2 adsorption, with a maximum of 2.66 wt. % H_2 adsorption for the IT-ACMAX sample. The shape of the isotherm for this sample indicated that it had not yet reached saturation at 1.2 bar, meaning even higher uptake capacities could be achieved at higher pressures. The isotherms also did not exhibit any hysteresis effects, meaning the H_2 uptake of the materials was reversible. Unlike the CO_2 uptake study, H_2 adsorption was much less dependent on the N content of the sample, but instead had a fairly linear relationship with surface area. This is in concordance with other reports which also conclude that surface area is the most important property for maximising H_2 adsorption.(11)

A comparison of the performance relative to other previously reported templated carbons is given in Table 1.5. in the introduction. It can be seen that materials tested under similar conditions (~1 bar, 77 K) have comparable H_2 uptake capacities of about 2 – 3 wt. %. For instance, Mokaya and co-workers reported a H_2 uptake capacity of 2.6 wt. % for a templated carbon prepared from a zeolite-β template and an acetonitrile carbon precursor.(43) In a another report they showed that the chemical activation of a zeolite-Y templated carbon would increase its H_2 sorption capacity to about 2.6 wt. % also.(24)

4.4.4. Supercapacitor Performance Evaluation

A supercapacitor is a device which stores energy through the formation of electrostatic double layers at the interface of its electrodes and an ionic electrolyte.(44) ACs are the most widely used electrode materials for supercapacitors due to their high surface areas, relatively low cost chemical stability and adequate electrical conductivity.(11)(45) ACs, as well other high-surface area carbon materials, with a high level heteroatom doping have also been shown to display superior performance as supercapacitor electrode materials compared with their un-doped counterparts.(11)

Having the highest specific surface areas of the prepared materials, the electrochemical behaviour of the samples IT-AC50 and IT-ACMAX were studied by cyclic voltammetry (CV) to assess their performance as supercapacitor electrode materials. Figure 4.12. shows the resulting CVs at potential scan rates of 10, 25 and 100 mVs^{-1}. It can be seen that at a scan rate of 100 mV s^{-1} the IT-ACMAX sample displays the typical rectangular shape which is characteristic of electrochemical double-layer capacitance behaviour.(44) At the lower scan rate of 10 mV s^{-1} the curve deviates from the idealised shape however – displaying a redox couple at ~0.2 V which was attributed to oxygen containing functional groups on the carbon surface. The IT-AC50 sample showed very different behaviour on the other hand; here distinct redox couples were observed at ~0.2 and -0.3 V, and the characteristic rectangular shape associated with supercapacitive behaviour was distorted even at the relatively fast sweep rate of 100 mV s^{-1}. These peaks were associated with charge-transfer reactions between the oxygen- and nitrogen-containing functional groups on the surface of the carbon, indicating a degree of pseudocapacitance occurring.(46) The values for gravimetric capacitance were calculated by employing Eq. 26. on the CV curves, however the obtained values were relatively poor at 24.2 and 11.6 F g^{-1} for the IT-ACMAX and IT-AC50 samples, respectively, at the slow sweep rate of 10 mV s^{-1}. This performance is an order of magnitude lower than for similar materials published in the literature (Table 1.4.) and so a more in-depth electrochemical study was not performed.

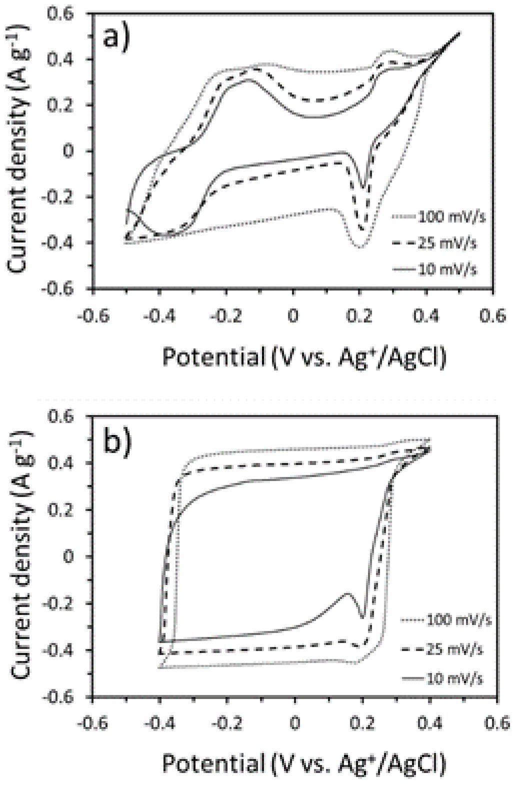

Figure 4.12. CV curves for a) IT-AC50 and b) IT-ACMAX at sweep rates of 10, 25 and 100 mV s^{-1}

4.5. Other activating agents

Although KOH is the most common chemical activating agent, other compounds such as $ZnCl_2$, $AlCl_3$, $MgCl_2$, NaOH among others can also be employed.(11) To demonstrate the versatility of our approach and to see if similar trends could be observed, the process was repeated using Na_2SO_4, Li_2SO_4 and K_2HPO_4 as the activating agents. These compounds were selected as it was hypothesised that they would introduce other heteroatoms (S and P) into the carbon matrix to co-dope with the N.

To achieve this, PAN10 monoliths were soaked in aqueous solutions of the salts at concentrations of 10, 20 and 30 w/v % and left stirring for 2.5 hours, before being removed from the solutions and dried in a vacuum oven at 60 °C. These samples were termed [X]-10, [X]-20 and [X]-30 respectively, where X is the chemical formula of the activating agent employed. Additionally, one sample was soaked in a 30 w/v % solution and left stirring at 60 °C for 24 h to maximise the salt uptake, this sample was termed [X]-MAX. The salt-loaded samples were then subject to oxidative annealing at 280 °C before carbonization at 800 °C under the same conditions as for the KOH-loaded samples. After carbonization, the materials were subject to an acid wash and three water washes to remove the residual salts and impurities. The carbonized and acid-washed samples were denoted [X]-[n]-C, where X is the chemical formula of the activating agent employed and n is the concentration of the salt soaking solution in w/v %. A TGA of the Na_2SO_4-MAX-C sample in air showed a residual ash content of 3.4 %, indicating that the majority of salts has been removed by the washing step (Figure Apx.3.).

SEM images of the carbonized samples revealed that the ice-templated macropores had been retained on carbonization (Figure Apx.4.). However, N_2 gas sorption revealed that only the Na_2SO_4-activated sample had attained a significant surface area increase – suggesting that the Li_2SO_4 and K_2HPO_4 had failed as activating agents (Figure Apx.5.). For the Na_2SO_4-asctivated sample, the gas sorption revealed similar shaped isotherms for each sample, which could be classified as type I(b) with a H1 hysteresis loop according to the IUPAC classification system.(40)(41) BET surface area values and pore volumes were calculated from the isotherms and are presented in Table 4.5. – here it can be seen that the highest surface area (620 m^2 g^{-1}) is significantly lower that the highest surface area for the KOH-activated samples (2206 m^2 g^{-1}). PXRD measurements revealed the characteristic (002) and (101) Bragg reflections associated with semi-graphitic carbons, with little change with increasing Na_2SO_4 uptake (Figure Apx.6.). CHNS analysis revealed relatively high N contents (12 – 15 wt. %) for the samples, along with a degree of S-doping (~5 %). Although the co-doping of N and S may infer useful properties to the carbon, the relatively low surface area for an activated carbon would likely make these materials perform poorly as supercapacitor electrodes or gas storage materials.

Table 4.5. Relationship between Na_2SO_4 soaking concentration and KOH uptake, BET surface area and CHNS elemental content

Material	*Mass Na_2SO_4 to PAN (wt. %)*	*BET Surface area (m^2 g^{-1})*	*Pore volume (cm^3 g^{-1})*	*C (wt. %)*	H *(wt. %)*	*N (wt. %)*	*S (wt. %)*
Na_2SO_4-10	30.1	97	0.07	66.0	1.2	15.5	4.4
Na_2SO_4-20	49.3	265	0.16	62.8	1.6	14.5	5.1
Na_2SO_4-30	77.2	594	0.38	68.2	1.7	13.7	4.7
Na_2SO_4-MAX	147.4	620	0.39	64.2	1.9	12.5	4.8

4.6. Conclusions and Remarks

In conclusion, we have demonstrated a relatively facile and green method for the preparation of hierarchically porous, templated carbons *via* an ice-templating and chemical activation process. The degree of activation, and hence surface area and N content, could be varied by simply changing the concentration of the initial KOH solution in which the monoliths were soaked. The material with the highest degree of activation (IT-ACMAX) had a surface area of 2205 m^2 g^{-1}, an N content of 1.29 wt. % and had the highest H_2 adsorption at 2.66 wt. % at 77 K and 1.2 bar. The material with the highest CO_2 adsorption (IT-AC50) had both a high surface area (1049 m^2 g^{-1}) and N content (14.9 wt. %) – with a maximum CO_2 adsorption of 16.12 mmol g^{-1} at 298 K and 10 bar of pressure. This performance is in league with the highest CO_2 uptake materials, despite the relatively facile material preparation process.

4.6. References

1. Haszeldine RS (2009) *Science* 325(5948):1647–1652.
2. D’Alessandro DM, Smit B, Long JR (2010) *Angew Chem Int Ed Engl* 49(35):6058–82.
3. Gibbins J, Chalmers H (2008) *Energy Policy* 36(12):4317–4322.
4. Metz B (2001) *Climate Change 2001: Mitigation: Contribution of Working Group III to the Third Assessment Report of the Intergovernmental Panel on Climate Change* (Cambridge University Press).
5. Jena P (2011) *J Phys Chem Lett* 2(3):206–211.
6. L.J.Murray, M.Dinca JRL (2009) *Chem Soc Rev* 38(5):1294–1314.
7. Sumida K, et al. (2012) *Chem Rev* 112(2):724–81.
8. Furukawa H, Yaghi OM (2009) *J Am Chem Soc* 131(25):8875–8883.
9. Chatti R, et al. (2009) *Microporous Mesoporous Mater* 121(1–3):84–89.
10. Woodward RT, et al. (2014) *J Am Chem Soc* 136(25):9028–9035.
11. Sevilla M, Mokaya R (2014) *Energy Environ Sci* 7(4):1250–1280.
12. Plaza MG, Garcia S, Rubiera F, Pis JJ, Pevida C (2010) *Chem Eng J* 163(1–2):41–47.
13. Radosz M, Hu X, Krutkramelis K, Shen Y (2008) *Ind Eng Chem Res* 47(10):3783–3794.
14. Dantas TLP, et al. (2009) *Sep Sci Technol* 45(1):73–84.
15. Roberts AD, Li X, Zhang H (2014) *Chem Soc Rev* 43(13):4341–4356.
16. Srinivas G, Krungleviciute V, Guo Z-X, Yildirim T (2014) *Energy Environ Sci* 7(1):335–342.
17. Hao GP, Li WC, Qian D, Lu AH (2010) *Adv Mater* 22(7):853–857.
18. Sevilla M, Valle-Vigõn P, Fuertes AB (2011) *Adv Funct Mater* 21(14):2781–2787.
19. Yu J, et al. (2014) *Carbon* 69:502–514.
20. Wang L, Yang RT (2012) *J Phys Chem C* 116(1):1099–1106.
21. Zhou Z, Gao X, Yan J, Song D (2006) *Carbon* 44(5):939–947.
22. Yang Z, Xia Y, Sun X, Mokaya R (2006) *J Phys Chem B* 110(37):18424–18431.
23. Nishihara H, Kyotani T (2012) *Adv Mater* 24(33):4473–4498.
24. Sevilla M, Alam N, Mokaya R (2010) *J Phys Chem C* 114(25):11314–11319.
25. Jiang H-L, et al. (2011) *J Am Chem Soc* 133(31):11854–11857.
26. Lee J-SM, et al. (2016) *J Mater Chem A* 4:7665–7673.
27. Chaikittisilp W, Ariga K, Yamauchi Y (2013) *J Mater Chem A* 1(1):14–19.
28. Nishihara H, Mukai SR, Tamon H (2004) *Carbon* 42(4):899–901.
29. Roberts AD, Wang S, Li X, Zhang H (2014) *J Mater Chem A* 2(42):17787–17796.
30. Roberts AD, Li X, Zhang H (2015) *Carbon* 95:268–278.
31. Zhang H, Cooper AI (2007) *Adv Mater* 19(11):1529–1533.

32. Gutiérrez MC, Ferrer ML, Del Monte F (2008) *Chem Mater* 20(3):634–648.
33. Estevez L, et al. (2013) *Energy Environ Sci* 6(6):1785.
34. Modak A, Bhaumik A (2015) *J Solid State Chem* 232:157–162.
35. Şanli O (1990) *Eur Polym J* 26(1):9–13.
36. Chen H, et al. (2014) *Green Chem* 16(4):2136–2141.
37. Foote HW (1907) *Elements of Physical Chemistry* (OUP Oxford).
38. Rahaman MSA, Ismail AF, Mustafa A (2007) *Polym Degrad Stab* 92(8):1421–1432.
39. Zhang H, et al. (2005) *Nat Mater* 4(10):787–793.
40. Sing KSW, et al. (1985) *Pure Appl Chem* 57(4):603–619.
41. Thommes M, et al. (2015) *Pure Appl Chem* 87(9–10):1051–1069.
42. Wang Y, Alsmeyer DC, Mccreery RL (1990) *Chem Mater* 2(5):557–563.
43. Yang Z, Xia Y, Mokaya R (2007) *J Am Chem Soc* 129(6):1673–1679.
44. Lu M, Beguin F, Frackowiak E (2013) *Supercapacitors: materials, systems and applications* (John Wiley & Sons).
45. Zhang LL, Zhao XS (2009) *Chem Soc Rev* 38(9):2520–2531.
46. Deng Y, Xie Y, Zou K, Ji X (2015) *J Mater Chem A* 4(4):1144–1173.
47. Zhao Y, et al. (2012) *J Mater Chem* 22(37):19726–19731.
48. He J, et al. (2016) *Adv Energy Mater* 6(14):1502491.
49. Furukawa H, et al. (2010) *Science* 329(5990):424–428.
50. Yuan D, Lu W, Zhao D, Zhou HC (2011) *Adv Mater* 23(32):3723–3725.
51. Lee JSM, Briggs ME, Hasell T and Cooper AI (2016) *Adv Mater* 28(44):9804–9810

Chapter 5

Sulfur-infused Porous Carbons *via* Ice-templating and *in-situ* Activation

The contents of this chapter have been published in the journal *Carbon*
(A. D. Roberts *et al.*; *Carbon*, **2015**, 95, 268-278)

List of Figures

List of Tables

5.1. Background and Context

In Chapter 3, a method was presented for the preparation of ITPCs by employing PAN, a well-known and widely used carbon precursor, as a starting material prior to ice-templating, crosslinking and carbonisation. In this chapter, it will be shown how another polymeric precursor, the ionomer sodium poly(sodium 4-styrenesulfonate) (PSS), can also successfully be subject to ice-templating and carbonisation. Interesting features, such as the non-requirement of a separate crosslinking step, high specific surface areas, and infusion of elemental sulfur (S) within the micropores were observed and investigated. To account for these observations, a detailed comparison of previous literature reports was made and our own mechanistic explanation was devised. The materials were optimised to maximise the S content before being evaluated for as Lithium-Sulfur (LIS) battery cathode materials.

5.2. Introduction

LIS batteries, if successfully commercialised, could prove to be high-performance and low-cost alternatives to established LIB technology.(1)(2) Although the operating voltage of LIS batteries would be lower than that of LIBs (2.2 V vs. 3.7 V), by employing a metallic lithium anode and a sulfur based cathode, energy densities over four times that of current LIBs (1700 vs. 410 Wh Kg^{-1}) can theoretically be obtained.(2) Li-S battery technology faces a number of significant hurdles before it can be considered commercially viable however, many of which are related to the sulfur-based cathode. The poor electrical conductivity of S and the discharge product Li_2S ($5x10^{-30}$ S cm^{-1} and ~$1x10^{-13}$ S cm^{-1}, respectively), destructive volumetric expansion upon lithiation and the solubility of Li_2S_x intermediates in organic electrolytes are significant issues that need to be addressed before LIS technology can be successfully adopted.(1)(2) One potential solution to these problems is the use of porous carbon-sulfur composites as cathode materials, where the carbon framework acts as a conductive support for S and mechanical buffer as it undergoes volumetric expansion, whilst also restricting the diffusion of Li_2S_x intermediates and maintaining good access of Li-ions *via* efficient diffusion through the porous network.(1)(2)(3)(4)(5)(6)(7)(8)(9)(10)(11)

The first significant example of a porous carbon-sulfur composite being utilised as a LIS battery cathode material was demonstrated by Nazar and co-workers in 2009.(11) By incorporating S within the pores of a mesoporous-silica (SBA-15) templated porous carbon (CMC-3) *via* a simple melt-infusion method, S loadings as high as 70 % could be obtained with excellent battery performance (C_{rev} up to 1320 mA h g^{-1}). Another notable example is the recent report by Ionov and co-workers, who melt-infused S within a macroporous PMMA colloidal-crystal templated carbon, attaining a C_{rev} of 1600 mA h g^{-1} as a LIS battery cathode material.(5) Table 1.3. compares a number of other carbon-S composites and their performance as LIS cathode materials. Despite the impressive performances of these examples and others, the relatively complex, multi-step synthesis routes, which involve sacrificial hard or soft templates as well as a post-infusion of sulfur step, erode the merits of these processes in terms of its cost-effectiveness and green credentials. Therefore, a relatively simple and green synthesis route for the fabrication of S-infused templated porous carbons is desirable.

Ice-templating is a relatively facile and green strategy for the fabrication of templated porous materials, in particular porous polymers.(12)(13) The carbonisation of ice-templated structures is challenging however, since the absence of a rigid template or chemical crosslinking, the physically bound polymer matrix may be lost through melting, foaming, decomposition or destructive volumetric shrinkage during high temperature treatment.(14)(15) Due to this difficulty, relatively few examples of ITPCs have been reported in the literature.(15)(16)(17)(18)(19)(20)

In this chapter, it is shown how a simple ice-templating and one-step pyrolysis method of the ionomer PSS leads to hierarchically porous S-infused activated carbons (ACs) (Figure 5.1.). Aligned macropores are introduced from the ice crystal templates, before the one-step thermal treatment process induces crosslinking with the *in-situ* generation of the activating agent Na_2SO_4 at ~400 °C, with carbonisation and activation upon continued heating to 800 °C. S, which was formed after a simple acid wash after carbonisation, was found to reside within the micropores of the material – the content of which was determined to be 14.0 % by TGA. Mechanisms which account for these observations are discussed in detail, and compared with similar literature reports and mechanisms proposed by other authors. The S content could be increased to 39.7 % with the incorporation of additional Na_2SO_4 prior to pyrolysis, and the optimised materials were evaluated for their potential as cathode materials for the Li-S battery.

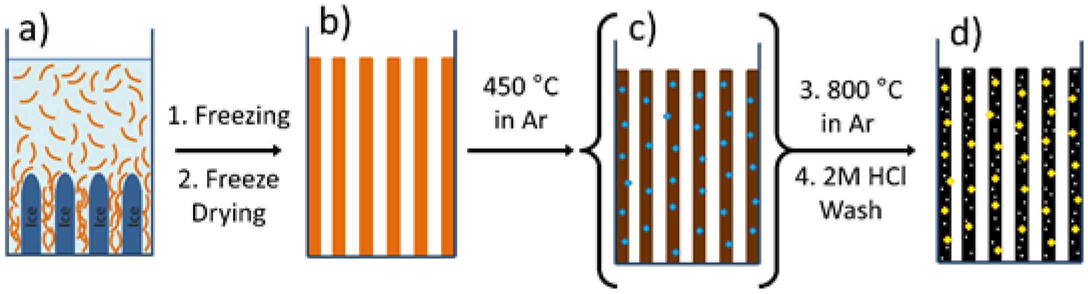

Figure 5.1. Schematic representation of the process to prepare the hierarchically porous S-infused activated ITPCs. a) Aqueous PSS solution, b) ice-templated porous PSS, c) crosslinked PSS with generated Na_2SO_4, d) S-infused, activated ITPC

5.3. Experimental

5.3.1. Chemical Reagents

Sodium poly(4-styrenesulfonate) (PSS, MW 70,000), sodium sulfate (>99.0 %, anhydrous), polyvinylidene fluoride (PVDF), N-methyl pyrrolidinone (NMP), lithium bis(trifluoromethane sulfonyl) imide, 1,3-dioxolane (99.8 %, anhydrous), dimethoxyethane (99.5 %, anhydrous), ethylene carbonate (anhydrous, 99 %), dimethyl carbonate (anhydrous, >99 %), lithium hexafluorophosphate (battery grade, ≥99.99) and $LiNO_3$ (anhydrous, 99 %) were purchased from Sigma Aldrich and used without additional purification. Super-P® carbon back was purchased from Timcal. GPR grade solvents, hydrochloric acid and deionised water were used routinely as required.

5.3.2. Preparation of Materials

Preparation of S-infused Activated ITPCs

In a typical procedure, PSS was dissolved in DI H_2O at a concentration of 150 mg ml^{-1} under stirring at room temperature. 1.5 ml aliquots of the aqueous solution were then transferred to 10 mm x 75 mm borosilicate glass test tubes (Fischer Scientific) before being immersed into a bath of liquid nitrogen at a rate of 5 – 10 mm min^{-1}. The frozen samples were then transferred to a Vitris Advantage Benchtop Freeze Drier and subject to lyophilisation for ~48 h, giving the dry, ice-templated PSS monoliths.

Carbonisation of the ice-templated PSS monoliths was achieved by heating the samples in a Carbolite ® horizontal compact tube furnace to 800 °C under an Ar atmosphere (heating rate 5 °C min^{-1}), before holding at that temperature for 2.5 h and then being allowed to cool naturally to room temperature. The carbonised samples were then removed from the furnace and subject to an acid wash (2M HCl) to remove residual salts and induce precipitation of the S. After the acid wash, the samples were rinsed with DI water 3 times to ensure removal of any remaining salts. The washed samples were then dried in a vacuum oven at 60 °C overnight.

5.3.3. Characterisation

Materials Characterisation

Oxygen-free thermogravimetric analysis (TGA) measurements was carried out using a Q5000IR TGA from TA instruments with an automated vertical overhead balance. Measurements were performed by heating the sample specimens at a rate of 5 °C min^{-1} to 1000 °C under a N_2 atmosphere for non-carbonised samples, and at 20 °C min^{-1} to 600 °C for carbonised samples. Oxidative TGA measurements were conducted on a TA Instruments SDT Q600 TGA instrument with a constant air flow of 50 mL min^{-1}. Samples were heated to 1000 °C at a heating rate of 20 °C min^{-1}. Sample morphology was determined *via* scanning electron microscopy (SEM) using a Hitachi S-4800 SEM, with samples adhered to Hitachi M4 aluminium stubs with conductive carbon tape. Non-conducting samples were additionally sputter-coated with a thin layer (~2 nm) of gold using an Emitech K550X automated sputter coater. Some samples were additionally imaged using a JSM-6700F FE-SEM to obtain high-resolution images. The microstructure of the carbon materials was imaged using a JEOL 2100 LaB_6 transmission electron microscope (TEM) at a working voltage of 200 kV. Fourier transform infrared spectroscopy (FTIR), employing a PerkinElmer Spectrum 2000 instrument, was employed to characterise the functional groups and crystalline species within the carbonised materials. Energy dispersive X-ray (EDX) spectroscopy was carried out on the JSM-6700F FE-SEM, where the working voltage was 10 kV and working distance was 15 mm. Brunauer–Emmett–Teller (BET) specific surface areas, Barrett-Joyner-Halenda (BJH) pore volumes and Density Functional Theory (DFT) pore size distributions were obtained by N_2 gas sorption at 77 K using a Micromeritics ASAP 2420 volumetric adsorption analyser. A pressure range of 0.01 – 0.1 P/P0 was taken for calculation of the BET surface areas and BJH pore volumes were given by the total single point adsorption of pores between 1.7 and 300 nm width at $P/P_0 = 1$. Samples were degassed for 24 h prior to measurement at the temperatures of 150, 200, 250 and 300 °C. Pore volumes and size distributions up to 200 µm were obtained by Hg-intrusion porosimetry using a Micromeritics Autopore IV 9500 porosimiter. Powder X-ray diffraction (PXRD) patterns were obtained using a Bunker GADDS XRD system with a Cu K-α radiation source. Crystalline species were identified by PXRD by comparison of the obtained patterns with the JCPDS database. Raman spectra were recorded using a Renishaw InVia Raman Microscope fitted with a 633 nm laser, calibrated against a silicon wafer reference. The surface chemistry of the samples was studied on a VG ESCA LAB-220i XL X-ray photoelectron spectrometer (XPS) with an exciting source of Al. CHNS elemental analysis was performed using a Flash EA 1112 Series CHNS Analyser using cysteine sulfanilamide methionine (BBOT) as a standard and 8 x 5 mm pressed Sn capsules to contain sample specimens.

Electrochemical (LIS battery) evaluation

The electrochemical performance of the materials as LIS battery electrodes was evaluated by cyclic voltammetry (CV) and constant current potentiometry (CCP) measurements using an Autolab PGSTAT302 workstation and NEWARE battery tester, respectively. The electrodes were fabricated by coating a slurry of the active material (80 wt. %), carbon black (10 wt. %) and polyvinylidine fluoride (PVDF) (10 wt. %) in N-methyl pyrrolidone onto an aluminium foil current collector, before drying under vacuum at 80 °C overnight. The dried electrode and Al current collector was then punched into 1 cm^3 disks (approx. 3 mg active material per disk) and assembled into 2032 button cells in an Ar-filled glove box with Li foil, a Celgard 2325 membrane and approximately 70 μL of 1 M Lithium bis(trifluoromethane sulfonyl) imide ($LiPF_6$) in 1,3-dioxolane/dimethoxyethane (1:1 v/v ratio) with 5 wt. % $LiNO_3$ as the counter electrode, separator and electrolyte, respectively. The current density for the CCP measurements was 100 mA g^{-1} and the voltage cut-off window was 2.0 – 2.6 V vs. Li/Li^+. The CV measurements also had a voltage window of 1.9 – 2.7 V vs. Li/Li^+ and a scan rate of 50 μV s^{-1}. When potentials < 1.9 V were employed, large, irreversible reduction peaks occurred which were attributed to the reduction of $LiNO_3$ in the electrolyte. This resulted in large irreversible capacity and poor subsequent cycling stability. CV had a slightly broader voltage window (0.1 V at +ve and –ve end) than CCP to ensure the peaks were not cut off prematurely.

5.4. Results and discussion

The initial ice-templated PSS porous polymer monoliths were prepared by directional submersion of aqueous PSS solutions into a liquid N_2 bath prior to freeze-drying. Initial solution concentrations of 50, 100, 150, 200 and 250 mg cm^{-3} gave stable, monolithic structures – whilst solution concentrations below 50 mg ml^{-1} were brittle and difficult to handle. When viewed by SEM, the stable ice-templated monolith structures displayed aligned macropores typically observed for ice-templated structures (Figure 5.2.).(12)(13) For this investigation, we focussed on the material prepared from a solution concentration of 150 mg ml^{-1} as a representative sample. This concentration was selected as it had good mechanical stability allowing for easy handling, and for its well defined ice-templated morphology as viewed under SEM (Figure 5.3. a)).

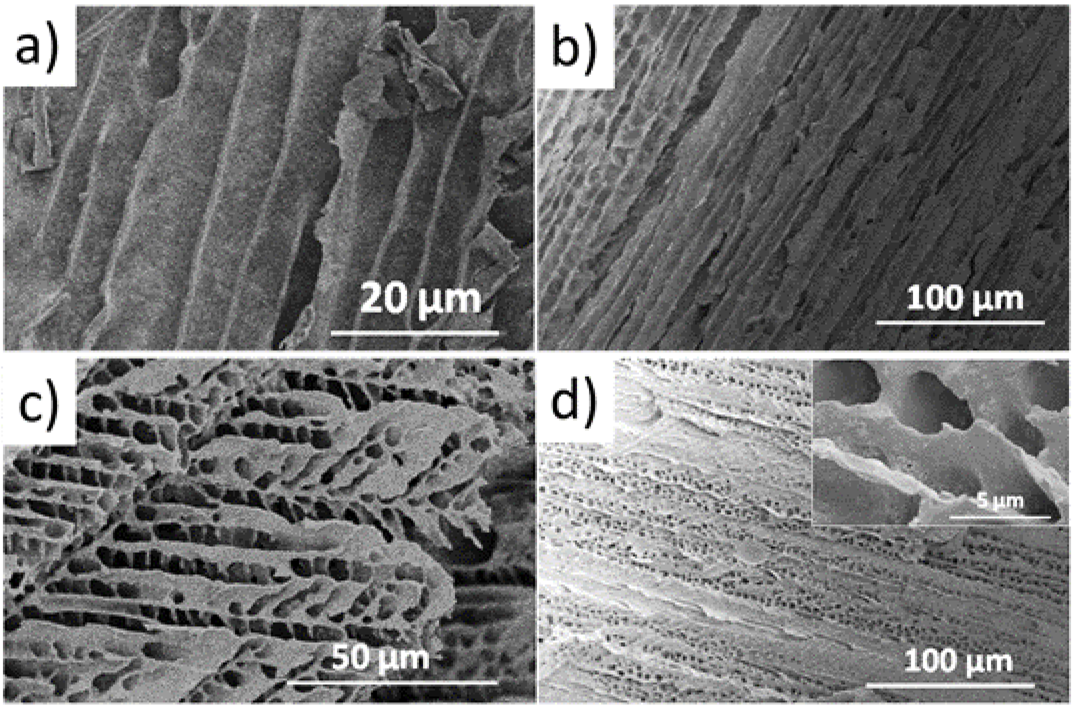

Figure 5.2. SEM images of ice-templated Na-PSS prepared from initial concentrations of a) 50, b) 100, c) 200 and d) 250 mg cm^{-3}

When carbon nanofibers or soft-template derived porous carbons are fabricated – the carbon precursors require crosslinking prior to pyrolysis to prevent melting or decomposition.(14)(15) This is also true for ice-template derived carbons – as there is no rigid template present during carbonisation as there is for hard-template derived porous carbons.(15)(16) In Chapters 3 and 4, this issue was overcome by employing the well-known carbon fibre precursor polyacrylonitrile (PAN) as the precursor polymer, which can be crosslinked with a simple oxidative annealing step prior to pyrolysis.

In this chapter however, it was found that the polymeric precursor PSS could, after ice-templating, be successfully carbonised *without* an apparent crosslinking step, suggesting that one may be occurring *in situ*. To investigate, the thermal decomposition of the ice-templated PSS monoliths was evaluated by TGA (Figure 5.3. b)). It can be seen that a significant mass loss occurs at the temperature range of 400 – 450 °C, before another between 500 – 700 °C. The latter can be attributed to the carbonisation of the polymer, with the associated release of various pyrolysis gasses (*e.g.* H_2O, CO, CO_2, CH_4, SO_2 and H_2S) as polycondensation, aromatisation and partial graphitisation of the remaining carbon occurs. The latter was atypical however, and suspected to be involved in the supposed crosslinking mechanism. A small mass loss at lower temperatures (< 200 °C) was also observed, which was attributed to the loss water physically bound to hydroscopic sodium sulfate groups.(21)

Further investigation was performed by heating the PSS monolith to 450 °C under Ar before analysing its properties. The first observation was that the polymer had changed from its initial light yellow colouration to dark brown – suggesting some kind of chemical reaction had occurred (Figure 5.4.). The 450 °C heat-treated monoliths were now also insoluble in water, whereas prior to heat treatment they were highly soluble; suggesting a now crosslinked structure. SEM imaging of the heat-treated material also revealed the presence of a crystalline species on the surfaces of the ice-templated structure (Figure 5.3. c)), which was identified as Na_2SO_4 by employing PXRD (JCPDS no. 1-990) (Figure 5.3. d)). The Na_2SO_4 is hypothesised to be a by-product from the intermolecular crosslinking reactions occurring – with mechanisms which account for its formation detailed upon in the forthcoming section.

SEM of the carbonised material also revealed the presence of a crystalline species on its surfaces (Figure 5.3. e)); this was identified by PXRD as $Na_2S.9H_2O$ (JCPDS no. 1-1085) as well as some residual Na_2SO_4 (JCPDS no. 1-990) (Figure 5.3. f)). Some smaller peaks were also present with could not be easily distinguished – but suggested minor species could also be forming from various side reactions. The fact that only Na_2SO_4 was detected after heating to 450 °C, but both Na_2SO_4 and Na_2S were detected after heating to 800 °C suggested that the following carbothermal reaction was occurring:

$$Na_2SO_4 + 2C \rightarrow Na_2S + 2CO_2$$

Eq. 5.1.

Furthermore, washing the carbonised monolith in 2M HCl released H_2S, identified by its characteristic noxious odour, which could be attributed to the occurrence of the following neutralisation reaction:

$$Na_2S + 2HCl \rightarrow 2NaCl + H_2S$$

Eq. 5.2.

Further washing with DI water removed the majority of the remaining salts and impurities, as indicated by SEM and PXRD (Figure 5.3. g) and 5.3. h)), the latter of which also revealed the characteristic (002) and (101) peaks associated with a semi-graphitic carbon. TGA in air revealed a residual ash content of 5.1 % (Figure Apx.3.), also indicating that the majority of the inorganic species had been removed through the acid wash step. The yield after carbonisation was 53.13 %, but this fell to 31.84 % after the acid and water wash due to the removal of these other species. For brevity the ice-templated and carbonised PSS will be denoted CPSS150 from here on, and the same material after acid and water washing will be denoted CPSS150-AW.

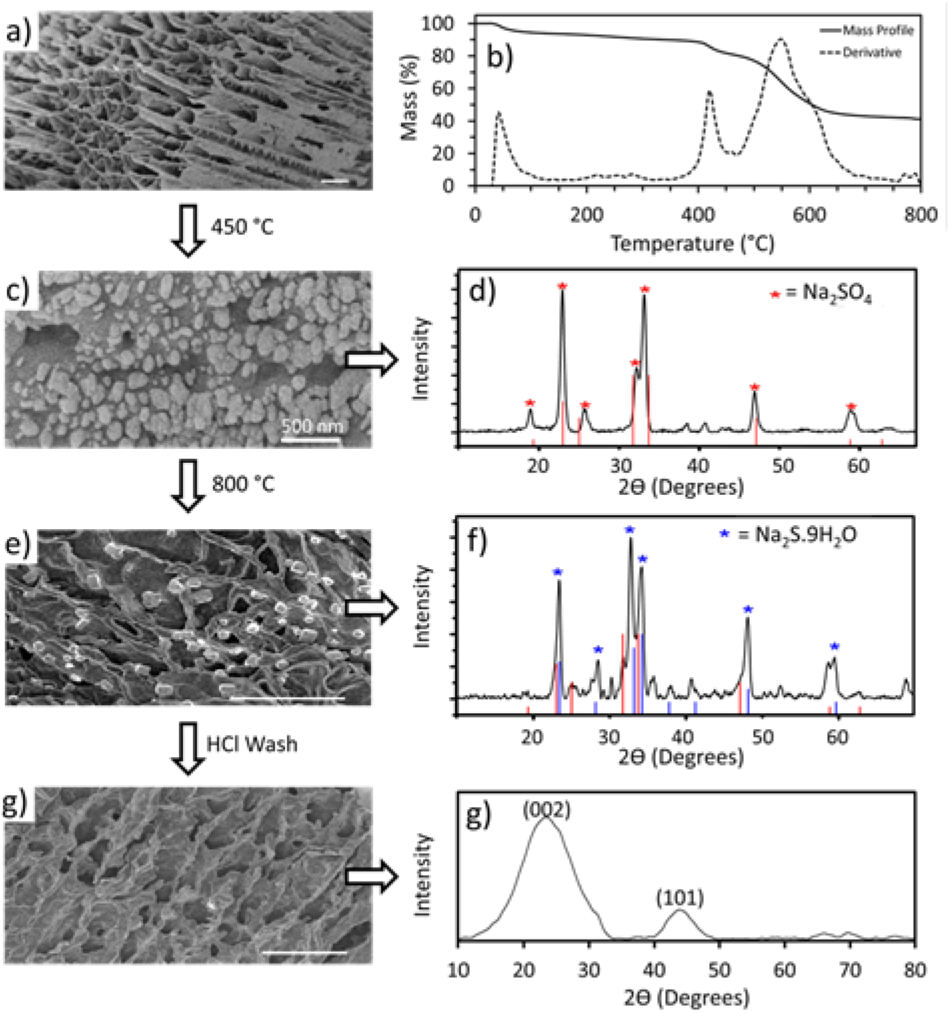

Figure 5.3. Ice-templated Na-PSS prepared from an initial solution concentration of 150 mg: (a) SEM image of ice templated Na-PSS before pyrolysis, (b) the mass loss profile by TGA, (c) SEM image of the monolith treated at 450 °C under Ar and (d) the resulting PXRD pattern, (e) SEM image of the monolith carbonised at 800 °C and (f) the resulting PXRD pattern, (g) SEM image of carbonised monolith after acid washing and (h) the resulting PXRD pattern. Scale bars are 20 µm unless otherwise stated

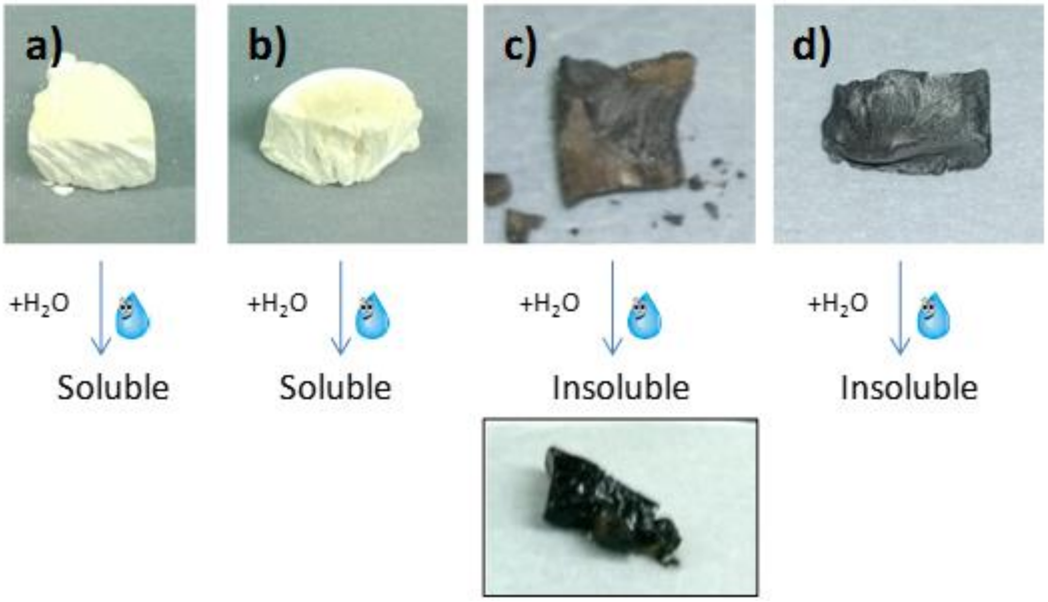

Figure 5.4. Images of a) ice templated Na-PSS, b) after 200 °C heat-treatment, c) after 450 °C heat-treatment and d) after 800 °C heat-treatment and acid wash. Arrows indicate behaviour on addition to water at room temperature

The surface areas and porosity of the CPSS150-AW sample was determined by N_2 gas sorption. To perform such a measurement, it is standard procedure to degas the sample prior to measurement by heating under vacuum for a prolonged period, in order to remove residual water adsorbed onto the surfaces or within the pores.(22) Interestingly, it was found that degassing the CPSS150-AW sample at 200 °C for 24 h left a yellow-white residue on the cooler portions of the BET sample (Figure 5.5 a)). Further, it was found that by simply varying the degas temperature, whilst maintaining the degas duration constant, the amount of this residue removed from the sample and deposited on the sides of the tube could be varied – with higher degas temperatures resulting in more of the substance being removed. The residue was identified as 100 % S by EDX analysis (Figure 5.5. b)); suggesting that elemental S (S_8) was contained within the porous structure. A control experiment in which a commercially obtained S_8 sample was subject to the same degassing conditions displayed the same behaviour – indicating that the yellow-white solid was indeed S in its elemental form. This sublimation behaviour of S_8 under vacuum has also been documented and studied by others and is concordant with our observations.(22)(23)

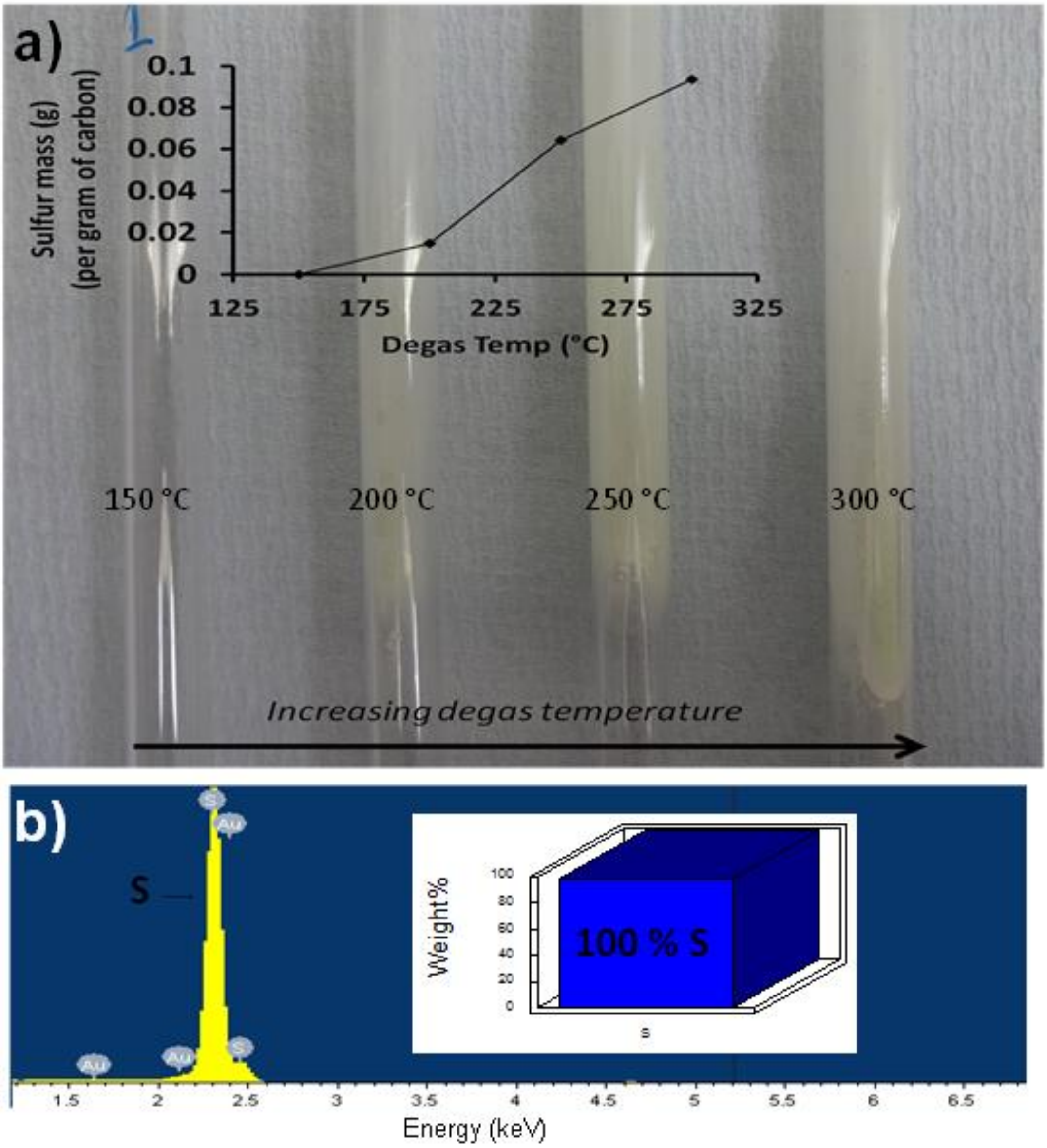

Figure 5.5. Images and graph (inset) showing the increasing amount of sulfur removed from the monoliths with increasing degassing temperature. b) EDX of the yellow substance showing 100 % sulfur

N_2 gas sorption found that the samples degassed at higher temperatures had an increased quantity of N_2 adsorbed than those degassed at lower temperatures (Figure 5.6. a)). DFT pore size distribution analysis revealed a substantial increase in the micropore volumes as the degas temperature increased, with only a minor increase in mesopore volume (Figure 5.6 b)). Plotting the BET specific surface area of the samples against the degas temperatures revealed a roughly linear positive correlation (Figure 5.6. c)), with a very similar trend also observed for the pore volume (Figure 5.6. d)). These observations suggest that elemental S resides predominantly within the micropores of the CPSS150-AW material prior to degassing, however it is acknowledged that the removal of S from the surfaces and walls of macropores could also account for these observations to an extent – since the removal of non-porous S would increase the apparent gravimetric surface area of the remaining material. EDX elemental mapping at high magnification showed that the S was uniformly distributed (Figure 5.7.).

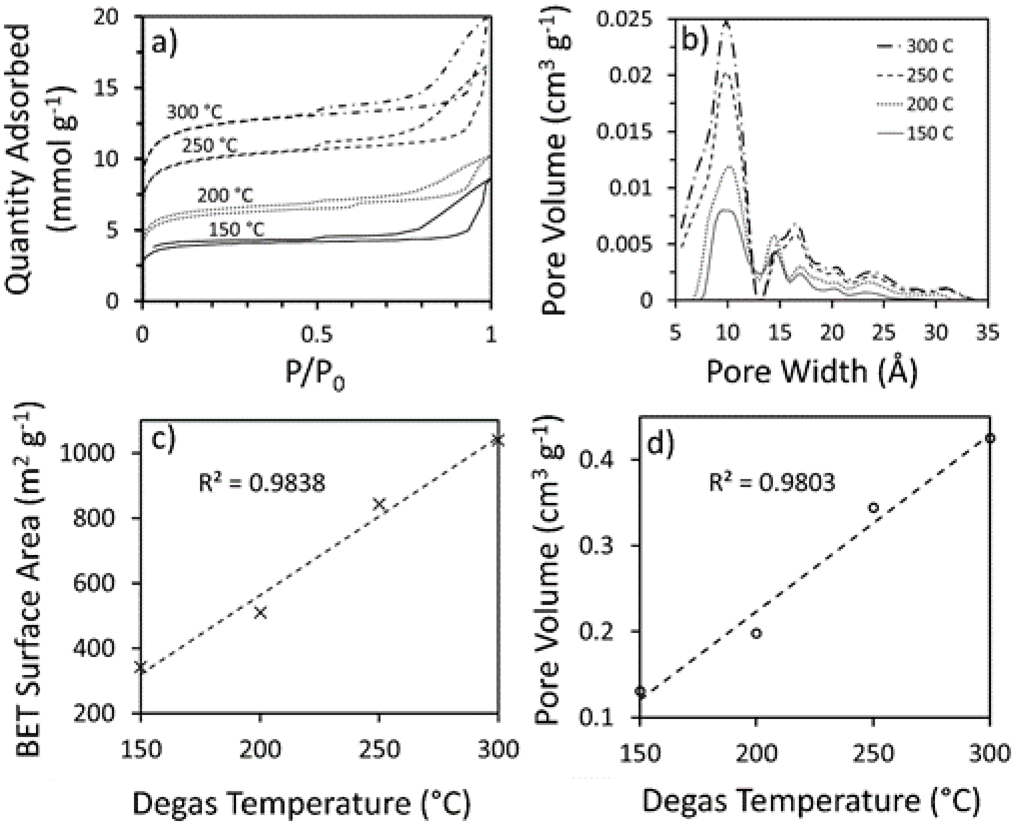

Figure 5.6. BET gas sorption data for the CPSS150-AW sample after degassing at different temperatures: a) N_2 sorption isotherms, b) pore size distribution profiles, c) relationship between degas temperature and specific surface area and d) degas temperature and pore volume

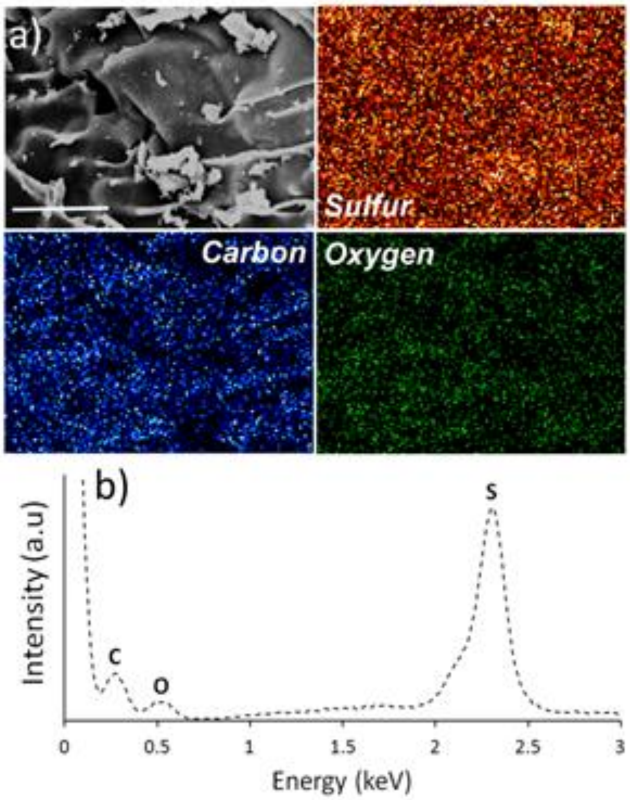

Figure 5.7. EDX analysis of the i-PSS-AW sample showing a) relatively inform distribution of C, O and S, and b) relative intensity of elements and absence of others. Scale bar = 20 µm

The high BET surface area and pore volume revealed after S removal at degassing temperature of 300 °C (1051 $m^2\ g^{-1}$ and 0.43 $cm^3\ g^{-1}$, respectively) suggested that the carbon had been activated *via* some mechanism, since ice-templating and carbonisation alone would not be expected give such high values. Activation mechanisms can be classified as being either chemical or physical processes.(24) Physical activation occurs with the exposure of carbon to mildly oxidising gasses (e.g. H_2O or CO_2) at temperatures typically above 900 °C, whereas chemical activation is achieved by forming a mixture of the carbon with a solid activation agent; examples of which include KOH, NaOH, $ZnCl_2$ and H_2PO_4.(24) In the case of KOH and NaOH activation, two mechanisms are thought to occur – they are: 1) oxidative etching of the carbon framework to generate pores, *via* the following reaction mechanism:

$$6KOH + 2C \rightarrow 2K + 3H_2 + 2K_2CO_3$$

Eq. 5.3.

And 2), the intercalation of metal cations between the graphitic domains, causing expansion and exfoliation of the graphene sheets to reveal a high surface area.(24) In the case of our material, it is proposed that the abovementioned carbothermal reaction of Na_2SO_4 to Na_2S (Eq. 5.1) has an analogous activation effect as to KOH or NaOH activation – *i.e.* oxidative etching of the carbon framework to generate pores. The presence of Na cations with our material could also mean that the second activation mechanism – *i.e.* intercalation and exfoliation of graphitic domains – could also be occurring. It is also plausible for the various pyrolysis gasses released, for instance H_2O, CO_2, CO and SO_2 to cause a degree of physical poor activation, however this would likely be only a minor contribution, if anything, to the activation process due to the relatively low carbonisation temperature (800 °C) and low concentration of such gasses.(24) The decomposition of various functional groups into these pyrolysis gasses could also play a role in the activation process, through a physical gasification activation process.(25)

Thus, it is proposed that the carbonisation of the ice-templated PSS is an example of an *in-situ* activation (or *in-situ* porogen formation) process, of which there are a few examples in the literature. One recent example is that of the carbonisation of the K salt of poly(acrylamide-co-acrylic acid), which resulted in a porous carbon with a specific surface area of 1372 m^2 g^{-1} and over 80 % of the pore volume attributed to micropores.(26) It was proposed that K_2CO_3 was generated *in-situ*, before oxidatively reacting with the carbon to create micropores through etching (chemical activation). By removing the need for a post chemical treatment and thermal treatment step, *in-situ* activation can be considered a useful and relatively simple process for the generation of activated carbons.

To shed further light on the nature of the prepared materials, additional characterisation was performed on the CPSS150 and CPSS150-AW samples. CHNS elemental analysis was performed on the carbonised material both before and after the acid wash. This revealed a large increase in the carbon content (from 34.7 to 71.1 wt. %), along with a small increase in the S content (14.1 to 17.1 wt. %) (Table 5.2.). This was accompanied with a large reduction on the H content (from 1.69 to 0.54 wt. %) and combined O and Na contents (from 49.6 to 11.4 wt. %.). The data implies that, upon acid and water washing of the material, that predominantly Na, O and H is removed, along with some S. TGA was performed on the CPSS150-AW sample as a measure of the elemental S content (Figure 5.8.). In this technique – which is common for determining the elemental S content within porous carbons – the sample is heated under an inert atmosphere to induce the sublimation of S from the sample, the quantity of which can be determined by the change in mass.(6)(7)(11) The TGA curve for the CPSS150-AW showed two distinct mass losses; the first occurring between approximately 160 – 300 °C, and the second occurring between 350 and 550 °C (Figure 5.8.). The former, lower temperature, mass loss was attributed to the sublimation of S_8, as expected, and corresponded to ~14 % of the original mass. The latter, higher temperature, mass loss was attributed to the decomposition of various S-, O- and H- containing functional groups (*e.g.* thiols, hydroxyl, sulfoxides and carboxylates), and corresponded to ~9 % of the original sample mass.

Table 5.1. Elemental microanalysis data for the carbonised Na-PSS monoliths before and after washing.

	C (wt. %)	*H (wt. %)*	*S (wt. %)*	*O (wt. %)*	*Na (wt. %)*
PSS (theoretical)	46.6	3.43	15.1	23.3	11.2
CPSS150	34.7	1.69	14.1	49.6	
CPSS150-AW	71.1	0.54	17.1	11.4	0

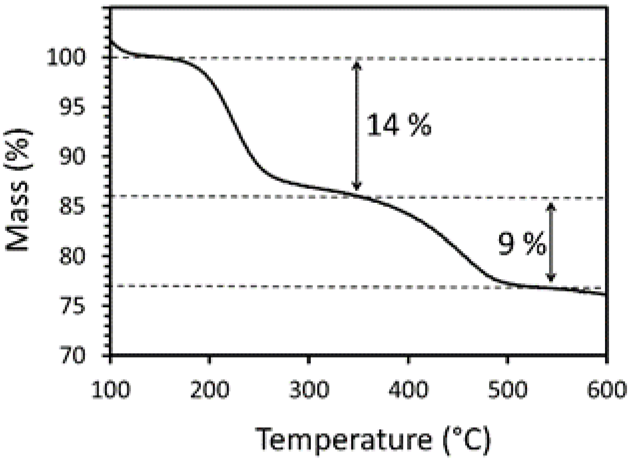

Figure 5.8. TGA profile of CPSS150-AW performed under a N_2 atmosphere (heating rate = 20 °C min^{-1}). The mass at 150 °C was normalised to 100 % since mass lost at lower temperatures was deemed to be residual water

To identify these functional groups, FTIR was employed on the CPSS150-AW sample (Figure 5.9.). The broad peak at ~3400 cm^{-1} is characteristic of H-bonded hydroxyl (-OH) stretching vibrations, with the other typical O-H stretching vibrations observed at ~2850 and 2925 cm^{-1}. The peaks at ~2320 and 2350 cm^{-1} were attributed to aromatic thiols, with the broad peak at ~1580 cm^{-1} attributed to skeletal aromatic C=C vibrations.(27) The broad peak at ~1110 cm^{-1} was identified as the overlapping peaks of aliphatic skeletal vibrations, along with the asymmetric S=O bond stretching vibrations of sulfoxide and sulphonyl groups. The peak at ~600 cm^{-1} was attributed to S-O stretching vibrations.(27) FTIR was also performed on the (non-washed) CPSS150 sample for comparison with the CPSS150-AW sample, and to help identify any metal salt species that may have eluded detection by PXRD measurement (Figure 5.9.). Sharper and more intense peaks at ~620 and 1100 cm^{-1} were observed for this sample, which could be attributed to the presence of S-O and S=O groups of the Na_2SO_4 species already detected by PXRD. XPS was also performed to further aid the functional group characterisation of the CPSS150-AW material. Here, a broad scan of 0 – 1100 eV detected the presence of C, O and S and no other elements, at atomic percentages of 55.7, 20.62 and 23.82 %, respectively (Figure 5.10. a)). A detailed scan of the S domain (160 – 174 eV) revealed two distinct doublets (Figure 5.10. b)) – where the splitting was due to the asymmetric spin orbit coupling commonly observed for S-containing compounds. The peak at ~169 eV was attributed to the presence of sulfoxide in concordance with FTIR and XRD measurements, whilst the peak at ~164 eV could be attributed to both elemental S and thiol groups.(28)

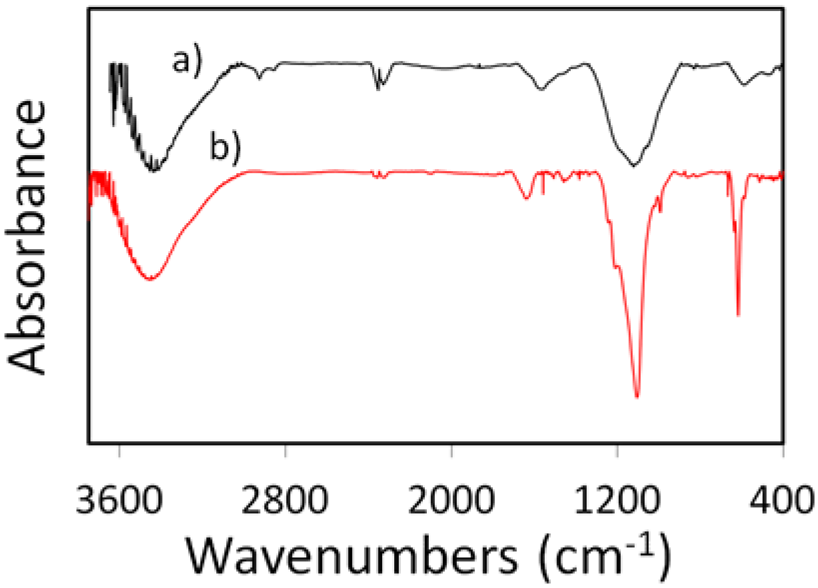

Figure 5.9. FTIR spectra of (a) CPSS150-AW and (b) CPSS150. Spectra have been baseline corrected and normalised for clarity

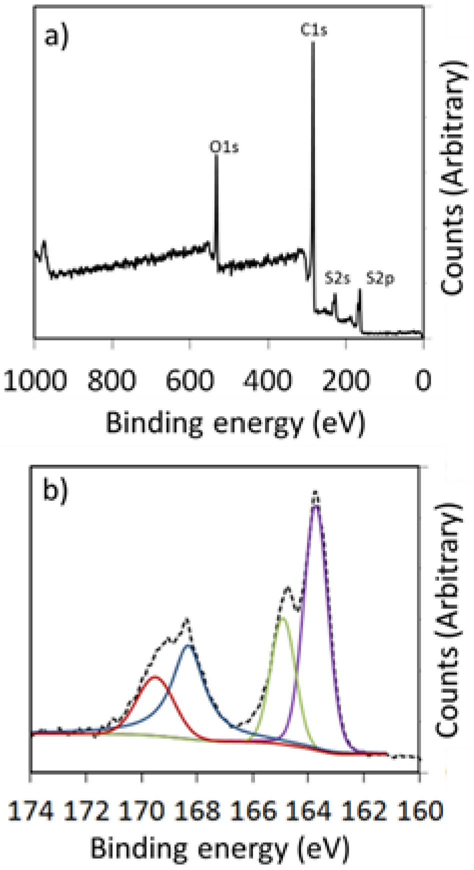

Figure 5.10. XPS data for the CPSSC150-AW sample: a) broad scan and b) narrow scan of the S energy region

Raman spectroscopy was employed to investigate the microstructure of the carbon; revealing characteristic shifts at 1321 and 1588 cm^{-1}, corresponding to the disordered (D) and graphitic (G) peaks of carbon respectively (Figure 5.11 a)). The ratio of the intensity of the D and G peaks (I_D/I_G) was 1.14 – indicating a disordered semi-graphitic structure in concordance with the PXRD data. TEM microscopy was also performed to image the microstructure of the carbon (Figure 5.11. c-f)); this too showed a disordered semi-graphitic structure in agreement with the Raman and XRD data. Hg-intrusion porosimetry was employed to characterise the macopore size distribution of the carbonised monoliths: revealing a total pore volume of 3.19 cm^3 g^{-1}, with macropores predominantly in the size ranges of 1-3 µm, 5-7 µm, and ~100 µm (Figure 5.11. b)). The smaller macropores were attributed to the ice-crystal templates (in concordance with the SEM data), whereas the larger ~100 µm macropores were likely due to cracks introduced during the ice-templating or carbonisation processes. The total pore area for macropores was 73.7 m^2 g^{-1}, with a median pore diameter of 2.80 µm.

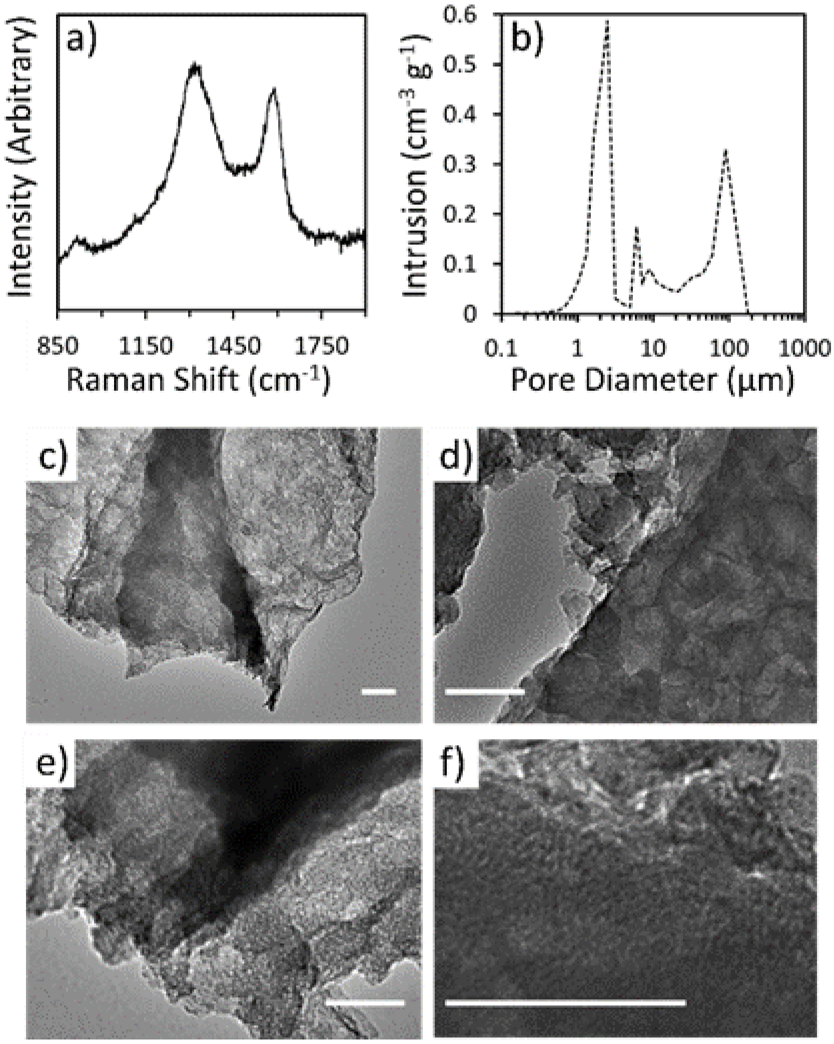

Figure 5.11. a) Raman spectrum and b) macropore pore size distribution for i-PSSC-AW material, c) – f) TEM images of the same material displaying the micromorphology (scale bars = 100 nm)

It should be noted, for safety reasons, that after pyrolysis – upon removal of the materials from the furnace and their exposure to oxygen/moisture in the air – they underwent a strongly exothermic reaction, to the point where the carbon materials would glow red-hot and were in danger of undergoing spontaneous pyrophoric combustion – or igniting any nearby flammable solvent vapours. To glow red hot (*i.e.* to exceed 500 °C) within seconds upon the exposure to air suggests a highly reactive species present within the material. This was also accompanied by the release of noxious H_2S odour. The cause of this pyrophoric behaviour isn't clear, but possible explanations include the quenching of dangling bonds/radical species upon exposure to O_2, or the reaction of elemental or intercalated Na, or reactive Na-containing species, with moisture/O_2. It should be noted that Heins *et al.* observed the same phenomenon (*i.e.* a strong exothermic reaction) upon the exposure of pyrolysed poly(styrene sulfonic acid)-based salts to air.(25) They suggested that the oxidation of sulfides and metals, or chemisorption of O_2 onto the carbon matrix with the formation of functional groups, were possible causes of this behaviour.

5.5. Mechanistic Discussion

In the results and discussion section, a body of evidence was given to support the fact that an *in-situ* crosslinking mechanism was occurring within the ice-templated Na-PSS upon heating – stabilising the structure upon carbonisation. A by-product for this reaction was the generation of Na_2SO_4, which was acting as an activation agent upon pyrolysis. Elemental S_8 was also detected within the micropores of the carbonised and acid-washed material, CPSS150-AW), which could be selectively removed by heating under vacuum. In this section, what are deemed to be the most plausible mechanisms to account for the empirical observations are presented. A number of alternative mechanisms have also been discussed, as well as a detailed comparison of previous literature findings.

5.5.1. Proposed Crosslinking Mechanism

As the ice-templated PSS is heated – the first significant process proposed to occur is the homolytic cleavage of the styryl-sulfonate bonds, with the generation of styryl and sulfite radicals:(29)

$$\text{Ar-SO}_3\text{Na} \rightarrow \text{Ar}\cdot + \cdot\text{SO}_3\text{Na}$$

Eq. 5.4.

This radical-based breakdown mechanism is supported by the work of Sigga and Whitlock, who analysed the decomposition of the salts of arylsulfonic acids *via* pyrolysis gas chromatography.(30) They found that with the addition of carbohydrazide – which acts as a H-atom donor – prior to pyrolysis would significantly increase the yield of the recovered hydrocarbons (*e.g.* from 51 % to 98 % in the case of benzene sulfonic acid), supporting a homolytic, radical-based breakdown of the sulfonic acid salts. The generated, highly reactive, sufite radicals could then engage in radical substitution to form the more stable dithionate – producing further styryl radicals:

$$^{\cdot}SO_3Na + Ar\text{-}SO_3Na \rightarrow Ar^{\cdot} + Na_2S_2O_6$$

Eq. 5.5.

With the dithionate decomposing at elevated temperatures *via* the following mechanism:(21)

$$Na_2S_2O_6 \rightarrow Na_2SO_4 + SO_2$$

Eq. 5.6.

This generation of SO_2 could account for the mass loss observed in the TGA at this temperature region: this is further supported by work done by Nakagawa *et al.* who detected SO_2 via TGA-Mass spectroscopy when studying the thermal decomposition behaviour of various poly(styrene sulfonate) ion-exchange resins.(31) The styryl radicals generated from these processes may then undergo biaryl coupling *via* radical recombination to form the proposed intermolecular covalent crosslinks:

$$Ar^{\cdot} + Ar^{\cdot} \rightarrow Ar\text{-}Ar$$

Eq. 5.7.

5.5.2. Other Plausible Mechanisms

As well as forming dithionate as in Eq. 5.5. above, it’s also plausible for the sulfate radicals (generated *via* Eq. 5.4.) to instead abstract hydrogen atoms from the styryl groups or from the carbon backbone of the polymer, generating sodium bisulphate and a radical:(21)

$$NaSO_3^{\cdot} + R\text{-}H \rightarrow NaHSO_3 + R^{\cdot}$$

Eq. 5.8.

The sodium bisulphate may then decompose *via*:

$$NaHSO_3 \rightarrow SO_2 + NaOH$$

Eq. 5.9.

NaOH is a common activation agent, providing another route to *in-situ* activation.(24) Due to stabilisation of adjacent π-bonds, it would be expected that the H abstraction would preferentially occur at the α- position of the aryl ring:

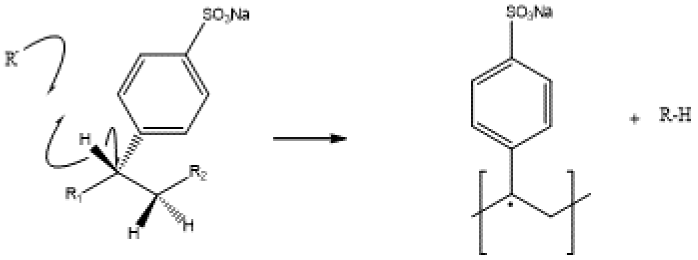

Eq. 5.10.

Delocalisation of the radical within the styryl ring may then induce further decomposition, regenerating ·SO_3Na radical and therefore propagating the reaction:

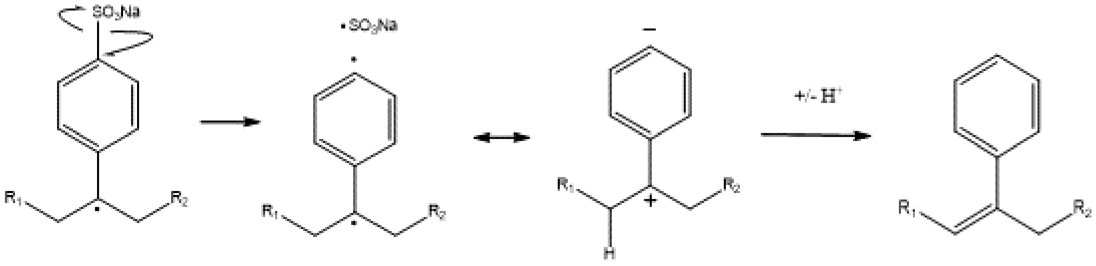

Eq. 5.11.

This pathway is analogous to that for sulfonated polyethylene which was studied computationally by Younker et al.(32) Another plausible explanation for the observations is through the formation of sulfone bridges at elevated temperatures, with Na_2SO_4 as the by product, as has been reported for aryl sulfonic acids at temperatures up to 160 °C.(33)(34) The sulfone bridges may then undergo decomposition at ~400 °C to produce styryl radicals and SO_2, the former then undergoing bi-aryl coupling (crosslinking) as in Eq. 5.7 above, and the latter accounting for the mass loss at this temperature region. The mechanisms can be written as follows:

$$2\ \mathrm{Ar\text{-}SO_3Na} \rightarrow \mathrm{Ar\text{-}SO_2\text{-}Ar} + \mathrm{Na_2SO_4}$$

Eq. 5.12.

$$\mathrm{Ar\text{-}SO_2\text{-}Ar} \rightarrow 2\mathrm{Ar}^{\cdot} + \mathrm{SO_2}$$

Eq. 5.13.

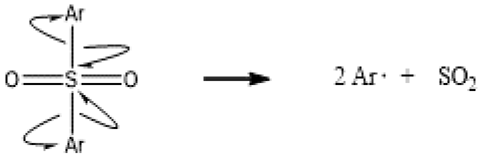

Eq. 5.14.

This hypothesised mechanism was not supported by a control experiment however; here a portion of the ice-templated Na-PSS was heated to 200 °C, above the temperature where this would be expected to occur, and compared with the un-treated sample. The optical and mechanical properties appeared to be identical (*i.e.* no colour change, shrinkage *etc.*), and both samples dissolved rapidly in water: suggesting no crosslinking had occurred (Figure 5.4.).

A non-radical based crosslinking mechanism can also be envisaged, with the generation of Na_2SO_4 and SO_2 in concordance with observations. Mechanistically, this can be written as:

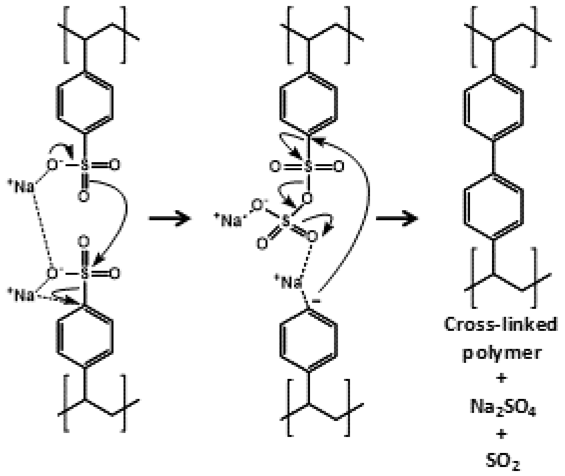

Eq. 5.15.

5.5.3. Comparison with Previous Reports

The unusual thermal decomposition behaviour PSS and its metal salts has been noticed by and studied by a number of other researchers, who have proposed their own explanations behind the behaviour. A relatively early report by Nakagawa *et al.* investigated the pyrolysis of PSS ion-exchange resins and a number of its metal salt equivalents (where the metal cations included Na^+, K, Ca^{2+}, Cu^{2+} Zn^{2+}, Ni^{2+}, Fe^{2+} and Fe^{3+}).(31) The authors suggested that a so-called *pillar-effect* mechanism was occurring during pyrolysis, in which *di*- or *tri*- valent cations were forming ionic crosslinks between adjacent sulfonate group, acting as *pillars* (or templates) for the observed micropores. Since our work employs *monovalent* Na^+ as the sulfonate cation, the same mechanism cannot be taking place. The authors also detected the presence of metal sulfides post-carbonisation, which is in concordance with our observations. In another related report, Heins *et al.* studied the properties of porous carbons obtained from the carbonisation of poly(styrene sulfonic acid-*co*-maleic acid) salts.(25)(35) They noted a number of observations similar to the ones seen by us; including a significant mass loss at ~ 450 °C by TGA, which was attributed to the decomposition of the sulfonate groups, a strongly exothermic reaction upon exposure of the carbonised materials to air, and the release of H_2S upon an acid wash. They also observed a high microporosity, the development of which was attributed the pillar-effect mechanism, as well as the release of pyrolysis gasses and the reduction of metal salts and their migration to the carbon surface. It may well be the case that, to some extent, the formation of various salt species act as pillar-like templates which, upon removal by washing, reveal pores – however in light of our investigation it is hypothesised that the main mechanism occurring is chemical activation by the *in-situ* generated Na_2SO_4. Another relevant example is that of Yadav *et al.*, who observed that the pyrolysis of the Na salt of again poly(styrene sulfonic acid-*co*-maleic acid) could result in porous carbons with specific surface areas as high as 1720 m^2 g^{-1}. Employing Raman spectroscopy, they observed the characteristic G' and 2D peaks of single-layer graphene, the origin of which they attributed to inter-chain cyclisation between maelic acid units, and decomposition and removal of the Na-styrene sulfonate units. Despite the interesting hypothesis, in light of our observations, we suggest that the Na-styrene sulfonate units would actually undergo carbonisation and *in-situ* activation following the mechanism proposed here. This could account for several observations found in their report, including the high surface area and small average pore diameter (< 1 nm) they had observed, however the G' and 2D Ramen peaks cannot be explained by our mechanism.

The thermal decomposition mechanisms of polymeric sulfonic acids and their Na salts were studied by Jiang *et al.* who performed an in-depth TGA/FTIR study.(21) They concluded that radical-based decomposition mechanisms were occurring for both Na-poly(vinyl sulfonic acid) and Na-PSS, which are analogous to the ones proposed by here. By employing FTIR, they detected to occurrence of mono-substituted benzenes during the decomposition process, which suggested a degree of H-abstraction by the generated styryl radicals, as could be expected to some degree.(30) They also reported similar TGA curves as the ones found by us, and interestingly found them to be almost identical when performed in air as under an inert atmosphere. They suggested that this was evidence of the formation of an inorganic species since an organic species would be expected to burn – in agreement with our findings. They also found that, upon pyrolysis of the material at 800 °C, significant foaming and volumetric expansion of the material occurred – which is at odds with our observations where morphology is retained upon carbonisation. It was hypothesised that, in their case, either relatively poor compression of the polymers, or the much faster heating rate of 20 C min^{-1}, may have resulted in an inadequate degree of *in-situ* crosslinking prior to carbonisation, and hence could account for this foaming behaviour. To test this hypothesis, an experiment was performed in which we pyrolysed a commercial sample of the Na-PSS power under the same conditions as described in their paper to see if we would observe the same result. However again no foaming was observed, leaving only a black carbonised powder. It's therefore not clear what could account for these differences in observations, but it should be noted that our method could be reproduced with another batch of PSS in another lab. In concordance with our observations however, they also observed that the polymer was still soluble after a lower (420 °C) thermal treatment step, but insoluble after heating above 450 °C (490 °C); suggesting that the *in-situ* crosslinking mechanism was still occurring. The same group also performed a subsequent study where blends of polystyrene and PSS, and the co-polymer Na-poly(styrene-*co*-styrene sulfonate) were carbonised.(36) They concluded that adjacent sulfonic acid groups were required in order to permit successful carbonisation – a finding which supports our proposed mechanism further. Lastly, Younker *et al.* studied the pyrolysis pathways of sulfonated polyethylene *via* computational methods, and found that a radical-based breakdown of the C-S bond occurred at 276 °C, similar to the radical breakdown of the styrene-sulfonate bond as proposed by our mechanism.(32) The findings of these previous reports therefore significantly overlap with our observations and are concordant with our proposed *in-situ* crosslinking and activation mechanism.

5.5.4. Origin of Sulfur

The mechanisms thus far discussed provide an explanation for the *in-situ* crosslinking and activation processes, however the origin of the elemental S found within the micropores of the carbon is not yet explained. There are a number of plausible mechanisms for the formation of S at elevated temperatures during the carbonisation process;(37)(38)(39) *however*, these mechanisms are deemed unlikely since any elemental S formed at such high temperatures would be expected to sublime and be lost – an effect which allows the determination of S content *via* TGA measurement.(40) Therefore, it is hypothesised that the elemental S forms not during, but after the carbonisation step upon the acid wash. Evidence for this can be seen when the carbonised materials are acid-washed: a cloudy, white suspension (characteristic of colloidal S) forms, along with the previously mentioned release of H_2S (Figure 5.12.) This cloudy suspension is similar to the one formed during the thiosulfate clock reaction:(41)

$$Na_2S_2O_3 + 2HCl \rightarrow 2NaCl + H_2O + S + SO_2$$

Eq. 5.16.

There was no direct evidence of $Na_2S_2O_3$ formed within the material however; *i.e.* its PXRD diffraction pattern (JCPDS no. 70-1909) did not match the experimental data, nor could FTIR or XPS conclusively detect its presence. Another possible route for the formation of S during the acid wash would be *via* the following reaction:(42)

$$Na_2S_x + 2HCl \rightarrow (x-1)S + H_2S + 2NaCl$$

Eq. 5.17.

However, the presence of Na_2S_x could not be clearly detected either. Lastly, it is known that aqueous SO_2 and H_2S can react with one another in a conproportionation reaction to give elemental S:

$$2H_2S + SO_2 \rightarrow 3S + 2H_2O$$

Eq. 5.18.

H_2S is clearly present due to the characteristic noxious odour, and through Eq. 5.2. where the presence of Na_2S has been confirmed by PXRD. SO_2 could very likely be formed through the neutralisation of various sulfur oxyanions. Therefore, the latter mechanism is deemed the most plausible route for the formation of S.

Figure 5.12. CPSS150 monoliths after addition of 2M HCl. A white/yellow precipitate forms immediately on addition of the acid with accompanied effervescence and H_2S odour

5.6. Optimisation for LIS Battery Application

Templated carbons with elemental S infused within the meso- and micropores are of interest as LIS battery cathode materials where they have been shown to overcome several issues associated with the LIS battery cathode.(2) Our simple ice-templating, carbonisation, *in-situ* activation and S-infusion method offers a facile route to prepare such materials, which avoids the use of relatively complex hard and soft templating routes, as well as multi-step activation and S infusion into the pores. The performance of our materials as LIS battery cathodes was therefore evaluated.

The first goal was to increase the S content of the prepared material – since the current material falls short of the amount required for a practical LIS cathode material (ideally > 40 wt. %). With the elucidation of the underlying mechanism behind the formation of elemental S within the material, it was hypothesised that the incorporation of additional Na_2SO_4 within the ice-templated structure prior to carbonisation would achieve this goal. This could be achieved with ease with the simple dissolution of Na_2SO_4 within the initial aqueous PSS solution prior to ice-templating. By employing this strategy, ice-templated PSS monoliths with Na_2SO_4 concentrations as high as 80 mg cm^{-3} (approx. 2:1 ratio of PSS to Na_2SO_4) could be obtained and carbonised successfully (carbonised materials denoted CPSS150-X, where X is the concentration of Na_2SO_4 in mg ml^{-1}). Higher concentrations of Na_2SO_4 were also attempted, however these monoliths were very brittle and burned away during carbonisation.

Table 5.2. Elemental content of Na-PSS monoliths with added Na_2SO_4 as determined by CHNS microanalysis.

	Added Na_2SO_4 (mg ml^{-1})	*C (wt. %)*	*H (wt. %)*	*S (wt. %)*	*O (wt. %)*
CPSS150-AW	0	71.0	0.54	17.1	11.4
CPSS150-40	40	69.9	1.22	19.9	8.02
CPSS150-80	80	54.3	1.10	39.7	4.26

CHNS elemental analysis of the successfully carbonised Na_2SO_4-incorporated samples found that the S content had indeed increased with increasing Na_2SO_4 concentration (Table 5.2.). The highest S-content was with the sample with the largest amount of Na_2SO_4 incorporated (CPSS150-80) at 39.7 wt. %. SEM confirmed the retention of the ice-templated morphology for this sample (Figure. 5.13.). TGA was performed on the material in order to differentiate between elemental S_8 and S in the form of functional groups; since only elemental S_8 would be active for LIS battery purposes. Unlike the standard CPSS150-AW material however, which displayed two distinct mass loss peaks allowing the differentiation between elemental and functional-group S, only one, broad mass loss peak was observed in this instance (Figure 5.14.). In an attempt to resolve the peaks, TGA was repeated at the slower heating rate of 5 °C min^{-1}, however still only one peak was observed meaning the proportions of elemental and functional-group S could not be distinguished.

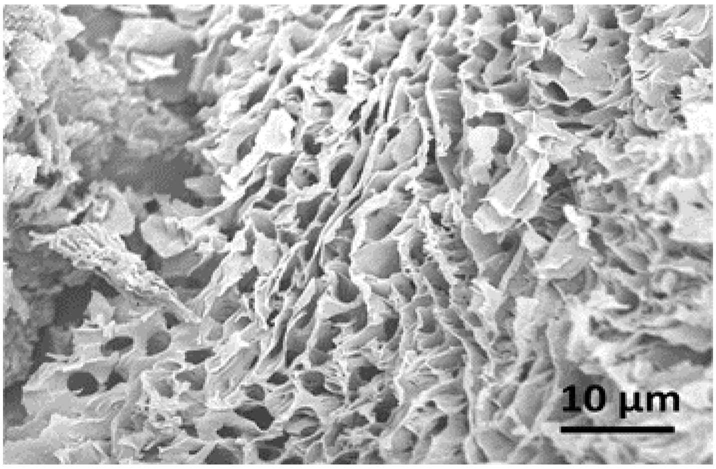

Figure 5.13. SEM image of CPSS150-80 showing a characteristic ice-templated morphology

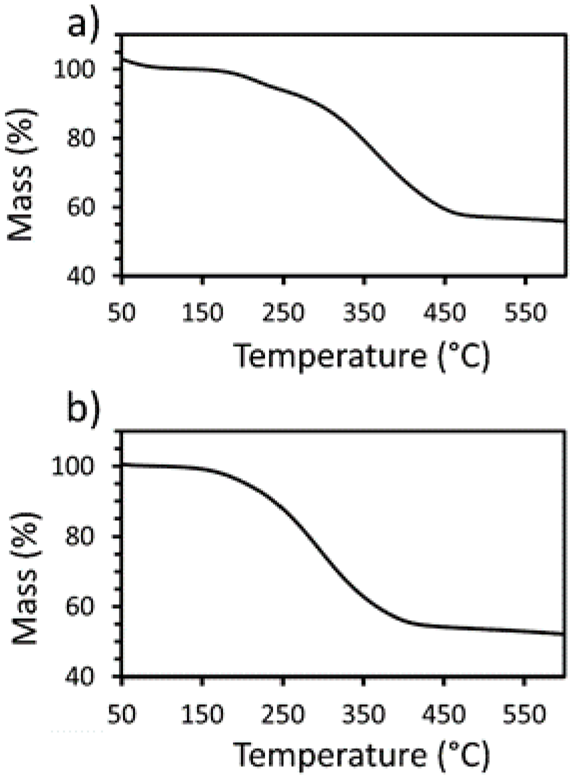

Figure 5.14. TGA profiles of PSSC-80 measured under N_2 at a) 20 °C min^{-1} and b) 5 C min^{-1}. The masses at 150 °C was normalised to 100 % since mass lost at lower temperatures was deemed to be residual water.

Having the highest S content, the PSSC-80 sample was selected for performance evaluation as a LIS battery cathode material. Here the 39.7 % S content as determined by elemental analysis was taken as the basis for calculations of active electrode mass. Electrodes were prepared before being assembled into coin cells with Li metal as the counter electrode. CV measurements, in the voltage range of 1.9 – 2.7 V, displayed the typical redox peaks associated for this kind of LIS cell – with two reductive peaks on the negative sweet at approximately 2.3 and 2 V (vs. Li/Li^+), attributed to the reduction of S_8 to Li_2S_4, and Li_2S_4 to Li_2S_2/Li_2S, respectively (Figure 5.15. c)).(3) The broad peak upon the positive sweep, occurring at ~2.3 V was attributed to the reverse reactions occurring, *i.e.* oxidation of Li_2S_x species back to LiS_8. CCP was also employed to investigate the charge-discharge behaviour of the material at constant currents (Figure 5.15. b)). This also displayed characteristic voltage profiles associated with a typical LIS battery system, having brief voltage plateaus at ~2.3 and 2 V, again attributed to the ring opening of S_8 to Li_2S_4 before Li_2S_4 to Li_2S_2/Li_2S in agreement with the CV data.(3) The measured capacity was however very low at only 183.4 mA h g^{-1} for the first discharge (with a current density of 100 mA g^{-1}), which stabilised at about 136 mAh g^{-1} after 15 cycles (Figure 5.15. a)). This disappointing performance is about an order of magnitude lower than for high-performance porous carbon-S composites reported by others.

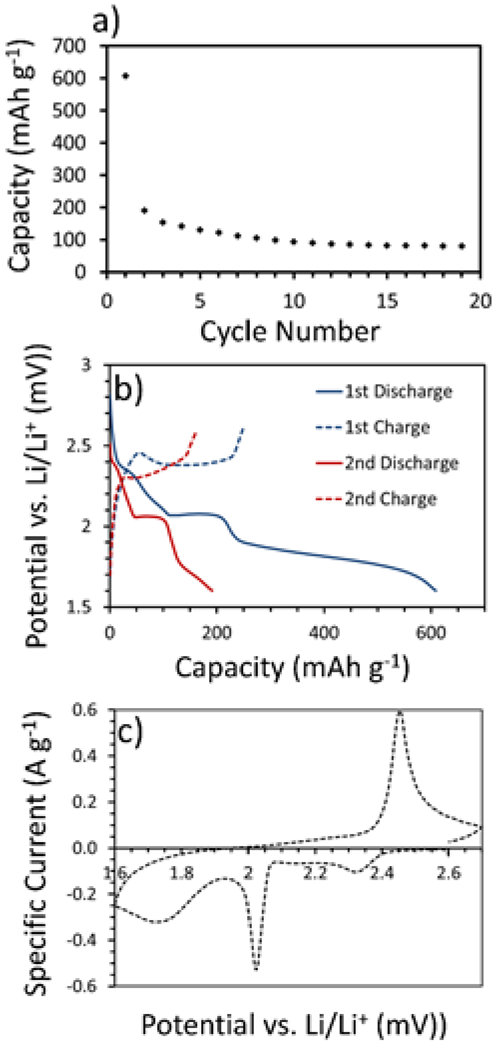

Figure 5.15. a) cycle stability profile, b) CCP curves and c) CV curves for the PSSC-80 material tested as a LIS battery cathode material

There are a number of publications which have shown how micropore-confined elemental S can exhibit high Li electrocativity in *carbonate*-based electrodes, rather than the 1,3-dioxolane/ dimethoxyethane/LiNO$_3$ typically employed for Li-S systems.(3)(43)(44) The CPSS150-80 material was therefore evaluated for Li-S battery performance with an electrolyte consisting of 1M LiPF$_6$ in ethylene carbonate/dimethyl carbonate (1:1 wt. %), however the performance was again poor. With a cut-off voltage of 1.0 V, the initial discharge capacity was reasonable at 583.0 mA h g^{-1}, but fell to 140.1 mA h g^{-1} on the second discharge (Figure 5.16.). Despite this low capacity, the shape of the CV curves were consistent with other reports for carbonate-based electrodes and porous carbons with micropore-confined S; with one broad reduction peak at ~1.6 V rather than the two distinct peaks with the standard electrolyte.(3)(43) The poor performance of these systems could be due to a significant proportion of the S not being utilised, either due to its restricted confinement within the micropores preventing access to Li-ions, or preventing the necessary volumetric expansion on lithiation. This phenomenon was observed by Zhang *et al.*, who found that the lithium electroactivity of micropore-confined S (in porous carbon spheres) decreased substantially upon full saturation of elemental S.(3)

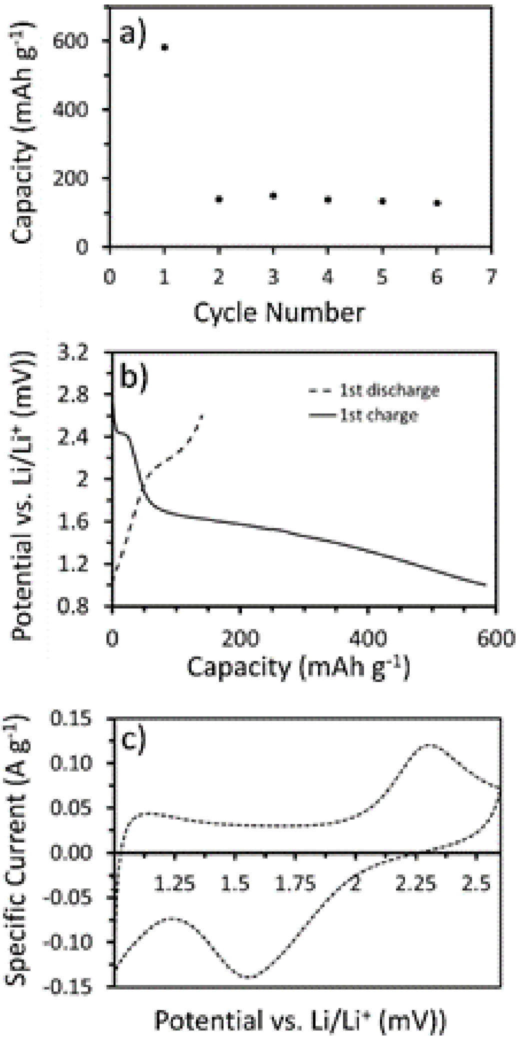

Figure 5.16. a) Cycle stability profile, b) CCP curves and c) CV curve for the the PSSC-80 material with a carbonate-based electrolyte and a lower cut-off voltage of 1.0 V vs, Li/Li$^+$

5.7. PSS-Derived Porous Carbon Spheres

In section 5.5.3. it was noted that the commercial PSS powder was subject to pyrolysis at 800 °C to see if the same observations as Jiang *et al.* were observed, namely significant foaming and volumetric expansion upon carbonization.(21) No foaming was observed in our case however with only a black carbonized powder being produced. This powder was subject to SEM imaging both before and after a 2M acid wash which revealed porous carbon microspheres of roughly 1 – 100 µm in diameter (Figure Apx.8.). SEM imaging of the uncarbonized powder also revealed microspheres, suggesting that the original morphology had been retained on carbonization. Furthermore, it was observed that a number of the particles had cracked to reveal a hollow interior (Figure Apx.9.).

Spray drying is a common technique for the processing of polymers into dry powders and is known to form hollow particles under certain conditions,(45) it was therefore hypothesised that these hollow particles were formed as a result of spray drying by the manufacturer. Hollow carbon spheres are typically produced *via* techniques such as CVD, hydrothermal carbonization, or other templating processes;(46) the direct carbonization of a commercially obtainable PSS powder is relatively simple in comparison and therefore has advantages over these more complex routes.

CHNS analysis of the acid washed material (hereafter denoted PSSP-AW) revealed a C content of 64.6 wt. %, H content of 0.44 wt. % and S content of 30.7 wt. %. Degassing of the PSSP-AW sample at temperatures between 150 and 400 °C progressively decreased the S content as was also observed for the CPSS150-AW sample (Figure Apx.10.). N_2 gas sorption of the degassed samples revealed each to have a similar shaped isotherm, which could be categorised according to IUPAC terminology as type 1(b) with a H1 hysteresis loop (Figure Apx.11.).(47)(48) Analysis of the isotherms showed that the BET surface areas increased fairly linearly with increasing degas temperatures up to 300 °C, before levelling off at higher temperatures at about 570 m^2 g^{-1} (Figure Apx.12.). The total pore volume also displayed a similar trend, attaining a maximum value of 0.51 cm^3 g^{-1} at the degas temperature of 350 °C. Pore size distributions were calculated using the BJH method and revealed little change with increasing degas temperature (Figure Apx.13.). PXRD of the PSSP-AW sample revealed the characteristic (002) and (101) Bragg reflections of a semi-graphitic carbon (Figure Apx.14.); calculation of the crystalline parameters gave values of 2.6 nm and 4.1 nm for L_c and L_a, respectively.

Porous activated carbon spheres infused with elemental sulfur have previously been applied at Li-S battery cathode materials.(3)(49) Having an S content of 28.9 %, the PSSP-AW sample was assembled into a coin cell and tested for this application through CCP measurements (Figure Apx.15.). The performance was relatively poor however with a reversible specific capacity of only about 25 mAh g^{-1} after 20 charge-discharge cycles, indicating that the materials suffer from the same issues as the ice-templated PSSC materials with regards to Li-S battery performance.

5.8. Conclusions and Remarks

Hierarchically porous S-infused activated carbons were prepared *via* a facile ice-templating and one-step pyrolysis and *in-situ* activation technique, employing PSS as the sole precursor. On heating under Ar, the ice-templated monoliths underwent intermolecular crosslinking at ~450 °C with the *in-situ* generation of Na_2SO_4. The crosslinking stabilises the monoliths, preserving the ice-templated morphology upon higher temperature carbonisation, whilst the

Na_2SO_4 acts as a chemical activating agent. Continued heating to 800 °C induces carbonisation and activation, with the generation of Na_2S and other sulfur salts. Upon a subsequent acid wash, these sulfur salts are converted to elemental S, which is primarily embedded within the micropores of the porous carbon. This S could be selectively removed by heating under vacuum at various temperatures, which would increase the surface area above 1000 m^2 g^{-1}. The process can be regarded as a highly straightforward way in which to prepare S-infused templated porous carbons, which would typically employ relatively complex multi-step hard or soft templating strategies along with post-activation and S-infusion. Underlying mechanisms behind the processes are proposed, which were supported by empirical observations, various characterisation techniques and previous literature reports. The S content could also be increased by simply adding Na_2SO_4 with the aqueous PSS prior to ice-templating, reaching a maximum of 39.7 wt. %. This optimised material was evaluated as a cathode for the LIS battery although performance was poor by literature standards. Further investigation and optimisation of the material, its analogues and/or composites could improve this performance, and the elucidation of the underlying mechanism may serve as a strategy for the synthesis of related materials.

5.9. References

1. Bruce PG, Freunberger S a., Hardwick LJ, Tarascon J-M (2011) *Nat Mater* 11(2):172–172.
2. Ji X, Nazar LF (2010) Advances in Li-S batteries. *J Mater Chem* 20(44):9821–9826.
3. Zhang B, Qin X, Li GR, Gao XP (2010) *Energy Environ Sci* 3(10):1531.
4. Zhou W, Xiao X, Cai M, Yang L (2014) *Nano Lett* 14(9):5250–5256.
5. Agrawal M, et al. (2014) *J Power Sources* 261(0):363–370.
6. Xu G, et al. (2013) *J Mater Chem A* 1(14):4490.
7. Zhang C, Wu H Bin, Yuan C, Guo Z, Lou XWD (2012) *Angew Chemie* 124(38):9730–9733.
8. Wang J, He Y-S, Yang J (2015) *Adv Mater* 27(3):569–575.
9. Zhao C, et al. (2014) *Nanoscale* 6(2):882–888.
10. Zheng G, Yang Y, Cha JJ, Hong SS, Cui Y (2011) *Nano Lett* 11(10):4462–4467.
11. Ji X, Lee KT, Nazar LF (2009) *Nat Mater* 8(6):500–506.
12. Zhang H, Cooper AI (2007) *Adv Mater* 19(11):1529–1533.
13. Zhang H, et al. (2005) *Nat Mater* 4(10):787–793.
14. Grundy M, Ye Z (2014) *J Mater Chem A* 2(47):20316–20330.
15. Roberts AD, Wang S, Li X, Zhang H (2014) *J Mater Chem A* 2(42):17787–17796.
16. Nishihara H, Mukai SR, Tamon H (2004) *Carbon* 42(4):899–901.
17. Hong YB, et al. (2014) *Synth Met* 196(0):33–37.
18. Ling Z, et al. (2015) *Nanotechnology* 26(37):374003.
19. Sahore R, Estevez LP, Ramanujapuram A, Disalvo FJ, Giannelis EP (2015) *J Power Sources* 297:188–194.
20. Choi Y-M, et al. (2015) *Energy Technol* 4(2):278–287.
21. Jiang DD, Yao Q, McKinney M a., Wilkie C a. (1999) *Polym Degrad Stab* 63(3):423–434.
22. Raiß C, Peppler K, Adelhelm P (2014) *Carbon* 79:1–11.
23. Nash DB (1986) *Lunar and Planetary Institute Science Conference Abstracts*, pp 603–604.
24. Sevilla M, Mokaya R (2014) *Energy Environ Sci* 7(4):1250–1280.
25. Hines D, Bagreev A, Bandosz TJ (2004) *Langmuir* 20(8):3388–3397.
26. Puthusseri D, Aravindan V, Madhavi S, Ogale S (2014) *Energy Environ Sci* 7(2):728.
27. Singare PU, Lokhande RS, Madyal RS (2010) *Russ J Gen Chem* 80(3):527–532.
28. Lichtman D, Craig Jr JH, Sailer V, Drinkwine M (1981) *Appl Surf Sci* 7(4):325–331.
29. Van Loon WMGM, Boon JJ, De Groot B (1993) *Environ Sci Technol* 27(12):2387–2396.
30. Siggia S, Whitlock LR (1970) *Anal Chem* 42(14):1719–1724.

31. Nakagawa H, Watanabe K, Harada Y, Miura K (1999) *Carbon* 37(9):1455–1461.
32. Younker JM, Saito T, Hunt MA, Naskar AK, Beste A (2013) *J Am Chem Soc* 135(16):6130–6141.
33. Di Vona ML, et al. (2009) *J Phys Chem B* 113(21):7505–7512.
34. Wu D, et al. (2010) *J Memb Sci* 348(1–2):167–173.
35. Hines D (2003) *Highly Porous Activated Carbons Derived from Polystyrene Sulfonic Acid Based Organic Salts* (City College of New York, 2004).
36. Yao Q, Wilkie CA (1999) *Polym Degrad Stab* 66(3):379–384.
37. Beavon DK Process for sulfur production. US patent 4406873 A, 1983.
38. Bandermann F, Harder K-B (1982) *Int J Hydrogen Energy* 7(6):471–475.
39. Humeres E, Peruch M da GB, Moreira RFPM, Schreiner W (2003) *J Phys Org Chem* 16(10):824–830.
40. Ryu HS, et al. (2013) *J Mater Chem A* 1(207890):1573.
41. Davis RE (1958) *J Am Chem Soc* 80(14):3565–3569.
42. Ji L, et al. (2011) *Energy Environ Sci* 4(12):5053.
43. Xin S, et al. (2012) *J Am Chem Soc* 134(45):18510–18513.
44. Li Z, et al. (2013) *Adv Energy Mater* 4(7):1–8.
45. Nandiyanto ABD, Okuyama K (2011) *Adv Powder Technol* 22(1):1–19.
46. Roberts AD, Li X, Zhang H (2014) *Chem Soc Rev* 43(13):4341–4356.
47. Sing KSW, et al. (1985) *Pure Appl Chem* 57(4):603–619.
48. Thommes M, et al. (2015) *Pure Appl Chem* 87(9–10):1051–1069.
49. Yang Y, Zheng G, Cui Y (2013) *Chem Soc Rev* 42(7):3018–3032.

Chapter 6

Conclusions and Outlook

6.1. Conclusions

Although templated carbons have displayed exceptional performances in various energy storage devices, their practical utilisation is hindered by their relatively complex fabrication procedures. This thesis investigated a relatively unexplored pathway for the fabrication of templated carbons, namely ice-templating, which can be considered relatively facile compared to other templating methodologies. Although far from perfect, the strategies developed and materials produced could be considered a step forward in realising the ultimate goal of commercialisation in practical devices.

In Chapter 3, the commercially available polymer PAN was used as the precursor for ITPCs and a host of composite materials were produced to demonstrate the simplicity of the process. The resultant ITPCs, which had relatively high residual N-contents and moderate BET surface area values, displayed fairly good performance as LIB anode materials – despite the relatively simple ice-templating process.

In Chapter 4, we continued with the work done in Chapter 3, but significantly simplified the ITPC preparation procedure by replacing cryogenic freezing with ordinary freezer freezing, and freeze-drying with a H_2O solvent exchange process. The materials, soaked in KOH solutions of various concentrations, could have their resultant BET surface area and N-content tuned to a degree, and showed good performance as CO_2 uptake materials and reasonable performance as H_2 uptake materials.

In Chapter 5, ITPCs which displayed the phenomenon of *in-situ* crosslinking and activation, and had elemental S confined within the micropores, were prepared from a PSS polymer precursor. These peculiar observations were investigated and compared with previous literature reports, and an alternative mechanism to the one accepted by previous publications was proposed. The S-infued ITPCs were evaluated for their performance as LIS battery cathode materials, where they displayed the characteristic electrochemical profiles although actual performance by literature standards was poor.

6.2. Future Outlook

This author believes that the use of ice-templating as a route to porous carbons for energy storage (and other) applications remains a relatively unexplored area, and that many more advancements could be made without great effort. In particular, the scope for producing various composite materials for specific applications is huge, with only the surface being scratched thus far. Despite this, however, this author finds it unlikely that ITPCs will reach the ultimate goal of practical use in energy storage devices, due to the fundamental limitations of the ice-templating process such as pore size-control and few suitable precursors.

6.3. Acknowledging Weaknesses and Reflecting on this PhD

The author acknowledges the limitations of work carried out for this thesis, particularly the relatively narrow scope of the work carried out. With hindsight, the quality and breadth of this work could have been expanded by exploring alternative strategies for materials fabrication – rather than focusing solely on ice-templating methodologies. Difficulties with access to equipment was also a significant problem which affected the quality of work produced, as these restrictions often bottlenecked studies and limited the number of samples that could be prepared and characterised fully. Having said this, the author learned a great deal on how to make the best of non-ideal situations from this PhD and has developed significantly as a person.

Appendix

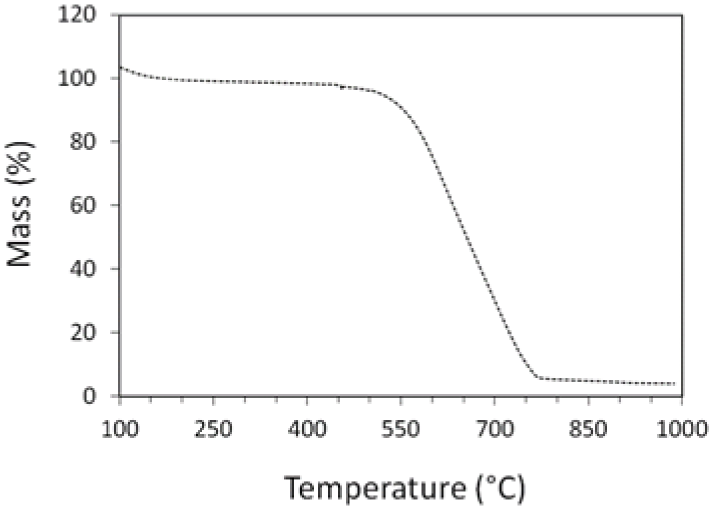

Figure Apx.1. TGA profile of CPAN50 heated under air

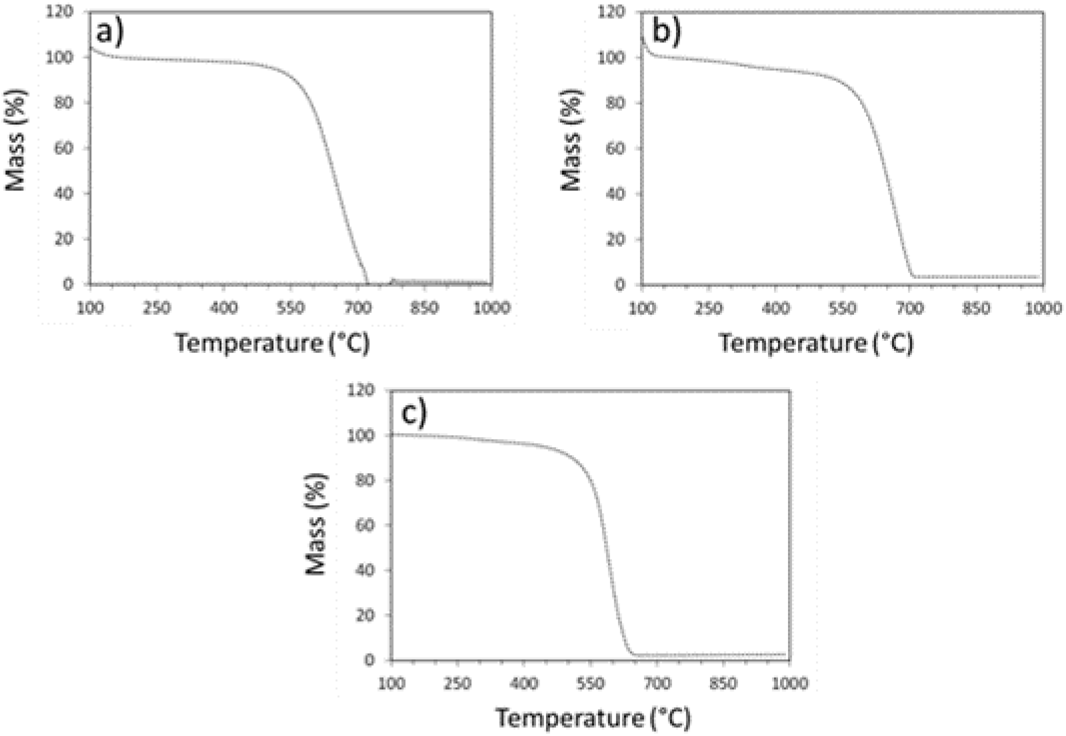

Figure Apx.2. TGA profiles of IT-AC0, IT-AC50 and IT-ACMAX heated under air

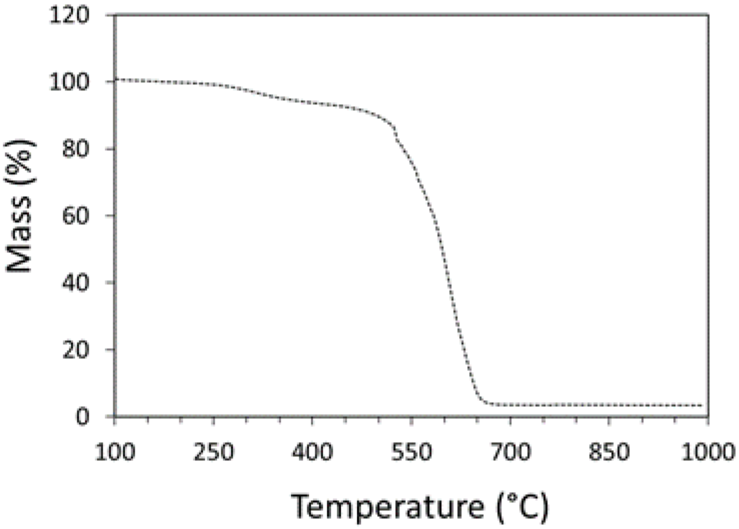

Figure Apx.3. TGA profile of Na_2SO_4-MAX-C heated under air

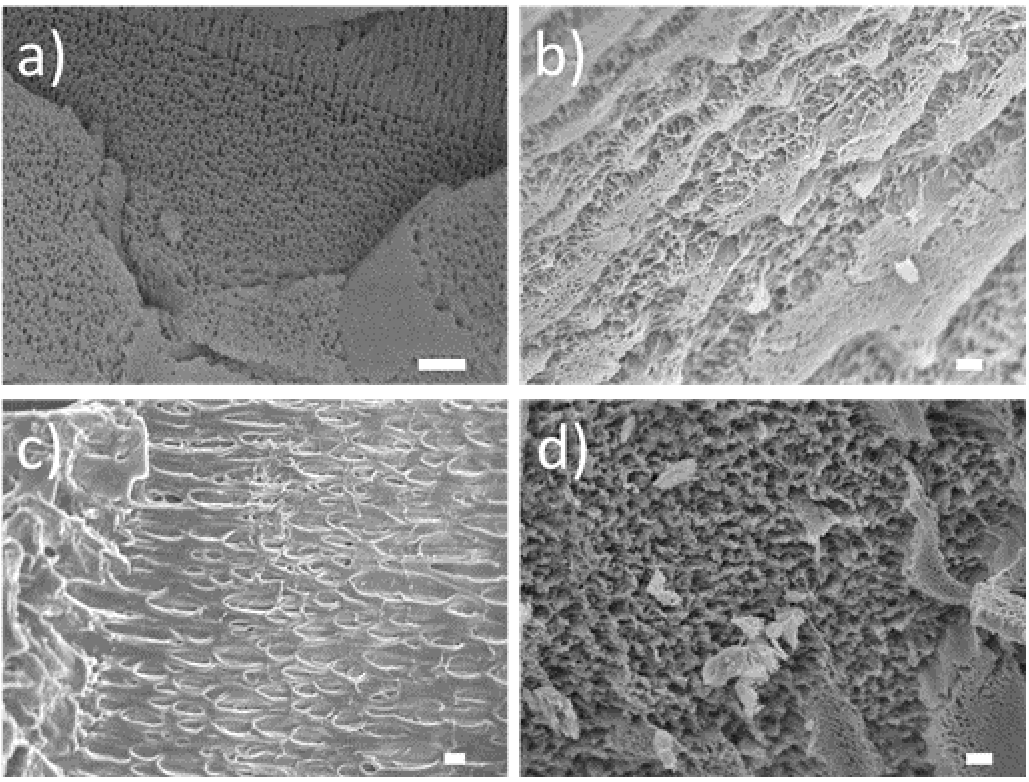

Figure Apx.4. SEM images of a) PAN10C, b) Na_2SO_4-30-C, c) Li_2SO_4-30-C and d) K_2HPO_4-30-C

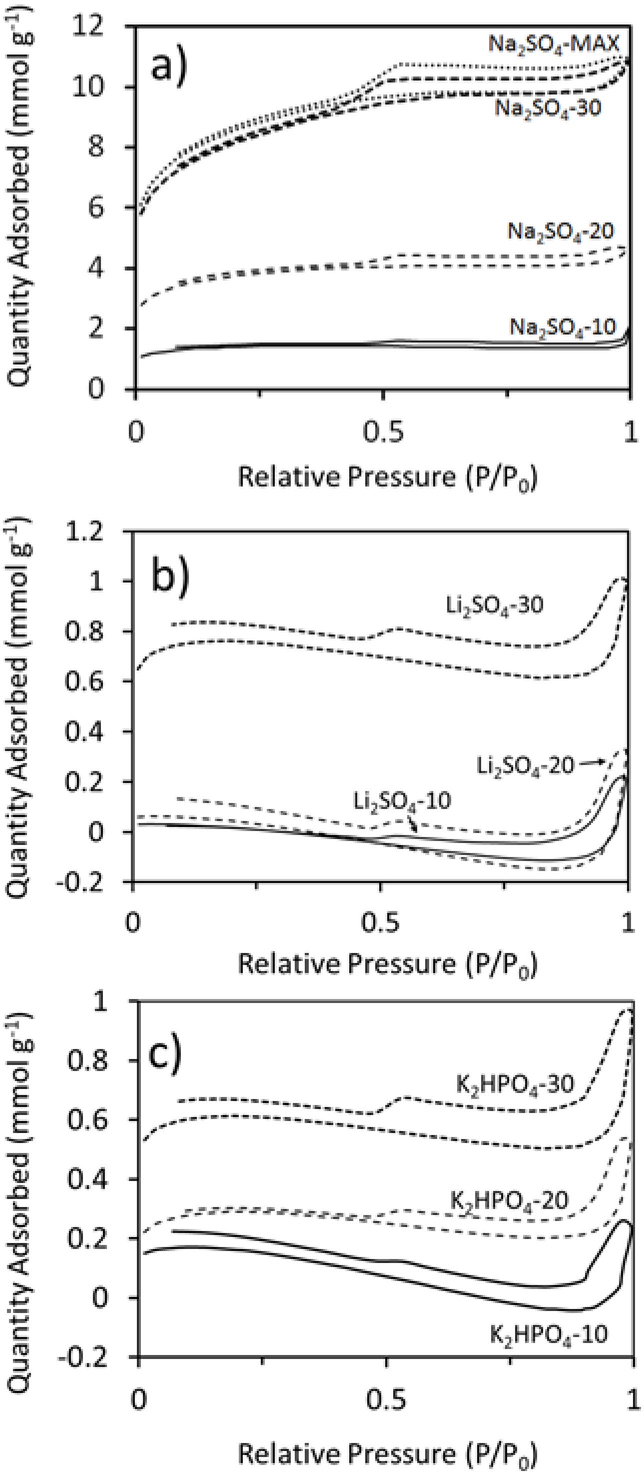

Figure Apx.5. N_2 gas sorption isotherms for materials activated with a) Na_2SO_4, b) Li_2SO_4 and c) K_2HPO_4

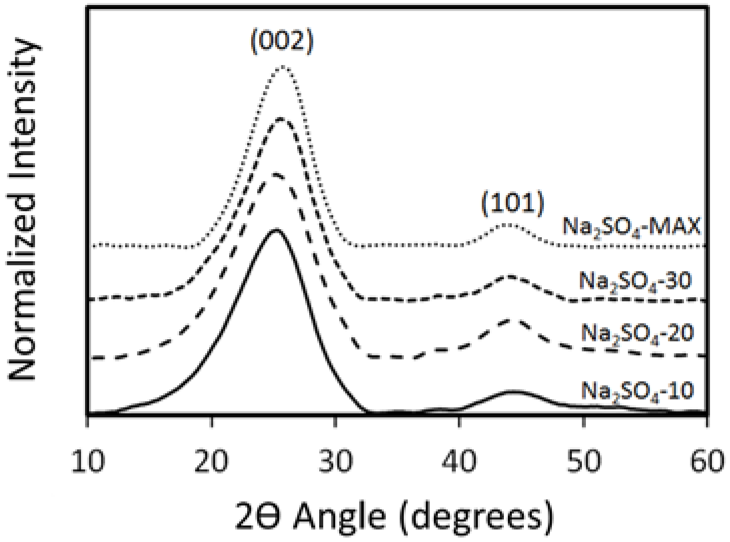

Figure Apx.6. XRD diffractograms for the Na_2SO_4 activated samples

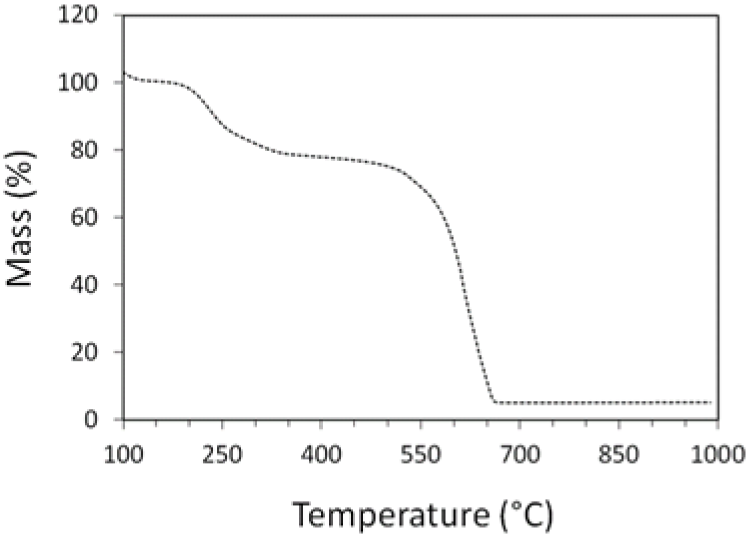

Figure Apx.7. TGA profile of PSS150C-AW heated under air

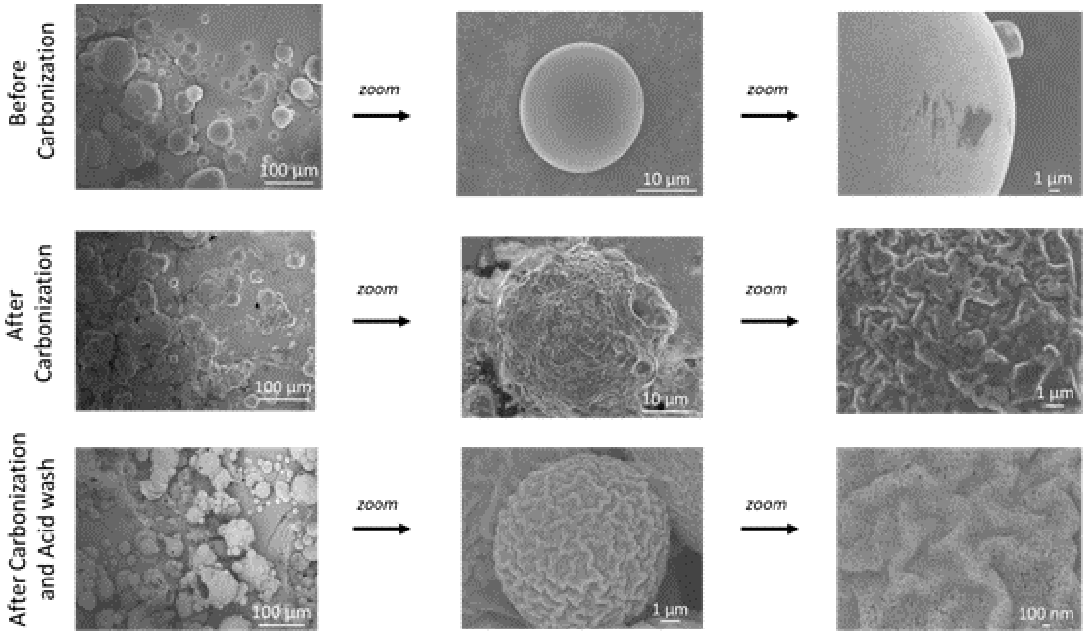

Figure Apx.8. SEM images of PSS powder before carbonization, after carbonization and after carbonization and an acid wash at various levels of magnification

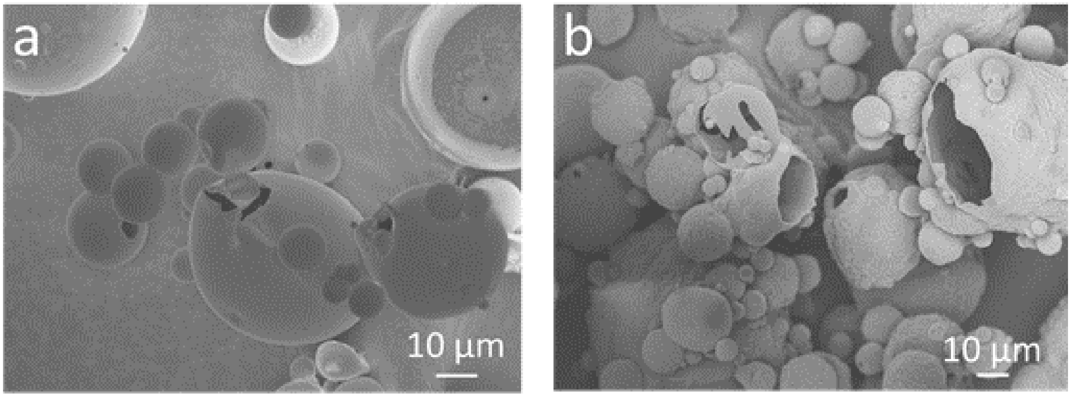

Figure Apx.9. SEM images showing hollow nature of PSS spheres a) before and b) after carbonization

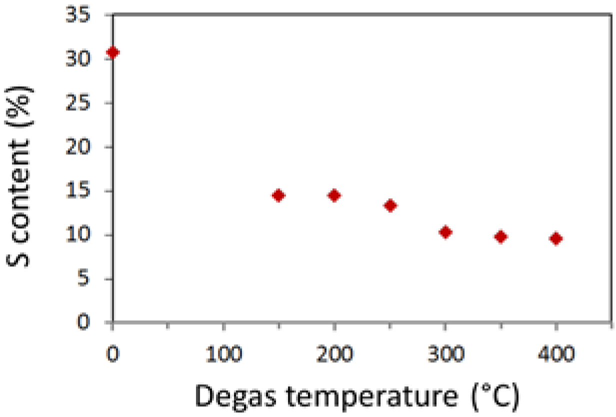

Figure Apx.10. Graph showing decreasing S content with increasing degas temperature for PSSP-AW

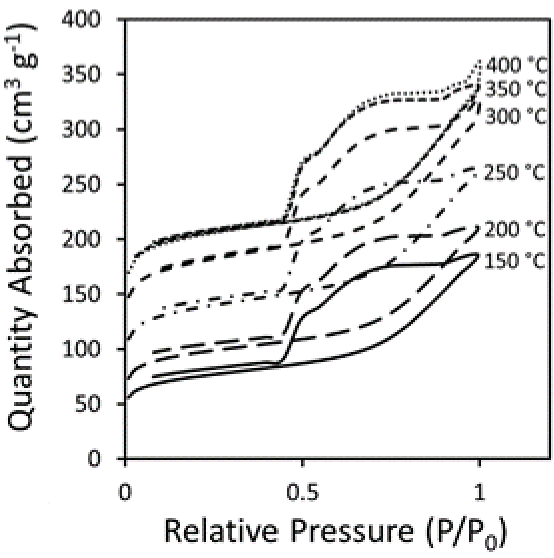

Figure Apx.11. N_2 gas sorption isotherms for PSSP-AW subject to degassing at various temperatures

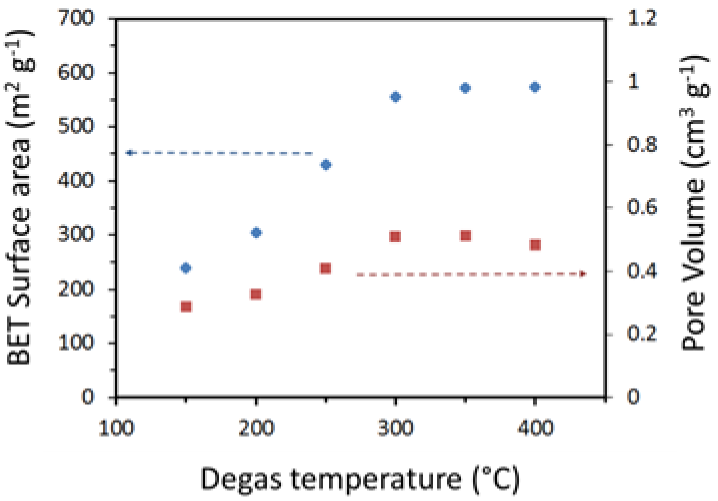

Figure Apx.12. BET surface areas and pore volumes for PSSP-AW subject to degassing at various temperatures

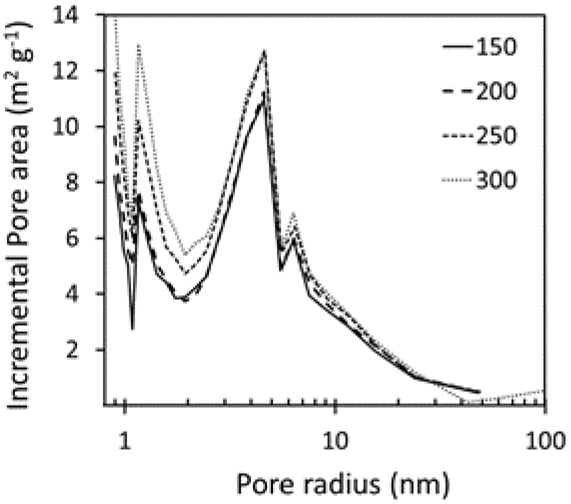

Figure Apx.13. BJH pore size distribution plots for PSSP-AW subject to degassing at various temperatures

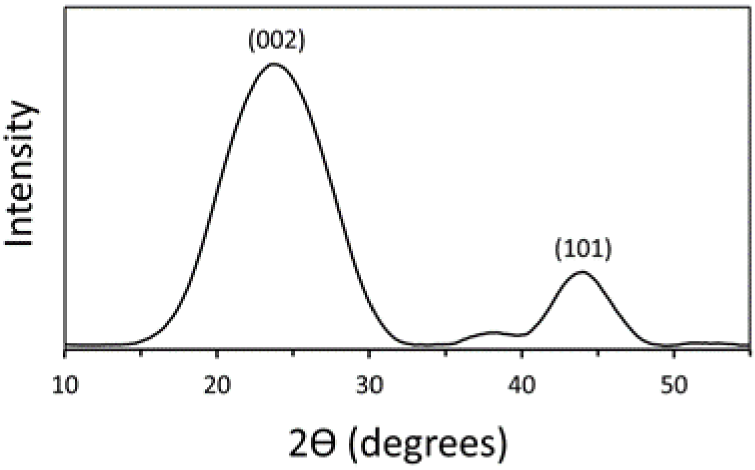

Figure Apx.14. PXRD diffractogram for PSSP-AW

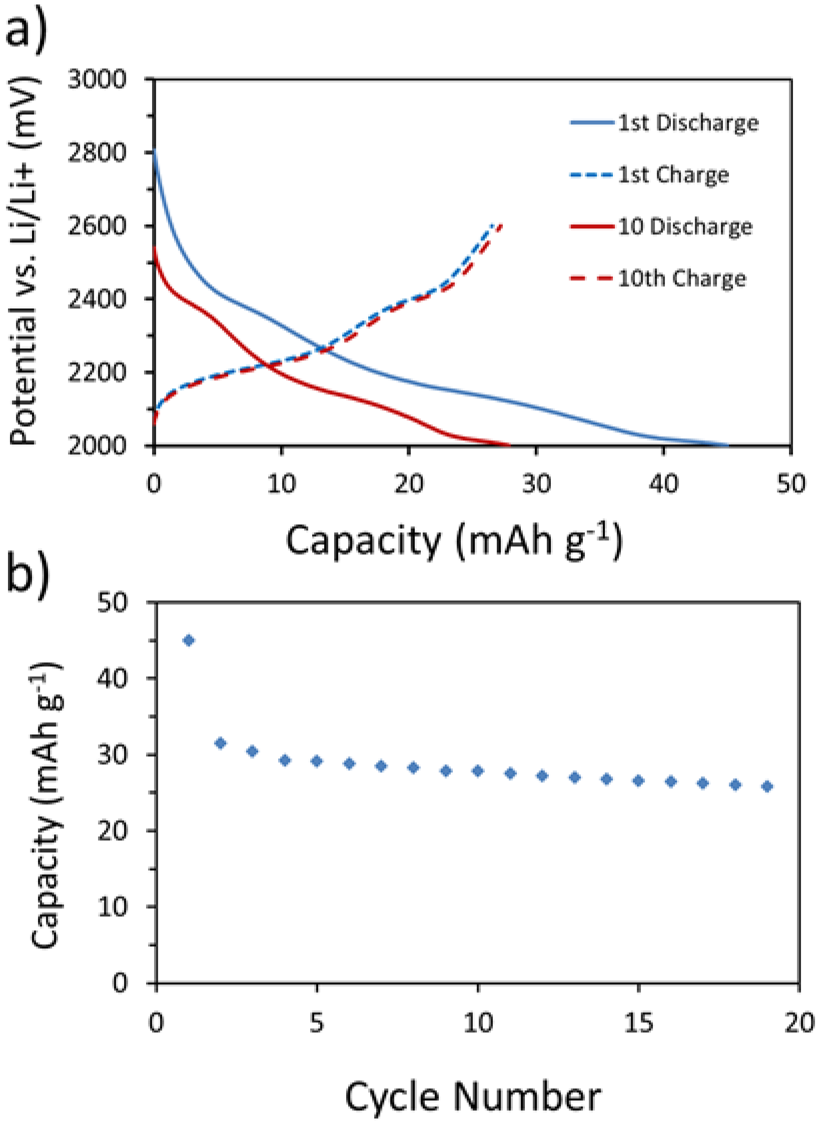

Figure Apx.15. a) CCP curves and c) cycle stability profile for the PSSP-AW material tested as a LIS battery cathode material